THESIS

FRACTURES WITHIN THE IRISH CANYON-VERMILLION CREEK AREA, NORTHEASTERN UINTA MOUNTAINS, NORTHWESTERN COLORADO

Submitted by

John Peter Detring

Department of Geosciences

In partial fulfillment of the requirements

for the Degree of Master of Science

Colorado State University

Fort Collins, Colorado

Fall 2009

COLORADO STATE UNIVERSITY

August 6, 2009

WE HEREBY RECOMMEND THAT THE THESIS PREPARED UNDER OUR SUPERVISION BY JOHN P. DETRING ENTITLED "FRACTURES WITHIN THE IRISH CANYON-VERMILLION CREEK AREA, NORTHEASTERN UINTA MOUNTAINS, NORTHWESTERN COLORADO" BE ACCEPTED AS FULFILLING IN PART REQUIREMENTS FOR THE DEGREE OF MASTER OF SCIENCE

Committee on Graduate Work

(Derek L. Schutt)

(Thomas J. Siller)

Advisor (Eric E. Erslev)

Departmental Head (Sally J. Sutton)

ABSTRACT OF THESIS

FRACTURES WITHIN THE IRISH CANYON-VERMILLION CREEK AREA, NORTHEASTERN UINTA MOUNTAINS, NORTHWESTERN COLORADO

In the northeast Uinta Mountains, fold axes are observed to be consistent with Laramide ENE-WSW shortening and Sevier NW-SE shortening. The structural trends and fracture patterns may be due to the cumulative effects of Laramide and Sevier deformation. This research addresses the timing and mechanisms of fracturing within eastern Uinta Mountains, as well as the controls on post-orogenic fracturing. These results will hopefully aid in testing current regional tectonic models, as well as aid in predictions of fracture permeability in analogous water and hydrocarbon producing, basement-involved orogenic basins worldwide. This study analyzes the kinematic indicators and structural geometries within the extreme northeastern Uinta arch, NW Colorado, USA, to resolve its complex strain history.

Fracture systems provide permeability as well as create traps in petroleum reservoirs. An understanding of the orientation and timing of fracture systems can test current tectonic models and allow for predictions of fracture orientation as well as allow for predictions of which fractures are open, closed, and fluid conducting.

Systematic fracture data collection, detailed field mapping, kinematic analyses, and a combination of 2D seismic interpretations and cross-section analyses were used to

address questions concerning the structural geometry and fracture history within the northeastern Uinta Mountains. Data from geologic mapping, 722 slickensided minor faults, 996 joints and the interpretation of a 2D seismic line were used to determine the fracture history and geometry of the Irish Canyon-Vermillion Creek area.

Fracture data were collected at 34 stations in pre- and post-Laramide rocks to obtain average joint orientations and to calculate the ideal σ_1 orientations of minor faults. Restoration of 2D structural models, constrained by map and 2D seismic data, were conducted using line length balancing techniques which showed that a significant amount of interlayer slip is necessary for a viable structural interpretation.

Fault analyses indicate multidirectional deformation with ENE-WSW and NNE-SSW σ_1 orientations. There is a predominance of left-lateral faulting associated with the first stage of deformation and a predominance of right-lateral faulting associated with the second stage of deformation. Evidence for this sequence is the observation of right-lateral faults associated with the NNE-SSW σ_1 cross-cutting left-lateral faults associated with the ENE-WSW σ_1.

Joint measurements are trimodal in distribution, with average strikes of N71E, N1E, and N40W. Abutting relationships suggest that the N71E-striking joints are primary and the N1E-striking joints are secondary. The N40W-striking joint set is only found within the Oligocene Bishop Conglomerate and Miocene Browns Park Formation and their strike parallels regional normal faults. Therefore, this set is likely due to extension during the Miocene to Holocene and post dates Laramide deformation.

Folding of the Mancos Shale and back-thrusting of the Browns Park Formation were observed in the northeastern portion of the field area. This deformation is possibly in

response to the overlying Browns Park Formation gravitationally sliding down dip along its contact with the Mancos Shale.

The tectonic history of the Irish Canyon-Vermillion Creek area is consistent with three stages of deformation. The first stage is characterized by N59E-directed thrusting, conjugate strike-slip faulting, and the N71E-striking joint set. The second stage is characterized by an E-W extension resulting in a system of NNW-directed right-lateral faults, localized NNE-directed transpressional thrust faulting, and the N1E-striking joint set. The third stage is by characterized by NE-SW extension resulting in N52W-striking normal faults and the N40W-striking joint set. The first stage of deformation can be attributed to Laramide compression. The second stage of deformation was probably due to a poorly documented late-Sevier/late-Laramide, or post-Laramide event, or a combination of these events. The third stage of deformation can be attributed to a Miocene to Holocene NE-SW extension.

John Peter Detring
Geosciences Department
Colorado State University
Fort Collins, CO 80523
Fall 2009

ACKNOWLEDGMENTS

This research was funded by grants from Colorado State University, Ed Warner, and ConocoPhillips. 2DMove software was donated to Colorado State University by Midland Valley Exploration. Erika Davis, Tony LeFevre, and Vincent Rigatti of Questar Market Resources, Inc. and Richard Newhart of Encana Oil and Gas (USA), Inc. provided helpful conversations, two 2D seismic lines, a structure contour map, subsurface fracture data of the area just north of the study area, and helpful seismic interpretation aid. Brian Horn of British Petroleum Exploration donated six 2D seismic lines to the project. Greg Anderson of Samson Resources donated a structure contour map as well as his and his staff's time to share 3D seismic images of the area.

The National Park Service Geologic Resource Division provided useful training in ArcGIS. Particular thanks go to Jim Chapple who provided invaluable guidance through the intricacies of GIS and the problems that arose while creating my digitized field map. Enormous thanks go to Fred and Joy Blevins of the Browns Park Store. This research would not have been possible without them.

Special thanks go to my advisor Eric Erslev who provided constant motivation and support. Without his knowledge and support this project would not have been completed. Thank you, Eric. Thanks go to my committee members Dr. Derek Schutt and Dr. Thomas Siller for their invaluable ideas and discussions. Thanks go to Dr. Dennis Harry for his insightful geophysical instruction and discussions. Thanks go to Scott Larson, Cyrus

Gillett, Dr. Chris Holm-Denoma, and Tim Riley for detailed help with my thesis. Warm thanks go to all my friends and colleagues at Colorado State University and Florida State University for making my days in the department a wonderful experience. Lastly, enormous thanks to my family, Reed, Margery, Erika, Kato, and Hadley for always being supportive and always being there for me.

TABLE OF CONTENTS

CHAPTER I. INTRODUCTION

The Rocky Mountains of the USA are a classic example of a basement-involved thrust system. Within the U.S., the range is characterized by a system of anastomosing and bifurcating basement arches that bound the northern and eastern margins of the Colorado Plateau (Fig. 1) (Erslev, 2005; Erslev and Larson, 2006). Basement arches are defined as elongate, upwardly bowed crustal segments which are typically bound by thrusts and or reverse faults on their flanks. Basement arches differ from uplifts in that horizontal motions are primarily responsible for the deformation, as opposed to suggested vertical motions.

The orientations of the Laramide arches vary greatly throughout the Rocky Mountains and range from more east-west-trending (Owl Creek arch, the Granite Mountains of Wyoming, and the Uinta Mountains of Colorado) to more north-south-trending (Front Range, Douglas Creek Arch, and Park Ranges of Colorado, the Laramie arch of Wyoming) (Fig. 1). In the NE Uinta Mountains, directly adjacent fold axes are consistent with Laramide ENE-WSW shortening and Sevier NW-SE shortening (fig. 2) (Gregson and Erslev, 1997; Erslev and Wiechelman, 1997). Laramide deformation extended from the Late Cretaceous to at least the end of the Paleocene and possibly into the Eocene (approximately 80 to 40 Ma) (Perry and Flores, 1997; Erslev, 2005). Sevier deformation extended from Late Jurassic to Paleogene (approximately 170 Ma to 40 Ma) (Paulsen and Marshak, 1999; Silliphant and Engelder, 2001).

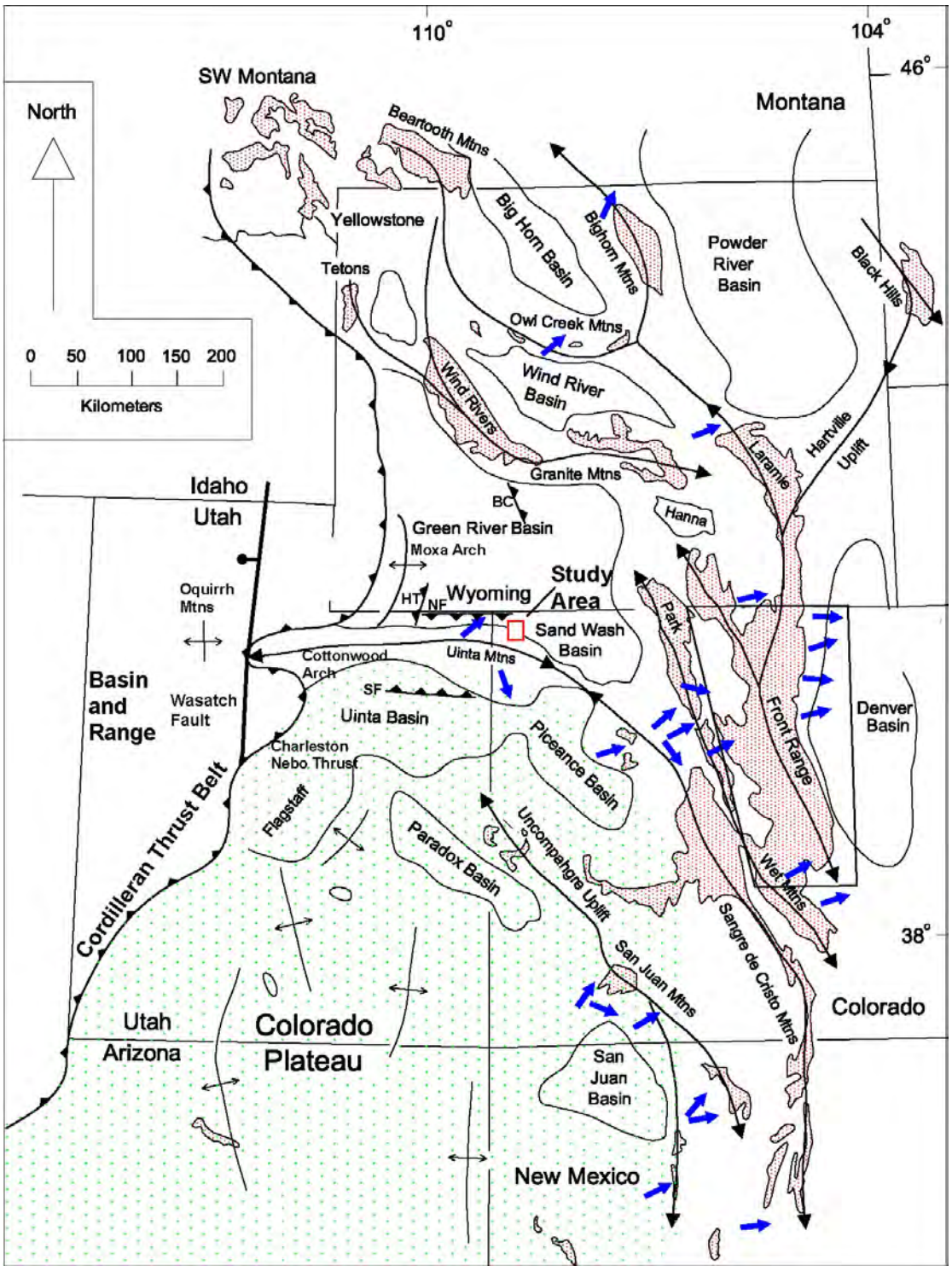

Figure 1. Map of the Laramide foreland illustrating anastomosing and bifurcating nature of basement-cored arches and spatial relationships with the adjacent basins, thrust belt, Colorado Plateau, and the North American Craton. The field site composed of the Irish Canyon-Vermillion Creek (IC-VC) area is represented by the red box located in NW Colorado. The thick, blue arrows represent shortening directions (Erslev and Larson, 2006). NF=North Flank thrust, SF=South Flank thrust, HT= Hogsback thrust, BC= Beavers Creek thrust.

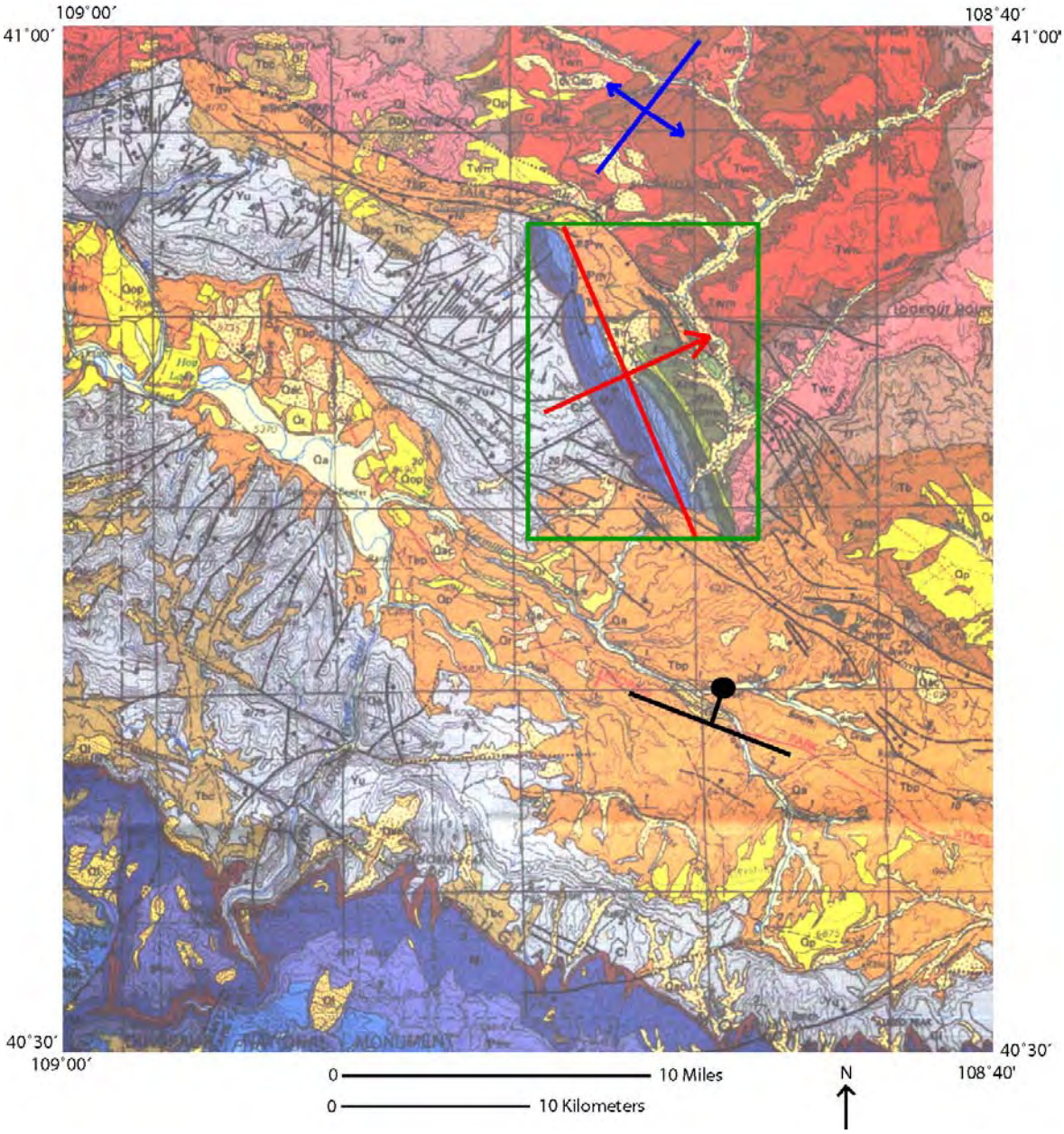

Figure 2. Geologic map of the Vernal 1˚X 2˚ quadrangle showing multiple tectonic stresses and differing structural grains in northwest Colorado. Red=Laramide, blue=Sevier, and black=Browns Park extension (Taken from Rowley et al., 1985). Study area and location of plate 1 outlined by green box.

Previous investigators throughout the Rocky Mountains (Smithson et al., 1979; Gries, 1983; Lowell, 1983; Lowell and Gries, 1983; Stone, 1984; Brown, 1984; Erslev, 1986; Spang and Evans, 1988) have shown that horizontal compression accommodated by basement-involved thrusting occurred throughout the Rocky Mountains; however, the large variations in fold axis orientations of the arches have spawned diverse tectonic models.

Enigmatic east-west-trending basement arches oriented oblique to the regional trend have been explained by numerous models formulated from studies conducted outside the field area (Erslev and Koenig, 2009). Such as: N-S compression (Gries, 1983), reactivation of pre-existing weaknesses (Hansen, 1986b), linkage in strike-slip bridge structures (Paylor and Yin, 1993), oblique reverse slip on planes of pre-existing weakness (Molzer and Erslev, 1995), and eastward translation of the Uinta aulacogen (Gregson and Erslev, 1997).

Hypotheses for the generation of fractures within the Rocky Mountains are equally diverse and include topographic release due to uplift and erosion (Hancock and Engelder, 1989), current Rio Grande rifting (Hancock and Engelder, 1989), syn-Laramide shortening (Narr, 1982; Stone, 1995), pre-Laramide Sevier shortening (Condon, 1997), Basin and Range extension (Erslev, 2001), Miocene Browns Park extension (Stevens, 2002), and elastic rebound of Laramide strain (Ruf and Erslev, 2005).

The study area lies within the 1300 km^2 Vermillion Basin, a sub-basin of the Green River Basin. The strata within the basin contain a full representation of sedimentation from the Proterozoic through the Holocene excluding the Ordovician through the Devonian. This area was selected due to excellent exposures of immediately adjacent pre-, syn-, and post-Laramide rocks containing a full array of fractures from the Mesozoic and Cenozoic orogenies.

The research conducted for this study used the detailed analysis of kinematic indicators of strain to resolve the complex strain history within the Irish Canyon-Vermillion Creek area (Plate 1). The premise of this study is that through additional data a better understanding of joint development in the area can be obtained. These results will then aid in testing current regional tectonic models, as well as aid in predictions of fracture permeability in analogous water and hydrocarbon producing, basement-involved orogenic basins worldwide. Studies of earthquake foci in the Sierra Pampeanas have shown that flat slab subduction is associated with the creation of basement-involved structures similar to those found in the Rocky Mountain foreland (Allmendinger and Jordan, 1983; Cahill and Isacks, 1985; Jordan and Allmendinger, 1986; Smalley and Isacks, 1987; Mpodozis and Ramos, 1989; Allmendinger et al., 1990; Ramos et al., 2002).

Faulting within rocks whose ages bracket orogenic events can be used to test current models of regional tectonic development and enhance our understanding of fracture networks within basement-involved orogens. Knowledge of fault systems is vital in that faults can act as barriers restricting the fluid flow of petroleum or water. Conversely, faults can act as first order permeability during fault dilation as well as create secondary porosity.

The timing of joint formation and the subsequent closure and sealing is vital to petroleum production. During the orogenic evolution, joints may have been sealed by subsequent processes and surficial uplift and erosional joints may not propagate to depth (Laubach and Tremain, 1994; Hancock and Engelder, 1989), leaving only ideally-oriented systematic joint sets open and viable for fluid migration.

This investigation attempts to ascertain the detailed geometry, timing, and the mechanisms responsible for the deformation within the Irish Canyon-Vermillion Creek area. These results will help determine the detailed stress and strain history within a complex structural zone as well as illuminate the controls on post-orogenic fracture networks within the area.

CHAPTER II. PREVIOUS WORK

Stratigraphic Summary

Northwestern Colorado was located near a continental margin during the Paleozoic and Mesozoic. Small variations in sea level caused transgressive and regressive sequences to fluctuate back and forth over the region and the strata within the field area reflect these fluctuations.

The Vermillion Basin (Fig. 3) is a sub-basin of the Sand Wash Basin and occupies 1300 km^2 at the borders of Colorado, Utah and Wyoming (Fig. 4). Both the Vermillion Basin and the Sand Wash Basin are sub-basins of the Green River Basin (Fig 1). These basins contain strata representing a relatively complete record of sedimentation from the Precambrian to the Holocene (Tweto, 1979; Hansen, 1986b). The only large hiatus occurs between the Uinta Mountain Group (Late Proterozoic) and the Madison Limestone (Early Mississippian) (Manion, 1961; Boyd, 1993).

Strata analyzed in this study span from the Precambrian Uinta Mountain Group to the Miocene Browns Park Formation (Fig. 5). These formations are briefly described below with respect to common lithofacies, mechanical stratigraphy, sequence stratigraphy and hydrocarbon potential.

Uinta Mountain Group

The Uinta Mountain Group is Late Proterozoic in age (De Grey, 2004; Weil et al., 2006). Detrital zircons yield protolith ages ranging from of 770 Ma to 3350 Ma (Fanning

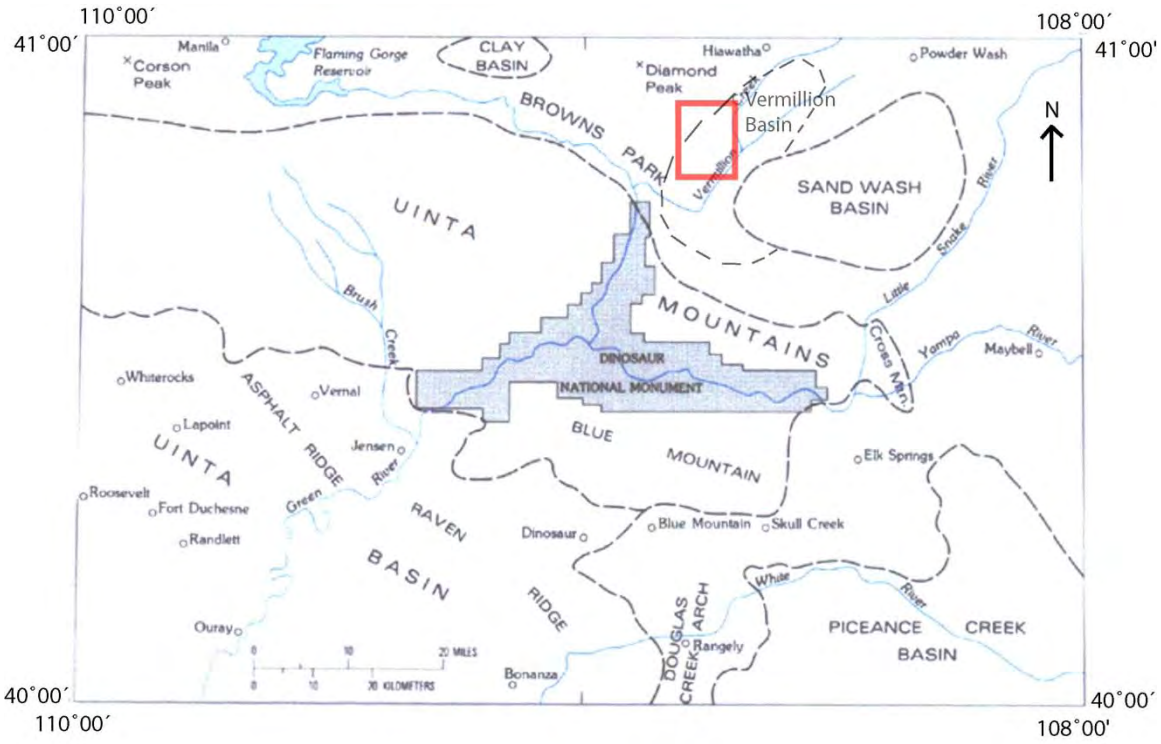

Figure 3. Locality map of major geographic features (Modified from Rowley et al., 1985). Note field site within the Vermillion Basin marked by red box.

and Dehler, 2005). The group consists of resistant, purple to dark-red, medium- to coarse-grained,siliceous, massive sandstones and conglomerates that are divided into three main lithofacies: 1) trough-cross bedded sandstone facies, 2) thickly-bedded to massive sandstone facies, and 3) fine-grained sandstone to shale facies (Miall, 1978; Dehler et al., 2007). The purple to dark-red color is due to ferric-staining. These lithofacies are interpreted as cycles of low energy deposition in braided stream system (DeGray, 2004). The thicknesses of these facies differ throughout the section. This group is 4 to 7 km in thickness (Dehler et al., 2007), however the above ground outcrop thickness is relatively small due to its deposition into a rapidly subsiding basin (Manion, 1961; Hansen 1986b).

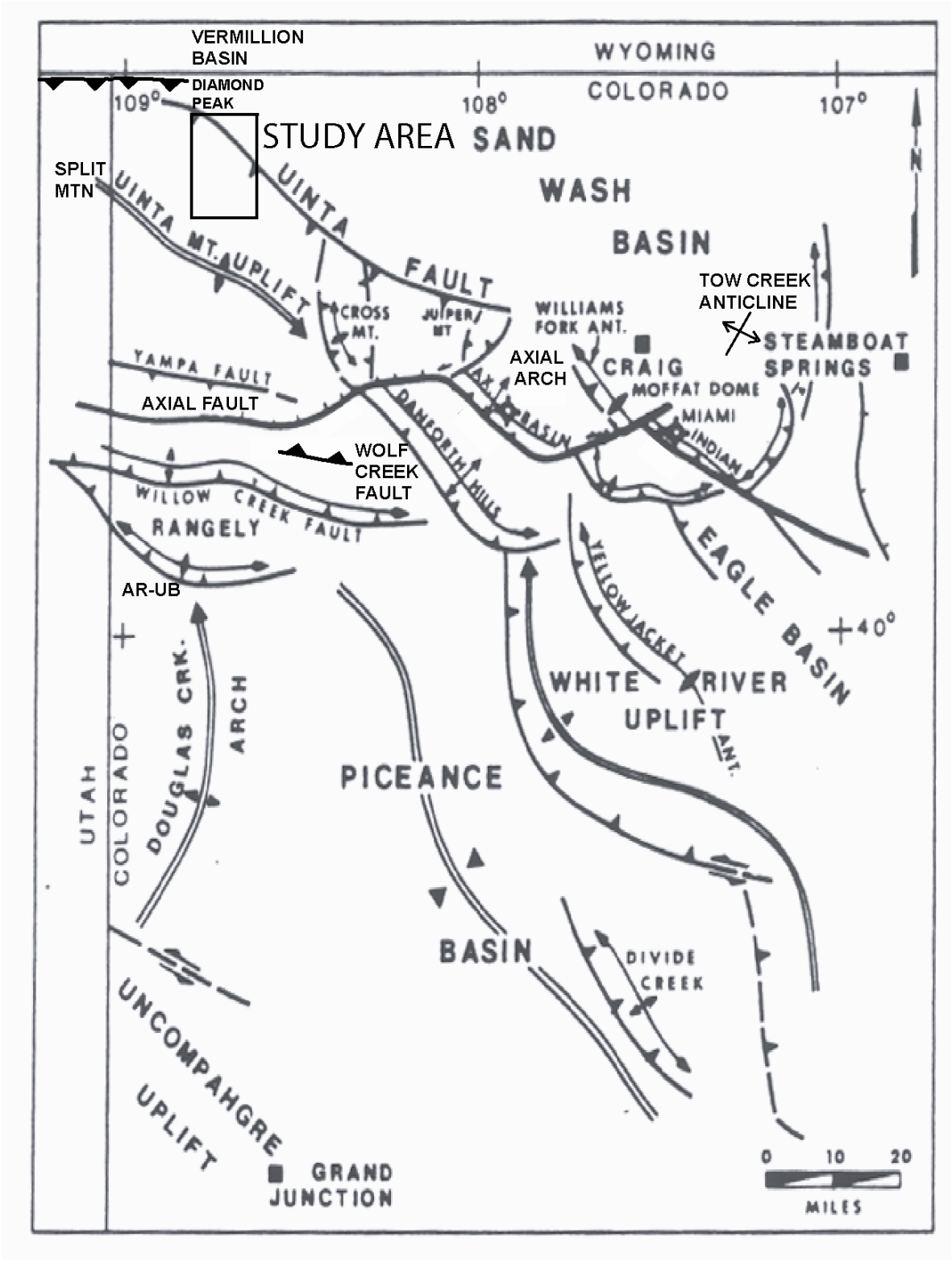

Figure 4. Structural index map of northwest Colorado (Reproduced from Stone, 1986). Irish Canyon-Vermillion Creek study area and location of Plate 1 outlined by black box. AR-UB represents the Asphalt Ridge-Uinta Basin Boundary fault.

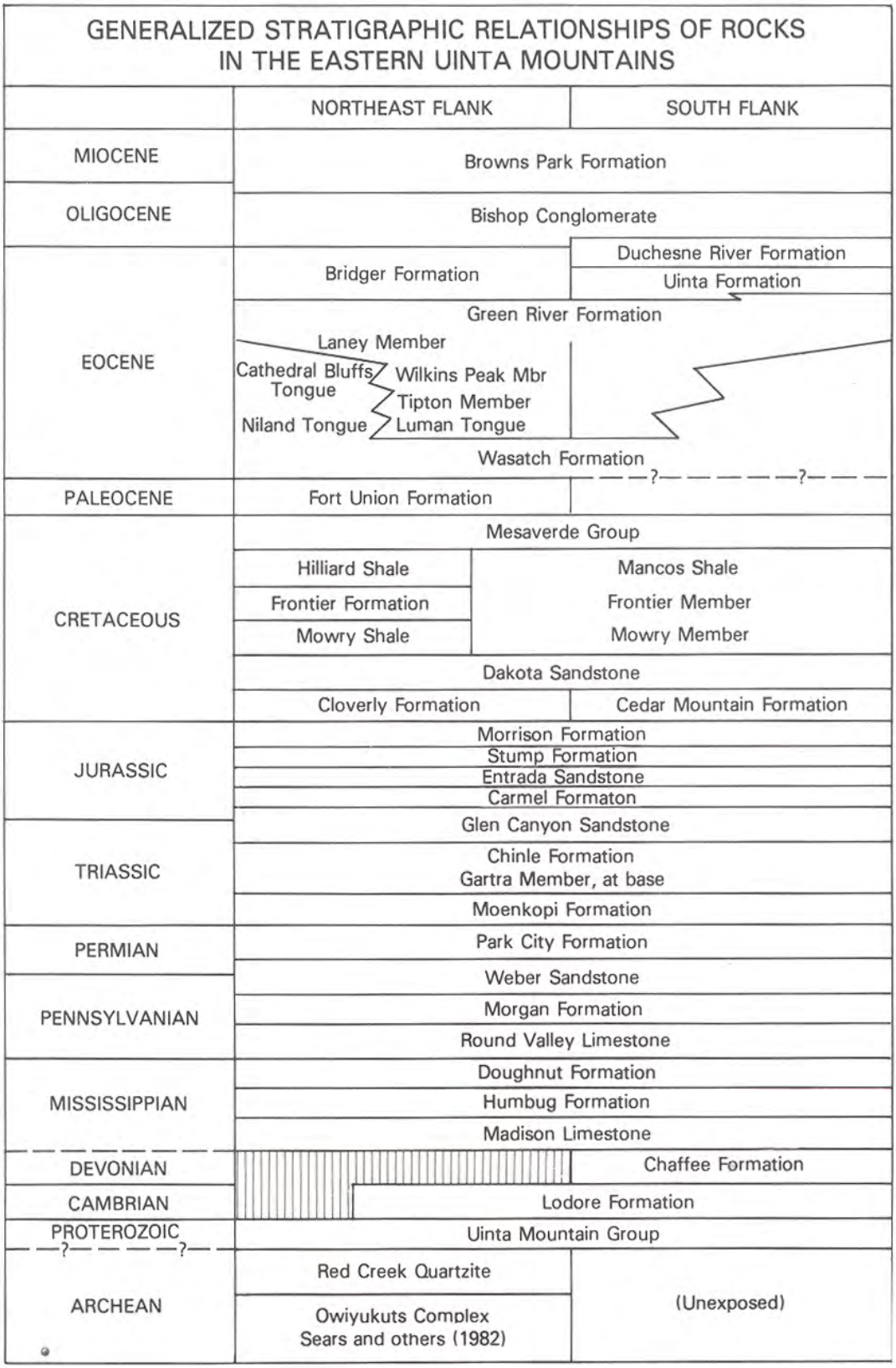

Figure 5. Generalized stratigraphy of the study area (Hansen, 1986b).

Lodore Formation

The Lodore Formation is Late Cambrian in age (Untermann and Untermann, 1954; Herr et al., 1982). It consists of white to red medium- to coarse-grained, massive, cross-bedded, sugary sandstones with interspersed thin beds of purple, muscovite-rich, calcareous shale and siltstone. These are interpreted as transgressive deposits (Manion, 1961). The thickness varies throughout the area from tens of meters in the southern and central portion of the field area to entirely pinching out in the northern portion of the field area (Manion, 1961) (Plate 1).

Madison Limestone

The Madison Limestone is Early Mississippian in age (Hansen, 1986b; Love et al., 1993). It consists of resistant, thin- to massive-bedded, light- to dark-gray, dense, crystalline limestone which is locally dolomitized, fractured, and important in hydrocarbon production (Manion, 1961; Love and Christiansen, 1985; Gregory and Debruin, 1991). The limestones are characterized by seven lithofacies: 1) bioturbated microskeletal wackestone and packstone, 2) heterolithic thin bedded, laminated and interbedded mudstone to grainstone, 3) skeletal grainstone and packstone, 4) ooid grainstone 5) medium-crystal dolomite, 6) structureless or burrowed mudstone, wackestone, and soft pelletal grainstone and 7) algal-laminated mudstone or stromatolites (Smith et al., 2004). These facies are interpreted as transgressive and highstand systems tracts that represent deposition from the middle ramp to coastal tidal flats (Smith et al., 2004). This formation ranges in thickness from 152 m to 305 m (Manion, 1961; Love and Christiansen, 1985).

Morgan Formation

The Morgan Formation is of Early Pennsylvanian age (Sprinkel, 2000) and

consists of white and tan quartz arenites and cross-bedded, fine- to medium-grained, sugary, sandstones interbedded with carbonaceous shales, thin layers of coal, and limestones. The paleoenvironments of the Morgan Formation range from marine transgressive, progradational subtidal carbonate-shelf to shoals, and eolian (Driese and Dott, 1984). This formation ranges in thickness from 195 m to 200 m (Driese and Dott, 1984).

Weber Formation

The Weber Formation is Late Pennsylvanian to Early Permian in age (Sprinkel, 2000). It consists of resistant, white, tan, and rust-colored, fine- to medium-grained, calcareous, massive, feldspathic arenites. These sandstones exhibit large-scale cross-beds. These are interpreted as eolian deposits formed as barchan and transverse dunes (Sprinkel, 2000). The sandstone produces oil in the Rangely Field in Colorado due to diagenetic porosity where dissolution of matrix material and precipitation of a complex sequence of carbonate cements developed a secondary porosity prior to or simultaneously with oil migration (Koelmel, 1986). This formation ranges in thickness from 200 m to 305 m (Manion, 1961; Van Leonen and Selner, 1999).

Park City Formation

The Park City Formation is Permian in age (Sprinkel, 2000). It is a mixed carbonate-siliciclastic-evaporite system consisting of interbedded, light to dark-gray, calcareous limestones, tan shaly sandstones, calcareous sandstones, dolomite, phosphatic shales, anhydrite beds, and cherts (Manion, 1961; Hendrix, 2000). The shaly units contain concretions of marcasite. The Park City caps the Weber Sandstone. These facies are

interpreted as sabkha and peritidal deposits (Whalen, 1991; Hendrix, 2000). This formation ranges in thickness from 38 m to 83 m (Peterson, 1984).

The Woodside Formation

The Woodside Formation is Early Triassic in age (Manion, 1961; Love et al., 1993) and consists of gray to gray-green shales with interbedded sandstones, siltstones, and gypsum (Love and Christiansen, 1985). These deposits are interpreted as marking the cessation of the Permian marine transgressive-regressive sequence (Manion, 1961). This formation ranges in thickness from 152 m to 395 m (Manion, 1961; Van Leonen and Selner, 1999).

Chinle Formation

The Chinle Formation is Late Triassic in age (Jensen et al., 2005). It consists of soft to medium-resistant, tan, light-gray, light-green, purple, and medium- to dark-red siltstone, sandstone, shale, gravel conglomerate, claystone, and mudstones. Commonly plant and vertebrate fossil remains are present (Ericson, 2006). The various fluvial and lacustrine lithofacies are interpreted as a meandering stream and floodplain deposits in a lowland setting (Ericson, 2006). This formation ranges in thickness from 100 m to 107 m (Manion, 1961; Van Leonen and Selner, 1999).

Navajo Sandstone

The Navajo Sandstone is Late Triassic or Early Jurassic in age (Love and Christiansen, 1980). It consists of resistant, fine- to medium-grained white, light-gray, and rust-colored, large-scale, trough cross-bedded quartz arenites that were deposited during the Jurassic in an erg. This unit is also referred to as the Glen Canyon or the Nugget

Formation (Manion, 1961; Ford and Gilman, 2000). This formation ranges in thickness from 152 m to 305 m (Maclachlan, 1972; Sprinkel, 2000).

Carmel Formation

The Carmel Formation is Middle Jurassic in age (Amar et al. 2006). It consists of non-resistant, tan, light-gray, and dark-red calcareous, sandy shales, siltstones, mudstones, limestones, and sandstones. The paleoenvironments of the Carmel ranged from fluvial, eolian, sabkha and open marine (Blakey et al., 1996). This formation ranges in thickness from 0 m to 15 m (Manion, 1961; Van Leonen and Selner, 1999).

Entrada Formation

The Entrada sandstone is Jurassic in age (Amar et al. 2006) and consists of white, tan, and light rust-colored, massive, cross-bedded, quartz arenites and a layer of thin, dark-red, very fine-grained siltstone (Eicher, 1955; Manion, 1961; Hansen, 1965). It is interpreted as eolian in origin and serves as a reservoir for fields in Utah (Sprinkel, 2000). This formation ranges in thickness from 27 m to 45 m (Manion, 1961; Van Leonen and Selner, 1999).

Curtis Formation

The Curtis Formation is Jurassic in age (Currie and Reeder, 2002) and consists of gray, dark-gray, and black shales with overlying light-gray calcareous, oolitic and crystalline limestone. Brachiopods and pelecypods are abundant (Manion, 1961; Currie et al., 2005). It is interpreted as a marine transgressive system tract (Eschner, 1982; Currie and Reeder, 2002). This formation ranges in thickness from 10 m to 42 m (Manion, 1961; Van Leonen and Selner, 1999).

Morrison Formation

The Morrison Formation is Jurassic in age and is further broken down into the Salt Wash and Brushy Basin members (Love, et. al., 1993; Currie, 1993). The formation contains green, gray-green, tan, red, light-purple, and violet calcareous shales, siltstones, gravel conglomerates, varicolored mudstones, lacustrine algal limestones, and massive planar and trough cross-bedded, fine to coarse-grained, lithic sandstones interbedded with red calcareous siltstones and bentonite. Paleosols are common and indicate seasonality in a semi-arid climate (Manion, 1961). The lithofacies of the Morrison are interpreted as meandering stream to floodplain deposits and were marginal to a large interior sea-way (Currie, 1998). This formation ranges in thickness from 165 m to 198 m (Manion, 1961; Van Leonen and Selner, 1999).

Dakota Sandstone

The Dakota Sandstone is Early Cretaceous in age (Hansen, 1986b; Stilwell, 1990; Currie et al., 1993) and consists of resistant, white, light-gray, yellow, tan, and rust colored medium- to coarse-grained sandstone, and trough cross-bedded basal gravel conglomerate with minor mudstone, coal, and carbonaceous shale intervals (Manion, 1961). The sandstone is interpreted as shore-face sediment deposited along the margins of the Western Interior Cretaceous Sea-Way (Johnson, 1990). The sandstone marks the end of a marine regression (Manion, 1961). This formation ranges in thickness from 18 m to 54 m (Manion, 1961; Van Leonen and Selner, 1999).

Mowry Shale

The Mowry Shale is Early Cretaceous in age (Cobban and Reeside, 1952; Stilwell, 1990) and consists of soft, silver and bluish-gray to black, thin-bedded siliceous shales and

thin bentonite lenses. Abundant fish scales are present (Manion, 1961; Sprinkel, 2000). These shales mark the beginning of a marine transgression and the bentonite is evidence of volcanic eruptions sourced from the northwest in Idaho (Manion, 1961; Johnson, 1990). This formation ranges in thickness from 18 m to 50 m (Manion, 1961; Van Leonen and Selner, 1999).

Frontier Formation

The Frontier Formation is Late Cretaceous in age (Love et al., 1993) and consists of resistant, fine-grained white, yellow, and tan calcareous sandstones with interbedded carbonaceous shales, limestones, and coal of continental origin (McGookey et. al, 1972). The sandstones are locally cross-bedded and fossiliferous (Sprinkel, 2000). The formation marks one of the four major Cretaceous regressions of the advancing and retreating Arctic sea from the north and a Gulf Coast sea from the south (Weimer, 1960; Johnson, 1990). This formation ranges in thickness from 53 m to 76 m (Manion, 1961; Van Leonen and Selner, 1999).

Mancos Shale

The Mancos Shale is Late Cretaceous in age (Brownfield, 2000) and consists primarily of gray, dark-gray, and light-bluish-gray, locally fossiliferous marine shales with interbedded brown, rust colored, and gray medium-grained mudstone and minor sandstone beds (Manion, 1961; Brownfield, 2000). Although these sandstones are thin, they produce gas in several parts of Colorado. The Mancos is also extremely organic rich and has vast reserves of hydrocarbon stored as oil shale (Molenaar and Wilson, 1990). The lithofacies of the Mancos are interpreted as open marine offshore deposits within the

Western Interior Cretaceous Seaway (Manion, 1961; Johnson, 1990). This formation ranges in thickness from 1220 m to 1825 m (Johnson 1979; Johnson, 1990).

Mesaverde Group

The Mesaverde Group is Late Cretaceous in age (Cobban and Reeside, 1952; Brownfield, 2000) and in the study area contains two formations: the Illes Formation and the Williams Fork Formation (Manion, 1961). These consist of massive, resistant to moderately-resistant, light- to medium-brown, tan, orange, and gray lenses of sandstones and shales, interbedded with sandy and carbonaceous shales, thin coal beds, and clay (Manion, 1961). These formations are interpreted as both marine shales and terrestrial littoral and lagunal layers deposited during a regression to the north (Manion, 1961; Johnson, 1990). This formation ranges in thickness from 525 m to 690 m (Brownfield, 2000).

Wasatch Formation

The Wasatch Formation is Eocene in age (Picard and McGrew, 1955; Love et al., 1993) and contains two members; the Hiawatha and Cathedral Bluff members, which are intertongued with the Tipton tongue of the Green River Formation (Fig. 5). These deposits consist of variegated clay shales, interbedded with gray, tan, and red sandstones and occasional conglomerates and coal beds (Manion, 1961). The shales range in color from red, gray, yellow, and buff. These lithofacies are interpreted as fluvial and lacustrine deposits (Sprinkel, 2000). This formation ranges in thickness from 914 m to 2743 m (Roehler, 1992).

Green River Formation

The Green River Formation is Eocene (Love and Christiansen, 1985) in age and contains two members: the Tipton tongue and Laney member (Bradley, 1961). These deposits consist of gray, fissile, lacustrine carbonate shales and oil shales with occasional gray sandstones, mudstones, and limestones (Manion, 1961; Sprinkel, 2000). This unit demonstrates gradational contact with the underlying Wasatch. It marks the onset of a regional marine regression and the influx of terrigenous clastic sediment into the Western Interior Cretaceous Seaway (Manion, 1961). This formation ranges in thickness from 152 m to 360 m (Manion, 1961; Roehler, 1992).

Bishop Conglomerate

The Bishop Conglomerate is the basal unit of the Browns Park Formation and is Oligocene in age (Hansen, 1986a). This coarse basal conglomerate consists primarily of clasts from the Uinta Mountain Group, but occasionally contains clasts of the Madison Limestone. These well-rounded clasts range from pebble to boulder size. These deposits range from 7 to 10 m in thickness (Manion, 1961) (Plate 1).

Browns Park Formation

The Browns Park Formation is Miocene (Hansen, 1986a) in age and consists of white to light-gray, non-resistant sandstones, tuffaceous sandstones, tuffs, and a basal conglomerate (Manion, 1961; Sprinkle, 2000). These volcaniclastic deposits overlie all older deposits with an angular unconformity and are approximately 400 m thick (Van Leonen and Selner, 1999; Counts, 2005).

Quaternary Alluvial Deposits

The alluvial deposits are Holocene in age and consist of silt, sand, gravel, and the

occasional boulder deposited within the Gilberts Peak erosional surface and in stream channels, flood planes, and tributaries along Vermillion Creek. Clasts are sub- to well-rounded, pebble-sized, and in a sandy, silty, clayey matrix. These unconsolidated deposits are mainly buff to gray and are easily eroded. Thicknesses vary throughout the area from meters to tens of meters.

Models of Laramide Tectonics: Debate of Regional Tectonics

During the 1970's and 1980's, two models of Laramide tectonics were developed. The vertical tectonics model was the most prevalent in the 1970's and was represented by upthrust models (Prucha et al., 1965) and block uplift models (Stearns 1971, 1978; Matthews and Work, 1978) (Fig. 6). In the 1980s, however, work by numerous investigators showed that horizontal compression due to lateral shortening dominated the Laramide (Smithson et al., 1979; Chapin and Cather, 1981; Chapin and Cather, 1983; Gries, 1983; Lowell, 1983; Brown, 1984; Stone, 1984; Erslev, 1986; Spang and Evans, 1988).

The Uinta arch is clearly of Laramide origin. However, the atypical east-west orientation of the arch requires special circumstances. The tectonic mechanism for Laramide deformation is still highly debated with hypotheses ranging from sub-crustal shear during low-angle subduction (Bird, 1988, 1998; Hamilton, 1988) to detachment of the upper crust during plate coupling to the west (Lowell, 1983; Oldow et al., 1989; Erslev, 1993). The highly varied Laramide structural geometries in the Rocky Mountains have produced an abundance of kinematic models throughout the years. The dominance of low-angle thrust and strike-slip slickenlines on minor fault planes further negates vertical tectonics hypotheses that call on dip-slip along high-angle faults (Erslev et al., 2004).

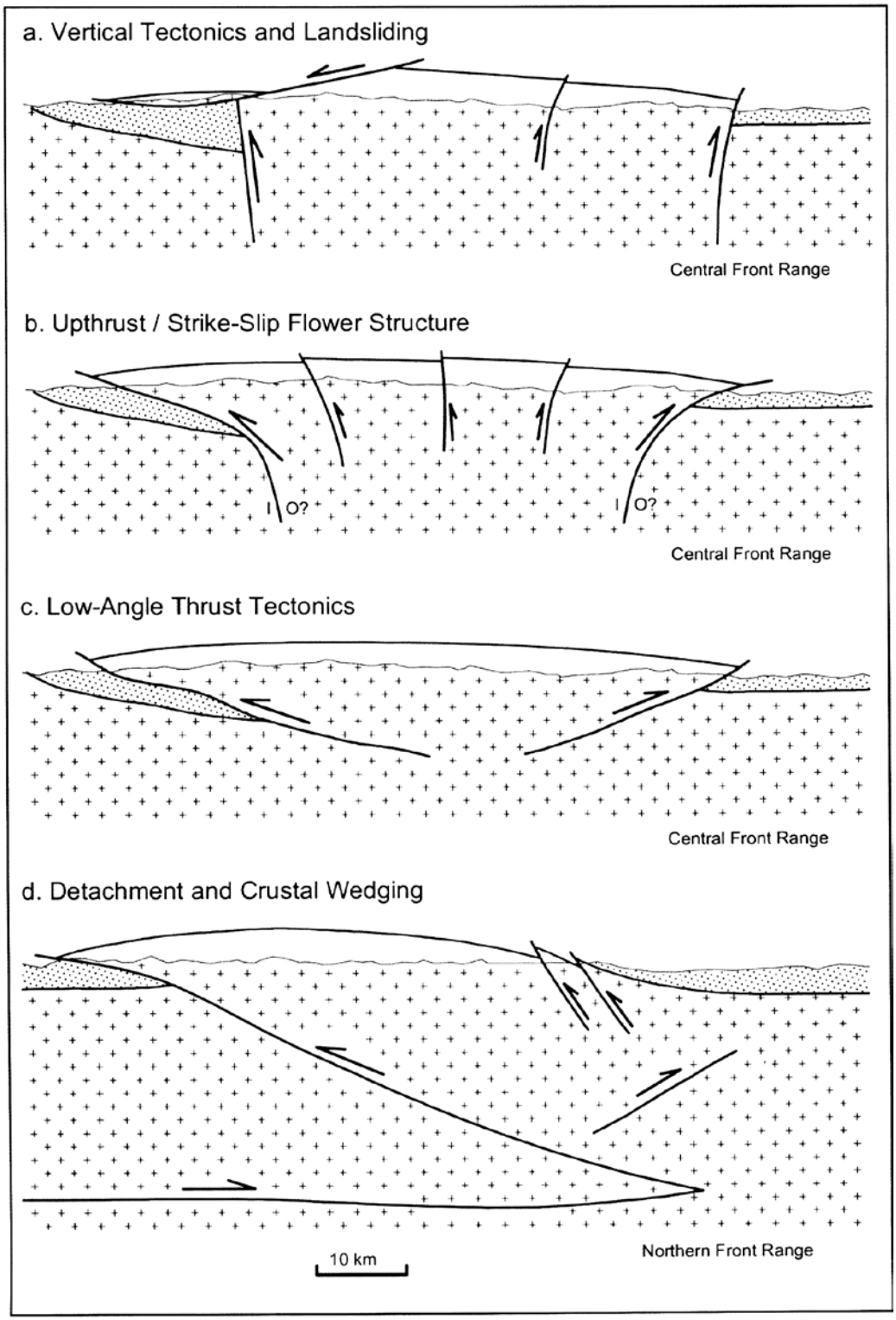

Figure 6. Simplified cross-sections of Laramide tectonic models for the Front Range a) vertical uplift, with gravity sliding on the western flank, b) symmetric upthrusts (Jacobs, 1983) and positive strike-slip flower structures (Kelley and Chapin, 1997), c) low angle, symmetric thrust faulting in the central Front Range (Raynolds, 1997), and d) backthrust of a basement wedge in the northern Front Range (Erslev and Holdaway, 1999) (from Erslev and Larson, 2006).

Within current horizontal compression models, three further subdivisions have emerged, one advocating a single phase of northeast-southwest compression (Kanter et al., 1981; Brown, 1988; Erslev, 1993) (Fig. 6d), another advocating multi-phase, multi-directional compression evolving over time (Chapin and Cather, 1981; Gries, 1983) (Fig. 7), and a third supporting strike-slip models (Chapin and Cather, 1981). The highly varied Laramide structural trends have been attributed to multi-stage, multi-directional compression (Chapin and Cather, 1981; Gries, 1983; Bergh and Snoke, 1992), change in compression directions due to changes in plate trajectories (Bird, 1998), reactivation of pre-existing basement weaknesses (Hansen, 1986b; Stone, 1986; Blackstone, 1990; Chase et al., 1993), transpressive motions (Cather, 1999), indentation by the Colorado Plateau (Hamilton, 1988), a mid-crustal detachment along a shallowly dipping listric fault (Lowel, 1983; Brown, 1988; Kulik and Schmidt, 1988; Oldow et al., 1990; Erslev, 1993), and the impingement of the Cordilleran fold and thrust belt (Gregson and Erslev, 1997). Other investigators have suggested that eastward translation of the Colorado Plateau and left lateral shear across the Uinta arch created the Laramide trends (Sales, 1968).

The single phase models call on NE-SW or ENE-WSW (Erslev and Koenig, in press) directed dip-slip faulting perpendicular to the arch axes for the more northwesterly-trending arches and oblique to lateral slip on arches that are oblique to the northeast-southwest σ_1 (ideal sigma one) (Kanter et al., 1981; Brown, 1988; Erslev, 1993; Gregson, 1994) (Fig. 8). These models call on left oblique slip for the E-W trending arches and right oblique slip for the N-S trending arches (Molzer and Erslev, 1995). The structures that are oblique to the regional σ_1 have been attributed to the reactivation of pre-existing weaknesses in basement (Stone, 1986), linkage in strike-slip bridge structures (Paylor and

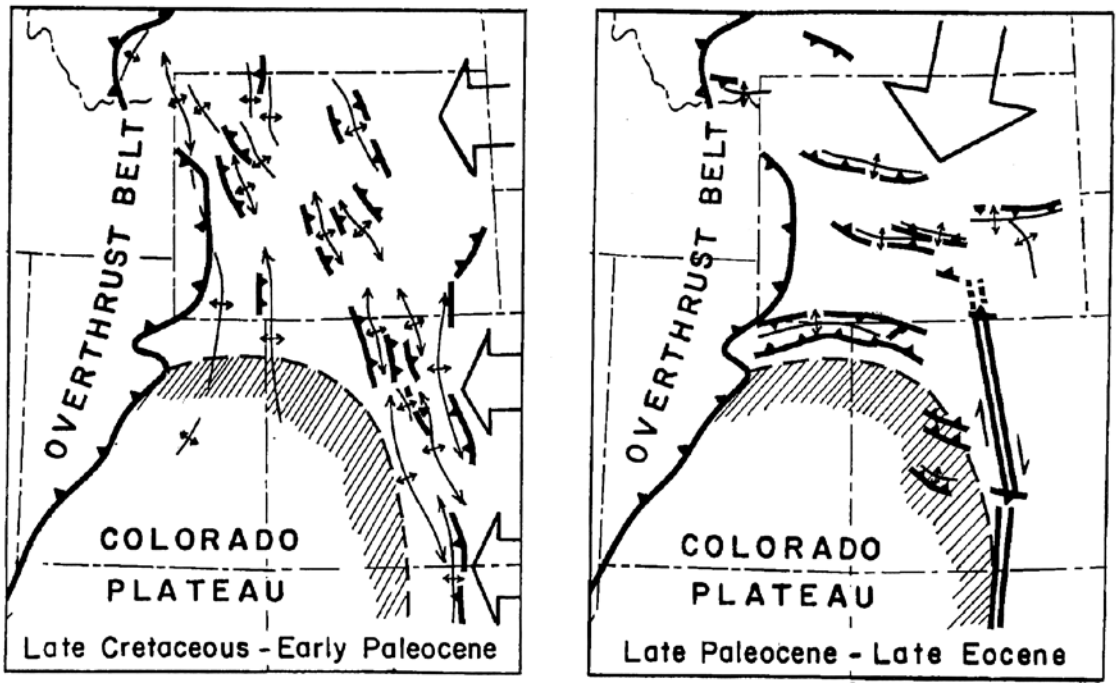

Figure 7. Protracted, multi-phase, multi-directional Laramide compression evolving over time (Gries, 1983).

Yin, 1993), and slip on lateral ramps (Molzer and Erslev, 1995). Past studies by Wise and Obi (1992), Robbins (1987), Paylor and Yin (1993), Molzer and Erslev (1997), and Larson and Erslev (2006) have used kinematics of minor faults and joint data to show sub-horizontal, uni-directional, northeast- to east-northeast shortening during the Laramide Orogeny. In contrast, Karlstrom and Daniel (1993) looked at right lateral offsets of lithologic and metamorphic trends in northern New Mexico to support northward translation of the Colorado Plateau.

The multi-phase advocates use multiple convergence directions to explain the highly varied Laramide structural trends, with the latest shortening direction being perpendicular to E-W arch trends and in a N-S direction. Gries (1983) suggested three phases of Laramide deformation; east-west shortening with a counterclockwise rotation of the stress field to a northeast-southwest and north-south shortening directions. Similarly,

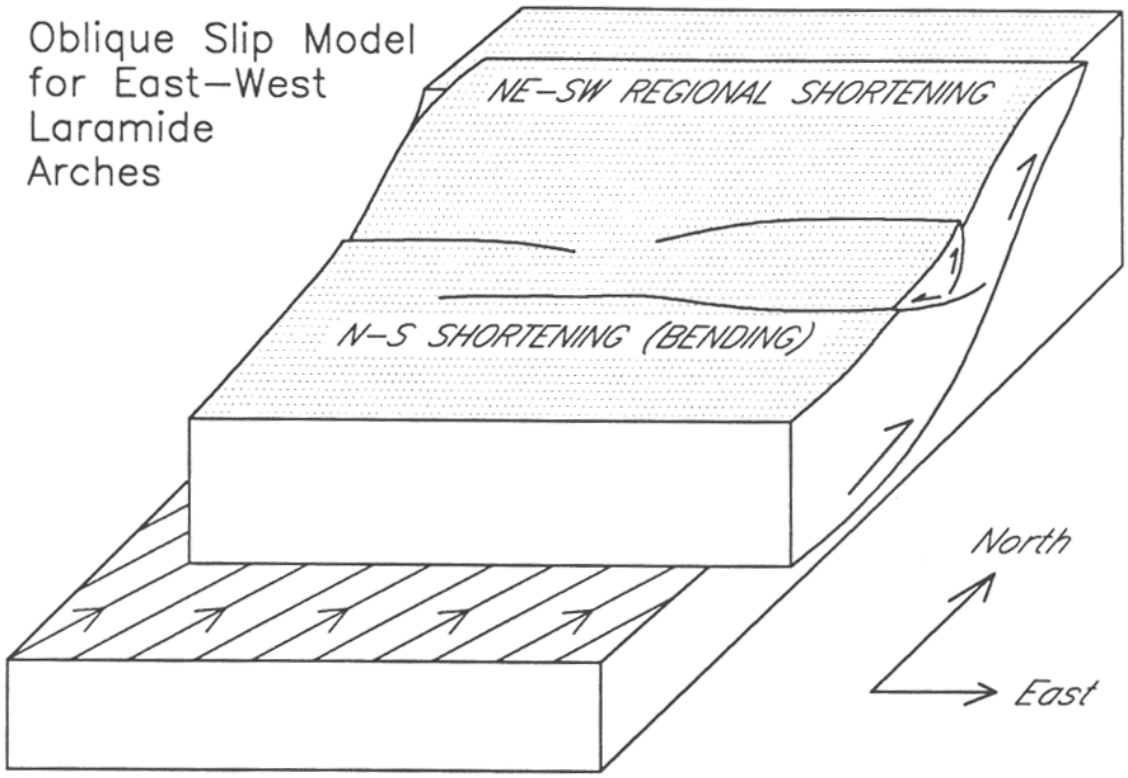

Figure 8. Model illustrating oblique slip (Gregson, 1994).

Chapin and Cather (1983) used evidence from elongate basins of possible right-lateral strike-slip origin to suggest two stages of Laramide deformation with northeastward transpression of the Rocky Mountains followed by northward translation of the Colorado Plateau.

Bergh and Snoke (1992) identified three overprinting Laramide structural trends within the Shirley Mountains of south-central Wyoming, suggesting a similar model of multi-phase Laramide deformation. Early N-S structures display similarities to the N-S Front Range structural trends developing in the late Cretaceous and the NW-SE and NE-SW structures display similarities to Wyoming foreland structural trends occurring late in the Laramide Orogeny. However, studies of sedimentation patterns, dating of synorognic sediments, and paleogeographic reconstructions have questioned multi-phase deformation

during the Laramide Orogeny (Hansen, 1986b; Dickinson et al., 1988; Perry et al., 1992; Steidtmann and Middleton, 1991) by showing that there was no correlation between orientation of the arch axes and the time of genesis.

Tectonics of Laramide Arches

Numerous investigators have suggested that Laramide and Cordilleran (Sevier) deformation could be accounted for by a common mechanism of crustal detachment during top-to-the-east or northeast shear (Lowell, 1983; Oldow et al., 1989; Erslev, 1993). Therefore, the regular spacing of Laramide foreland basement arches and their corresponding basins can be attributed to the buckling of the upper crust above a lower crustal detachment zone followed by fault break through (Fletcher, 1984; Kulik and Schmidt, 1988). The spatial regularity of the Laramide foreland arches as well as their continuous nature can be explained by a linkage of the faults responsible for forming the arches with an underlying detachment zone (Erslev, 1993). Linkages through a common detachment zone can also explain the lateral changes in arch amplitude, and the anastomosing and spatially variable symmetry of the Laramide arches are characteristic of detachment folds (Dahlstrom, 1990; Erslev, 1993; Epard and Groshong, 1995).

The structural geometry of the larger asymmetric arches can be effectively modeled as rotational fault-bend folds with movement on a listric master thrust fault rotating a decoupled basement fragment upward (Erslev, 1986). This style of faulting also explains an array of second-order, basement involved fault propagation folds that are directly related to the first-order arches and basins (Erslev, 2005). Taken as a whole, orientations of Laramide first-order arches and their associated second-order structural geometries can be explained

by faulting on shallowly-dipping, listric thrust faults during thick-skinned tectonics (Erslev, 2005).

It is likely that the Laramide detachment was rooted in the west under the area now occupied by the Basin and Range Province (Erslev, 2005). This is consistent with the analogous slip trends indicated by the main Cordilleran and Laramide thrust belts as well as the west-to-east progression of Laramide thrusting in Wyoming (Brown, 1988). Additionally, the coupling of thick- and thin-skinned thrusting in Wyoming illustrates that the major Laramide and Sevier deformation was characterized by ENE- and SE-directed thrusting accompanied by little deformation in the lower plate.

Regional Geology and Tectonic Setting

During the late Archean and the early Proterozoic, an east-trending continental margin rift began to open along the location of the present day Uinta Mountains (Bradley, 1995). During the Proterozoic, between 2.4 and 1.5 Ga, almost 4 km of Red Creek Quartzite was deposited along this rift (Bradley, 1995; Sprinkel, 2000). After the deposition of the Red Creek Quartzite, the rift was reactivated by a period of compression and was then thrust northward over Archean rocks along the Cheyenne suture zone (Stone, 1993). The minimum age of thrusting was established as 1.5 Ga by the radiometric dating of post-orogenic pegmatites that intruded the Red Creek Quartzite (Hansen, 1965).

At around 1.1 Ga, after a long period of erosion, the Uinta Mountain Group was deposited by fluvial processes into the reactivated east-trending rift valley formed in the present day location of the Uinta Mountains (Bressler, 1981; Chaudhuri and Hansen, 1980). The sediments composing the Red Pine Shale were dated to around 950 Ma with Rb/Sr age dating (Crittenden and Peterman, 1975; Sprinkel, 2000). The entire group resides only

within the confines of the rift valley. Subsequently the upper Cambrian Lodore Formation was deposited on the Uinta Mountain Group above an angular uncomformity (Hansen, 1986b; Stone, 1993).

The Uinta arch is a predominantly east-west-trending anticline located in northeastern Utah and northwestern Colorado. The Uinta arch is expressed by elongate west and east domes whose culminations are adjacent to the north-south-trending Moxa arch and Douglas Creek arches (Fig. 1 and 4). The Wasatch fault and Cottonwood uplift cut the Uinta range, but the axial trace of the arch may span as far west as the Oquirrh Mountains in the Basin and Range province (Ritzma, 1969; Hansen, 1986a, b) (Fig. 1 and 4). The eastern edge of the Uinta arch plunges beneath the Miocene Browns Park Formation, but seismic and borehole data suggest the arch may extend as far east as the Cross and Juniper mountains (Stone, 1986) (Fig. 4). The trend of the eastern margin of the Uinta arch coincides with the trend of the White River uplift just south of the Juniper Mountains at the Axial arch (Hansen, 1986b).

Structural inversion of Precambrian extensional structures took place along the Axial and Beaver Creek thrust in the Pennsylvanian, during the Ancestral Rocky Mountain Orogeny, and these faults were reactivated again in the Late Cretaceous during the Laramide Orogeny (Stone, 1969, 1986, 1993; Morel, 1986). The rheological contrast between the relatively weak Uinta Mountain Group and the much stronger Precambrian basement to the north and south may have had some control on the east-west trend of the arch. Therefore the geometry of the Laramide deformation may have been affected by the pre-existing weaknesses created by Precambrian normal faults and the rheological contrasts created along depositional trends (Bradley, 1995).

Major Laramide faulting took place on the south-dipping North Flank thrust, the Henry's Fork fault, and the Uinta thrust north of the range (Fig. 1 and 3). Laramide deformation also took place along the north-dipping Uinta Basin Boundary thrust, the Asphalt Ridge fault, the Willow Creek fault, and the Miner's Draw-Wolf Creek fault to the south. Between 11 and 13 km of structural relief relative to the adjacent basins were formed by the Laramide rise of the Uinta arch, with the most deformed terranes being located in the eastern portion of the arch (Sales, 1971; Ritzma, 1969; Hansen, 1986b).

The post-Laramide deformation of the Uinta Mountains is characterized by intermittent quiescence and deformation. After the deposition of the youngest Eocene rocks along the flanks of the range and the adjacent basins, a time of tectonic stability occurred, allowing the Oligocene Gilberts Peak erosional surface to form. The Gilbert Peak erosional surface and the Oligocene Bishop Conglomerate overlie the Laramide structures of the eastern Uinta Mountains. Offsets of the unconformity in relation to the conglomerate suggest Miocene regional tilting to the northeast and subsequent subsidence may have been responsible for the formation of the Browns Park graben (Hansen, 1984, 1986a, b). This northeast tilting was followed by tilting to the south and the majority of the deformation occurred prior to the deposition of the Miocene Browns Park Formation (Hansen, 1986a, b).

During two pulses of rifting during the Oligocene and Miocene, the Rio Grande rift formed in central Colorado, New Mexico, and Mexico. The E-W directed extension created a series of N-S- trending asymmetric grabens containing both high and low angle normal faults (Olsen et al., 1987). The fault patterns created by the rifting are in predominately N

and NE trends, with NW and W trends being less common (Kelley, 1956). These fault patterns likely extended as far north and west as the Irish Canyon-Vermillion Creek area.

Effects of the Sevier Orogeny

Paulsen and Marshak (1999) suggested that as the eastward propagating Sevier fold-thrust belt impinged on a pre-existing asymmetric basement high located at the Wasatch culmination, the Uinta recess was formed. Variations in the thickness of the stratigraphic sequences involved in thrusting may have been responsible for differential propagation of the thrust belt into the Rocky Mountain foreland (Paulsen and Marshak, 1999). This hypothesis suggests that NW-SE compression resulted in the southern Uinta arch when the Charleston Nebo thrust sheet lost lateral continuity and formed a strike-slip accommodation zone along the southern flank of the Uinta arch. Gregson and Erslev's (1997) results lend further support that the NW-SE stress trajectories found on the northeastern and southern limb of the Uinta arch may be a product of impingement of the Sevier fold-and-thrust belt.

While a single stage of NE-SW to E-W shortening and compression has been suggested by recent data collected in the Rocky Mountain Front Range (Erslev et al., 2004; Erslev and Koenig, in press), evidence for regional multi-stage, multi-directional Laramide slip was found in a few locations of the northeast and western Front Range. In several locations along the northwestern Front Range, WNW-trending slickenlines overprint ENE-trending slickenlines. In the Gore Range, evidence for NW-SE slip and compression along minor faults was also documented (Copfer, 2005). NW-SE compressional faults were also seen in northwestern (Gregson and Erslev, 1997) and southwestern Colorado (Ruf and Erslev, 2005). The differing compression directions are predicted by a change in plate

trajectories (Bird, 1988), but also may be the result of late-stage impingement of the Sevier thrust belt (Gregson and Erslev, 1997) or synchronous, non-plane-strain shortening in two horizontal directions caused by transpression (Ruf and Erslev, 2005).

Within the eastern Owl Creek Arch, the Casper Arch of Wyoming (Molzer and Erslev, 1995), and in the San Juan Basin (Ruf and Erslev, 2005), variable heterogeneous stress was observed and the evidence suggests that oblique slip on E-W-striking faults was responsible for the deformation.

Gregson and Erslev's (1997) study in the Uinta Mountains tested models to explain heterogeneous stress within the Uinta arch. There were three local effects that may have been responsible for the inconsistent slip and σ_1 directions: 1) N-S contraction as the NE-directed thrust slab moves over a south dipping listric ramp (Fig. 9a), 2) local stresses from transition in structural vergence between the Uinta arch and White River uplift (Fig. 9b), and 3) detachment and translation of the Uinta aulacogen from impingement of the Sevier fold and thrust belt (Fig. 9c). The third hypothesis, the impingement of the Sevier thrust belt translating the entire Uinta aulacogen into the Rocky Mountain foreland, includes the first two hypotheses and also explains the radial pattern of slip directions on faults around the Uinta arch (Gregson and Erslev, 1997).

The analysis of minor fault kinematics using slickenlines showed that the faults contain a component of thrust and strike-slip motion. The minor faults in the northern limb of the Uinta arch suggest NE slip and σ_1 in both Precambrian and Phanerozoic rocks, which are consistent with the average regional trends and foreland studies. However, in the southern limb of the Uinta arch, SSE slip and σ_1 directions sub-perpendicular to the local

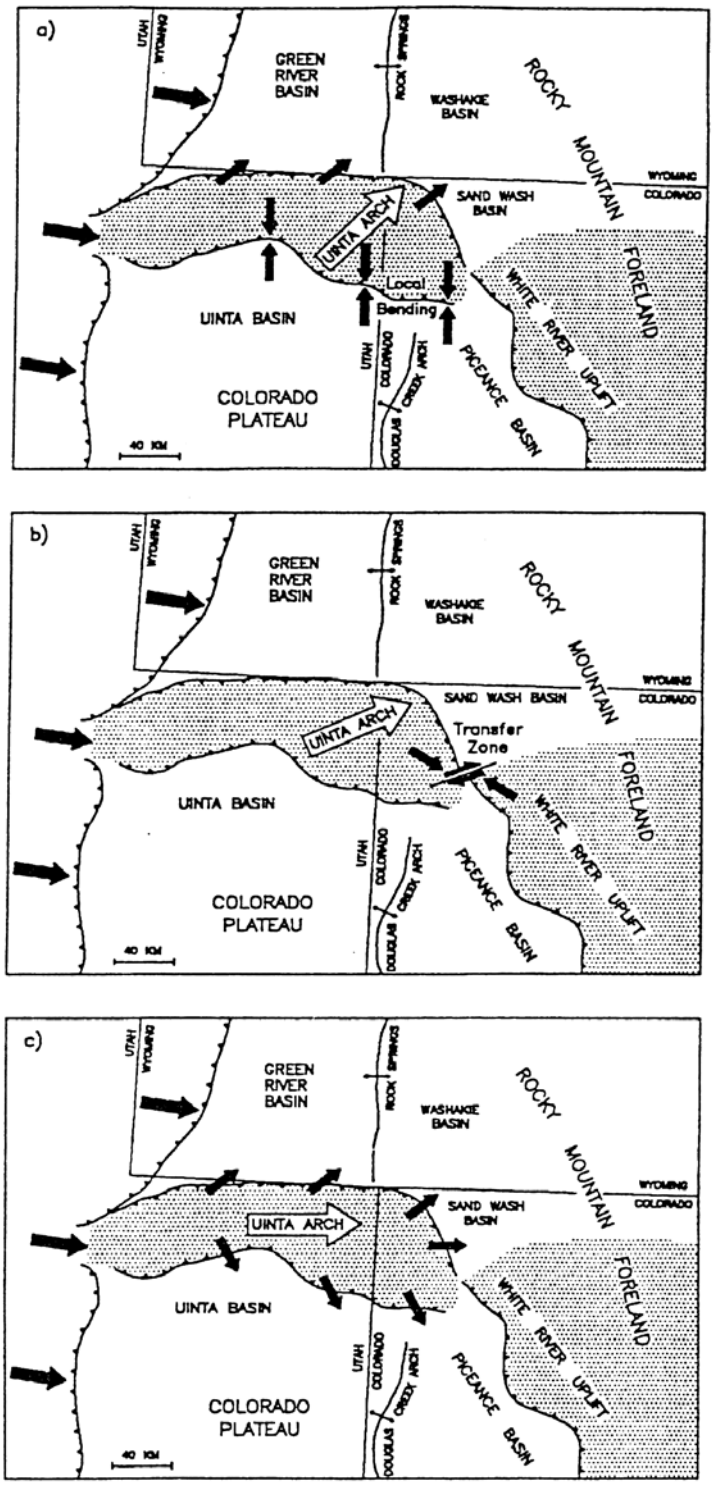

Figure 9. Hypotheses explaining variable heterogeneous stress within the southeastern Uinta Mountains a) N-S contraction as the NE directed thrust slab moves over a south dipping listric ramp, b) local stresses from transition in structural vergence between the Uinta arch and White River uplift, and c) detachment and translation of the Uinta block from impingement of the Sevier fold-and-thrust belt (Gregson and Erslev, 1997).

faults and folds were observed (Gregson and Erslev, 1997). Three dimensional cross-section restorations of the Weber Sandstone in Dinosaur National Monument confirmed the NNW-SSE shortening, suggesting right-oblique contraction and clockwise rotations of individual crustal blocks (Gregson and Erslev, 1997). The study showed evidence for oblique-slip displacements with oblique stress orientations.

Additionally, the east-directed slip and compression suggested from data collected from the top of the eastern limb suggests the σ_1 may radiate out from the center of the arch (Gregson and Erslev, 1997). They concluded that the variable heterogeneous stress within the northern Uinta arch is consistent with the combination NE-directed left oblique slip on the S-dipping master thrust and with existing Laramide models (Gregson and Erslev, 1997).

Effects of Basin and Range and Rio Grande Rift Extension

The Basin and Range province of the southwestern United States extends from central Utah to eastern California and from southern Washington to Mexico (Fig. 1). Basin and Range deformation began in the Middle Miocene and continued to the Pliocene and possibly to present. The deformation was characterized by gravitational collapse and E-W extension in response the crustal thickening due to Sevier fold-and-thrust belt shortening (Liu, 2001).

The Rio Grande rift is comprised of a series of asymmetrical grabens extending over a 1000 km from Chihuahua Mexico well into central Colorado (Olsen et. al., 1987) and as far as North Park Colorado (Erslev, 2001). Rio Grande rift deformation manifested as two pulses of E-W extension, one during the late-Paleogene and other during the Neogene (Fig. 10). Erslev (2001) noted a possible link between the Paleogene end of

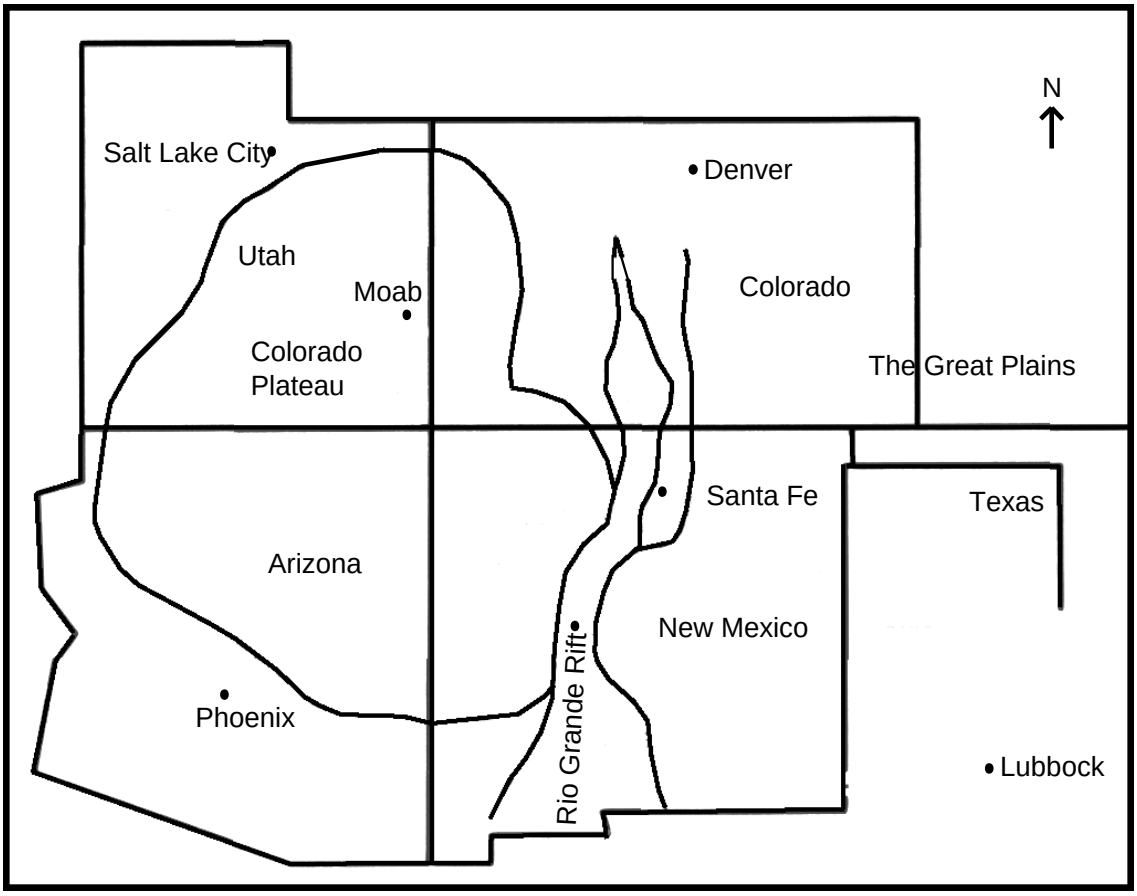

Figure 10. Map showing the location of the Rio Grande rift (Modified from Davis et al., 1984).

Laramide compression and the Neogene beginning of Rio Grande rifting within the Galisteo Basin. The study showed that there was late Laramide strike-slip faulting with a NE-SW σ_1 followed by mid-Tertiary, predominantly right-lateral strike-slip faulting coupled with minor E-W extension. North-striking right-lateral faults and N-NE-striking left-lateral faults cut rocks younger than 25 Ma, 15 Ma after the commonly cited end of the Laramide (Fig. 11). This suggests that either Laramide strike-slip faulting continued into the Oligocene or the faulting was re-initiated after the Laramide in response to Rio Grande rifting.

Anderson and Barnhard (1991; 1993) obtained similar results from their study of the Virgin River Depression and the Mormon Mountains near the Nevada, Utah, and

Arizona common borders. They observed a predominance of right-lateral strike slip faulting, with the right-lateral faults striking NW and N-S and the left-lateral faults striking NNW to NE. These fault patterns were attributed to Neogene E-W extension followed by NE-SW extension associated with Basin and Range (Fig. 12).

Right-lateral strike-slip faulting associated with a nearly N-S σ_1 combined with E-W extension may be a transition from Laramide compression to Neogene Rio Grande rift or Basin and Range extension. These investigations are critical to this study in that remarkably similar orientations of strike-slip faulting were observed with in the field area.

Previous Work within or Near Irish Canyon-Vermillion Creek Area

The first geologic maps of the Irish Canyon-Vermillion Creek area were drafted by the King Survey in 1871 or 1872 (Hague and Emmons, 1877) and by Powell in 1874 and 1875 (Powell, 1876). Powell (1876, p. 205-209) was the first to recognize the extensional reactivation of the south-dipping Uinta thrust fault:

> We know that the Browns Park beds were involved in a part at least of this downthrow, and hence were deposited before the downthrow was accomplished, because the beds themselves were involved in the displacement; they are severed by faults and bend by fractures where they are seen to overlap or extend beyond the area of downthrow.

Other early geologic investigations of the area were described in master's projects (White, 1889; Weeks, 1907) and publications (Schultz, 1920; Sears, 1924; Bradley, 1936, 1964). Nightingale (1930) created a large scale geologic map of the Vermillion Creek area when studies of the gas field were underway. Roehler (1979) created a much smaller scale regional map of northwest Colorado which included the Irish Canyon-Vermillion Creek area. The majority of the early investigations were predominately stratigraphic due to the

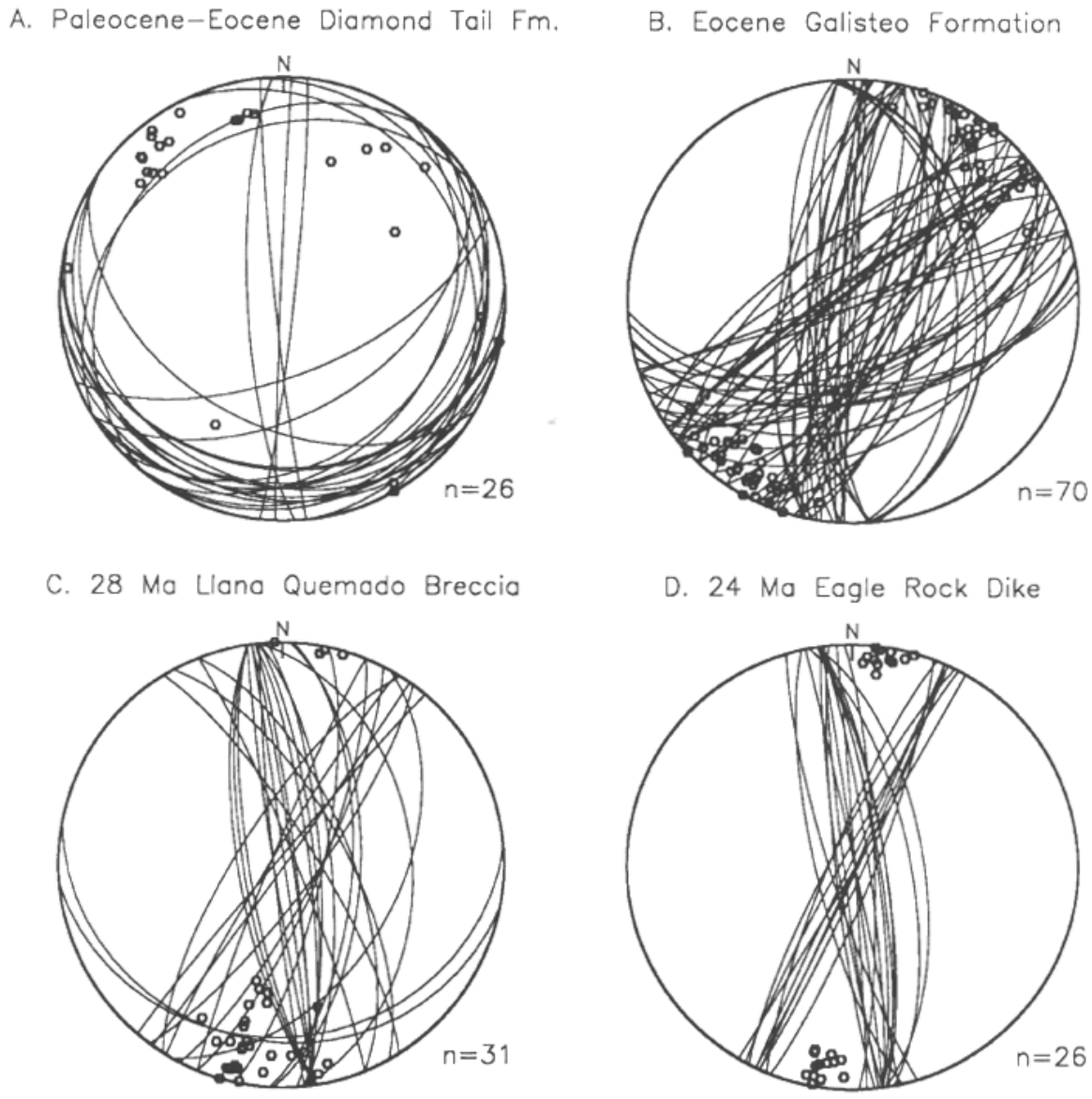

Figure 11. Stereonets of minor fault planes collected from the Galesteo Basin in northern New Mexico (Erslev, 2001).

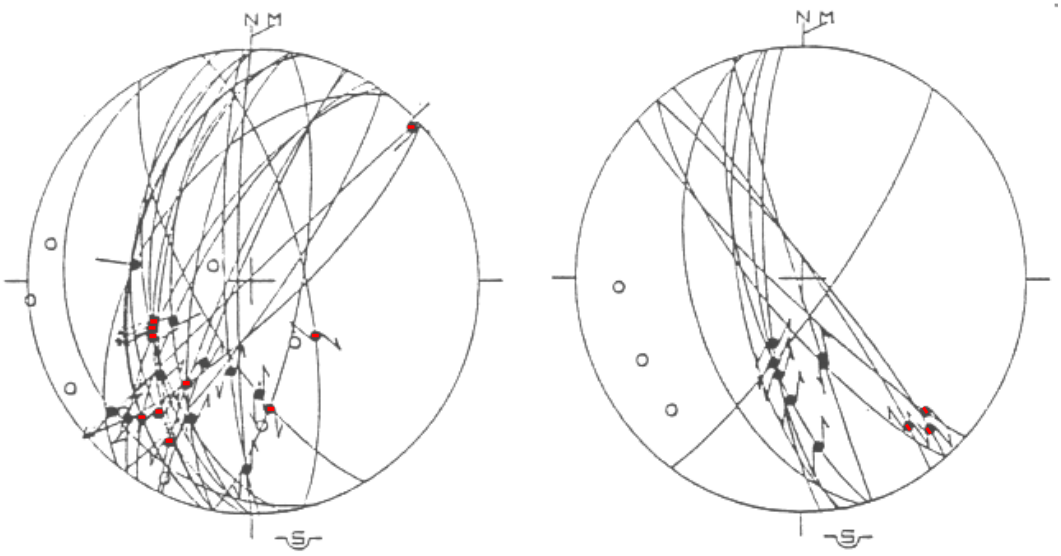

Figure 12. Stereonets of fault planes and slip-sense indicators gathered from the Mormon Mountains along the Utah, Nevada, Arizona border (Anderson and Barnhard, 1993).

excellent exposures within the area (Thomas and others, 1945; Reeside, 1955; Bradley, 1955; Sikich, 1960; Mayer, 1960; Manion, 1961). Hansen et al. (1960) conducted a detailed study on the physiographic significance of the Miocene Browns Park Formation at the Flaming Gorge, Red Canyon, and surrounding areas of Colorado and Utah, showing that it caps, fills, or overtops pre-existing landforms.

Geometric and kinematic relationships between the thin-skinned overthrusts of the Sevier fold-and-thrust belt and thick-skinned Laramide arches in the Rocky Mountains of north-central Utah, southwestern Wyoming, and northwestern Colorado have been perplexing (Roberts and others, 1965; Hansen, 1965, 1984; Sales, 1968; Beutner, 1977; Crittenden, 1967; Bruhn and others, 1983, 1986). Two proposed models consistent with observed field data for the rise of the Uinta arch include right-lateral wrench strain along the southern termination of the Hogsback thrust and right-lateral transpression along a

south-dipping ramp where the Hogsback thrust cuts down the northern boundary of the basin in which the Middle Proterozoic Uinta Mountain Group was deposited (Bradley and Bruhn, 1988). Northwest- and north-northeast-striking cleavage planes and extensional veins in north-central Utah were interpreted as the result of two phases of deformation as opposed to a sequential clockwise rotation of the stress field (Bradley and Bruhn, 1988). Further research by Bradley (1988a) in his dissertation studying the structural evolution of the Uinta Mountains and a subsequent publication (Bradley, 1988b), demonstrated that the development of Uinta arch is related to the development of the Sevier fold-and-thrust belt.

Bump (2004) related the kinematics and timing relationships gathered from field mapping and analysis of structural trends to 6 Colorado Plateau Laramide arches, 4 of which formed as the result of northeast-directed shortening and at least 2 as the result of southeast-directed shortening. The results of this study suggested that all the arches were formed at approximately the same time (~72- 50 Ma), as opposed to a sequential response to a progressive rotation of regional stresses. Differing shortening directions may be predictable within a zone of three-dimensional stress where σ_1 approaches that of σ_2. This hypothesis suggests that the σ_1 is the result of horizontal subduction of the Farralon slab under the North American plate and the increased σ_2 values are the result of the far field stresses created as the Sevier fold-and-thrust belt wraps around the western edge of the Colorado Plateau (Bump, 2004).

During the geologic investigations of the Vermillion Creek Coal bed, structural, paleoenvironment, sedimentologic, stratigraphic (Roehler, 1987), palynologic (Nichols, 1987), paleoecologic (Robbins, 1987), petrographic (Stanton et al., 1987), geochemical (Hatch, 1987; Bostick and others, 1987), and isotopic (Rye, 1987) investigations were

conducted. The results of these studies, along with additional studies of the structural development of the coal and oil occurrence near Irish Canyon, (Roehler, 1979, 1985) demonstrated that three major events were responsible for the deformation. The events included Late Cretaceous uplift of the Uinta Mountains, Paleocene and Eocene thrust movements of the Sparks Ranch (Uinta) thrust fault, and late Tertiary normal faulting associated with a collapse of the eastern Uinta Mountains. The location of the Uinta thrust within the area was also found to be along the contact between the vertical to overturned Cretaceous Mesaverde and the Eocene Wasatch and Green River Formations (Roehler, 1985). Additional investigations of the paleomagnetic poles and correlation of the Proterozoic Uinta Mountain Group within Irish Canyon showed that there has been no major rigid body rotations in the NE Uinta Mountains (Bressler, 1981).

Seismic and borehole data were studied along the Axial arch in northwest Colorado and important evidence for pre-Laramide faulting was discovered. Stone (1986) found that the west to northwest structural grain of the Uinta Mountains-Axial arch was inherited from Precambrian time and then reinforced by later orogenic events. This study also suggested that there were at least four important fault displacements. First was normal faulting occurring during the 400 Ma period represented by the angular unconformity between the late Middle Proterozoic and the Late Cambrian. The second was a structural inversion of pre-existing, northwest-trending listric normal fault segments and wrench faulting along the northeast-trending portions of the Ancestral Axial fault zone during the Ancestral Rocky Mountain Orogeny. The third was a stage of thrust faulting that occurred during the Laramide Orogeny in Late-Cretaceous to Paleogene time which reactivated many of the

older structures as well as creating new structures. Finally, the fourth was a stage of Miocene normal faulting.

Fracture Studies

Contrary interpretations of NW-SE-striking joints observed throughout NW Colorado and the surrounding areas have been proposed. NW-SE-striking joint sets have been interpreted as pre-Laramide in age within the Piceance, Uinta, and SE Sandwash Basins (Verbeek and Grout 1992, 1997), the Paradox Basin (Grout and Verbeek, 1998) and in the Green River Basin (Laubach and Lorenz, 1992). A similar interpretation was made at Split Mountain along the Utah-Colorado border (Silliphant and Engelder, 2002) (Fig. 13). This interpretation was based on the idea that if the strata are restored to their pre fold orientation and the fractures return to vertical, then their genesis is of pre-fold age. However, if a preexisting anisotropy exists, joints will form perpendicular to that anisotropy whether it is horizontal or not. Additional investigations observed parallel joints within Eocene strata within the Uinta Basin and these joints were interpreted to be of post-Laramide age (Hucka, 1991).

Other investigators proposed that NW-SE-striking joint sets were syn- and post-Laramide in origin. Narr (1982) studied the relationship between the surface and subsurface rocks within the Bluebell Altamont Field, Uinta Basin, Utah. He found that the subsurface joints in the Eocene formations have a single dominant NW trend (Fig. 14). Harthill's (1997) investigation conducted within the Bluebell Altamont Field utilized fault characterization, P-wave seismic reflection data, and amplitude variation with offset and azimuth (AVOA) to define the patterns of micro-fracturing, yielding an average joint orientation of N30W within the Eocene Green River and Mahogany Bench intervals. The

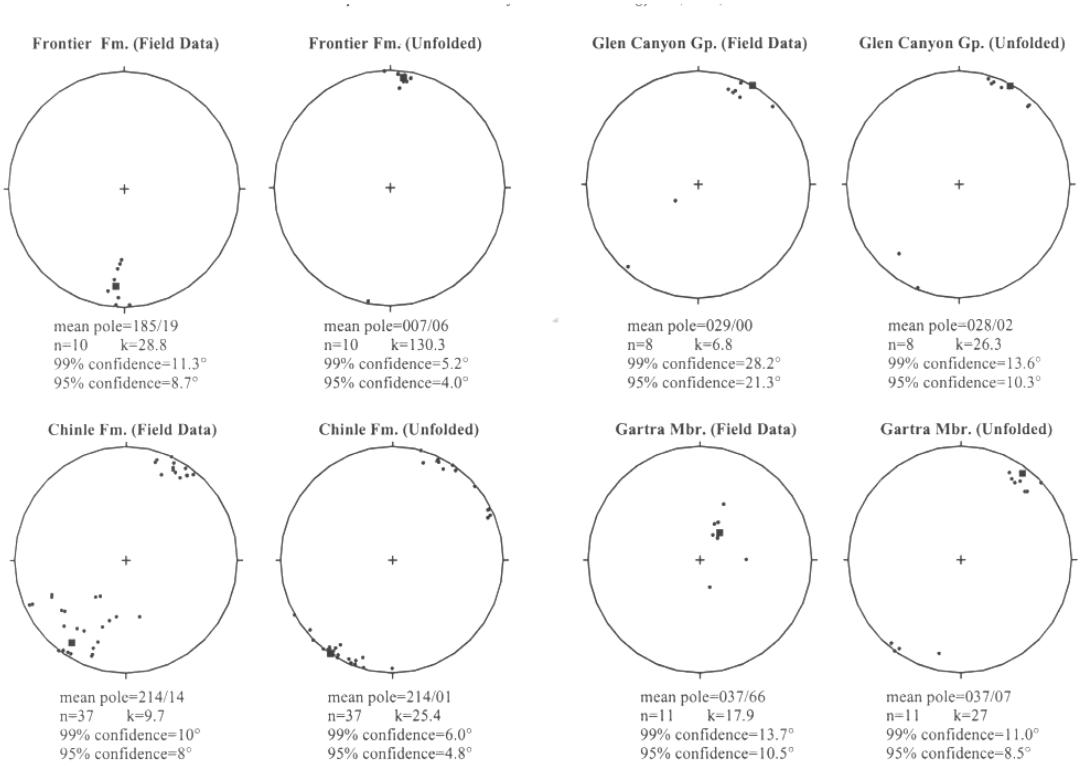

Figure 13. Stereonets of the poles to joint plane strikes, Split Mountain (Silliphant and Engelder, 2002).

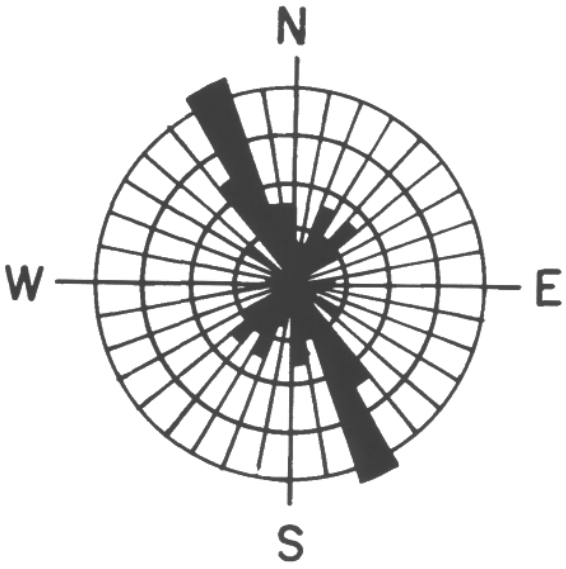

Figure 14. Rose diagram of joint strikes collected from Altamont Field, Uinta Basin (Narr, 1982).

micro-fracture and joint data were corroborated by subsurface data. Aeromagnetic data were also used to reveal regional east-west basement faulting which controlled the subsidence of the basin. Gravity techniques were utilized to show that the basement faulting extended into the sedimentary cover and that the south flank of the Uintas was thrust to the south (Harthill, 1997). The formation of the NW-SE-striking joints in Eocene strata rules out the possibility of a pre-Laramide genesis and suggests a syn- or post-Laramide genesis.

Hansen (1986b), Newhart and Longman (2005), Gregson and Erslev (1997), and S. Larson (2007, personal communication) conducted pertinent stratigraphic and kinematic investigations within the Irish Canyon-Vermillion Creek area and adjacent areas. Newhart and Longman (2005) created a cross-section of Sugar Loaf Butte (Fig.15), just north of the field site in the Vermillion Basin. Hansen (1986b) created a cross-section through Douglas Mountain, along the longitude 108º52`30`` and between the 41st and 40th parallels, south of the field site (Fig.16). Both cross-sections show the northeastern Uinta arch bounded in the north and south by listric thrust faults. Gregson and Erslev (1997) (Fig. 17-18) and Larson (personal communication, 2007) collected complimentary minor fault measurements illustrating NE-SW slip and σ_1 in the northern Uinta arch. The observed slickenline orientations and fault planes for conjugate strike-slip faults and thrust faults were extremely corroborative.

Johnston and Yin (2001) conducted kinematic analyses along the northern Uinta arch and found average slip directions of N50E to N70E for all faults. They also created a tectonic model of the evolution of the Uinta arch during the Laramide (Fig. 19a, b). The model provides two hypotheses indicating an overall left-slip system. One shows left-slip

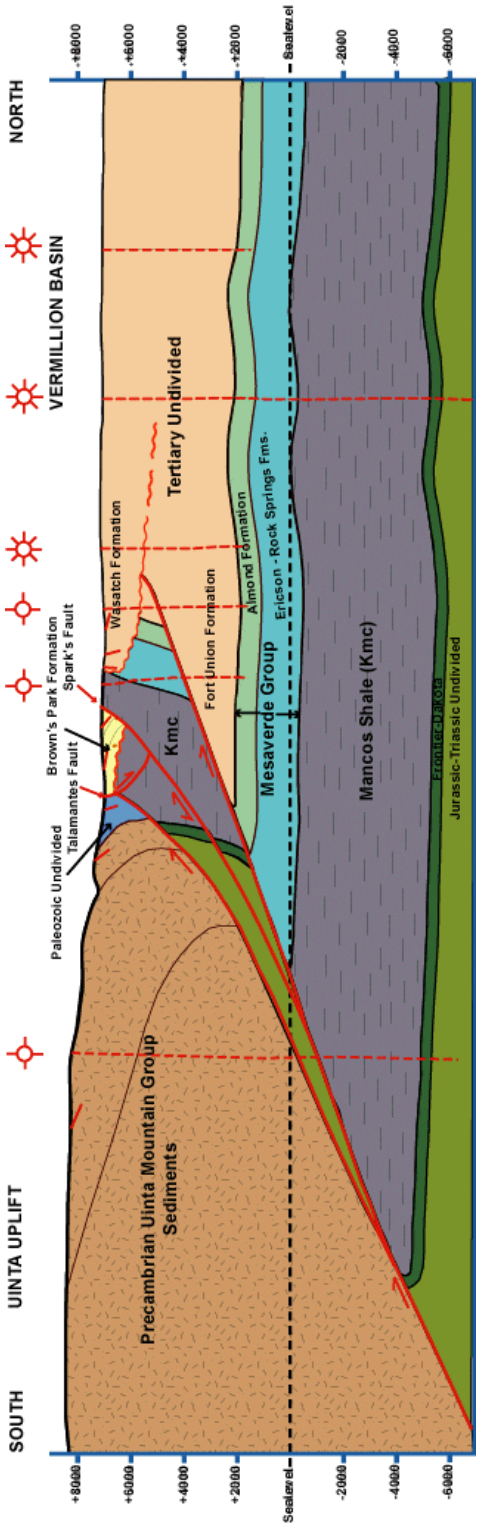

15)

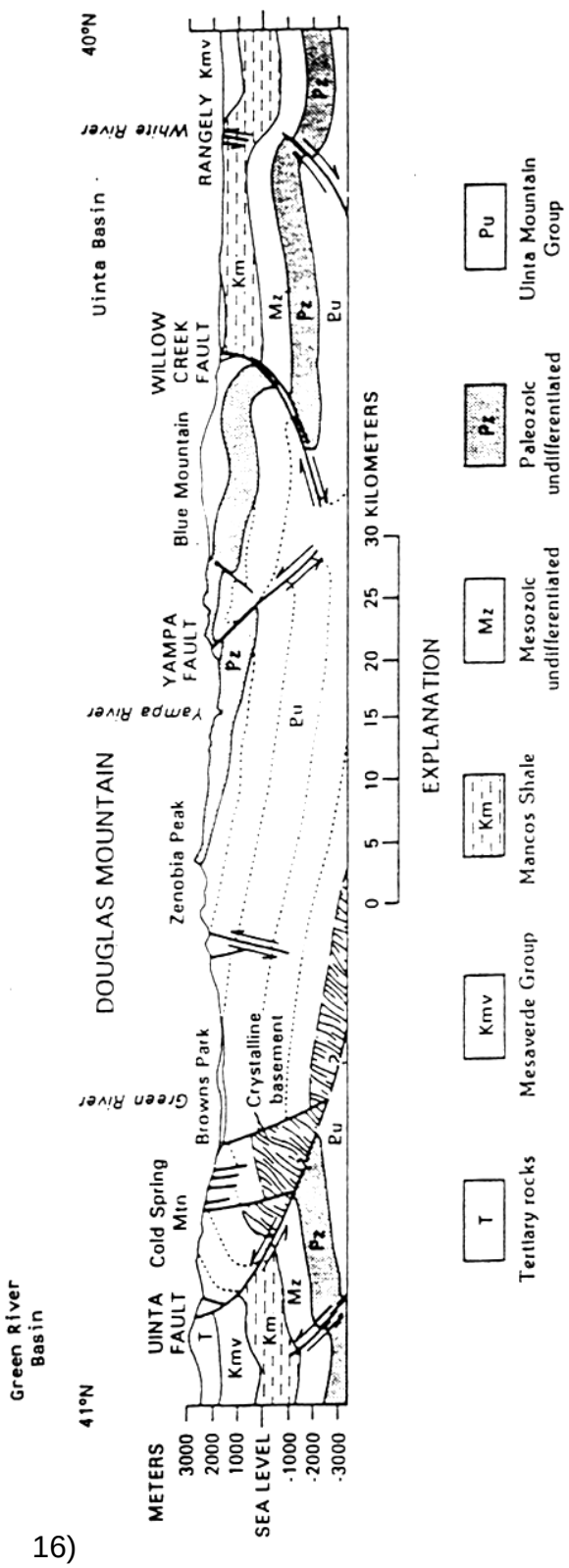

16)

Figure 15. Cross-section of Sugarloaf Butte just north of field area (Newhart and Longman, 2005).
Figure 16. Structural cross-section of the eastern Uinta arch (Hansen, 1986b).

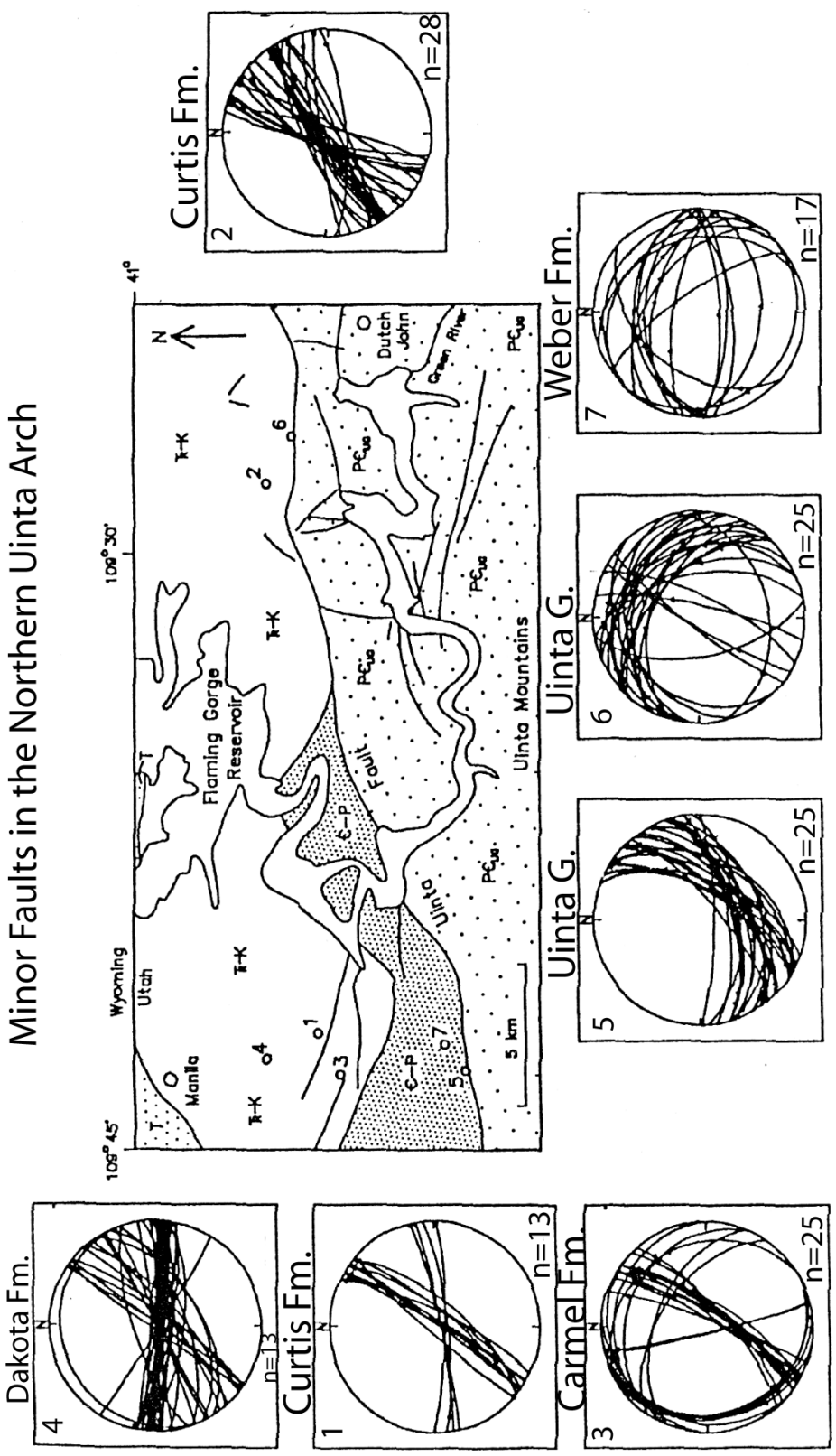

Figure 17. Stereonets of minor fault data and the corresponding locations within the northern Uinta arch (Reproduced from Gregson and Erslev, 1997).

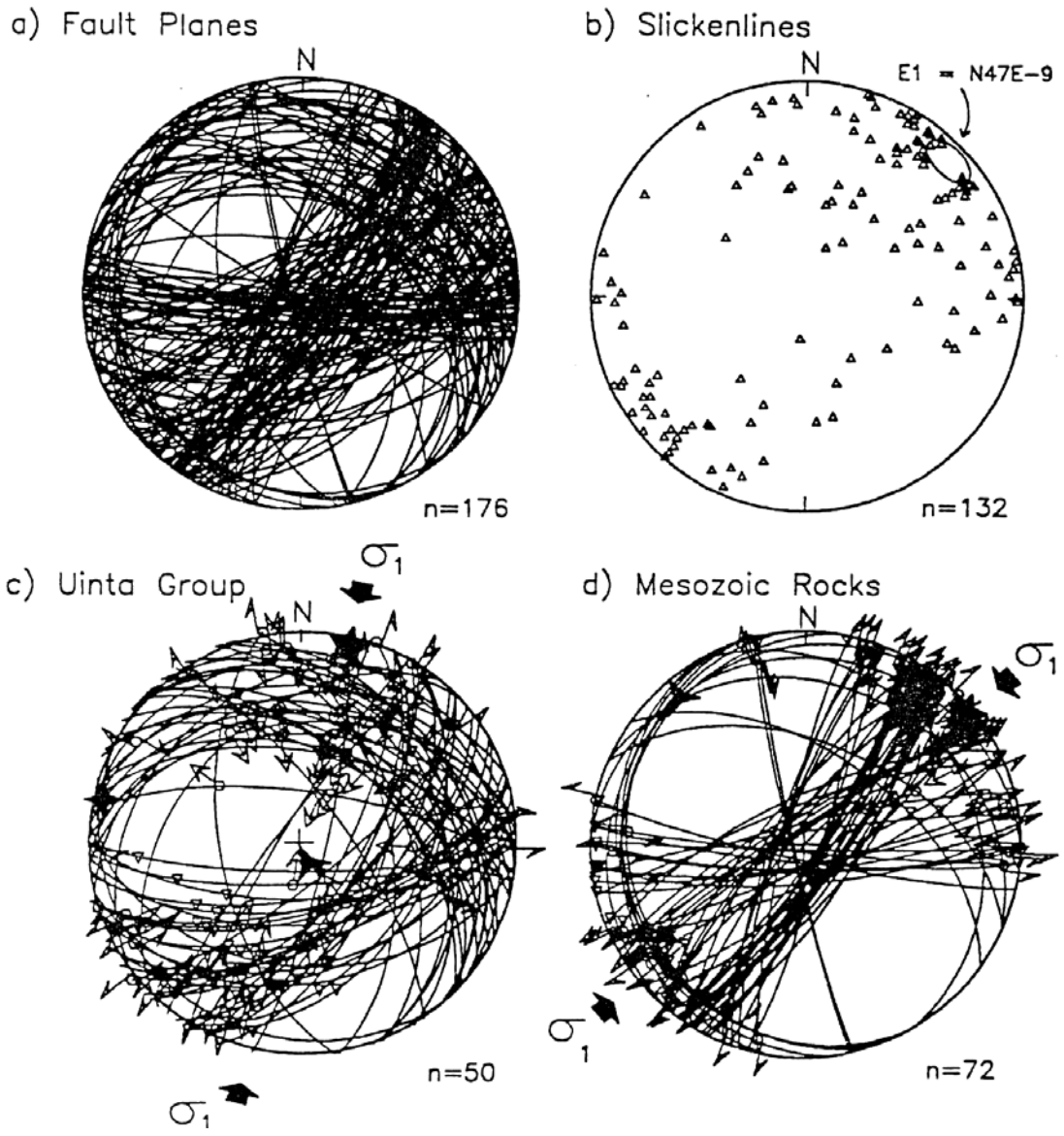

Figure 18. Stereonets illustrating complementary minor fault data measurements from within the northern Uinta arch (Gregson and Erslev, 1997).

transpression along both northern and southern bounding faults (Fig. 20a) and the other shows the northern bounding fault as a left-slip transpressional structure and the southern bounding fault as a pure thrust (Fig. 20b).

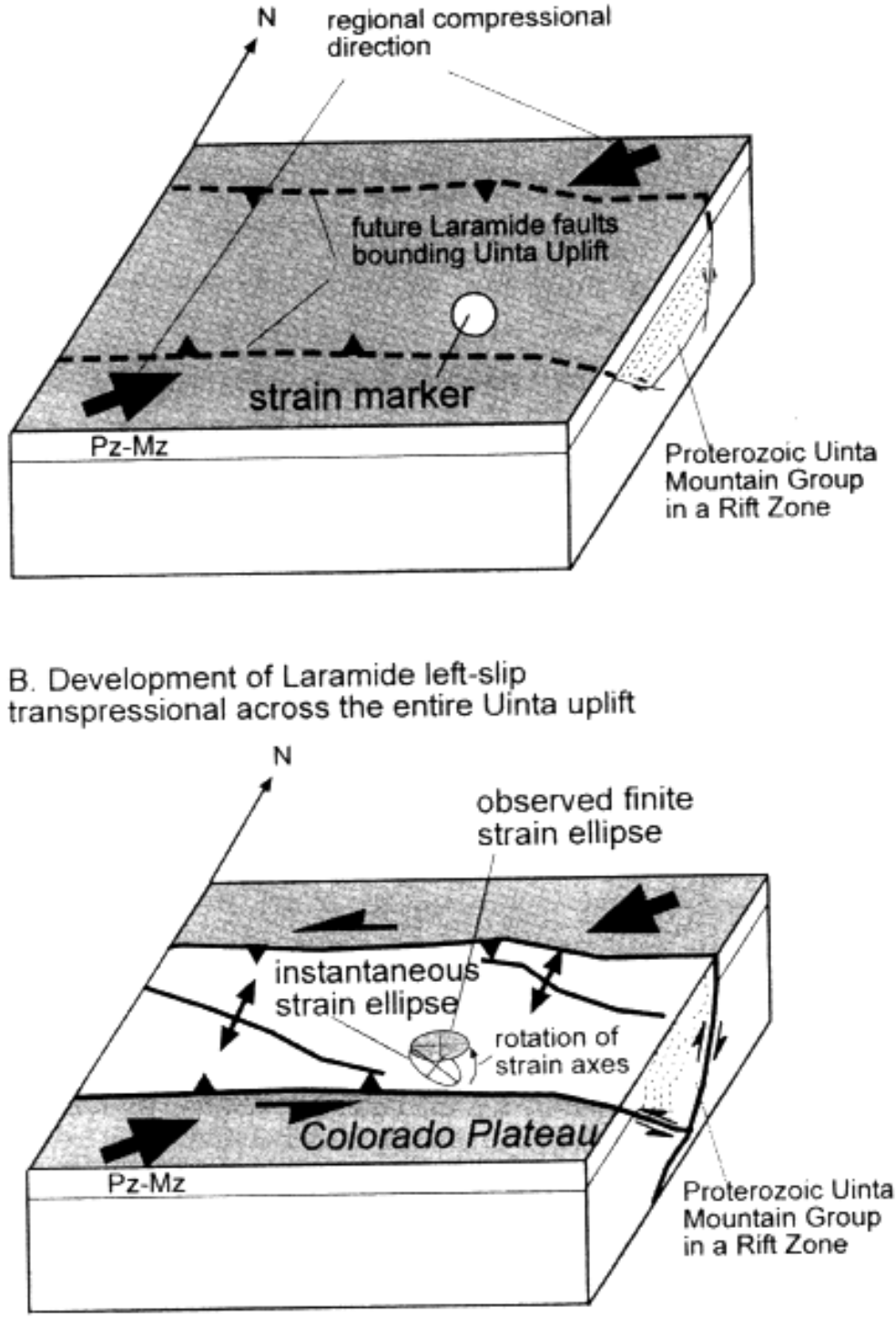

Figure 19a, b. Tectonic model of the evolution of the Uinta arch during the Laramide (Johnston and Yin, 2001).

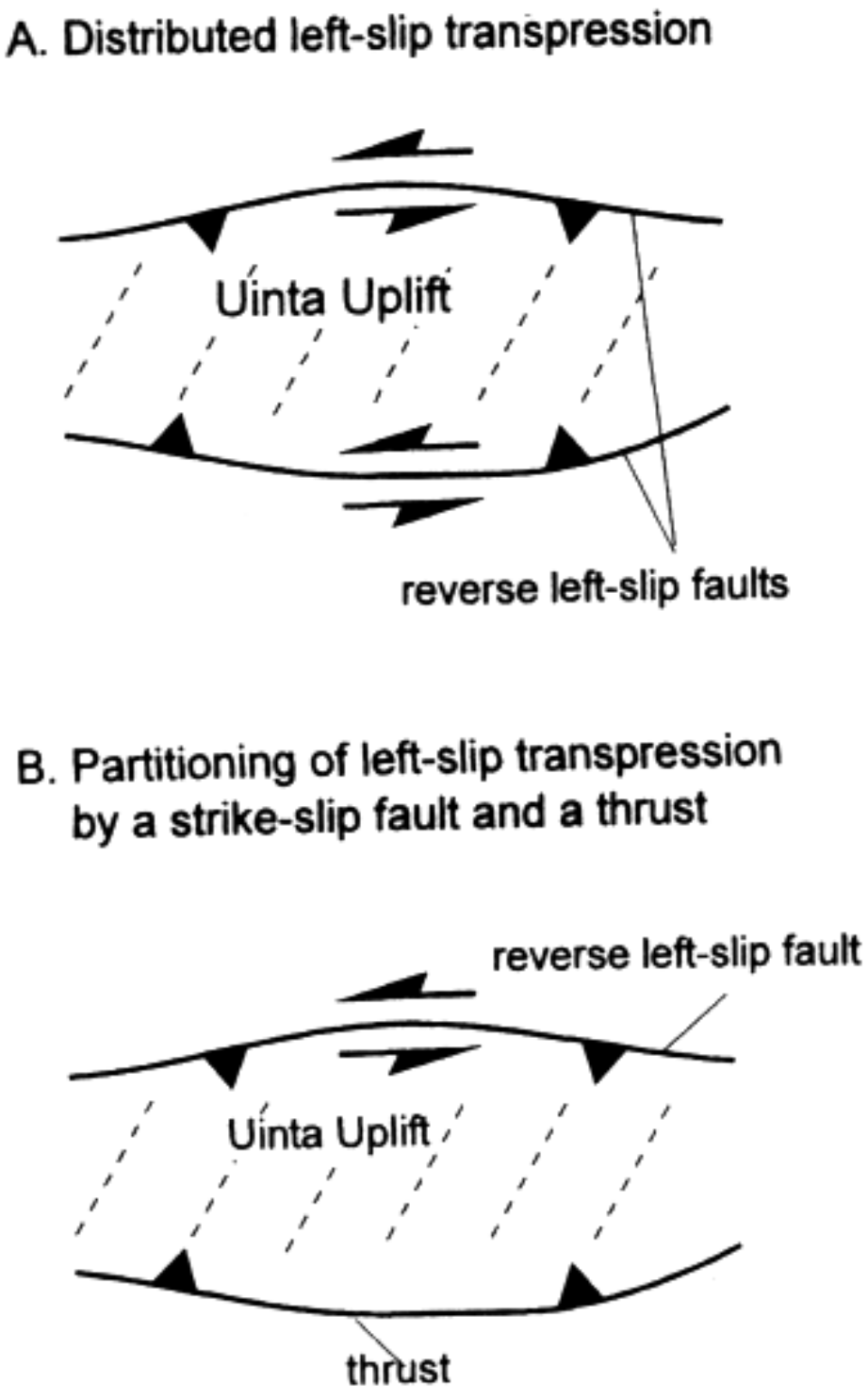

Figure 20. Hypotheses explaining an overall left-slip system a) with left-slip transpression along both northern and southern bounding faults b) with the northern bounding fault as a left-slip transpressional structure and the southern bounding fault is pure thrust (Johnston and Yin, 2001).

Faulting within the Irish Canyon-Vermillion Creek Area

The Irish Canyon-Vermillion Creek area is located on the extreme northeastern flank of the Uinta Mountains (Fig. 1, 2, and Plate 1). The major fold within the area is a monocline which dips homoclinally off to the northeast. Within the strata, each period is represented from the Precambrian to Tertiary, excluding the Ordovician, Silurian, and Devonian. The major fault within the area has been given multiple names including the Uinta, Uinta-Sparks, or the Uinta-Sparks Ranch thrust fault (Fig. 4). Previous investigators have differentiated the Uinta-Sparks fault into two separate faults, labeling the strand west of Diamond Peak the Uinta fault and labeling the strand east of Diamond Peak the Sparks fault (Sears, 1924; Bradley, 1964a and b). Others have interpreted the fault as a single continuous fault (Powell, 1876; Hansen, 1986b) and labeled it simply the Uinta fault. This low-angle thrust fault trends sinuously eastward and south-eastward, dies out just southwest of the area, but continues north to just south of Manila Utah (Blackstone, 1955). South of Vermillion Creek, the fault divides into a broad zone of fractures that continues to Maybell, Colorado and possibly to Craig, Colorado. This fault zone extends approximately 160 km and displays a maximum stratigraphic throw of approximately 10,000 m (Hansen, 1986b). The fault surface is concave upward and nearly vertical at the surface, but becomes shallower at depth. The fault motions to the northeast began in the Paleocene and continued until the Eocene (Roehler, 1987).

Other investigators suggested that the movement of the Uinta fault most likely initiated in the Precambrian and ceased in the late Early Eocene (Sears et al., 1982; Hansen, 1984, 1986b). High mountains and short transport distances are indicated by the coarse conglomerates of the Wasatch Formation (Niland Tongue, Early Eocene) and the overlying

members of the Green River Formation (Tipton and Wilkins Peak, Eocene), and syn-depositional faulting is implied. Overlying the Tipton and Wilkins Peak members is the undeformed late Early Eocene Cathedral Bluffs Tongue of the Wasatch Formation, supporting the Eocene cessation of fault movements (Ritzma, 1955; Rowley et al, 1985).

A blind thrust was interpreted a few kilometers north of the Uinta fault in Wyoming (Gries, 1981, 1983). Although no surface exposure exists, this fault could merge westward in the subsurface with the Henrys Fork fault or the North Flank fault in Utah (Hansen, 1986b). Near Flaming Gorge, another zone of east-west faulting merges with the Uinta fault along shorter linking fractures, possibly tear faults (Hansen, 1986b).

There is over 4500 m of Paleozoic and Mesozoic rocks exposed on the hanging wall of the Uinta Thrust (Manion, 1961) with the Paleozoic rocks dipping to the northeast at about 25 degrees. The dip increases to vertical and even overturned within some of the Cretaceous rocks. Two high-angle, imbricate faults within the south-central section of the area are indicated by displacements of the Miocene Browns Park Formation and repetitions of the Mississippian Madison Limestone and Pennsylvanian Morgan Formation. These faults roughly parallel the Uinta fault and are likely caused by relaxation of the thrust plate (Roehler, 1987), gravitational collapse of the Uintas, or Browns Park extension.

CHAPTER III. METHODS

In order to elucidate the timing and mechanisms responsible for fracturing within the Irish Canyon-Vermillion Creek area, data from 722 slickensided minor faults and 996 joint measurements were compiled with detailed geologic mapping and a 2D seismic line to determine the kinematics of the area. Field mapping, fracture data collection, kinematic fracture analyses, and 2D seismic and cross-section analyses were utilized to test hypotheses for regional tectonics as well as regional fracturing.

If the structural trends are in response to a late N-S compression (Gries, 1983), the calculation of a N-S ideal σ_1 (σ_1 = the maximum compressive stress direction) from minor fault data and evidence of a rotation of the ideal σ_1 direction from E-W counterclockwise to N-S over time would be expected. If oblique slip were responsible (Molzer and Erslev, 1995), then a shortening direction oblique to the E-W structure as well as slickenlines with a component of both dip-slip and strike-slip motions would be expected. If reactivation of pre-existing weakness was responsible for the structural trends (Hansen, 1986b), then multiple orientations of overprinting slickenlines would be observed along fault planes. For example, evidence for reactivation of pre-existing weakness might be observed as slickenlines on a single plane indicating south-directed normal fault motions that were then overprinted by slickenlines indicating NE-SW-directed thrust fault motions.

If the fracture genesis occurred in response to pre-Laramide Sevier shortening (Condon, 1997; Silliphant et al., 2002) then the fractures would only be found within strata

pre-dating the Laramide. If the fractures are of syn-Laramide origin (Stone, 1995; Hansen, 1986b), they would be found within both pre-Laramide and syn-Laramide strata and would cross-cut or abut against pre-Laramide fractures. If the fractures were due to topographic release due to uplift and erosion (Hancock and Engelder, 1989), the fracture patterns would mirror the orientation of topography. If elastic rebound of Laramide strain was responsible for the fracturing (Ruf and Erslev, 2005), then fractures orthogonal to the regional Laramide σ_1 direction would be observed. Finally if current Rio Grande rifting (Hancock and Engelder, 1989), Basin and Range extension, or Miocene Browns Park extension (Stevens, 2002) were responsible for the fracturing, the fractures would be found in pre-, syn- and post-Laramide strata and cross-cut or abut against all pre- and syn-Laramide fractures. Detailed kinematic analyses can illuminate the mechanism responsible for a locations fracture history.

Field Mapping

Detailed large scale field mapping was conducted at a 1:12,000 scale using the USGS Irish Canyon topographic map for a base (Plate 1). Field mapping was done on a base map and contacts, faults, attitudes, and data stations were transcribed onto a full sized 1:12000 scale base map upon return to base camp. The locations of contacts were mapped by walking contacts, traversing the area perpendicular to strike, and by viewing the topography from overlooks.

The base map was digitized into ArcGIS adhering to the National Park Service's Geologic Resources Evaluation Division's (GRE) protocol for positional accuracy for all map features. Layers were created for all map features including contacts, attitudes, faults, wells, folds, station locations, and roads, as well as a layer for faults gathered from other

field investigators' maps (Plate 1). Additional map resources consisting of regional geology, base maps of seismic shotlines, regional structure contour maps (Fig. 21), a structure contour map of the Frontier Formation just north of the area (Fig. 22), and a structure contour map of the Madison Limestone just north of the area were then georeferenced to the field map. This compilation of maps allowed comparisons of field map relationships and maps from other investigations, as well as illumination of structural relationships that had previously gone unnoticed. Finally, using ArcSCENE, a 3D model of the topography of Irish Canyon-Vermillion Creek area was created using the ArcGIS features and the digital elevation model (DEM) (Fig. 23a b, c).

Systematic Fracture Measurement

Data from minor fault stations (15) and joint stations (19) were systematically collected throughout the area. A location was a suitable station if no less than 25 measurements could be acquired. The fault stations were located within the Permian Park City Formation, Triassic Navajo Sandstone, Jurassic Curtis Formation, and Cretaceous Dakota Formation and the joint stations were located within the Triassic Navajo Sandstone, the Cretaceous Mesaverde Group, Oligocene Bishop Conglomerate, and Miocene Browns Park Formation. Data were collected using a Brunton compass using the right rule to measure strike, dip, trend, and plunge of minor fault planes and slickenlines, as well as strike and dip of joint surfaces. These data were recorded into a field notebook and later input into Excel and Select 1.2 data tables (Erslev, 1998). All stations were recorded using a handheld GPS unit to insure positional accuracy. Minor fault stations were primarily found within the Curtis Formation and Dakota Formation because sufficient numbers of slickenlines could readily be viewed in outcrop.

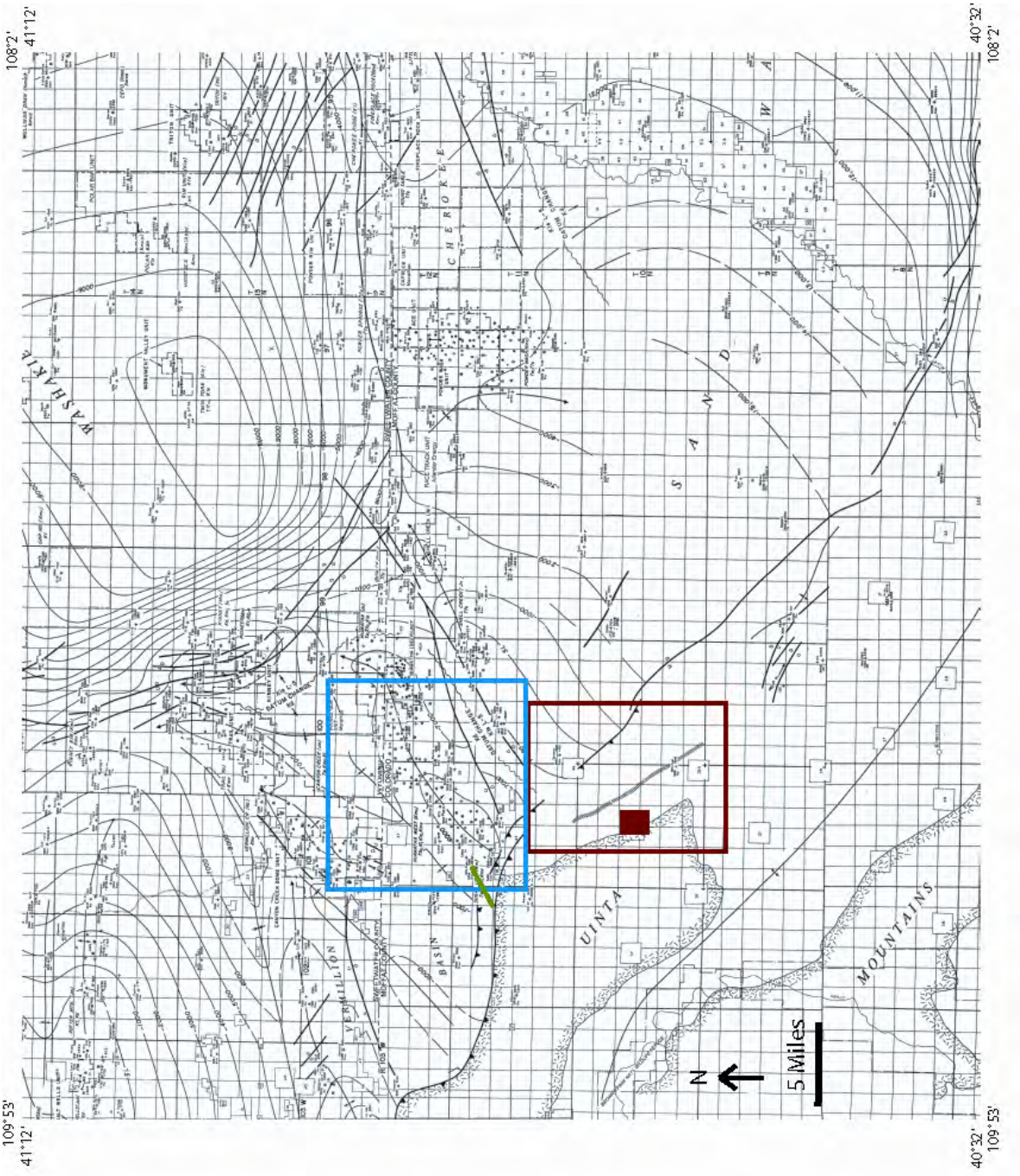

Figure 21. Regional structure contour map of the top of the Dakota Formation (Barlow and Haun, 1998). Reddish-brown box corresponds to the Irish Canyon quadrangle, the location of Plate 1, and Figures 23, 28-30, and 34-35. The solid reddish brown box marks the location of Irish Canyon. The blue box marks the location of Figure 22. The green line marks the approximate location of the cross-section at Sugar Loaf Butte.

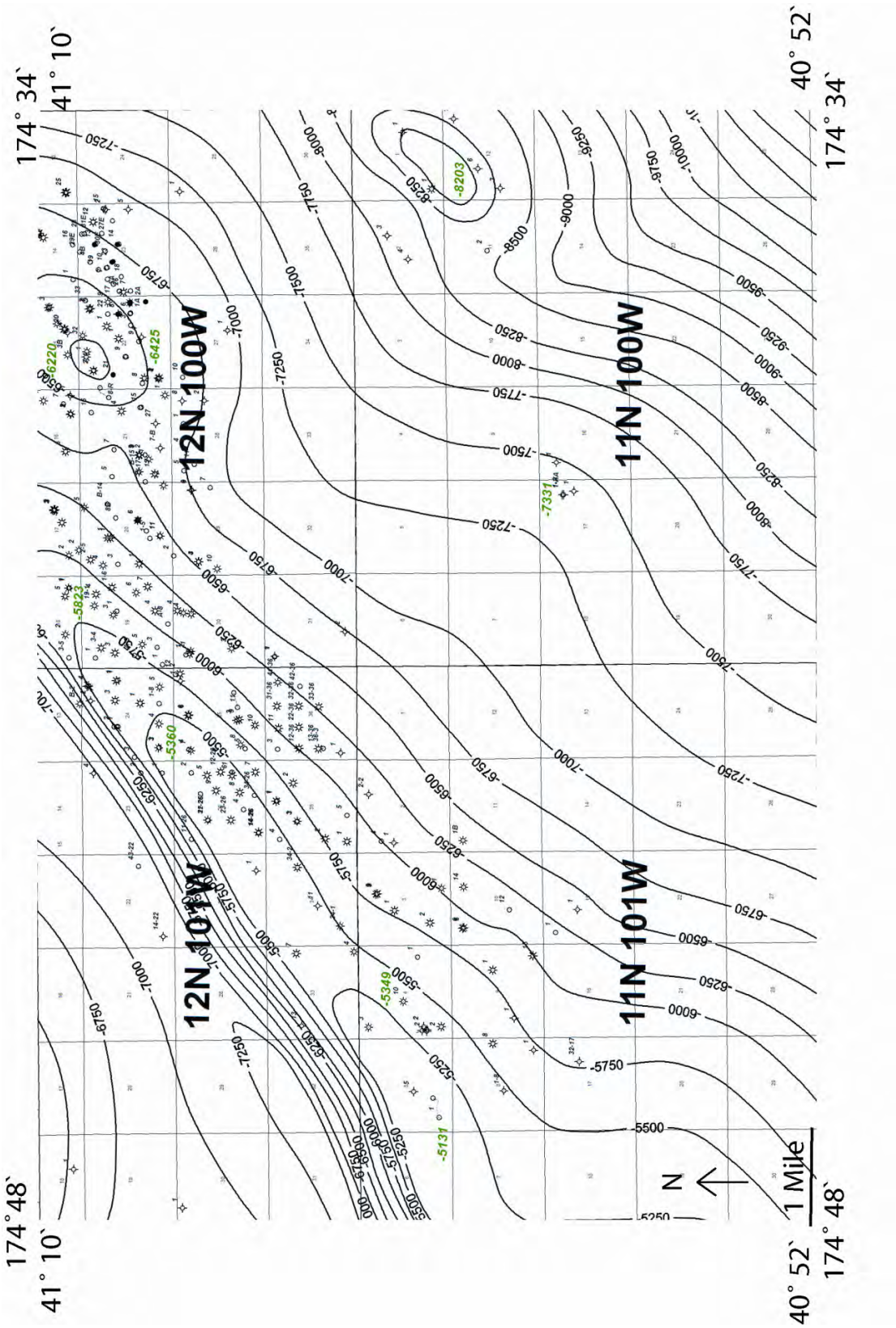

Figure 22. Large scale structure contour map of the top of the Frontier Formation from just north of the area illustrating differing structural trends (Donated by Questar Market Resources, Inc.).

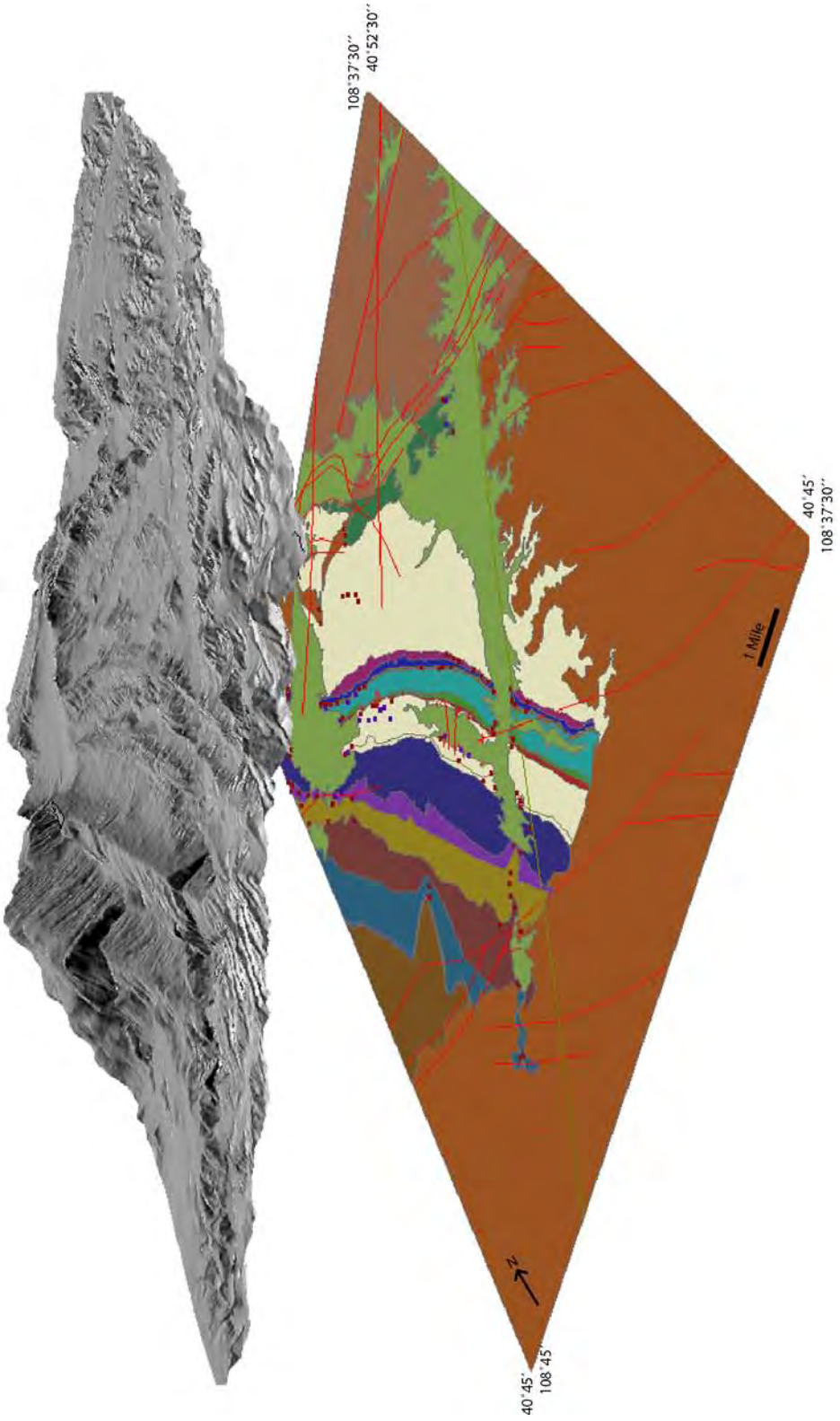

Figure 23a. Projection of mapping attributes onto the Irish Canyon DEM using ArcScene. Explanation of attributes on Plate 1.

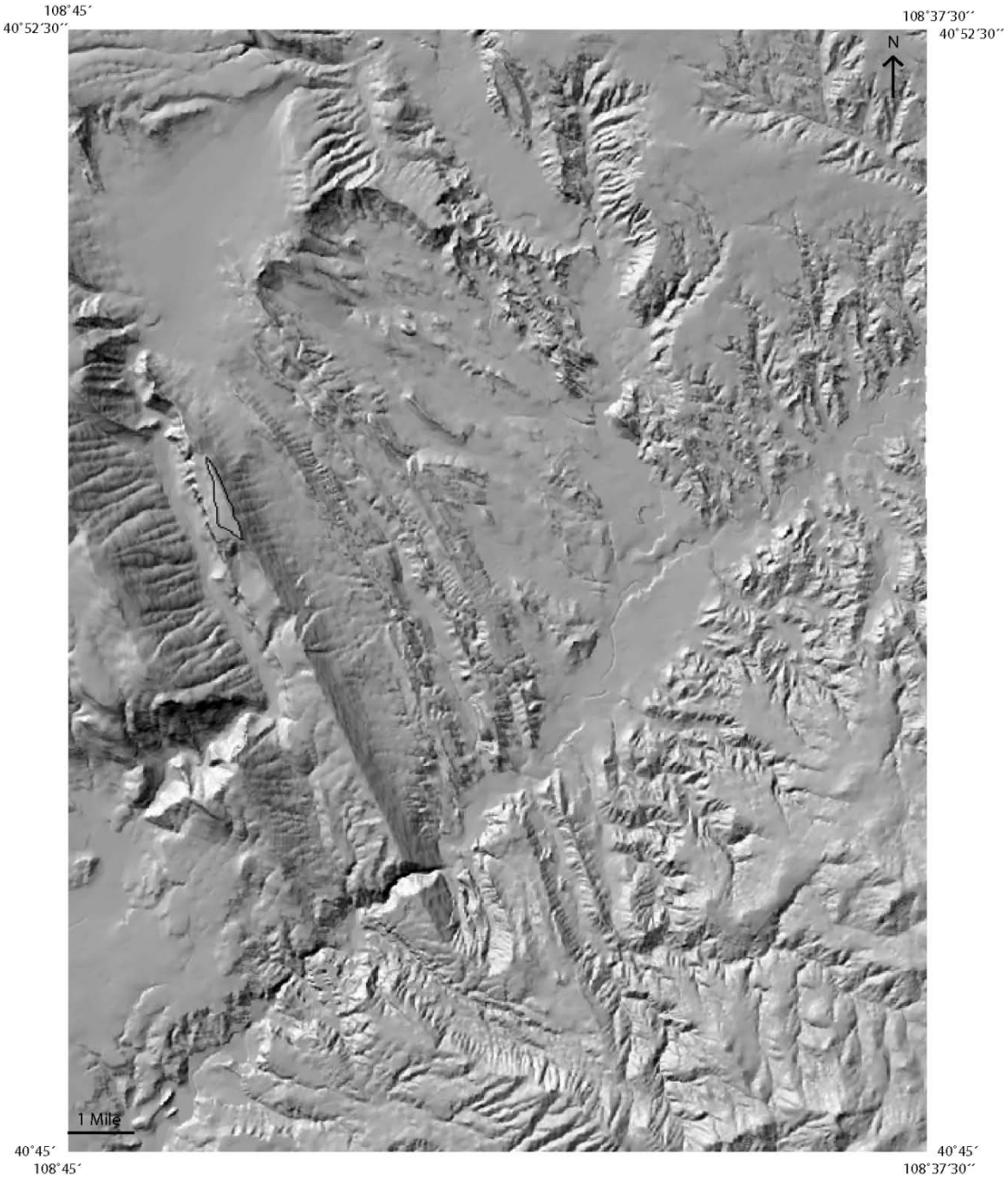

Figure 23b. Map view of 3D model of Irish Canyon-Vermillion Creek area topography created in ArcScene.

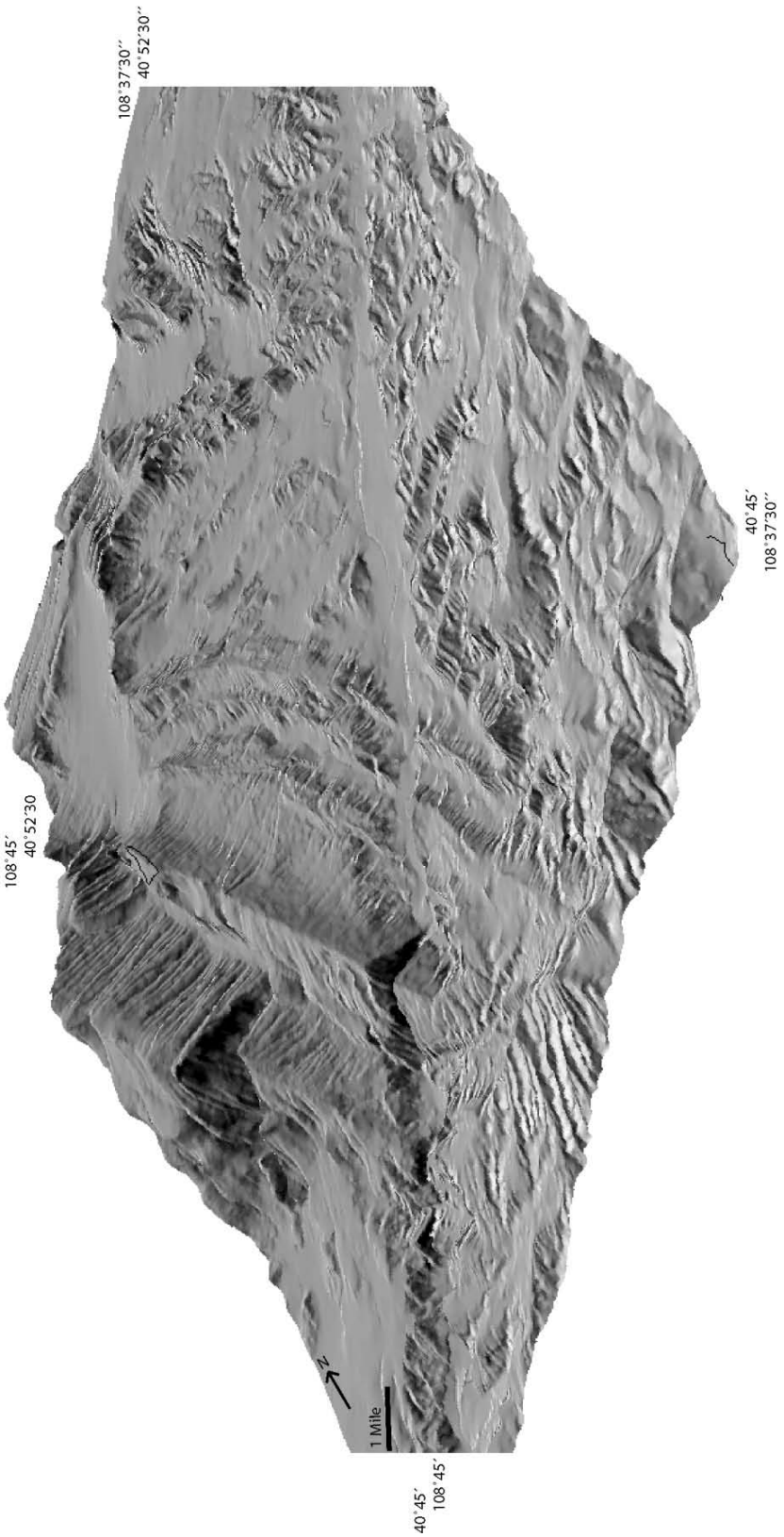

Figure 23c. Oblique view of 3D model of Irish Canyon-Vermillion Creek area topography created in ArcScene.

Occasional slickenlines were also found within the Park City Formation and the Navajo Sandstone, but accessibility was limited and few measurements were collected. Due to the nature and quality of the outcrops, the majority of slickenlines were found in the central portion of the area and usually only within the more resistant layers. While fewer in number, slickenlines were also located in the northern and southern portions of the area. These minor fault data were collected directly off fault planes, to avoid bias, not more than one measurement was collected from within the area of about a clipboard. Shear sense was determined using Petit's (1987) RO criteria (Fig. 24). When possible, cross-cutting relationships were carefully observed so that timing relationships between different faulting events could be assessed. The Curtis Formation functioned as a pre-Laramide marker, the Dakota Formation functioned as a pre-Laramide marker, and the Browns Park Formation functioned as a post-Laramide marker.

Joint data were collected within the Triassic Navajo Sandstone, Oligocene Bishop Conglomerate, and Miocene Browns Park Formation. These rocks were chosen because they possess laterally continuous joint sets with ages bracketing the Laramide Orogeny, allowing for optimal opportunity for establishment of timing relationships. Bedding measurements were taken at each station, noting layer thickness, formation, and lithology (see Appendix C). Joint surfaces were discriminated from faults by lack of gouge, slicks, or cataclasite, and whether plumose structures (hackles, ribs, or arrest lines) were present. The joint set measurements within the Navajo Sandstone were gathered by traversing the unit along strike and collecting data first along the dip-slope, then along the Navajo Formation's contact with the Chinle Formation. Within the Oligocene Bishop Conglomerate and the Miocene Browns Park Formation, stations were collected at

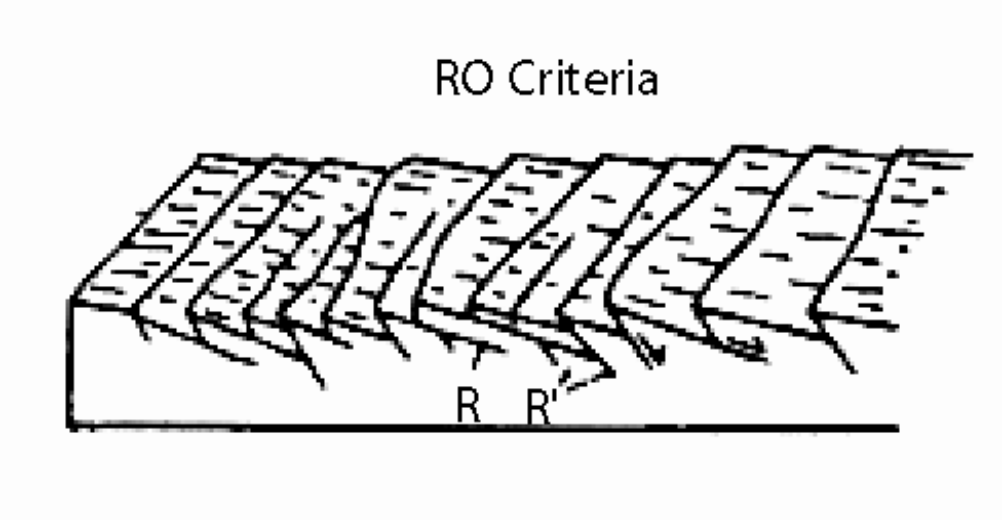

Figure 24. Petit's (1987) RO criteria of shear sense classification.

localities where sufficient non-topographical joints existed. Due to the fracture response created by the lithologic properties, the extent of weathering, and the minimal amount of outcrop, acceptable joint station localities were infrequent.

The full fracture data set was then systematically analyzed to reveal kinematic relationships. Orient v. 1.6 (Vollmer, 1989) and StereoWin v. 1.1 (Allmendinger, 2002) were used to create stereonet plots of the data split by locality, age of strata, type of measurement or calculation (i.e. joint or fault plane, slickenline, or σ_1), and type of fracture (i.e. Mode I, II, or slip sense). Rose plots, rounded with a smoothing increment of 10 degrees, of average σ_1 trend, average slickenline trend, average joint strike, and average shearband trend were created using LDIS (Erslev, 2006); (see Appendix B,C). For all localities, the angle α used for the calculation of the ideal σ_1 for preliminary analyses was assumed to be 25 degrees in accordance with Byerlee (1978). An α angle of 20 degrees was deemed more accurate for the field area and therefore used for the final analyses.

2D Dimensional Seismic Cross-Section Analyses

In order to gain an understanding of the 2D geometry of the Irish Canyon-Vermillion Creek area, line 407-12, the highest quality 2D seismic line, was interpreted (Fig. 25). The mappable horizons were picked and velocity analysis and depth conversions were conducted. The illuminated geometry was then used to help construct a 2D cross-section.

This restorable cross-section, oriented nearly perpendicular to the local shortening direction, was created using 2DMove and AutoCAD software. The strata represented in the section consists of the Precambrian Uinta Mountain Group; the Cambrian Lodore Formation; the Mississippian Madison Limestone; the Pennsylvanian Morgan Formation; the Pennsylvanian-Permian Weber Formation; the Permian Park City Formation; the Triassic Woodside Formation, Chinle Formation, and Navajo Sandstone; the Jurassic Entrada Formation, Curtis Formation, and Morrison Formation; the Cretaceous Dakota Formation, Mowry Formation, Frontier Formation, Mancos Shale, and Mesaverde Group; and the Tertiary undivided, Bishop Conglomerate, and Browns Park Formation. Sections were constrained using 1:12000 scale field mapping (conducted over summer 2006) and industry 2D seismic data donated by Questar Market Resources, Inc. and British Petroleum Exploration. The two dimensional cross-section was further constrained using 2DMove restoration algorithms for line length unfolding and area balancing. For additional geometric constraint, the length and area balanced section was checked against a parallel, velocity analyzed and depth converted 2D seismic line (Fig. 25) and against adjacent cross-sections (Fig. 15, 16). During this cross-check, the geometries of the major thrust fault and

the bedding dips were checked, specifically taking note of the listric nature and angle of the major fault and whether the bedding dips changed from moderate in the west to highly inclined and even overturned in the east.

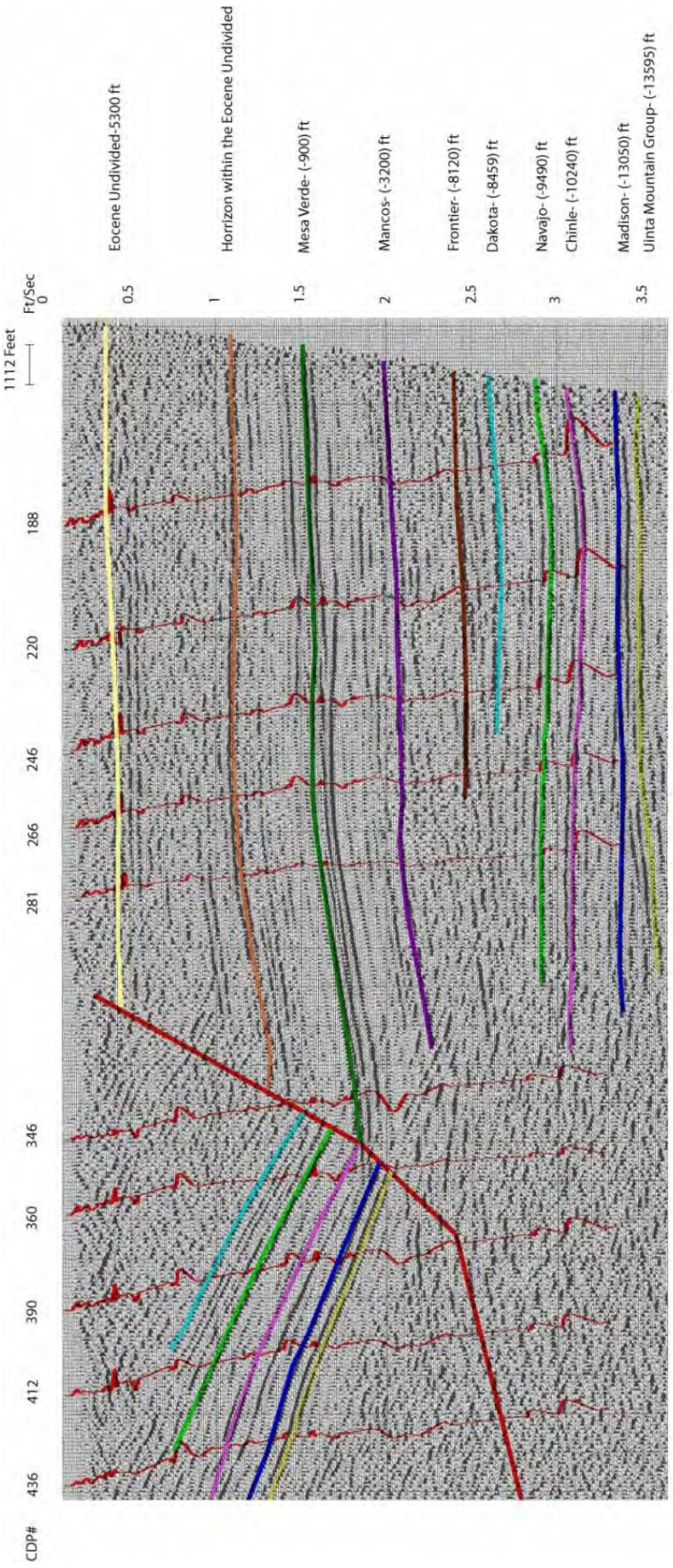

Figure 25. Line 407-12 (Processed by British Petroleum Exploration) with interpreted horizons and interval velocity plots calculated from stacking velocities overlain. See Plate 1 for location.

CHAPTER IV. MAP ANALYSES AND INTERPRETATION

To gain a regional perspective and the most diagnostic understanding of the area, a number of different types of maps were georeferenced and analyzed using ArcGIS (ESRI, 2006). This cartographic compilation includes a regional structure contour map (Barlow and Haun, 1998); (Fig. 21), a structure contour map of the Frontier horizon donated by Questar Market Resources, Inc. (Fig. 22), a structure contour map of the Madison horizon donated by Samson Resources, 2 regional geology maps (Newhart and Longman, 2005), base maps of 2D-seismic donated along with 2D lines by British Petroleum Exploration, and the geologic field map (Plate 1).

Observations and Interpretations

From the comparisons of these 6 maps several interesting observations can be gathered.

1) An obvious NW-SE structural grain of fold axes was observed within the field area (Plate 1) and this was corroborated by the regional structure contour map (Fig. 21).

2) Multiple geologic and structure contour maps (Tweto, 1979; Rowley, et. al., 1985; Barlow and Haun, 1998) illustrate a NE-SW structural grain of fold axis with a vector mean of N53E directly north of Irish Canyon in the Vermillion Basin. This orientation is nearly perpendicular to the N30W structural grain of the field area (Fig. 2, 22, and 26).

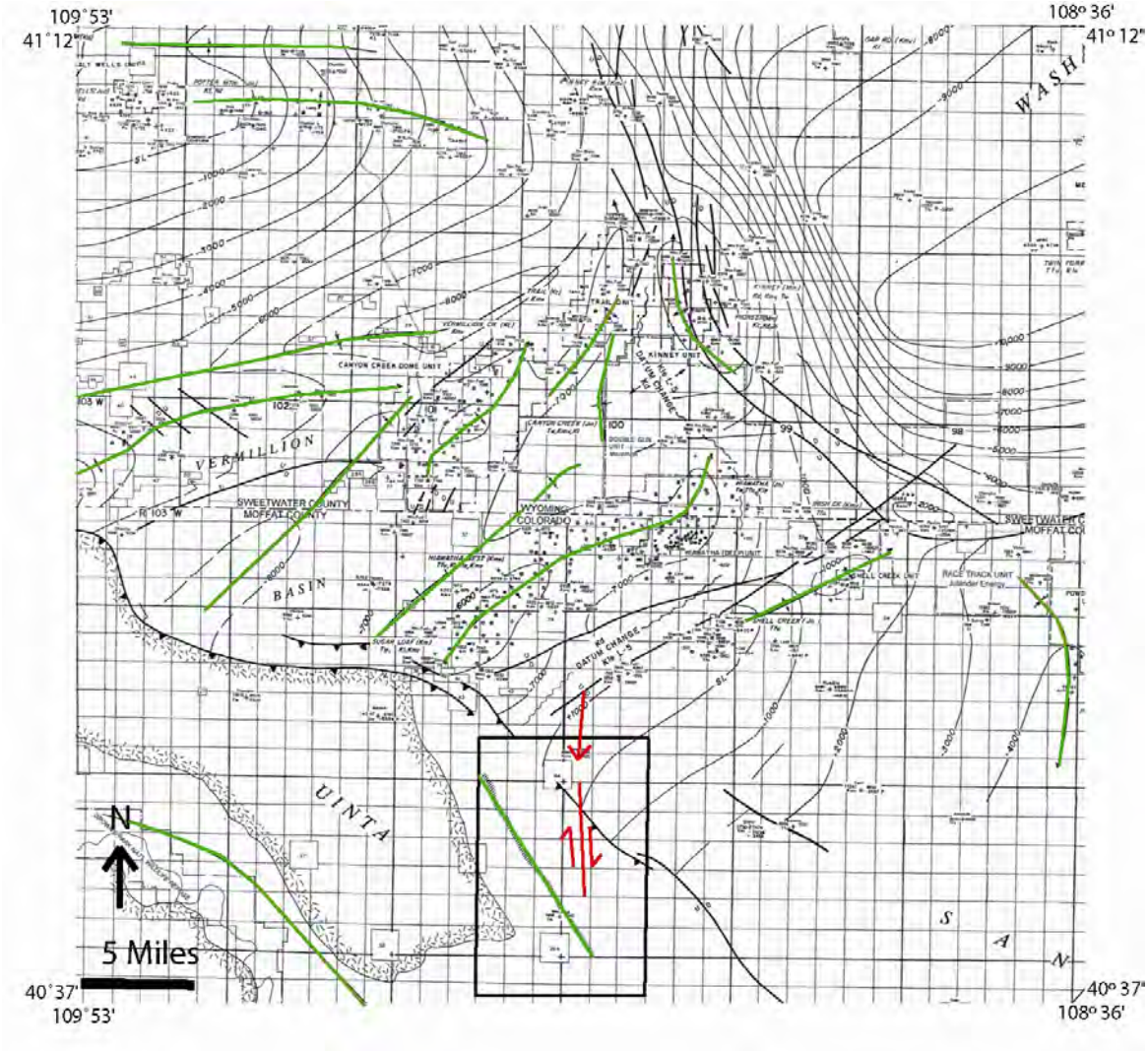

Figure 26. Structure contour map showing location and orientation of fold axes in green. Study area location highlighted by the black box. Red shows the right-lateral strike-slip fault system.

3) E-W trending fold axes are observed north of the field area and the fold axes 10 km north of the area trend N46E and 5 km north of the area trend N64E (Fig. 21 and 26).

4) The regional structure map (Fig. 21) as well as field observations attest to numerous NW-SE striking normal faults which are parallel to the joints seen within the Oligocene Bishop Conglomerate and Miocene Browns Park Formation, as well as normal faults to the east at Toe Creek Anticline, near Craig Colorado (Fig. 4); (Tweto, 1979; Gillett, 2009).

The integration of maps from different sources illuminated structural relationships that were not evident from observations in the field. For example, why would nearly orthogonal structural grains exist immediately adjacent to each other? The existence of a NE-SW structural grain directly adjacent to the NW-SE structural grain observed within the field area suggests a complicated multi-directional or multi-stage stress history. It is interesting that just north of the field site the Vermillion Basin demonstrates a NE-SW structural grain consistent with Sevier NW-SE shortening and that just south, the Irish Canyon-Vermillion Creek area demonstrates a NW-SE grain consistent with NE-SW to ENE-WSW Laramide shortening. This suggests that the border between the two locations marks the end of deformation within the critical taper of the Sevier fold-and-thrust belt. However, the E-W and ENE-WSW trending fold axes north of the area suggest a refraction of Sevier stress from NW- to more NNE-directed shortening.

Additionally, the maps allowed for the identification of a regional NW-SE-striking normal fault set. These normal faults closely parallel a NW-SE-striking joint set. These fractures were then identified to be in response to Browns Park extension by Hansen, (1984). The maps showed that this event spans much of NW Colorado and surroundings areas. Thus, the cartographic integration allowed for a better understanding of regional tectonic history.

V. KINEMATIC ANALYSES AND INTERPRETATIONS

Minor Fault Analyses

The kinematics of minor fault data (722) collected at 15 stations in pre- and post-Laramide strata were analyzed by stereonets, rose diagrams, and eigenvector analyses to calculate average fault plane strike, slickenline trend, and ideal σ_1 (Fig. 27). Because the field area is relatively small and all the kinematic data were collected from two sections with congruent dips, all the data was restored to pre-fold orientation by being rotated SW 40 degrees about a N30W axis. These analyses were conducted for the full data set and then subdivided by station, unit, and slip-sense (See Appendix B).

Viewing the fault data by station, the fault planes appear to have large variances in strike orientation (Fig. 28). The slickenlines have an average trend of N27E (Fig. 29) and the σ_1 orientations have an average trend of N30E (Fig. 30). Looking at the minor fault data sets subdivided by station (Appendix B), it is observed that on average clusters of fault planes strike NW, NNW, N-S, NNE, NE, and ENE. The slickenlines trend from NNW to ENE, with the average trend to the NNE. The ideal σ_1 calculated from minor faults range from NNW-SSE trends to ENE-WSW trends with the average ideal σ_1 trend in a NNE orientation.

The fault plane strikes and average trend for slickenline and σ_1 measurements are in agreement with those gathered from within the Curtis and Dakota Formations just west

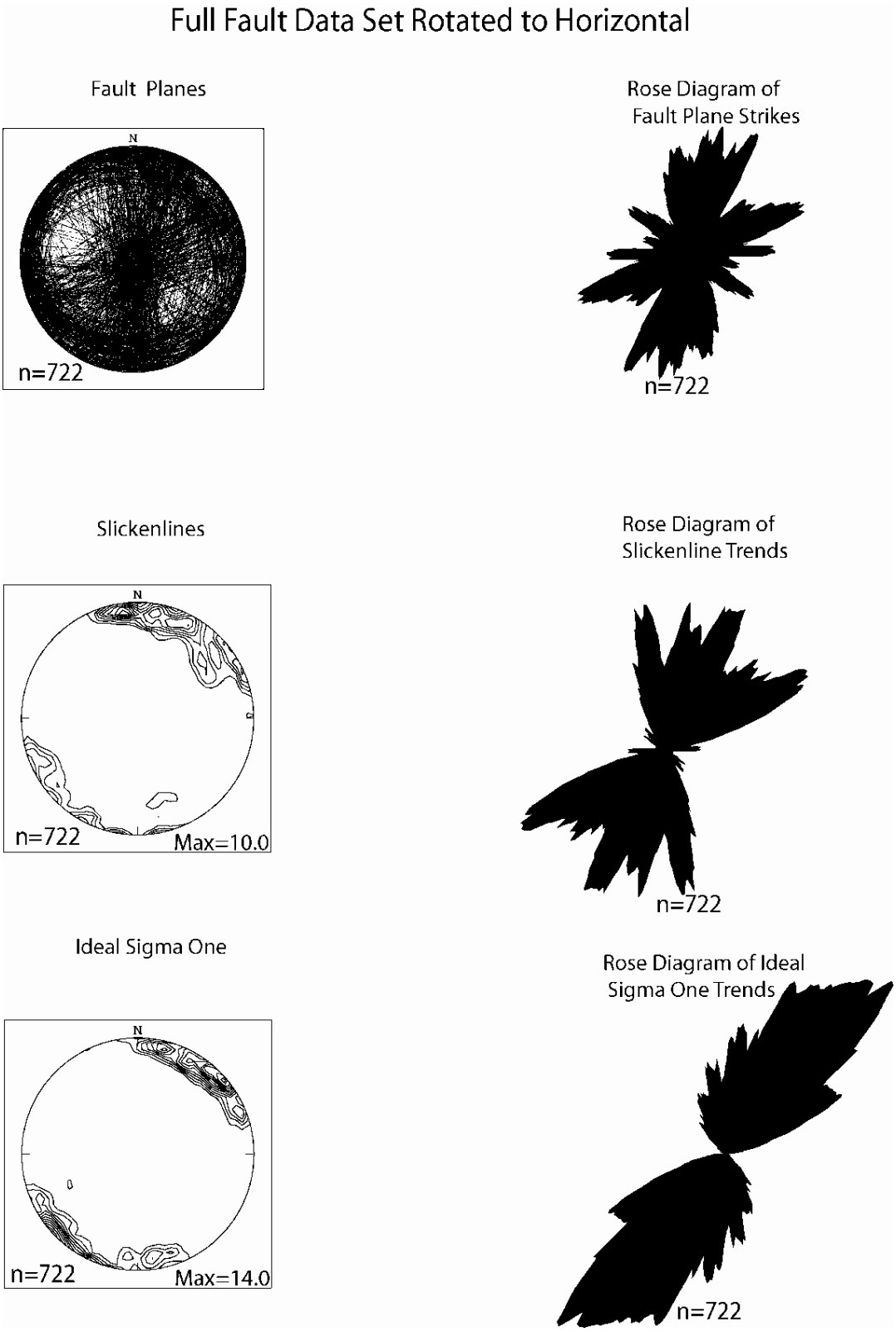

Figure 27. Stereonets of full minor fault data set with bedding restored to horizontal. An interval of 2 percent was used for all contoured plots. Rose diagrams have a smoothing increment of 10 degrees. Data rotated 40 degrees SW about a N30W axis so that average bedding is horizontal.

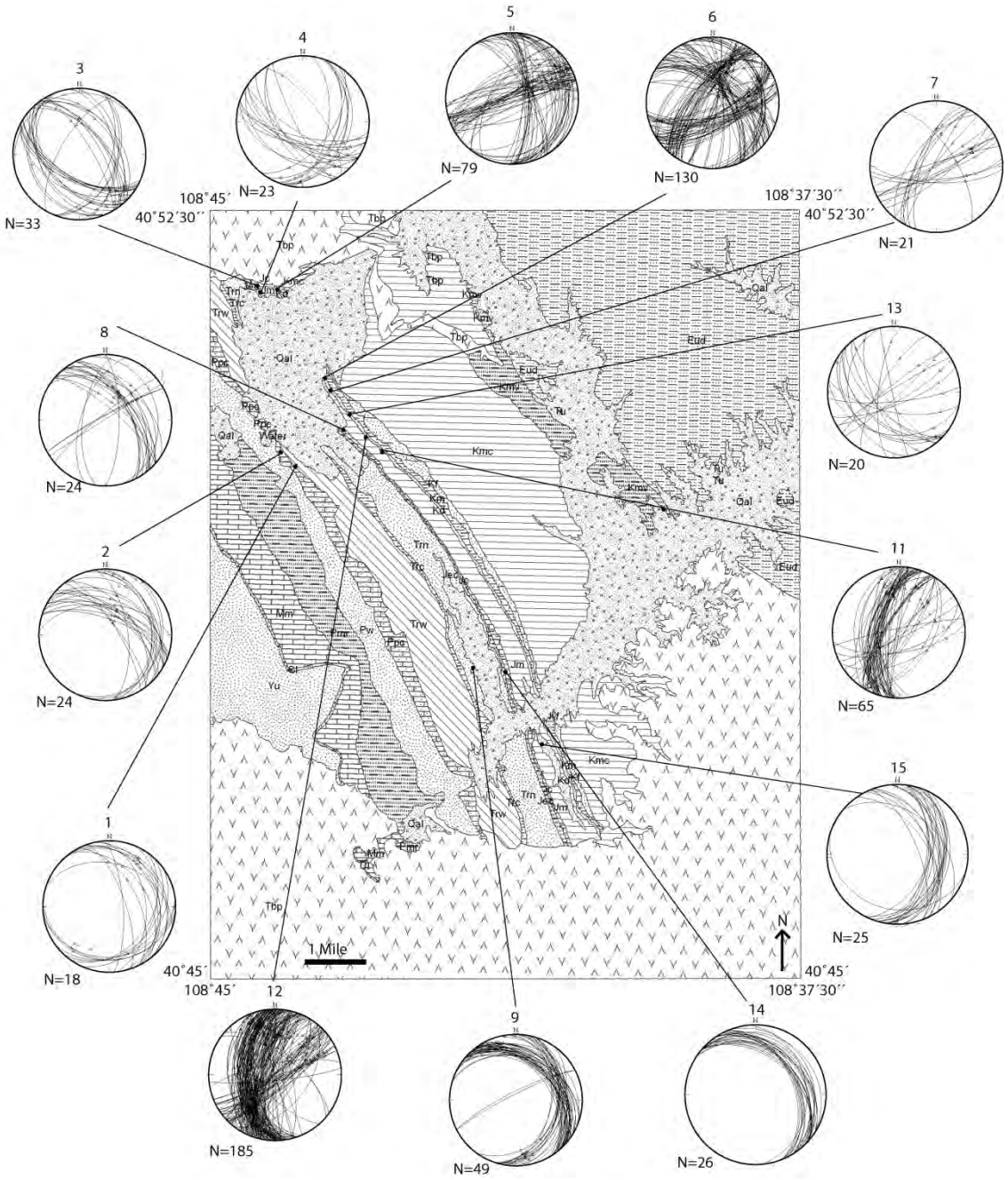

Figure 28. Stereonets overlain on field map illustrating fault planes superimposed on the geologic map (raw data, see Appendix B). Detailed unit descriptions are located in Appendix A and Plate 1.

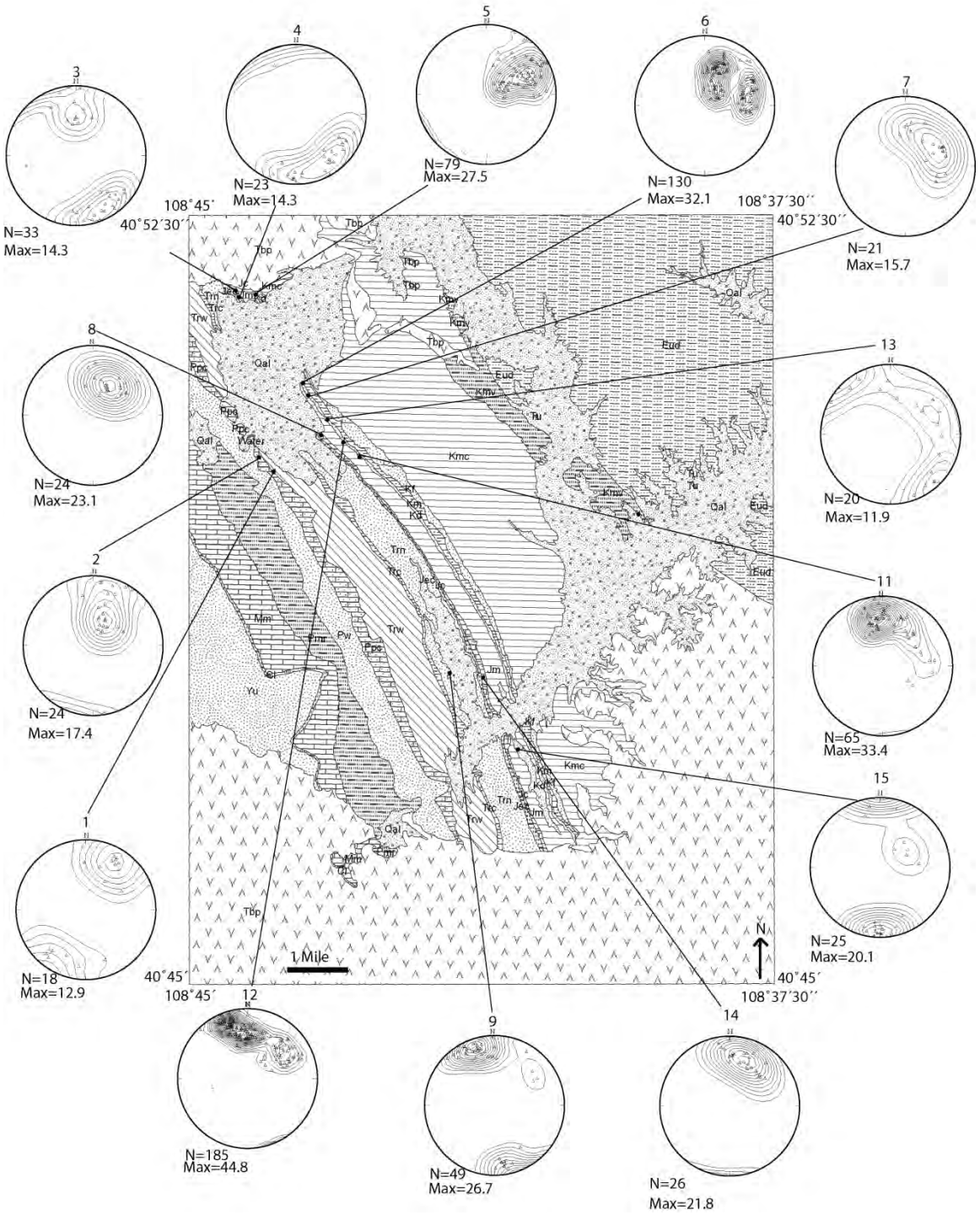

Figure 29. Stereonets of contoured slickenline trends superimposed on the geologic map (raw data, see Appendix B). Contour interval of 2 percent was used for all plots. Detailed unit descriptions are located in Appendix A and Plate 1.

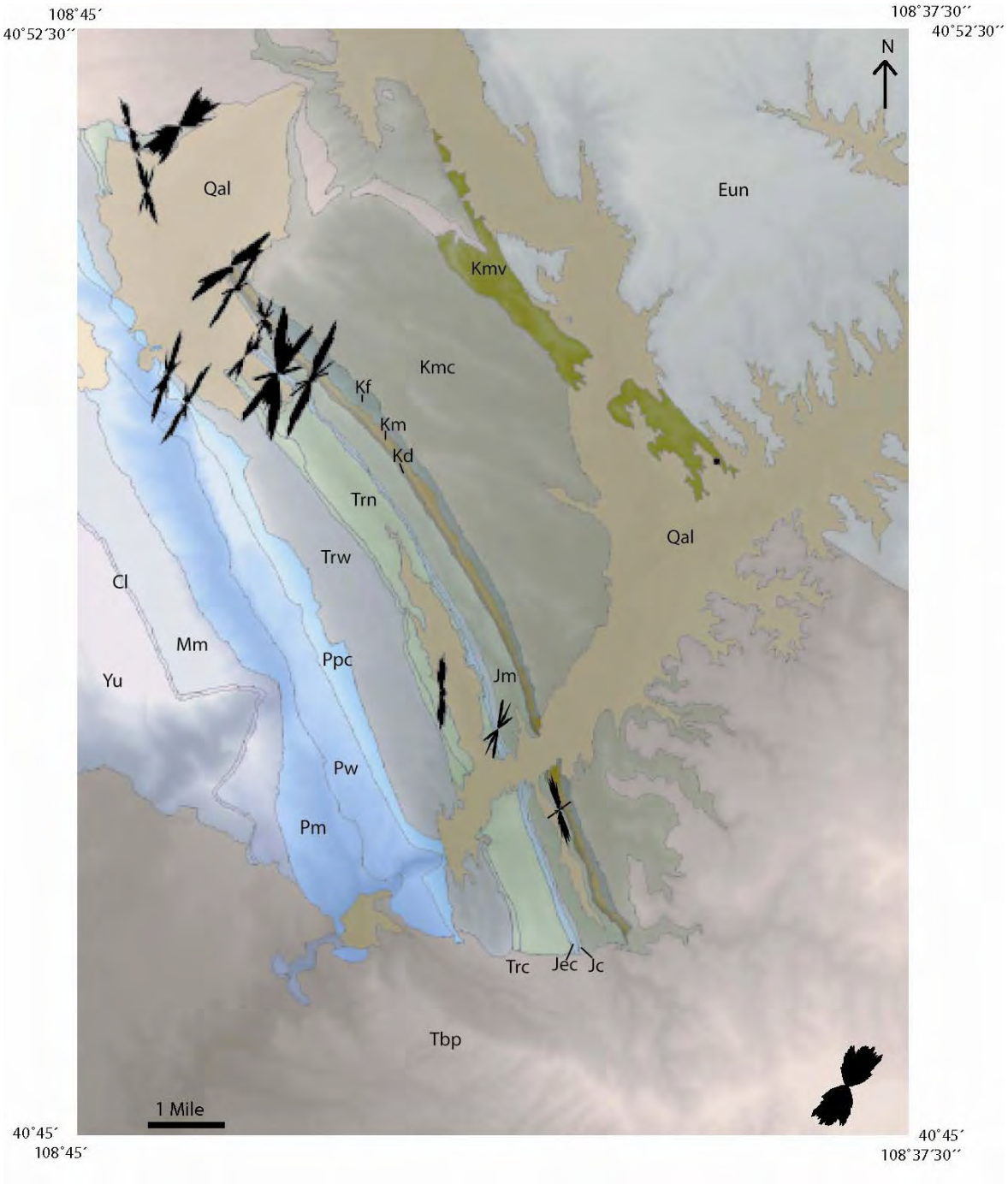

Figure 30. Rose diagrams of average ideal σ_1 superimposed on the geologic map. Detailed unit descriptions are located in Appendix A and Plate 1 (raw data, see Appendix B). Rose diagram of full data set in bottom right corner.

of the study area at Flaming Gorge (Fig. 17 and 18) and from the Dakota Formation within Irish Canyon (S. Larson, 2007, personal communication).

Overall, the faults demonstrate variable fault plane, slickenline, and σ_1 orientations throughout the area. This is evidenced by a large amount of scatter observed within the data (See Fig. 27 and Appendix B). Several observations arise where the fault data is subdivided by slip-sense (Fig. 31). The slickenlines for all slip-senses show trends of NNW, N-S, NNE, ENE, and a small node of NW-SE (See Fig. 31 and Appendix B). However, the NNW-SSE node within the left-lateral data set is likely mislabeled right-lateral faults (Fig. 32).

The ideal σ_1 calculated from minor faults for thrust, left-lateral, and right-lateral faults are consistent with a NW-SE, NNW, N-S, NNE, NE-SW, and ENE-WSW compression, as illustrated by the rose diagrams (See Fig. 32 and Appendix B). However, the majority are in a NNE to ENE orientation. It appears that there are separate phases of deformation and nodes for the different phases of σ_1 were calculated to be N10E and N59E (Fig. 32). The separate phases were determined by analyzing the conjugate strike-slip faults, thrust faults, joints, and the cross-cutting relationships. For example, if the σ_1 orientation for strike-slip faults paralleled the average slickenline orientation for thrust faults and a joint sets average strike, then these fractures were attributed to the same phase of deformation.

There is a predominance of right-lateral faults, consisting of 44 percent of the data set. Thrust faults make up 26 percent of the data set, left lateral faults make up 18 percent of the data set, and normal faults make up 12 percent of the entire data set.

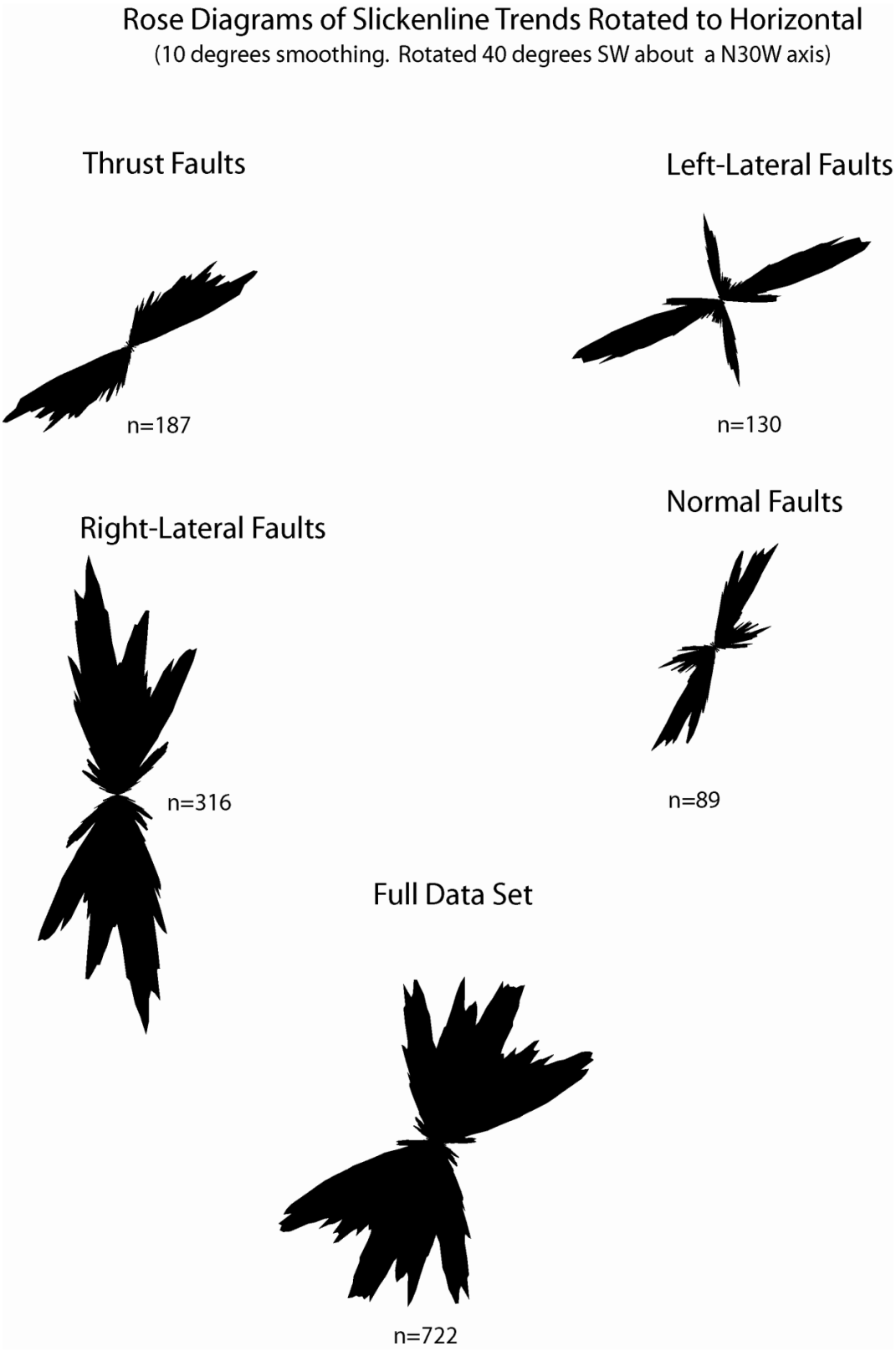

Figure 31. Rose diagrams of minor fault slickenlines separated by slip-sense and fold corrected.

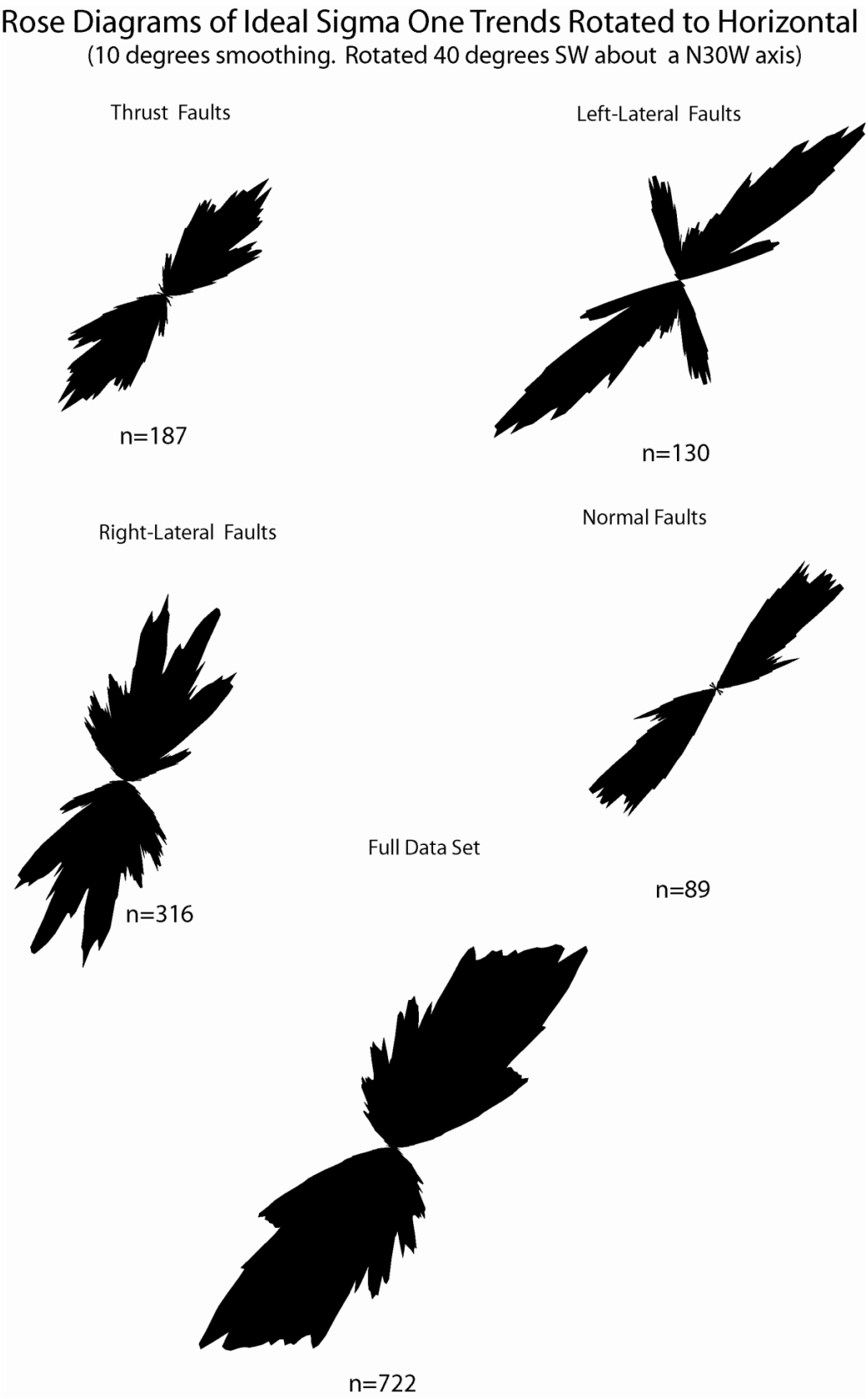

Figure 32. Rose diagrams of minor fault ideal σ_1 separated by slip-sense and fold corrected.

The slickenline data for Laramide normal faults gathered in the Dakota Formation suggest slip in NNE-SSW to ENE-WSW directions. The σ_1 calculated from the normal fault data suggests NW-SE extension. However, it is likely that the normal fault data set is associated with rotated Laramide thrust faults and is not indicative of extension. For example, if early Laramide Orogeny low-angle thrust faults were rotated along with the strata, this would increase their dips, reverse the slipsense and would create the appearance of normal faults. In fact, the normal faults are consistent with a N59E σ_1 which parallels the σ_1 for Laramide thrust faults. A post-Laramide regional NW-SE-striking normal fault and joint set have been viewed within the Oligocene Bishop Conglomerate and Miocene Browns Park Formation both in the field site and surrounding areas.

The majority of the right-lateral strike-slip faults are consistent with a NNE-SSW σ_1 orientation with less substantial subsets showing NW-SE, NNW-SSE, NE-SW, and ENE-WSW σ_1 orientations.

The thrust faults, thrust faults rotated to normal faults, and left-lateral strike-slip faults are consistent with NW-SE, NNE-SSW, NE-SW, and ENE-WSW σ_1. While no slickenline measurements were gathered from the normal faults within the Miocene Browns Park Formation, numerous NW-SE striking faults with normal separations were viewed in the field and during the regional map compilation and interpretation portion of the study (See Plate 1). Fifteen of these normal faults (94) were viewed in the field area and the rest of the orientations were gathered from existing regional maps. The fault set has an average strike of N52W.

Joint Analyses

The joint data (996) collected at 19 stations in pre- and post-Laramide strata were analyzed using stereonets and rose diagrams (Fig. 33). Joint analyses were conducted as two subsets and then subdivided by station within each of the subsets. One subset was comprised of the joints found within the Navajo Formation and the other subset was comprised of the joints found within the Miocene Browns Park Formation. Analyses show a trimodal distribution of average joints strikes of N71E, N40W, and a less substantial set averaging N1E (Fig. 33).

The dominant set within the Navajo Sandstone is the N71E set (Fig. 34) and the dominant set within the Miocene Browns Park Formation is the N40W set (Fig. 35). Abutting relationships suggest that the N71E-striking joint set is primary and that the N1E-striking joint set is secondary. The N40W-striking set showed no abutting relationships, but must be Miocene to Holocene in age (See Appendix C). The N40W joints within the Miocene Browns Park Formation deviate from vertical when rotated to horizontal. This suggests that they are post-orogenic fractures (see Appendix C8).

The joint surfaces are commonly oxidized. The majority of joints within the Navajo Sandstone, primarily the N71E-striking joints, are commonly sealed by the transport of subsequently precipitated fluids along joint surfaces. The N40W-striking joints within the Miocene Browns Park Formation are always open at the surface. The average joint strike of this joint set closely parallels the strike of regional normal faults. A significant amount of scatter and topographic jointing was also observed in the Miocene Browns Park Formation data.

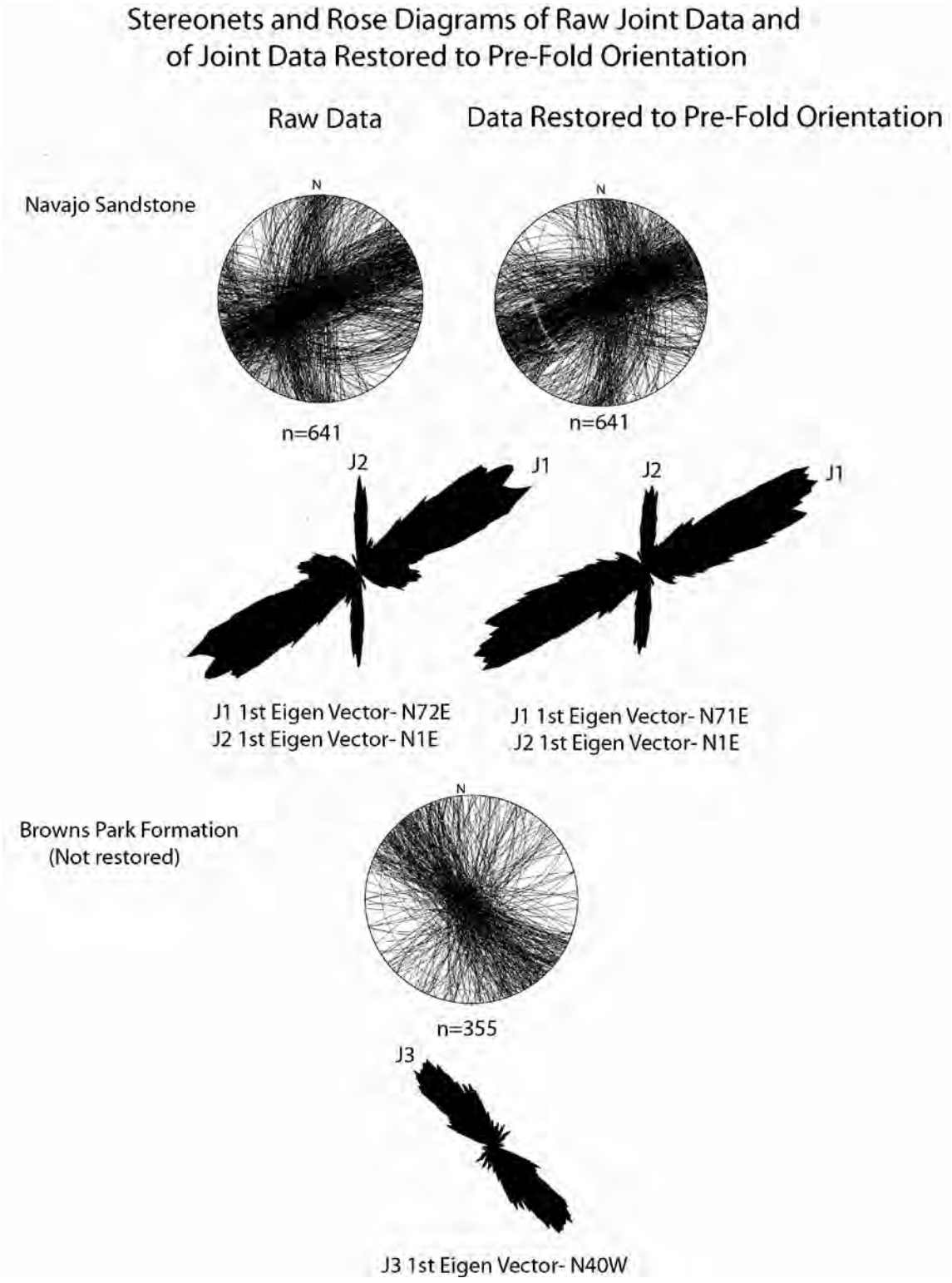

Figure 33. Stereonets and rose diagrams of the full joint data sets restored to horizontal. Data rotated 40 degrees SW about a N30W axis. Note there is a deviation from vertical as the joints within the Browns Park Formation are rotated to horizontal, therefore, this set was not restored.

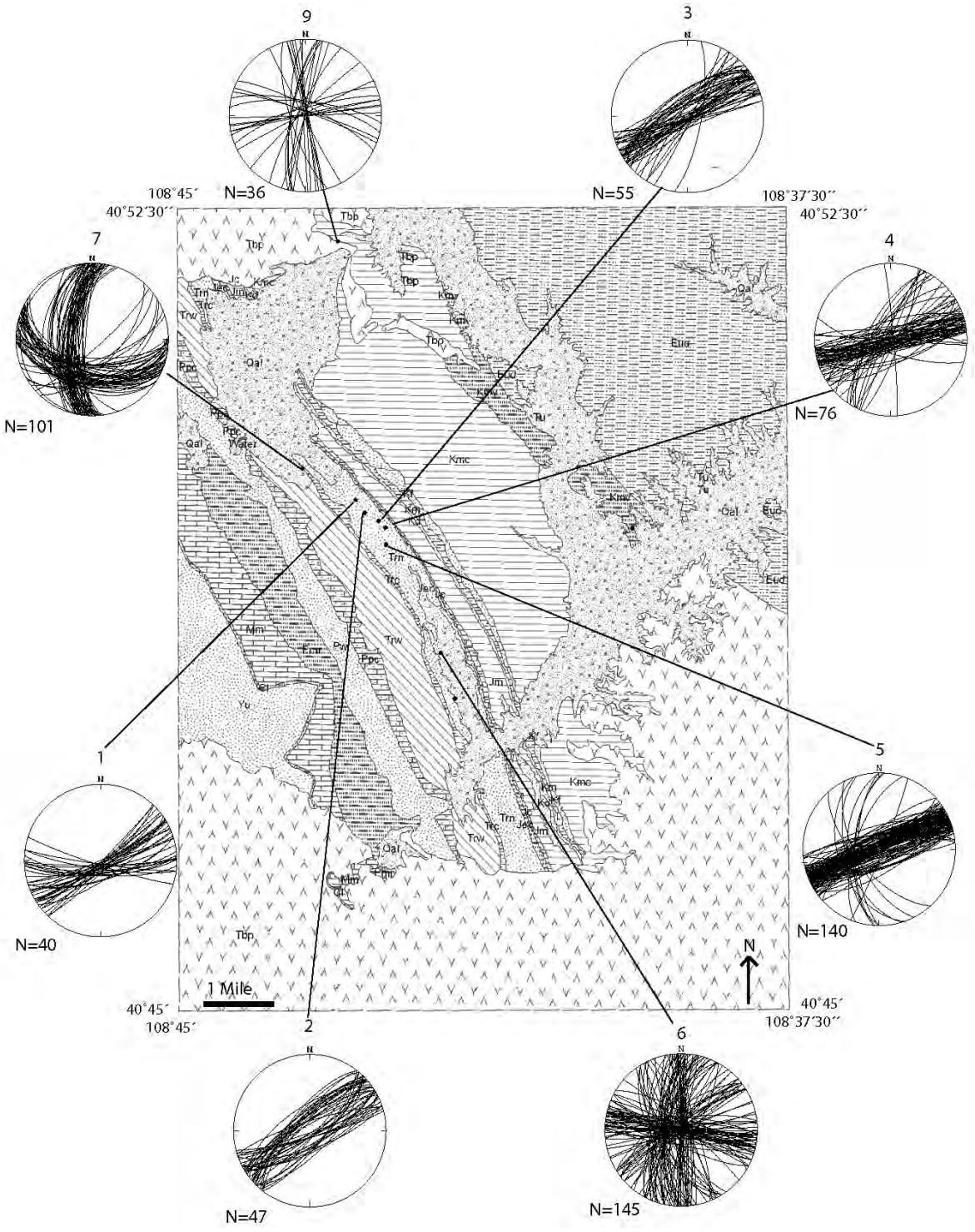

Figure 34. Stereonets of joint planes within the Navajo Sandstone superimposed on the geologic map (raw data, see Appendix C). Detailed unit descriptions are located in Appendix A and Plate 1.

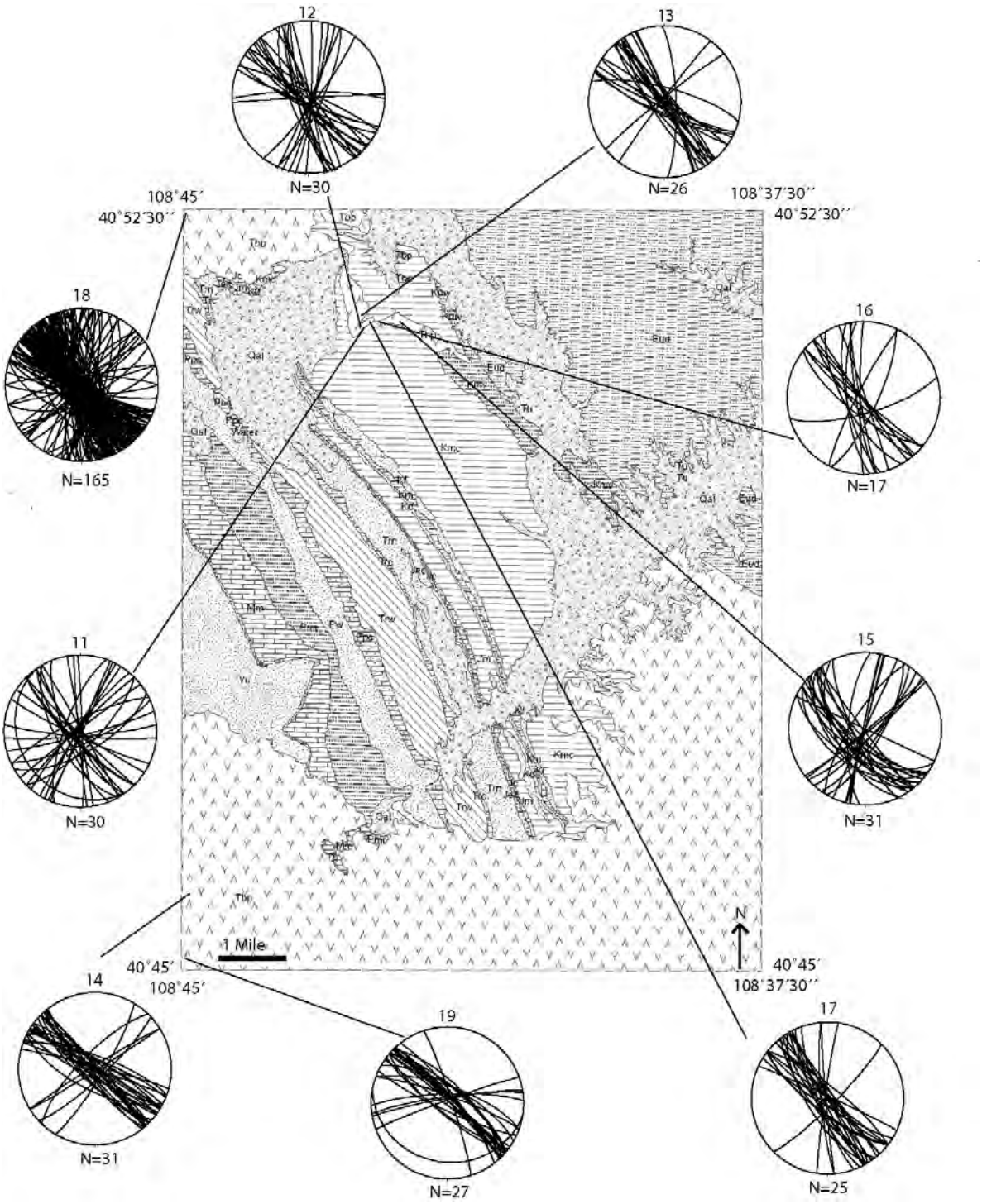

Figure 35. Stereonets of joint planes within the Miocene Browns Park Formation superimposed on the geologic map (raw data, see Appendix C). Detailed unit descriptions are located in Appendix A and Plate 1.

Timing relationships were ascertained from the abutting relationships observed in the field. The measurements were gathered first along the dip slopes of the Triassic Navajo Sandstone, then along the cliff faces of the Oligocene Bishop Conglomerate and Miocene Browns Park Formation. The Triassic Navajo Sandstone contains two of the three orientations of joint sets and the Oligocene Bishop Conglomerate and the Miocene Browns Park Formation contain only the N40W-striking set. It is puzzling that the Triassic Navajo Sandstone does not contain the N40W joints. Perhaps due to the Navajo Sandstones highly fractured nature, the extensional stress release in a northwesterly orientation was achieved along pre-existing fractures.

Interpretations - Minor Faults

If the minor faults formed due to ENE-WSW Laramide compression, then conjugate strike-slip faults as well as thrust faults would be expected with a ENE-WSW σ_1 trend. If Sevier compression was responsible, NW-SE-directed thrust faults and strike-slip faults would be expected. However, if stress refraction or a rotation of the stress field occurred, then NNW- to NNE-directed thrust faults and strike-slip faults could be possible. If the minor faults were caused by eastward translation of the Uinta aulacogen along pre-existing fault planes (Gregson and Erslev, 1997) in response to tectonic crowding of the Colorado plateau and the Laramide arches, then a less consistent array of minor faulting would be expected due to local rigid body rotations. A multi-phase deformational history (Gries, 1983) would call for multi-directional minor faulting demonstrating cross-cutting relationships. If Browns Park extension is responsible, normal fault planes would be predicted to have NW-SE strikes. If the fractures were in response to Basin and Range extension or Rio Grande rifting, primarily NNW, N, and NNE-striking faults would be

expected. If the minor fault patterns were in response to more local stresses such as strain partitioning or outer arc extension, variations in fault patterns would be seen along strike and highly variable fault patterns would be observed. If strain partitioning were responsible, a predominance of differing slip-senses would be observed in different locations throughout the area.

Folding of the Mancos Shale and back-thrusting of the Browns Park Formation were observed in the northeastern portion of the field area. This deformation is possibly in response to the overlying Browns Park Formation gravitationally sliding down dip along its contact with the Mancos Shale.

There is a small node of NNE-directed thrust faults with an associated N1E-striking joint set which could be attributed to the Sevier Orogeny. More than 10 km north of the field area the fold axes range from E-W-trending, to NE-SW-trending 10 km north of the field area, to more ENE-WSW-trending 5 km north of the field area (Fig. 26). It is possible that as Sevier Orogeny stress contacted the Uinta aulacogen, the stress refracted from NW-SE compression to more NNE-SSW compression (Fig. 36). This type of deformation would explain the NNE-SSW compression seen in the study area as well as the ENE-WSW fold axes 5 km to the north.

It is interesting that just 5 km north of the field site a NE-SW structural grain of fold axes are prominent. The directly adjacent NE-SW fold axes make it difficult to rule out the Sevier Orogeny as a contributor to the deformation in the field area. However, the small amount of NW-directed thrusting and NW-striking joints in pre-orogenic strata suggest that deformation from the Sevier Orogeny does not extend far beyond the critical taper, but may still play a role within the field area.

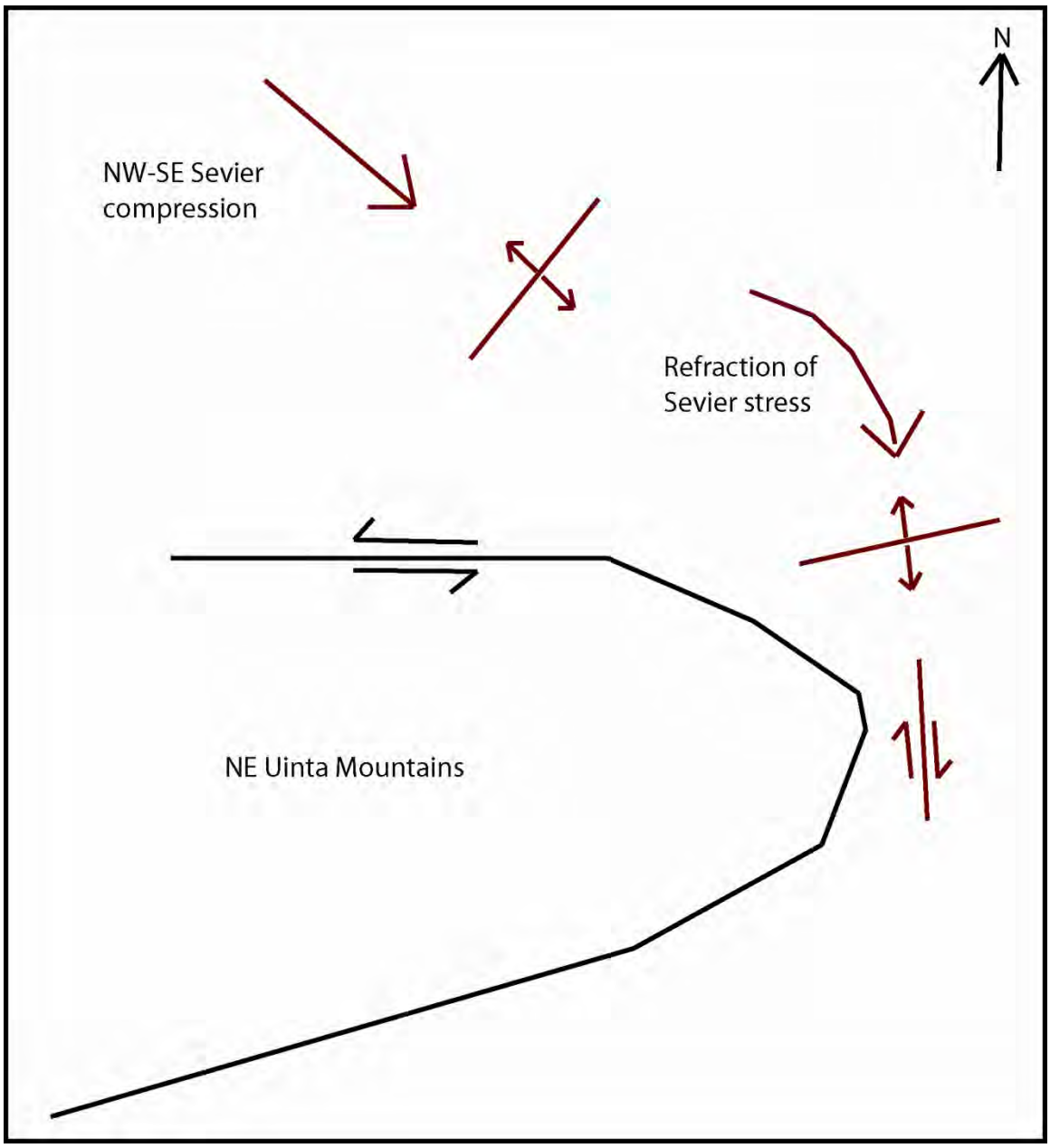

Figure 36. Model showing the formation of a NNW-directed transpressive right-lateral strike-slip system in response to refraction of Sevier Orogeny stress.

The NNW-SSE-directed right-lateral strike-slip faults, associated NNE-SSW $\sigma_{1,}$ and N1E-striking joints could also be explained as antithetic faulting within an overall left-lateral system during the late-Laramide (Fig. 37 and 38). However, paleomagnetic data collected from within Irish Canyon suggest that there have been no rigid body rotations (Bressler, 1981). The fault plane dips of the NNE-striking right-lateral strike-slip faults approach vertical when rotated to horizontal. This suggests that they are of at least syn-orogenic age.

This NNW-SSE right-lateral deformation may also be due to E-W extension in response to Basin and Range extension, Rio Grande rifting, or the collapse of the North American Cordilliera (Fig. 39). The timing relationships for these hypotheses are problematic, thus, the NNW-SSE right-lateral deformation is probably due to a poorly documented late-Sevier/late-Laramide, or post-Laramide event, or a combination of these events. During ENE-WSW Laramide compression a zone of pre-existing weakness was created by the NW-SE structural grain of dipping strata as well as by the faults. Perhaps as E-W to ESE-WNW extension began this anisotropy was then reactivated creating a zone NNW-SSE-directed right-lateral shear with associated NNE-SSW transpressional thrust faulting and a N1E-striking joint set.

Detailed kinematic analyses of the fracture data of the Irish Canyon-Vermillion Creek area revealed multistage fracturing exhibiting components which could be attributed to at least three deformational events. The first stage of deformation was characterized by ENE-WSW Laramide compression resulting in ENE-WSW to NE-SW directed thrust faulting and predominately left-lateral strike-slip faulting. Kinematic analyses suggest that Laramide deformation was achieved by N59E-directed shortening. This deformation

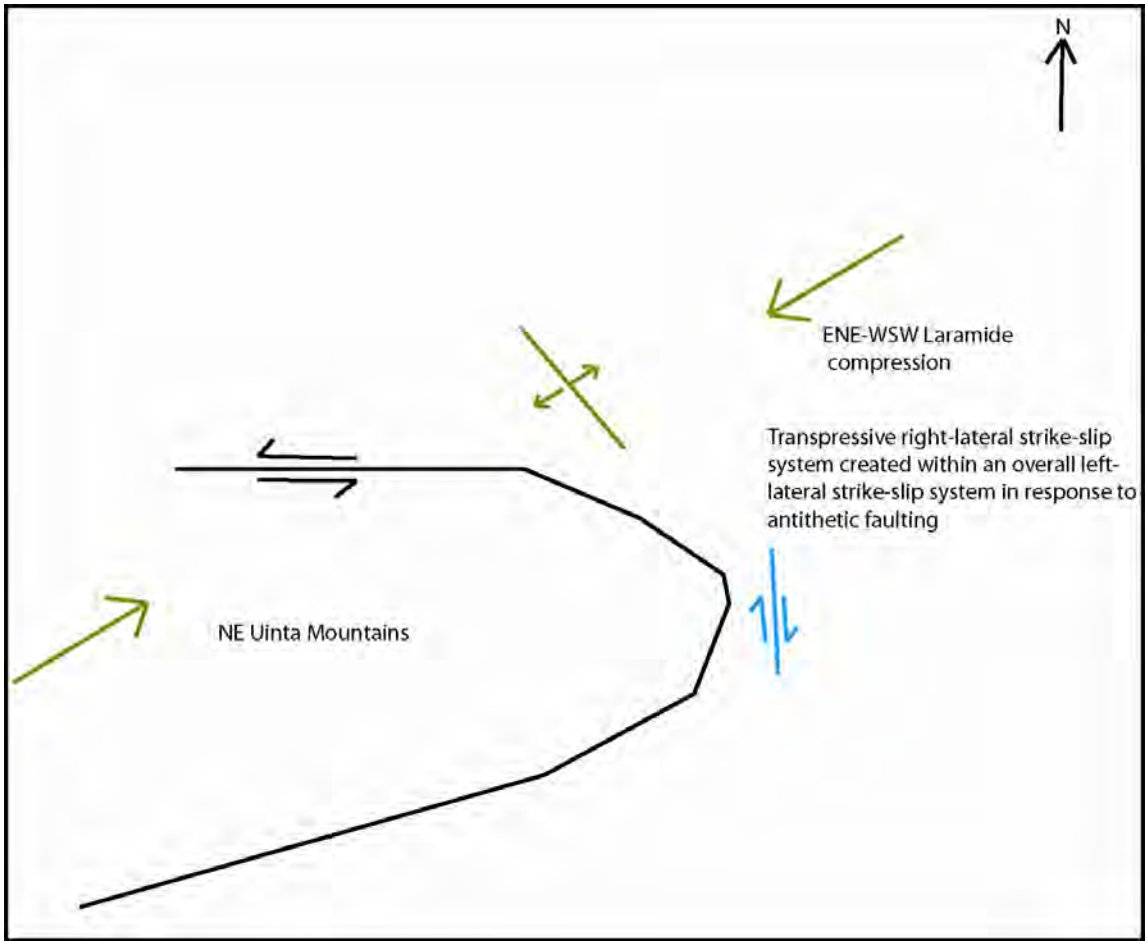

Figure 37. Model showing formation of a transpressive right-lateral strike-slip system within an overall left-lateral strike-slip system.

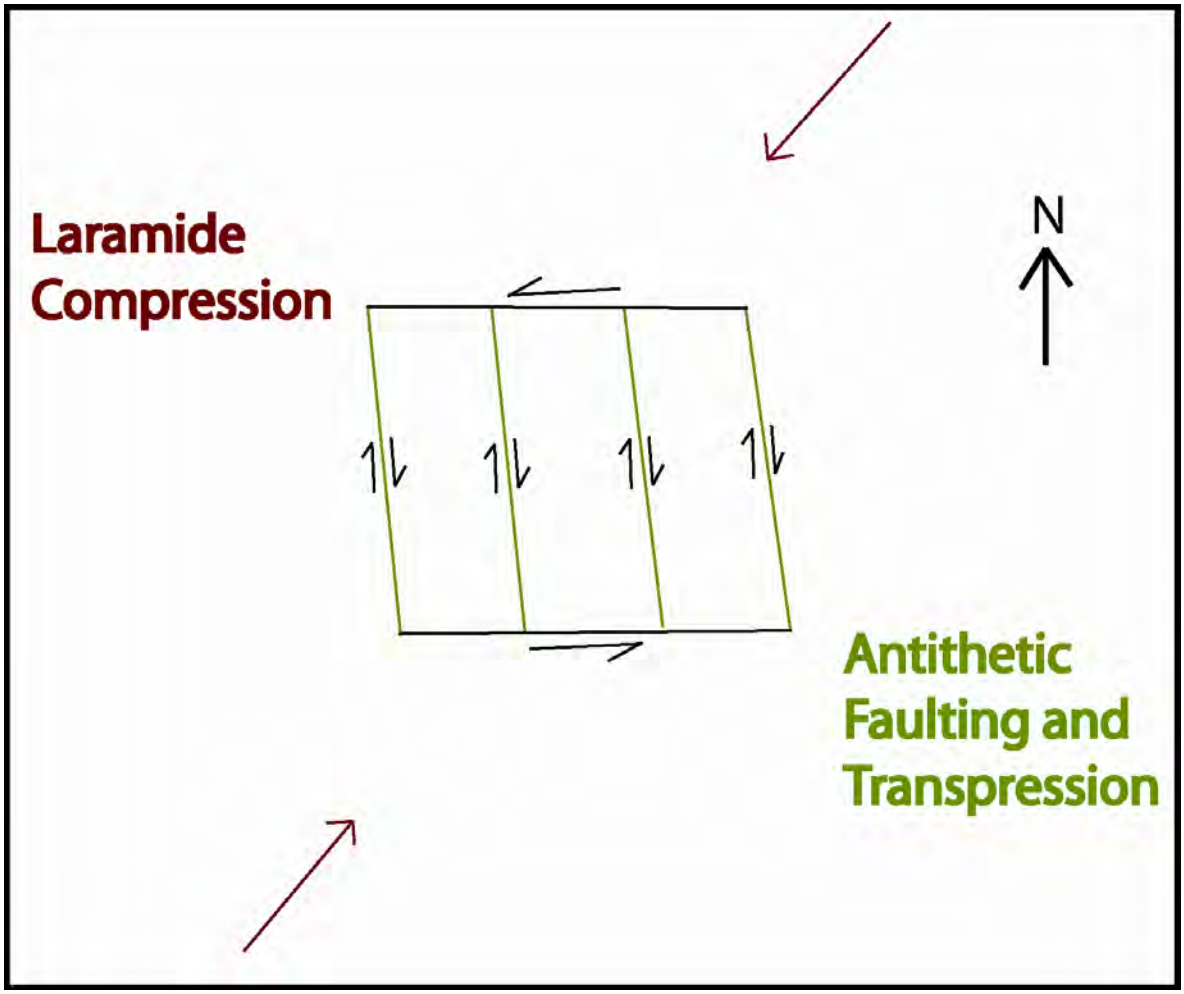

Figure 38. Model showing a transpressive right-lateral strike-slip system created by antithetic faulting within a left-lateral shear zone. This model is a close up of the blue right-lateral system in figure 37.

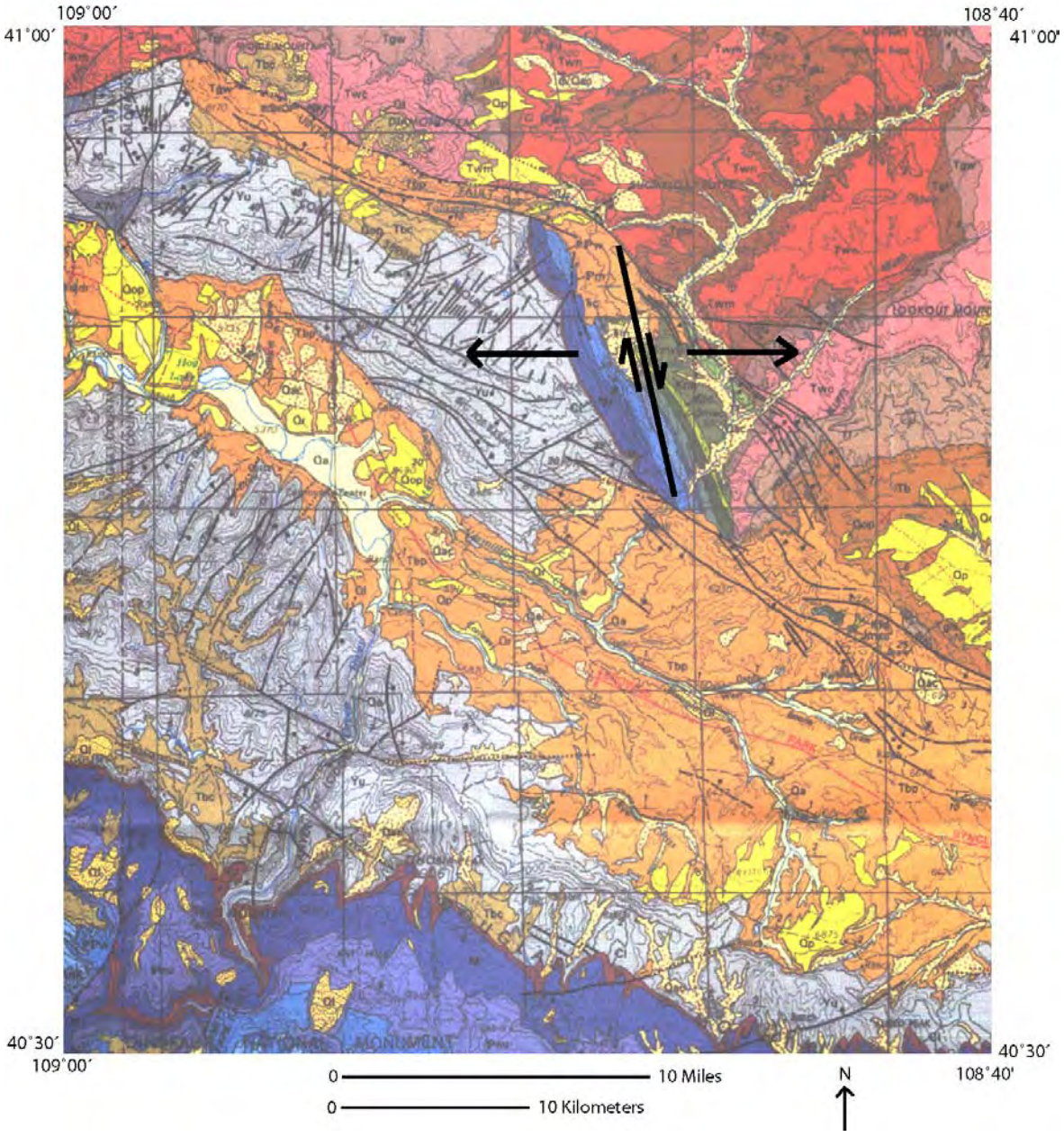

Figure 39. Regional geologic map including study area illustrating the formation of a right-lateral transtensional shear zone in response to a poorly documented late-Sevier, late-Laramide, or post-Laramide event (Taken from Rowley et al., 1985).

resulted in large amounts of interlayer flexural slip and a joint set with an average strike of N71E.

The second stage of deformation was characterized by E-W extension probably due to a poorly documented late-Sevier/late-Laramide, or post-Laramide event, or a combination of these events. This may have resulted in a transtensional and locally transpressional right-lateral strike-slip fault system. This system created a predominance of right-lateral strike-slip faults and a joint set with an average strike of N1E (Fig. 39). Evidence for this local transpression includes a node of NNE-directed thrust faults associated with the right-lateral strike-slip system. Similar transtensional right-lateral strike-slip systems have been seen in New Mexico east of the Rio Grande rift (Erslev, 2005) and in the Mormon Mountains along the Utah, Nevada, Arizona border (Anderson and Barnhard, 1993) (Fig. 40).

This deformation would have had to have been late or post-Laramide because the NNW-striking right-lateral strike-slip fault planes associated with the NNE-SSW σ_1 were observed cross-cutting the strike-slip fault planes associated with the ENE-WSW Laramide σ_1. Additionally, the dip of the fault planes of the right-lateral strike-slip faults approach vertical when the bedding is rotated back to pre-fold orientation. The N1E-striking joint set also abuts against the N71E Laramide joint set.

The third stage of deformation was characterized by NE-SW Browns Park extension resulting in a regional normal fault set with an average strike of N52W and a joint set with an average strike of N40W.

The majority of the thrust faults (79 percent) and a substantial portion of the conjugate strike-slip faults (67 percent of left-lateral faults and 11 percent of right-lateral

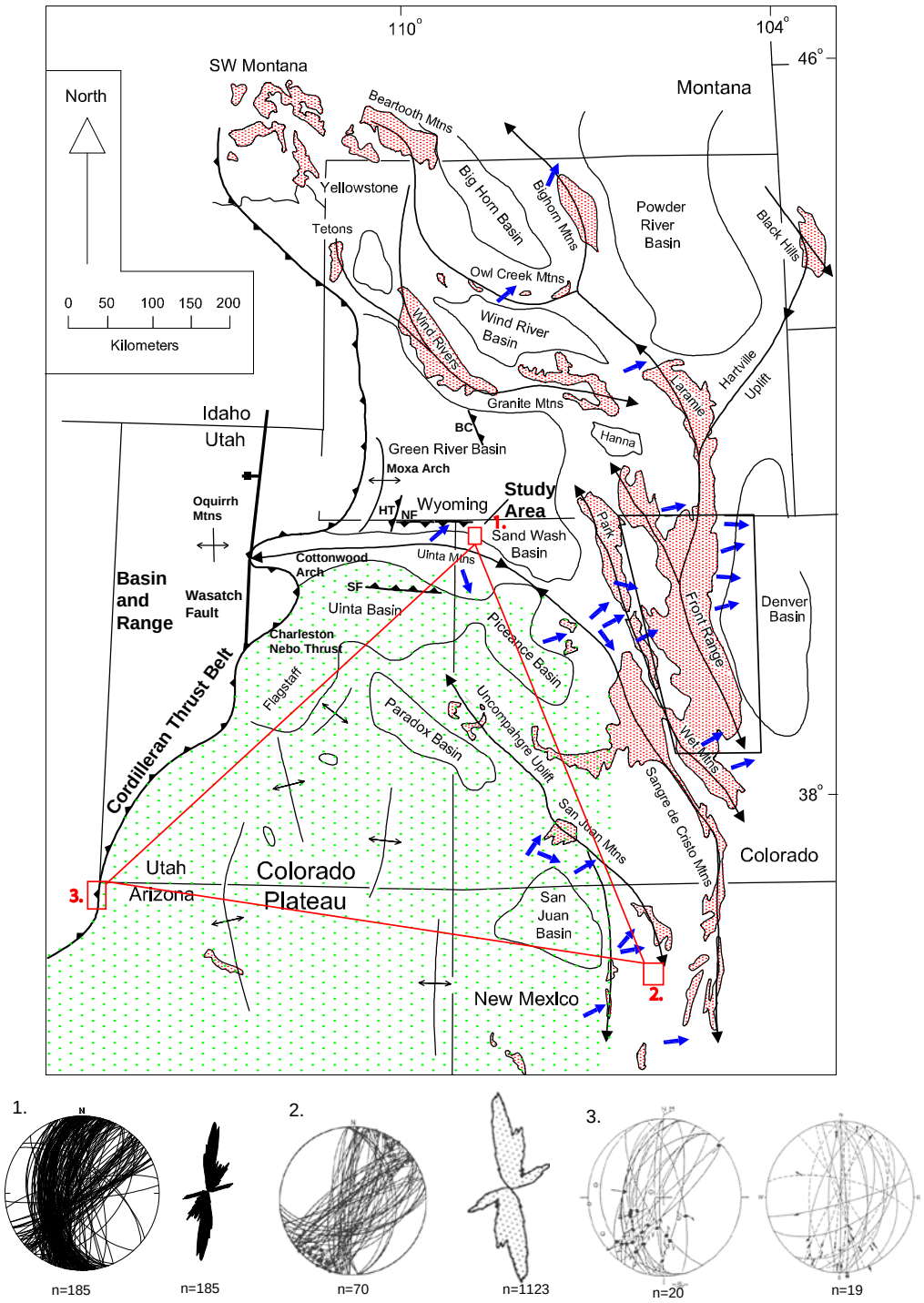

Figure 40. Regional map showing locations with similar right-lateral strike-slip faulting associated with a nearly N-S σ_1 due to E-W extension in response to a poorly documented post-Laramide event. 1) Stereonet of fault planes and rose diagram of sigma σ_1 for right-lateral faults from location 6 Irish Canyon-Vermillion Creek study area. 2) Minor fault planes from Galisteo Basin New Mexico and rose diagram of all σ_1 data collected east of the Rio Grande Rift (Erslev, 2005) 3) Stereonets of minor fault planes from the Mormon Mountains along the Utah, Nevada, Arizona border (Anderson and Barnhard, 1993).

Table of fault slip-sense percentages	Number of each slip-sense (n=)	Percentage of total faults	Number of faults associated with each stage	Percentage of each stage
Thrust Faults	187	26%	Post-Laramide Event-32	Post-Laramide Event-21%
			Laramide-155	Laramide-79%
Left-Lateral Faults	130	18%	Post-Laramide Event-32*	Post-Laramide Event-33%
			Laramide-98	Laramide-67%
Right-Lateral Faults	316	44%	Post-Laramide Event-286	Post-Laramide Event-89%
			Laramide-30	Laramide-11%
Normal Faults (Rotated Thrust and Strike-Slip)	89	12%	Post-Laramide Event-0	Post-Laramide Event-0%
			Laramide-89	Laramide-100%
Total Faults	722			
*Actually rotated thrust faults				

Table 1. Table showing percentages of each slip-sense and their contributions to each deformational event. This table excludes Browns Park data.

faults) are consistent with ENE-WSW Laramide compression (Table 1). The Laramide component appears to be expressed predominantly as thrust and left-lateral faults and the late-Sevier/late-Laramide or post-Laramide component appears to be expressed predominantly as transtensional right-lateral faults and localized transpressional thrust faults. Laramide deformation probably occurred in an overall left-lateral system and the poorly documented late-Sevier/late-Laramide or post-Laramide deformation occurred in an overall right-lateral system.

. Interpretations – Joints

If the jointing patterns are in response to encroachment of the Sevier Orogeny, then NW-SE joints would be expected. If ENE-WSW Laramide compression was responsible, then joints parallel to the ENE-WSW Laramide σ_1 would be expected. If structural vergence and eastward translation of the Uinta aulacogen via pre-existing fault planes was responsible for the deformation, then a less consistent array of fractures would be predicted (Gregson and Erslev, 1997). Similarly, if small scale local stresses were the cause, a less consistent fracture history would be expected. A multi-phase deformational history would

call for multiple orientations of joints sets exhibiting abutting relationships (Gries, 1983). If joints were in response to Browns Park extension, NW-SE joints would be observed abutting ENE-WSW to NE-SW Laramide and possibly NW-SE Sevier joints. If Basin and Range extension, Rio Grande rifting, or a later stage of E-W extension were responsible, N-S joints abutting against the earlier ENE-WSW to NE-SW Laramide and NW-SE Sevier joints would be predicted.

The dominant joint set's average strike of N71E within the Navajo Sandstone is likely coeval with the N59E node of Laramide σ_1 (Fig. 41). The N1E joints are seemingly parallel to the NNE σ_1 and appear to be in response to the same deformation. This deformation is likely caused by a complicated response to a transtensional system of right-lateral faulting probably due to a poorly documented late-Sevier/late-Laramide, or post-Laramide event, or a combination of these events. The N40W joints are in an orientation parallel to Miocene to Holocene NE-SW Browns Park extension (Fig. 42).

Abutting relationships confirm that three jointing events occurred in the area and these sets were subdivided and averaged. The Laramide N71E-striking joints are primary and the N1E-striking joints are secondary. The N40W-striking joints show no abutting relationships. However, they are found within Miocene strata and diverge from vertical when the strata are restored to pre-fold orientation. Therefore, these joints are post-Laramide and the youngest joints. Additional constraint for the age of these joints is provided by the observation that they are parallel to the Miocene regional normal fault set (Fig. 42).

All joint sets are present within the pre-Laramide units except the N40W-striking set. The N40W-striking joint set is only present in the Oligocene Bishop Conglomerate and

the Miocene Browns Park Formation; therefore these joints are post-Laramide. This corroborates Hansen's (1986b), Hucka's (1991), and Narr's (1980, 1982, and 1998) assessment of the timing of the generation of the regional NW-SE-striking joints, while opposing Laubach and Lorenz's (1992), Verbeek and Grout's (1992, 1997), and Silliphant et al.'s (2002) assessment of a pre-Laramide origin.

The N40W-striking set found within the Miocene Browns Park Formation is in a very similar orientation to open fractures found within the Uinta basin by Narr (1982) (Fig. 14) and Harthill (1997) and the fractures seen near Craig, Colorado (Gillett, 2009). This joint set would be the most likely to be open at depth, creating the most effective fluid conduits for water and petroleum extraction. However, because these joints are not present in the underlying strata, the prediction of which joints are open at depth was not fully achieved by this study.

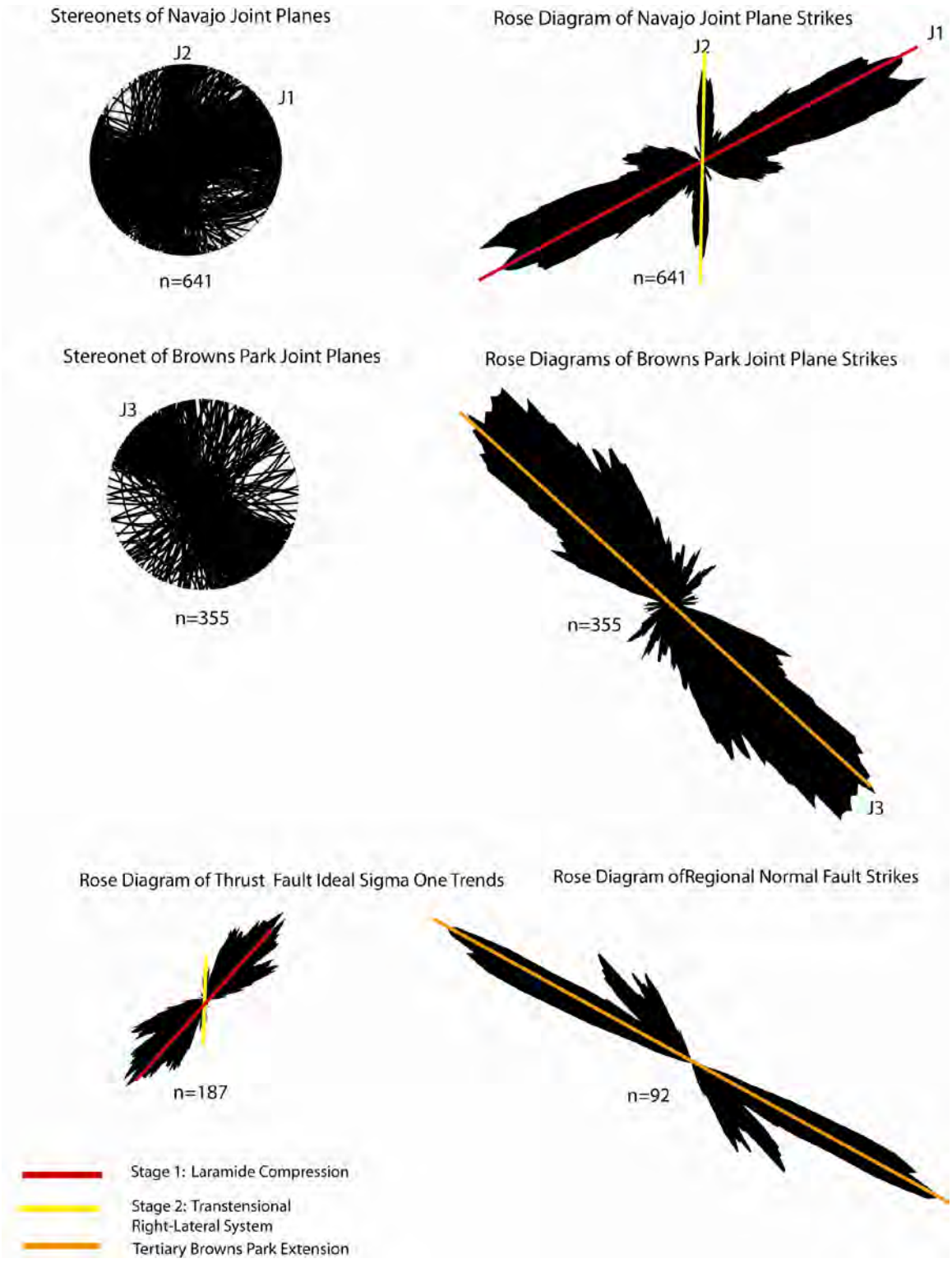

Figure 41. Stereonets of joint strikes and rose diagrams of joint strikes, trends of minor fault σ_1 for thrust faults, and the strike of regional normal faults. Colored bars used to illustrate the correlation between strike of joint sets and the trend of ideal σ_1. Red = J_1, Yellow = J_2, and Orange= J_3.

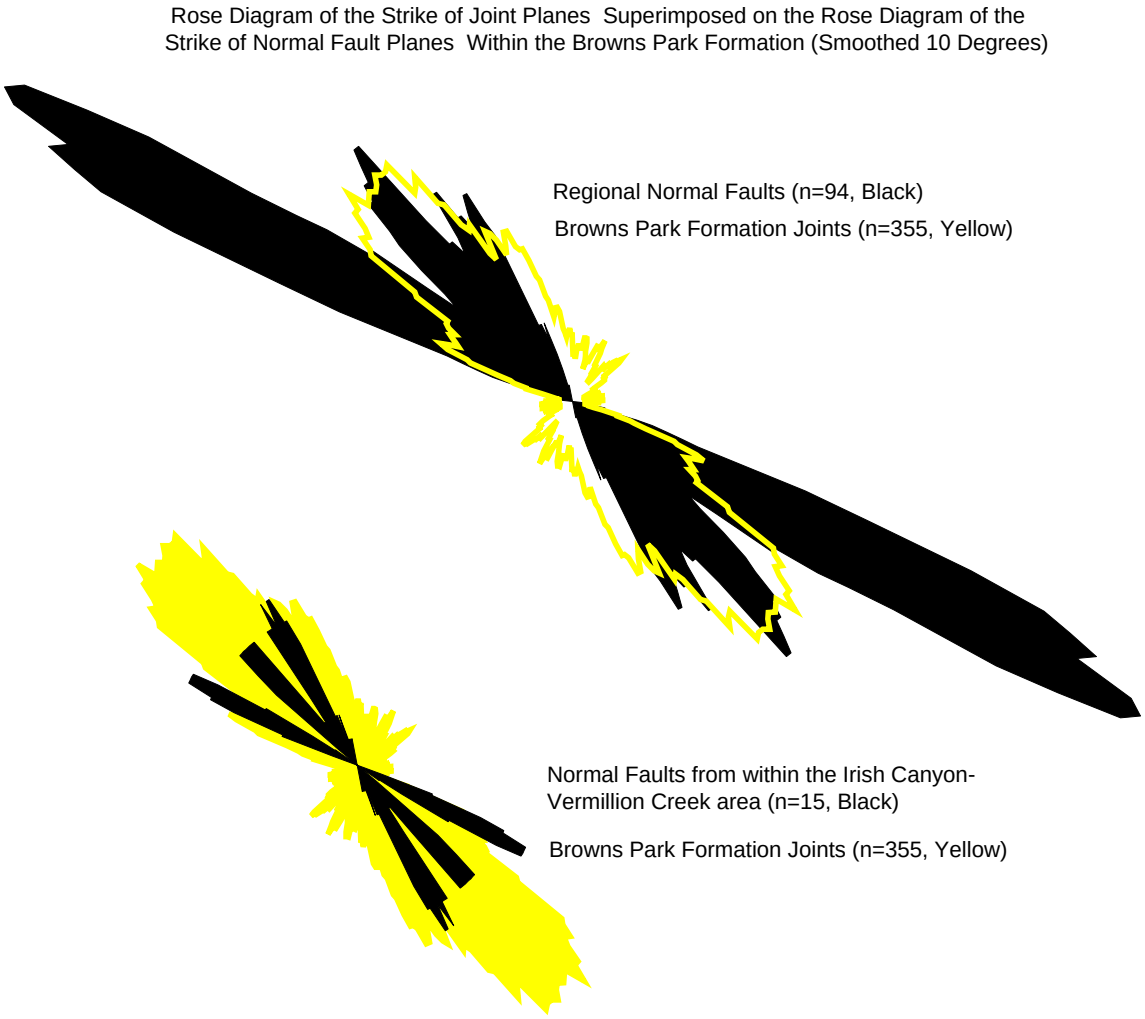

Figure 42. Rose diagram of the strike of the Browns Park Formation joints (n=355) superimposed on the rose diagram of the strikes of the regional normal faults (n=94) and rose diagram of the strike of normal faults within the Irish Canyon-Vermillion Creek area (n=15) superimposed on the rose diagram of the strike of the Browns Park Formation joints (n=355). The yellow rose corresponds to the Browns Park Formation joints.

CHAPTER VI. TWO-DIMENSIONAL STRUCTURAL INTERPRETATION AND ANALYSES

Velocity Analyses and Depth Conversion

A sub-surface velocity analysis was attempted using the data from line 407-12 (See Plate 1 for line location). The goal was to obtain unit thicknesses that could be used with out crop thicknesses to further constrain the cross-section. However, the results were less useful than expected. The formation tops from the seismic interpretation were converted from two-way travel time to depth using the interval velocities calculated from the seismic stacking velocity data. Assuming that the layers are horizontal, the stacking velocities are approximations of the root mean square (RMS) velocities. These stacking velocities can be plugged in to calculate the interval velocities between travel times where stacking velocities were estimated (Sherriff and Geldart, 1995). This is done using the Dix equation:

$$V_i^2 = (V_n^2\, t_n - V_{n-1}^2\, t_{n-1}) / (t_n - t_{n-1})$$

Where V_i is the interval velocity in a given layer, V_n is the stacking velocity to the top of that layer, and t_n is the zero-offset travel time corresponding to the reflection of that layer (Sherriff and Geldart, 1995). RMS velocities are equal to the stacking velocities when the data are gathered from horizontal strata. However, if the strata are inclined, the stacking velocities may not be good approximations of the RMS values and may yield less than ideal values from the analyses. The strata within the study area are moderately to highly

inclined, therefore seismic stacking velocities had to be used. Line 407-12 is directly parallel to cross-section A-A' and extends about a quarter mile beyond the field site to the NE and SW (Plate 1). These interval velocities were plotted against the travel time to obtain an envelope containing the minimum, maximum, and average interval velocities (Fig. 43).

Small errors in stacking velocity create large errors in interval velocity values. Therefore, obvious outlier interval velocity values were omitted at this stage (Fig. 44). To ascertain if the intervals observed on the interval velocity plots corresponded to certain reflectors across the section, interval velocities from ten CDP's were chosen where the data resolution was best, with 5 gathers within the hanging wall and 5 gathers within the footwall of the structure. Appropriately scaled curves were then superimposed directly upon the seismic section 407-12 (Fig. 25).

A good correlation exists between spikes in interval velocity and the interpreted seismic horizons of the Navajo Sandstone, Chinle Formation, and the Eocene undivided along the relatively horizontal foot wall of the structure (Fig. 45). However, the steep dips across the hanging wall prevented a reliable estimation of the stacking velocity. Therefore, the data from the hanging wall were omitted from the study. A close up of the quality of the correlations can be viewed in Figure 46. The average interval velocities were then subdivided into 8 intervals based on correlation with mappable reflections. The interval velocities were then used to calculate the thicknesses of each interval. The depth conversions based on the average interval velocities are over estimates yielding velocities that are too high. These results are in disagreement with the stratigraphic thicknesses

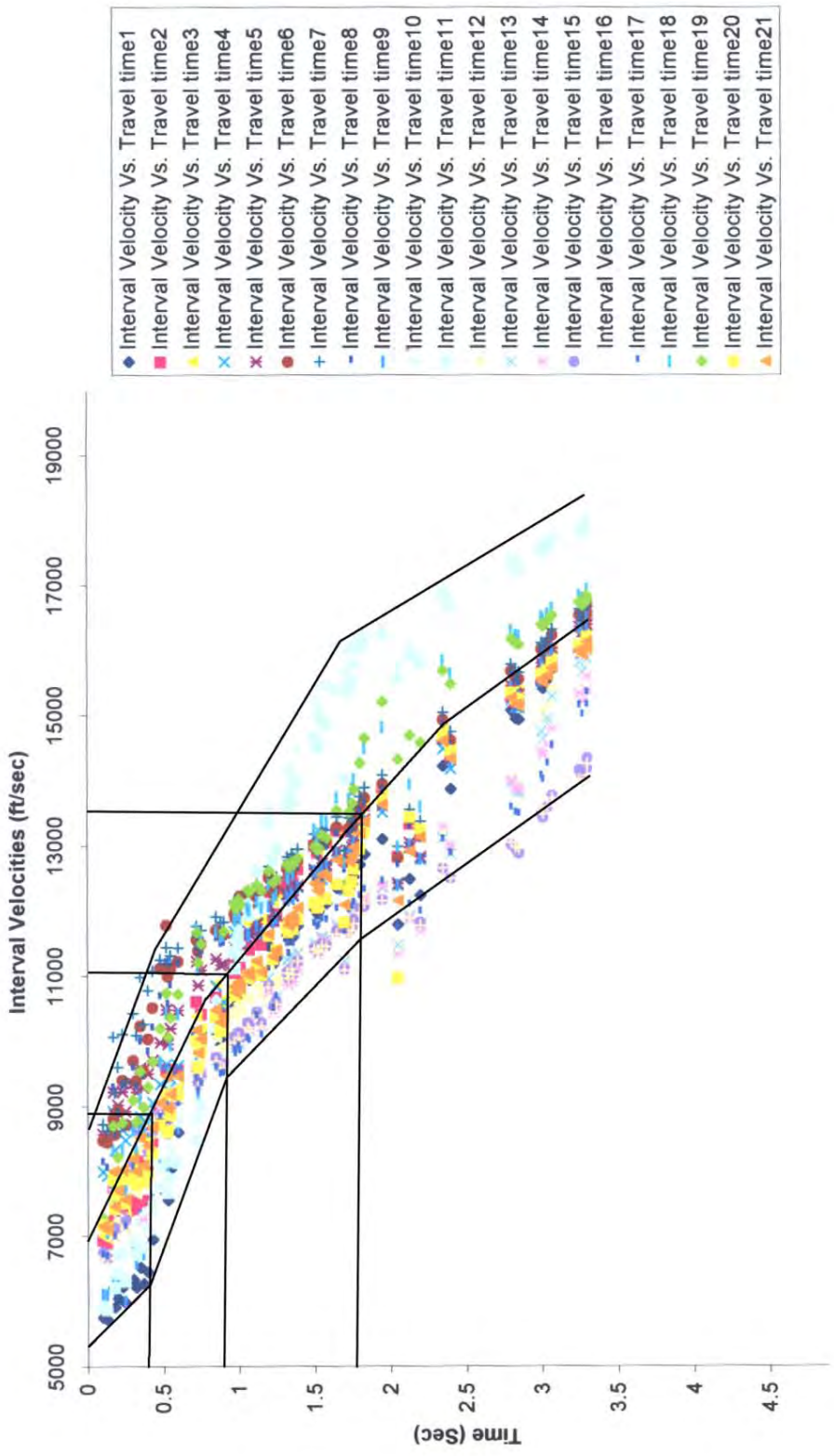

Figure 43. Plot of all interval velocities calculated from stacking velocity data verses travel-time showing minimum, average, and maximum velocity envelopes.

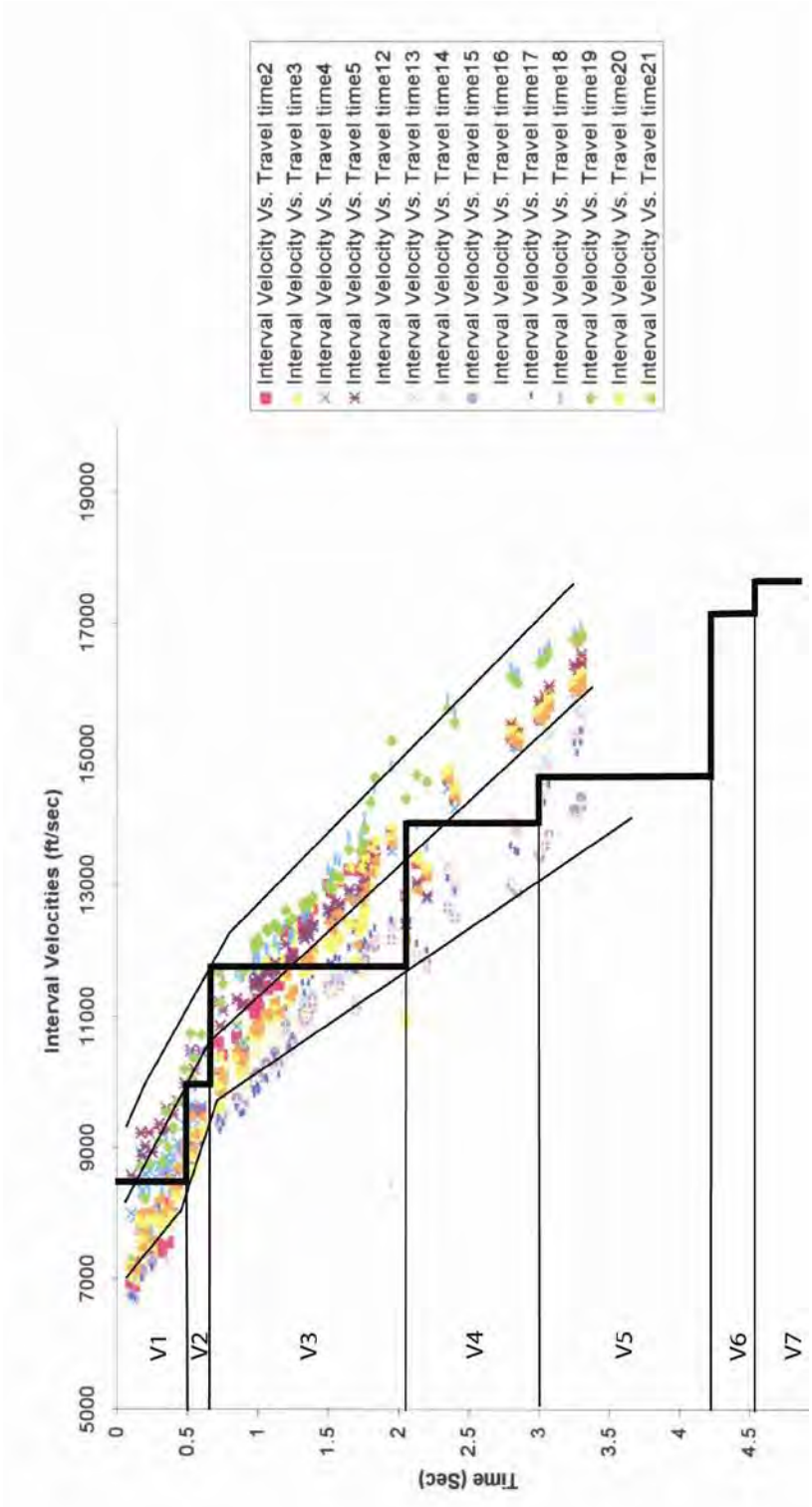

Figure 44. Plot of interval velocities calculated from stacking velocity data verses travel-time showing minimum, average, and maximum velocity envelopes (Outliers omitted). The step diagram of the average interval velocity is superimposed upon the graph. See Table 1 for lithologic units corresponding to intervals.

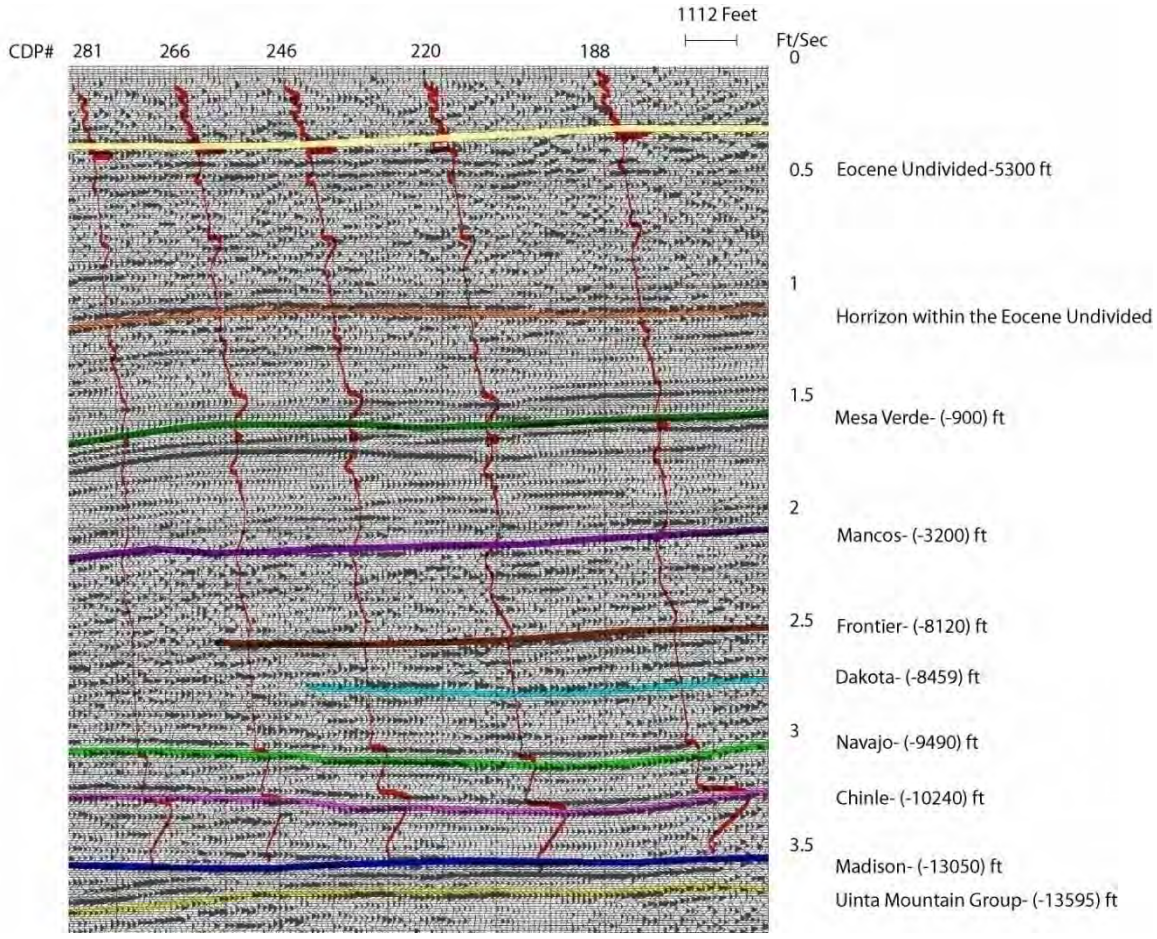

Figure 45. Close up of the foot wall structure of line 407-12 with interpreted horizons and smoothed interval velocity plots overlain.

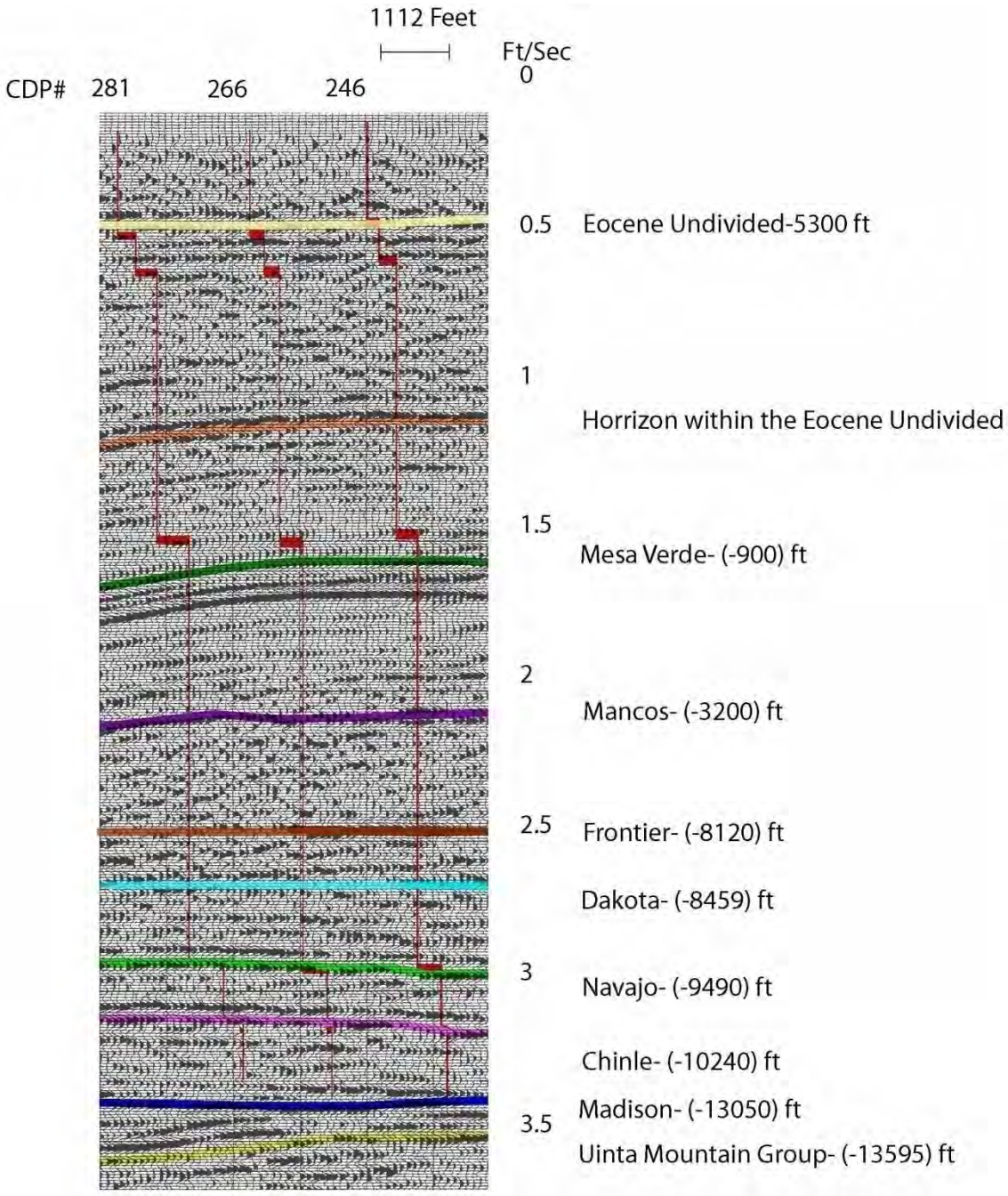

Figure 46. Close up of correlation of interval velocity plots and interpreted horizons.

Average Velocity	Corresponding Units	Thickness from Depth Conversion (meters)	Combined Thickness from Outcrop (meters)	%Thickness Difference
7800.02	Qal/Tbp	464.2906492	365.76	21
8865.70	Eun	174.6067592	365.76	52.00
10252.26	Eun	1419.775967	1524	7
11883.99	Kmv	1133.844501	701.04	38.00
12780.28	Kmc-Jec	1517.507108	1995.2208	24.00
14480.26	Trn	431.5511206	228.6	47.00
14721.53	Trc	506.4610757	72.8472	86.00

Table 2. Table of percent difference between depths from conversion and wells.

observed in the field and the thickness seen in well data (Table. 2), suggesting that stacking velocities are not good approximations of the RMS values and that the interval velocities are erroneous. Thus, the stratigraphic thicknesses observed in outcrop were honored. In the end, the seismic analyses contribution was simply a very clear view of the area's geometry.

Two-Dimensional Constraints

Geologic cross-section analyses can be very useful when trying to illuminate the 2-D structural geometry of an area and can also act as a test of regional tectonic models (Erslev, 1986; 2005). Models of 2-D geometries calling upon vertical tectonics (Prucha et al., 1965; LeMasurier, 1970; Stearns, 1971; 1978; Matthews and Sherman, 1976; Matthews and Work, 1978) have been called into question by later investigators use of line- and mass-balancing techniques (Brown, 1984; 1988; Erslev, 1986; Spang and Evans, 1988; Spang et al., 1985; Erslev et al., 2004; Stone, 2005; Groshong and Epard, 1996).

A detailed 1:12,000 scale geologic map was the result of four weeks of mapping within the Irish Canyon-Vermillion Creek area. The field map of the Irish Canyon 7.5` quadrangle was scanned and georeferenced into ArcGIS and surface contacts, surface bedding attitudes, fault, and data from two wells were digitized (Plate 1). The 3D elevations for polylines and point data were acquired by placing these attributes upon a

10 m DEM in ArcScene (Fig. 23a, b, and c). The surface dip data were projected parallel to strike and were imported directly into 2DMove using the X,Y,Z coordinates from an ArcGIS database. This integrated field mapping and DEM data and allowed for accurate projection of field mapping data into cross-section. ArcCatalog was then used to convert the features consisting of the contacts, faults, geologic units, and cross-section into 3D attribute .dxf files, which were then imported into 2DMove (Midland Valley Exploration, 2006). Data from two wells were acquired from the Denver Earth Science Library, and the coordinates were converted from NAD83 Lat/Long to UTM NAD27 using Corpscon v.5.11.08 (U.S Army Corps of Engineers, 2005). The depths to formation tops from the well data along with the stratagraphic thicknesses observed in outcrop were used to constrain the 2D geometry of Irish Canyon-Vermillion Creek area. The 2D seismic line was used to corroborate this geometry (Fig. 25)

The majority of the field data as well as the orientation of the fold axes within the area suggests that deformation occurred predominantly in response to a N59E-directed shortening and this is therefore the most optimal orientation for 2D cross-section construction (Fig. 47) and restoration (Fig. 48a, b, and c) (see figure Plate 1 for cross section location). Depths to formation tops were determined using apparent dips and formation thicknesses observed in the field. The methods of Erslev (1986) were used to estimate restorable geometries of reverse faults.

To obtain the most diagnostic restoration, several restoration methods can be utilized within 2DMove, including fault-parallel flow, flexural-slip unfolding algorithms, and line length balancing. Fault-parallel flow allows the basement nonconformity to be restored across the fault while preserving any regional folding within the basement.

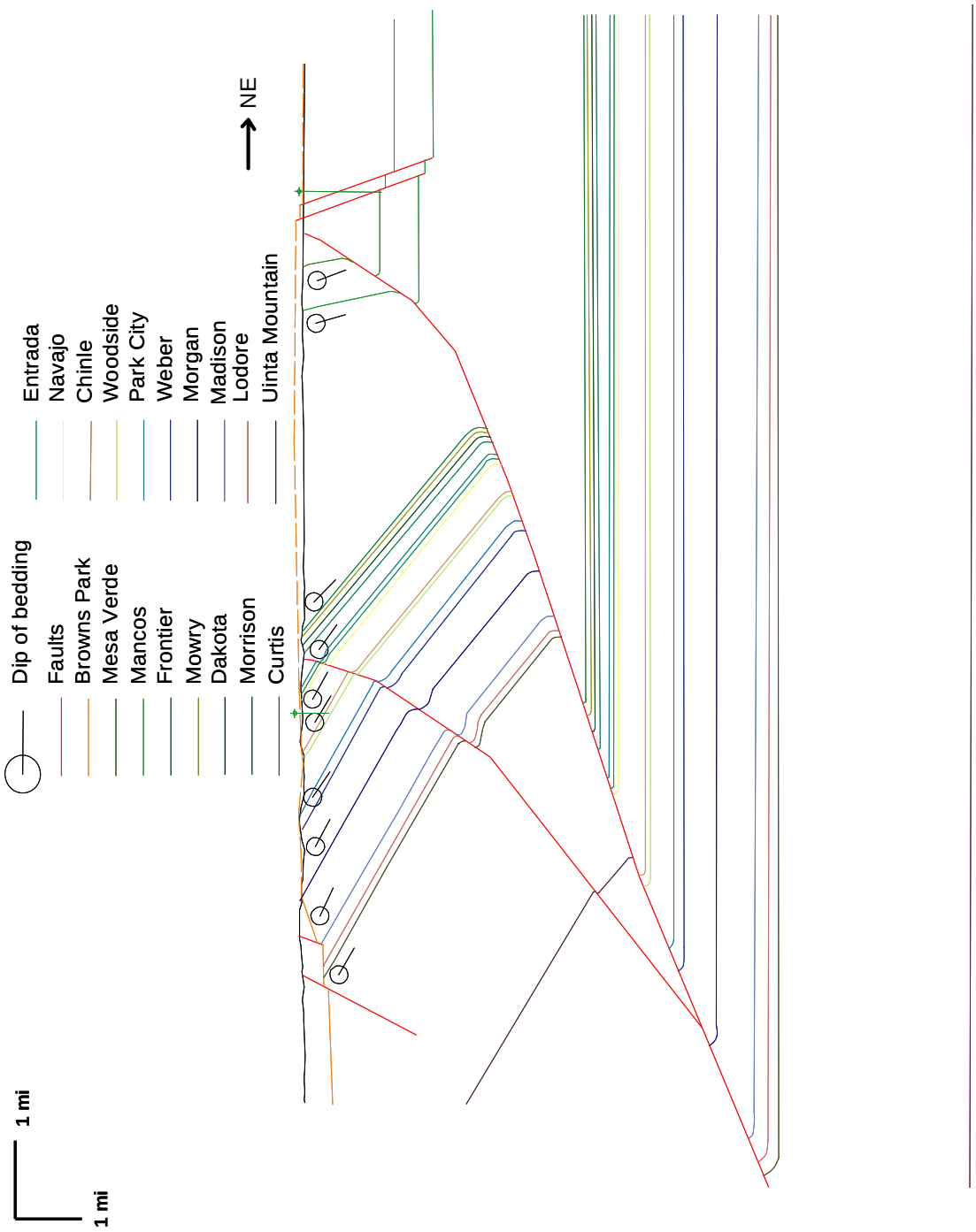

Figure 47. Cross-section A-A`. Large listric fault is the Uinta thrust fault. See Plate 1 for location.

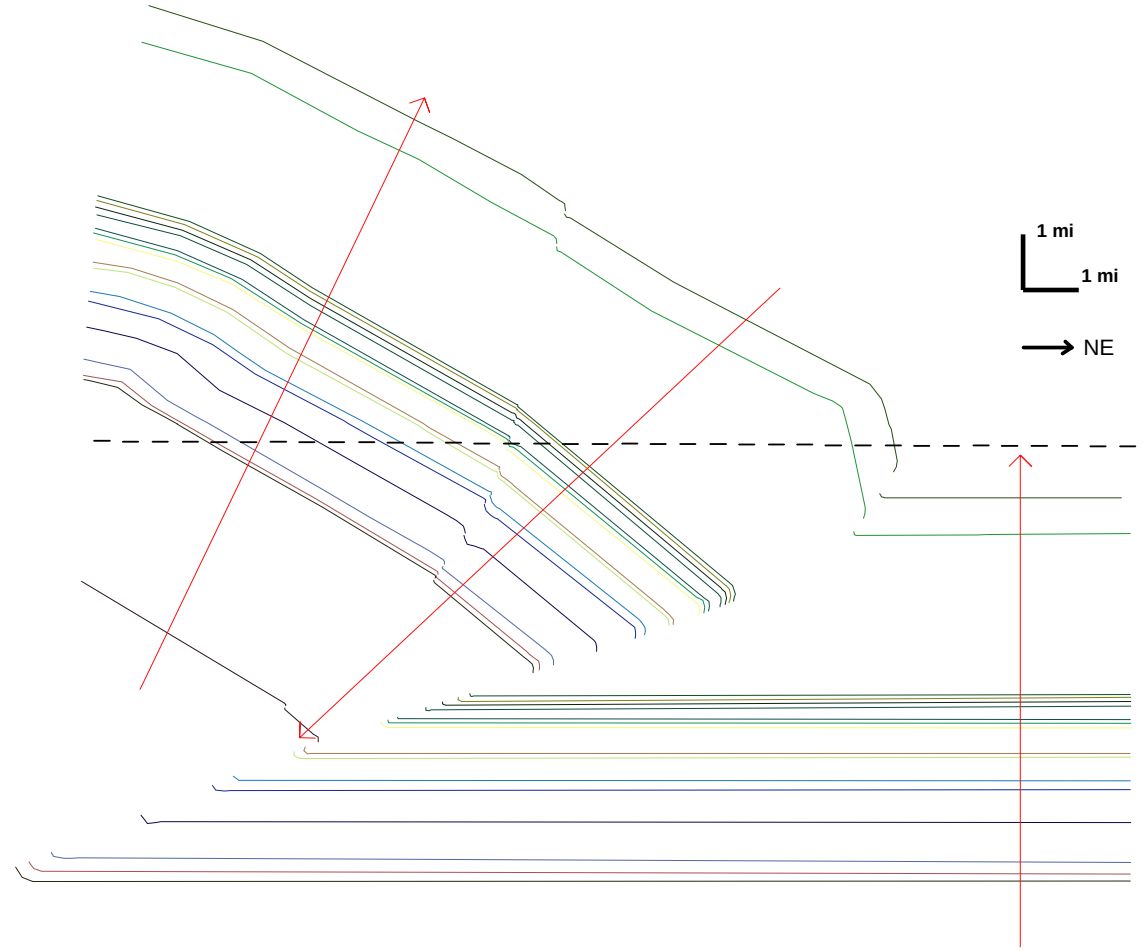

Figure 48a. Cross-section A-A’ with pin lines added to each structural block. See Plate 1 for location.

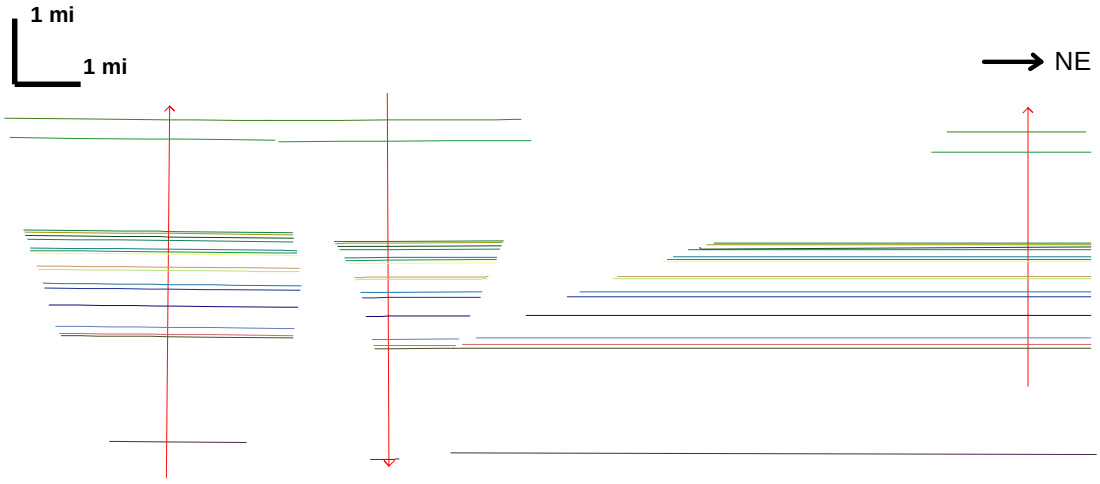

Figure 48b. Cross-section A-A’ line-length restoration. Note line length imbalances due to flexural shear.

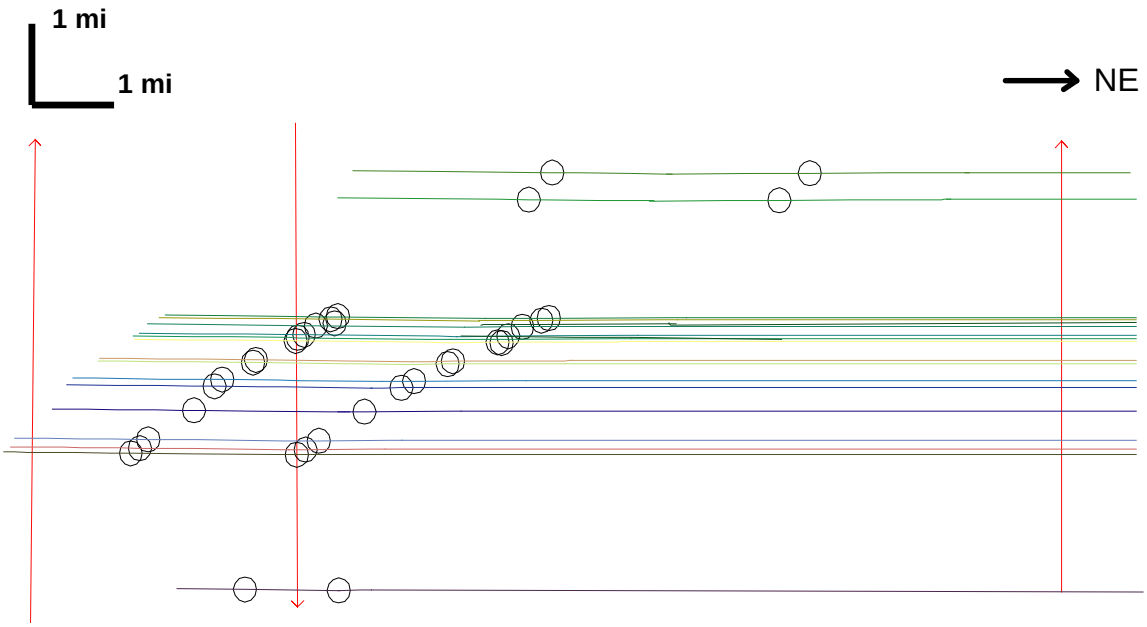

Figure 48c. Cross-section A-A' line-length restored showing shear. Far right pin is fixed. Note line length imbalances due to flexural shear.

Flexural-slip unfolding allows for restoration of the basement nonconformity to a regionally planar surface, while preserving area and line length balancing in the overlying sedimentary strata. However, for this study only line length balancing was deemed necessary to further test restorability and to identify flexural slip and thickening or thinning of strata during folding. Flexural shear and line length variations related to folding were then illustrated by inserting fixed and non-fixed pins and restoring the cross section (Fig. 48a, b, and c).

Observations and Interpretations

The Uinta Mountains are bounded in the north and south by low-angle, symmetric thrust faults (Fig. 15 and 16), with the north dipping Uinta Basin Boundary thrust to the south and the south dipping Uinta thrust to the north (Stone, 1986). There are two thrust faults within the area, the main Uinta thrust and a splay just off to the southwest. Four normal faults were observed along the cross section. The Uinta thrust fault cuts through the

eastern portion of the field area. This is supported by previous investigations and industry seismic data. A large amount of displacement is visible along the Uinta thrust. The strata to the west of the Uinta thrust is folded to a moderate dip of 30 degrees and the dip increases to overturned near the trace of the main thrust.

The strata to the east of the thrust are relatively non-deformed. However, a fold was observed along the seismic line 407-12. This fold was not corroborated by field observations and due to this lack of evidence, was left out of the cross-section interpretation. The main ridge of the structure is created by the Mississippian Madison Limestone and the structure dives into the subsurface near the center of the field area. The basement non-conformity is not visible at the surface within the field area.

The line length balancing of the basement through the Wasatch Formation suggests that flexural-slip and internal shortening occurred within the sedimentary section, and a combination of block rotation and folding of the basement occurred during deformation. At the Irish Canyon-Vermillion Creek area, the units must be sheared with the top to the SW to restore the section. This suggests that top to the NE shear occurred during the deformation. The line length discrepancy increases moving up section. This line length imbalance is likely due to the effects of differing mechanical stratigraphy. The less-resistant, shale-rich upper portion of the section may have allowed for greater interlayer flexural slip than the relatively more cohesive and resistant limestone and sandstone units of the Paleozoic and lower Mesozoic formations. This deformation was not evident in the fault analyses. Additional line length discrepancies are likely due to shear out of the section.

The main thrust in the area has been interpreted as having a concave-up listric geometry. The fault is steep at the surface and becomes less steep at depth. The strata are moderately dipping in the western portion of the field area and increase to highly dipping and even overturned in the eastern portion of the area. The structural interpretation illustrated by cross-section A-A' is corroborated by the structure observed on line 407-12.

CHAPTER VII. DISCUSSIONS, CONCLUSIONS, AND FUTURE WORK

Discussion

The extreme northeastern Uinta arch displays structural trends and fracture patterns due to the cumulative effects of the tectonic stresses of the Laramide Orogeny, a poorly documented late-Sevier/late-Laramide or post-Laramide event, and Miocene to Holocene Browns Park extension. This is evidenced by the differing structural trends and fracture patterns within the area. The results of the detailed kinematic analyses suggest multistage fracturing with fracture sets that can be attributed to each of these major deformational events. The observation of NE-SW-trending fold axes just north of the field area suggests that the Sevier Orogeny was responsible for the deformation directly adjacent to the Irish Canyon-Vermillion Creek area and make it difficult to fully dismiss the Sevier Orogeny as a contributor. However, very few NW-SE-directed thrust faults were observed in the area. This suggests that Sevier Orogeny deformation is largely limited to the critical taper. It is likely that the zone in between the Irish Canyon-Vermillion Creek area and that of the Vermillion Basin to the north is a transition zone where Sevier deformation is greatly diminished. The NNW-SSE-directed right-lateral strike-slip faults, associated joint patterns, and NNE-SSW σ_1 appear to be younger than the ENE-WSW Laramide fractures.

Proposed Tectonic History

The deformation within the Irish Canyon-Vermillion Creek area is clearly multistage. The first stage of deformation was characterized by ENE-WSW Laramide

compression resulting in ENE-WSW-directed thrust faulting and strike-slip faulting. Kinematic analyses suggest that Laramide deformation was achieved in response to N59E-directed shortening. This deformation resulted in large amounts of interlayer flexural-slip and a joint set with an average strike of N71E.

The second stage of deformation was characterized by E-W extension probably due to a poorly documented late-Sevier/late-Laramide, or post-Laramide event, or a combination of these events. This stage resulted in a transtensional and locally transpressional right-lateral strike-slip fault system which created a predominance of right-lateral strike-slip faults and a joint set with an average strike of N1E. Evidence for this interpretation includes a node of NNE-directed thrust faults associated with the right-lateral system.

This deformation would have had to have been late-Sevier, late-Laramide, or post-Laramide because the NNW-striking right-lateral strike-slip fault planes associated with the NNE-SSW σ_1 were observed cross-cutting the ENE-WSW strike-slip faults associated with the ENE-WSW Laramide σ_1. The N-S-striking joint set also abuts against the N71E-striking Laramide joint set.

The third stage of deformation was characterized by NE-SW Miocene to Holocene Browns Park extension resulting in a regional normal fault set with an average strike of N52W and a joint set with an average strike of N40W.

Conclusions

Field mapping, field observations, detailed kinematic analyses, interpretation of 2-D seismic data, and 2-D cross section analyses conducted within the northeastern Uinta arch, yielded the following conclusions:

1. Joint analyses yielded a trimodal distribution of joint strikes with the primary joints having an average strike of N71E, the secondary joints having an average strike of N1E, and the third generation joints having an average strike of N40W.

2. Eigenvector analyses of minor fault slickensides indicate an average slip direction of N17E and the average ideal σ_1 calculated from minor fault data is N29E. However, due to the multiple tectonic events, these average results are of diminished importance. The main Laramide stage had a σ_1 of N59E and the stage of NNE-SSW compression had a σ_1 of N10E.

3. The discrepancy between average slip and ideal σ_1 directions is due to a preponderance of right-lateral strike-slip faulting (44 percent of faults).

4. Analyses of the minor fault data sets subdivided by station reveals that the variability in slip and shortening directions is likely due to differing large-scale regional mechanisms as opposed to local small-scale mechanisms.

5. Folding of the Mancos Shale and back-thrusting of the Browns Park Formation were observed in the northeastern portion of the field area. This deformation is possibly in response to the overlying Browns Park Formation gravitationally sliding down dip along its contact with the Mancos Shale.

6. Cross-cutting of NNW-striking right-lateral strike-slip faults and ENE-WSW-striking left-lateral strike-slip faults indicate a multistage deformational history, with the NNW-striking right-lateral faults being the younger faults.

7. Regional joints which are parallel to the N40W joint set are open at depth in surrounding areas, therefore, the N40W joints may be the most effective fluid conduits for water and petroleum extraction.

8. The 2D cross-section coupled with the 2D seismic analyses showed that a large amount of flexural slip was necessary for a balanced interpretation.

9. Both minor fault analyses and joint analyses indicate an overall Laramide ENE-WSW σ_1 direction.

10. The observed transtensional and locally transpressional right-lateral strike-slip system associated with a predominantly NNE σ_1 is probably due to a poorly documented late-Sevier/late-Laramide, or post-Laramide event, or a combination of these events.

11. Regional normal faults with an average strike of N52W and joint sets with an average strike of N40W indicate NE-SW extension due to Miocene to Holocene Browns Park extension.

12. Kinematic analyses of fractures identified three deformational events and joint patterns: ENE-WSW Laramide compression creating the primary joints in pre-Laramide strata, E-W extension probably due to a poorly documented late-Sevier/late-Laramide, or post-Laramide event, creating the second generation joints, and NE-SW Browns Park extension creating the third generation joints.

Future Work

Folding of the Mancos Shale and back-thrusting of the Browns Park Formation were observed in the northeastern portion of the field area. This deformation is possibly in response to the overlying Browns Park Formation gravitationally sliding down dip along its contact with the Mancos Shale. Additional research is necessary into the role that gravitational sliding plays in the field area with respect to the Browns Park Formation and the Mancos Shale.

There is uncertainty with respect to what was responsible for the second stage of regional deformation that appears to have occurred late-Sevier, late-Laramide, or post-Laramide. Previous researchers hypothesized that the deformation in the area could have been in response to protracted Laramide stress or current Rio Grande rifting. Additional field work in the area and surrounding areas in search of minor fault cross-cutting relationships within the Eocene and younger strata and additional fractures within the Browns Park Formation is necessary.

If a definite N-S-striking joint set is found within the Bishop Conglomerate or Browns Park Formation, then it is possible that the deformation seen within the Irish Canyon-Vermillion Creek area is due to Rio Grande rift extension and not a poorly documented late-Sevier or late-Laramide event. Some N-S-striking joints were observed, however they were few in number and were attributed to topographic jointing. A more regional fracture study of the Bishop Conglomerate and Browns Park Formation might help define the timing of deformation in the area.

REFERENCES CITED

Allmendinger, R.W. and Jordan, T.E., 1983, Andean tectonics related to geometry of subducted Nazca plate, Geological Society of America Bulletin, v. 94, p. 341-361.

Allmendinger, R.W., Figueroa, D., Snyder, D., Beer, J., Mpodozis, C., Isacks, B.L., 1990, Foreland shortening and crustal balancing in the Andes at 30˚ S latitude: Tectonics, v. 9, p. 789-809.

Allmedinger, R., 2002, Stereonet v. 1.1 for Windows, compiled by Compaq ProFortran v.7.

Amar, J.R., Brenneman, E.V., Dickinson, W.R., Anderson, and C.E., 2006, U-Pb ages of detrital zircons in middle to Upper Jurassic eolianites of the Colorado Plateau: Abstracts with Programs - Geological Society of America, v. 38, i. 5, p. 10.

Anderson, R.E., and Barnhard, T.P., 1991, Heterogeneous Neogene strain and its bearing on horizontal extension and horizontal and vertical contraction at the margin of the extensional orogen, Mormon Mountains area, Nevada and Utah: U.S. Geologic Survey Bulletin 2011, p. 1-43.

Anderson, R.E., and Barnhard, T.P., 1993, Aspects of three-dimensional strain at the margin of the extensional orogen, Virgin River depression area, Nevada, Arizona, and Utah: GSA Bulletin, v. 105, p. 1019-1052.

Barlow, J.A., and Haun, J.D., 1998, Structure Contour map of the SE ¼ of the Green River Basin, Wyoming and Colorado: Barlow and Haun Inc. Geologists, Rocky Mountain Map Company.

Bergh, S., and Snoke, A.W., 1992, Polyphase Laramide deformation in the Shirley Mountains, south central Wyoming foreland: Mountain Geologist, v. 29, n. 3, p. 85-100.

Beutner, E.C., 1977, Causes and consequences of curvature in the Sevier orogenic belt, Utah to Montana, *in* E.L. Heisey and others, eds., Rocky Mountain Thrust Belt Geology and Resources: Wyoming Geological Association, 29th Annual Field Conference Guidebook, p. 353-365.

Bird, P., 1988, Formation of the Rocky Mountains, western United States; A continuum computer model: Science, v. 239, n. 4847, p. 1501-1507.

Bird, P., 1998, Kinematic history of the Laramide Orogeny in latitudes 35 degrees-49 degrees N, Western United States: Tectonics, v. 17, n. 5, p. 780-801.

Blackstone, D., 1990, Rocky Mountain foreland structure exemplified by the Owl Creek Mountains, Bridger Range and Casper Arch, central Wyoming: Guidebook – Wyoming Geological Association, v. 41, p. 151-166.

Blakey, R., Havholm, K.G., and Jones, L. S., 1996, Stratigraphic analysis of eolian interactions with marine and fluvial deposits, Middle Jurassic Page Sandstone and Carmel Formation, Colorado Plateau, U.S.A: Journal of Sedimentary Research, v. 66, n. 2, p. 324-342.

Bostick, N.H., Hatch, J.R., Daws, T.A., Love, A.H., Lubeck, C.M., and Threlked, C.N., 1987, Organic geochemistry and organic petrography, *in* Roehler H.W., eds., Geologic investigations of the Vermillion Creek coal bed in the Eocene Niland Tongue of the Wasatch Formation, Sweetwater County, Wyoming: U.S Geological Survey Professional Paper, 1314-H, p. 135-163.

Boyd, D., 1993, Paleozoic history of Wyoming: *Memoir - Geological Survey of Wyoming*, 5:164-187.

Bradley, W.A., 1955, Jurassic and pre-Mancos Cretaceous stratigraphy of the eastern Uinta Mountains, Colorado-Utah: Guidebook to the Geology of Northwest Colorado, 6th Annual Field Conference, p. 21-26.

Bradley, W.H., 1936, Geomorphology of the north flank of the Uinta Mountains: U. S. Geological Survey Professional Paper, p. 163-199.

Bradley, W.H., 1961, Miscellaneous Geologic Investigations Map: Geologic map of a part of southwestern Wyoming and adjacent sites: U. S. Geological Survey, Reston, VA, United States.

Bradley, W.H., 1964a, Geomorphology of the north flank of the Uinta Mountains: U.S. Geological Survey Professional Paper 185-I, p. 163-199.

Bradley, W.H., 1964b, Geology of the Green River Formation and associated Eocene rocks in southwestern Wyoming and adjacent parts of Colorado and Utah: United States Geological Survey Professional Paper P0496-A, p. A1-A86.

Bradley, M.D., 1988a, Structural evolution of the Uinta Mountains, Utah, and their interactions with the Utah-Wyoming salient of the Sevier overthrust belt: Doctoral Thesis, University of Utah, p. 1-178.

Bradley, M. D., 1988b, Sevier and Laramide structural evolution of the Uinta Mountains, Utah-Colorado: Abstracts with Programs - Geological Society of America, v. 20, n. 6, p. 408-408

Bradley, M. D., 1995, Timing of the Laramide rise of the Uinta Mountains: Wyoming Geological Association field conference guidebook, p. 31-44.

Bradley, M.D., and Bruhn, R.L., 1988, Interaction of the Rocky Mountain Foreland and the Cordilleran thrust belt: Memoir - Geological Society of America, v. 71, p. 431-445.

Bressler, S., 1981, Preliminary paleomagnetic poles and correlation of the Proterozoic Uinta Mountain Group, Utah and Colorado: Earth and Planetary Science Letters, v. 55, n.1, p. 53-64.

Brown, W.G., 1984, Basement involved tectonics in foreland areas: American Association of Petroleum Geologists, Continuing Education Course Note Series, v. 26, p. 1-92.

Brown, W.G., 1988, Deformational style of Laramide uplifts in the Wyoming foreland: Memoir - Geological Society of America, v. 171, p. 1-25.

Brownfield, M., 2000, A summary of the stratigraphy, coal resources, and coal-bed methane potential of Northwest Colorado: U.S. Geological Survey professional paper, p. I1.

Bruhn, R.L., Picard, M.D., and Beck, S.L., 1983, Mesozoic and Early Tertiary structure and sedimentology, central Wasatch Mountains, Uinta Mountains, and Uinta Basin: Utah Geological and Mineral Survey, Special Studies, v. 59, p. 63-105.

Bruhn, R.L., Picard, M.D., and Isby, J.S., 1986, Tectonics and sedimentology of Uinta arch, western Uinta Mountains, and Uinta Basin, *in* Petersen, J.A., eds., Paleotectonics and sedimentation in the Rocky Mountain Region, United States: American Association of Petroleum Geologists Memoir, v. 32, p. 333-352.

Bump, A., 2004, Three-dimensional Laramide deformation of the Colorado Plateau; competing stresses from the Sevier thrust belt and the flat Farallon slab: Tectonics, v. 23, n. 1, p. 1-15.

Byerlee, J., 1978, Friction of rocks; Pure and applied geophysics: v. 116, n. 4-5, p. 615-626.

Cahill, T. and Isacks, B.L., 1985, Shape of the subducted Nazca Plate, Eos Transactions, American Geophysical Union, v. 66, p. 299.

Cather, S.M., 1989, Uses of epifluorescent microscopy in evaluation of Mesaverde tight gas sands: AAPG Bulletin, v. 73, n. 9, p. 1150-1151.

Cather, S.M., 1999, Implications of Jurassic, Cretaceous, and Proterozoic piercing lines for Laramide oblique-slip faulting in New Mexico and rotation of the Colorado Plateau: Geological Society of America Bulletin, v. 111, i. 6, pp. 849-868.

Chapin, C.E., and Cather, S.M., 1981, Eocene tectonics and sedimentation in the Colorado Plateau - Rocky Mountain area: Arizona Geological Society Digest, v.14, p. 173-198.

Chapin, C.E., and Cather, S.M., 1983, Eocene paleotectonics and sedimentation in the Rocky Mountain-Colorado Plateau region: AAPG Bulletin, v. 67, n. 8, p. 1331-1332.

Chase, R.B., Schmidt, C.J., and Genovese, P.W., 1993, Influence of Precambrian rock compositions and fabrics on the development of Rocky Mountain foreland folds, *in* Erslev, E.A., ed., Laramide basement deformation in the Rocky Mountain foreland of the western United States: Special Paper - Geological Society of America, v. 280, p. 45-72.

Chaudhuri, S., and Hansen, W.R., 1980, Rb-Sr ages of the Uinta Mountain Group of Utah and Colorado: Abstracts with Programs - Geological Society of America, v. 12, n. 6, p. 269-269.

Cobban, W.A., and Reeside, J.B., 1952, Correlation of the Cretaceous formations of the western interior of the United States: GSA Bulletin, v. 63, p. 1011-1044.

Compton, R.R., 1966, Analysis of Pliocene-Pleistocene deformation and stress in northern Santa Lucia Range, California: GSA Bulletin, v. 77, p. 1361-1380.

Condon, S.M., 1997, Fracture studies in Pictured Cliffs and Fruitland Formations, *in* Close, J.C., and Casey, T.A., eds., Natural fracture systems in the Southern Rockies: Durango, Colorado, Four Corners Geological Society, p. 85-96.

Copfer, M.N.N., 2005, Kinematic analysis of the Gore fault and surrounding region, Eagle County, Colorado: M.S. Thesis, Colorado State University, p. 77-81.

Counts, R.C., 2005, The Quaternary stratigraphy of the Henrys Fork and western Browns Park, northeastern Uinta Mountains, Utah and Wyoming: Masters Thesis, Utah State University, p. 1-158.

Crittenden, M.D., 1967, Mineral resources of the High Uintas primitive area, Utah: U. S. Geological Survey Bulletin, p. I1-I27.

Crittenden, M.D., and Peterman, Z.E., 1975, Preliminary isotopic dating of Uinta Mountain Group: Abstracts with Programs - Geological Society of America, v. 7, n. 5, p. 600-600.

Cross, T., 1986, Tectonic controls of foreland basin subsidence and Laramide style deformation, Western United States: Special Publication of the International Association of Sedimentologists, v. 8, p. 15-39.

Currie, B.S., 1993, Sequence stratigraphy of the Jurassic-Cretaceous Morrison and Cedar Mountain formations, NE Utah-NW Colorado: Geological Society of America, 89th annual Cordilleran Section meeting and 46th annual Rocky Mountain Section meeting, Abstracts with Programs - Geological Society of America, v. 25, i. 5, p. 26-27.

Currie, B.S., 1998, Upper Jurassic-Lower Cretaceous Morrison and Cedar Mountain formations, NE Utah-NW Colorado; relationships between nonmarine deposition and early Cordilleran foreland-basin development: *Journal of Sedimentary Research*, *68*(4), 632-652.

Currie, B.S., Pankow, K.C., Ritts, B.D., 1993, Depositional architecture and sequence stratigraphy of the Mid-Cretaceous Dakota Formation, NE Utah-NW Colorado: Geological Society of America, 89th annual Cordilleran Section meeting and 46th annual Rocky Mountain Section meeting, Abstracts with Programs - Geological Society of America, v. 25, i. 5, p. 26.

Currie, B.S., and Reeder, M.D., 2002, Sequence stratigraphy of the Jurassic Curtis, Summerville, and Stump Formations, Utah-Colorado: Abstracts with Programs - Geological Society of America, v. 34, i. 6, p. 278.

Currie, B.S., Schwartz, R.K., Wilcox, W.T., 2005, Sequence stratigraphy of a regional-scale tidal embayment, Upper Jurassic Curtis and Summerville Formations, central Utah Geological Society of America, 2005 annual meeting, Abstracts with Programs - Geological Society of America, v. 37, i. 7, p. 141.

Davis, P.M., Parker, E.C., Evans, J.R., Iyer, H.M., and Olsen, K.H., 1984, Teleseismic deep sounding of the velocity structure beneath the Rio Grande Rift, *in* New Mexico Geological Society Guidebook, 35th Field Conference, Rio Grande Rift: Northern New Mexico, P. 30.

Dahlstrom, C., 1990, Geometric constraints derived from the law of conservation of volume and applied to evolutionary models for detachment folding: AAPG Bulletin, v. 74, n. 3, p. 336-344.

De Grey, L., 2004, Stratigraphic investigations of the Neoproterozoic Uinta Mountain Group: combating 'the curse of the Proterozoic sandstones': Abstracts with Programs - Geological Society of America, v. 36, n. 5, p. 570-570.

Dehler, C.M., Porter, M.P., De Grey, L.D., Sprinkel, D.A., and Brehm, A., 2007, The Neoproterzoic Uinta Mountain Group revisited: A synthesis of recent work on the Red Pine Shale and related undivided clastic strata, northeastern Utah, USA, i*n* Proterozoic geology of eastern North America and Siberia: SEPM special publication 86, p. 151-166.

Dickinson, W.R., Lawton T.F., and Inman, K.F., 1986, Sandstone detrital modes, central Utah foreland region: stratigraphic record of Cretaceous-Paleogene tectonic evolution: Journal of Sedimentary Petrology, v. 56, n. 2, p. 276-293.

Dickinson, W.R., Klute, M.A., Hayes, M.J., Janecke, S.U., Lundin, E.R., McKittrick, M.A., and Olivares, M.D., 1988, Paleogeographic and paleotectonic setting of Laramide sedimentary basins in the central Rocky Mountain region: Geological Society of America Bulletin, v. 100, n. 7, p. 1023-1039.

Driese, S.G., and Dott, R.H., 1984, Model for sandstone-carbonate "cyclothems" based on upper member of Morgan Formation (middle Pennsylvanian) of northern Utah and Colorado: AAPG Bulletin, v. 68, p. 574-597.

Eicher, D., 1955, Microfossils of the Curtis Formation, eastern Uinta Mountains, Utah, Colorado: Guidebook to the geology of north west Colorado, p. 27.

Epard, J.L., and Groshong, R.H., Jr., 1995, Kinematic model of detachment folding including limb rotation, fixed hinges, and layer-parallel strain: Tectonophysics, v. 247, n. 1-4, p. 85-103.

ESRI Inc., 2006, ArcGIS v. 9.2, Redlands California.

Ericson, R., 2006, Sequence stratigraphy of the Chinle Formation in Dinosaur National Monument, UT and CO: Abstracts with programs – Geological Society of America, v. 38, i. 7, p.129.

Erslev, E.A., 1986, Basement balancing of Rocky Mountain foreland uplifts: Geology, v. 14, p. 259-262.

Erslev, E.A., 1993, Thrusts, backthrusts, and detachment of Laramide foreland arches, *in* Schmidt, C.J., Chase, R., and Erslev, E.A., eds., Laramide basement deformation in the Rocky Mountain foreland of the western United States: Special Paper - Geological Society of America, v. 280, p. 339-358.

Erslev, E.A., 1998, SELECT 1.2 worksheet and computer program, Department of Earth Resources, Colorado State University.

Erslev, E.A., 2001, Multi-stage, multi-directional Tertiary shortening and compression in north-central New Mexico: Geological Society of America Bulletin, v. 113, p.63-74.

Erslev, E.A., 2004, Laramide minor faulting in the Colorado Front Range: Bulletin - New Mexico Bureau of Geology & Mineral Resources, p. 181-204.

Erslev, E.A., 2005, 2D Laramide geometries and kinematics of the Rocky Mountains, Western U.S.A., *in* Karlstrom, K.E., and Keller, G.E., eds., The Rocky Mountain Region; An Evolving Lithosphere: Geophysical Monograph Series, v. 154, p 7-20.

Erslev, E.A., 2006, LDIS2 v. 2.1: Program to plot rose diagrams and calculate line statistics for an unlimited set of lines, Department of Earth Resources, Colorado State University.

Erslev, E.A., and Holdaway, S.M., 1999, Laramide faulting and tectonics of the northeastern Front Range of Colorado: GSA Field Guide, v. 1, p. 41-49.

Erslev, E.A., Holdaway, S.M., O'Meara, S.A., Jurista, B., and Selvig, B., 2004, Laramide minor faulting in the Colorado Front Range: New Mexico Bureau of Geology and Mineral Resources Bulletin 160, p. 181-204,

Erslev, E.A., and Koenig, N.V., 2009, 3D kinematics of Laramide, basement-involved Rocky Mountain deformation, U.S.A.: Insights from minor faults and GIS-enhanced structure maps: Department of Geosciences, Colorado State University, Fort Collins, CO 80523.

Erslev, E.A., and Koenig, N.V., in press.

Erslev, E.A., and Larson, S.M., 2006, Testing of Laramide hypotheses for the Colorado Front Range arch using minor faults: The Mountain Geologist, v. 43, n. 1, p. 45-64.

Erslev, E.A and Wiechelman, 1997, Fault and fold orientations in the Central Rocky Mountains of Colorado and Utah *in* Hoak, T.E., Klawitter, A.L., Blomquist, P.K., eds., Fractured reservoirs; characterization and modeling, Rocky Mountain Association of Geologists, p. 131-136.

Eschner, T.A., 1982, A transgressive tidal sand bar complex; Jurassic Curtis Formation, northeastern Utah: Abstracts; abstracts of papers; eleventh International Congress on Sedimentology, McMasters University, Hamilton, Ontario, Canada, p. 98.

Fanning, C., and Dehler, C.M., 2005, Constraining depositional ages for Neoproterozoic siliciclastic sequences through detrital zircon ages; a ca.770 Ma maximum age for the lower Uinta Mountain Group, Abstracts with Programs - Geological Society of America, v. 37(7), p. 42.

Fletcher, R., 1984, Instability of lithosphere undergoing shortening; a model for Laramide foreland structures: Abstracts with Programs - Geological Society of America, v. 16, n. 2, p. 83-83.

Ford, R.L., and Gillman, S.L., 2000, Geology of Coral Pink Sand Dunes State Park, Kane County, Utah: Utah Geological Association Publication, v. 28, p. 365-389.

Gillett, C., 2009, Mechanisms of fracturing in northwestern Colorado: multi-stage deformation and the importance of post-Laramide extension: Master's Thesis, Colorado State University, p. 1-98.

Gregory, R.W. and DeBruin, R.H., 1991, Map Series - Geological Survey of Wyoming Oil and gas fields map of the Greater Green River basin and Overthrust Belt, southwestern Wyoming Authors: Map Series - Geological Survey of Wyoming, v. 36.

Gregson, J., 1994, North-northwest shortening across Laramide structures in the southeastern Uinta Mountains, Colorado and Utah: M.S Thesis, Colorado State University, p. 136-139.

Gregson, J., and Erslev, E.A., 1997, Heterogeneous Laramide deformation in the Uinta Mountains, Colorado and Utah, *in* Hoak, T.E., Klawitter, A.L., and Bloomquist, P.K., eds., Fractured reservoirs; characterization and modeling: Denver, Colorado: Rocky Mountain Association of Geologists Guidebook, p.137-154.

Gries, R., 1981, Oil and gas prospecting beneath the Precambrian foreland thrust plates in the Rocky Mountains: The Mountain Geologist, v. 18, p. 1-18.

Gries, R., 1983, North-south compression of Rocky Mountain foreland structures: Rocky Mountain Association of Geologists, p. 9-32.

Hague, A. and Emmons, S.F., 1877, Report of the geological exploration of the 40th parallel: Descriptive geology, v. II.

Hamilton, W., 1988, Laramide crustal shortening, *in* Schmidt, C.J., and Perry, WJ., Jr., eds., Interaction of the Rocky Mountain foreland and the Cordilleran thrust belt: Memoir - Geological Society of America, v. 171, p. 27-39.

Hancock, P.L., and Engelder, T., 1989, Neotectonic joints: Geological Society of America Bulletin, v. 101, p. 1197-1208.

Hansen, W.R., 1965, Geology of the Flaming Gorge area, Utah-Colorado-Wyoming: U.S. Geologic Survey Professional Paper P 0490, 196 p.

Hansen, W.R., 1984, Post-Laramide tectonic history of the eastern Uinta Mountains, Utah, Colorado, and Wyoming: The Mountain Geologist, v. 21, n.1, p. 5-29.

Hansen, W.R., 1986a, Neogene tectonics and geomorphology of the eastern Uinta Mountains in Utah, Colorado, and Wyoming: U. S. Geological Survey Professional Paper, P 1356, p. 1-78.

Hansen, W.R., 1986b, History of faulting in the eastern Uinta Mountains, Colorado and Utah, *in* D.S Stone, ed., New interpretations of northwest Colorado geology: Rocky Mountain Association of Geologists, 1986 Symposium, p. 5-17.

Hansen, W.R., Kinney, D.M., and Good, J.M., 1960, Distribution and physiographic significance of the Browns Park formation, Flaming Gorge and Red Canyon Areas, Utah-Colorado: U.S. Geol. Survey, Professional Paper 400-B, p. 257-259.

Harthill, N., 1997, Cost-effective fracture mapping in Rocky Mountain basins: AAPG Bulletin, v. 81, n. 7, p. 1225-1225.

Hatch, J.R., 1987, Element geochemistry, *in* Roehler, H.W., eds, Geologic investigations of the Vermillion Creek coal bed in the Eocene Niland Tongue of the Wasatch Formation, Sweetwater County, Wyoming: U.S Geological Survey Professional Paper, 1314-G, p. 128-131.

Hendrix, M., 2000, Stratigraphy and sedimentology of Permian strata, Uinta Mountains, Utah; allostratigraphic controls on the accumulation of economic phosphate: Special publication-Society for Sedimentary Geology, v. 66, p. 349.

Herr, R.G., Picard, M.D., and Evans, S.H., 1982, Age and depth of burial, Cambrian Lodore Formation, northeastern Utah and northwestern Colorado: Contributions to Geology, v. 21, i. 2, p. 115-121.

Hucka, B., 1991, Analysis and regional implication of cleat and joint systems in selected coal seams, Carbon, Emery, Sanpete, Sevier, and Summit counties, Utah: Special Studies – Utah Geological and Mineral Survey Report 74, p. 1-47.

Jacobs, A.F., 1983, Mountain front thrust, southeastern Front Range and northeastern Wet Mountains, Colorado: Field Conference - Rocky Mountain Association of Geologists, p. 229-244.

Jensen, P.H., Kowallis, B.J., and Morris, T.H., 2005, Stratigraphy across the Jurassic/Triassic boundary along the south flank of the Uinta Mountains, northeast Utah; the Bell Springs Member of the Nugget Sandstone: Abstracts with Programs - Geological Society of America, v. 37, i. 7, p.141.

Johnson, R.C., 1979, Northwest to southeast cross section of Cretaceous and Lower Tertiary rocks across the eastern part of the Uinta Basin, Utah, *in* USGS Uinta-Piceance assessment team's petroleum systems and geologic assessment of oil and gas in the Uinta-Piceance province, Utah and Colorado: U.S. Geological Survey Digital Data Series DDS–69–B, U.S. Department of the Interior, U.S. Geological Survey, p. 6-6.

Johnson, R., 1990, Cretaceous rocks of the Piceance Basin area, northwestern Colorado: AAPG Bulletin, v. 74, p. 1329-1330.

Johnston, R.E., and Yin, A., 2001, Kinematics of the Uinta fault system (southern Wyoming and northern Utah) during the Laramide Orogeny: International Geology Review, v. 43, p. 52-68.

Jordan, T.E., and Allmendinger, R.W., 1986, The Sierra Pampeanas of Argentina: A modern analogue of Rocky Mountain foreland deformation: American Journal of Science, v. 286, p. 737-764.

Kanter, L.R., Dyer, R., and Dohmen, T.E., 1981, Laramide crustal shortening in the northern Wyoming province: Contributions to Geology, v. 19, no.2, p. 135-142.

Karlstrom, K.E., and Daniel, C.G., 1993, Restoration of Laramide right-lateral strike slip in northern New Mexico by using Proterozoic piercing points; tectonic implications from the Proterozoic to the Cenozoic: Geology Boulder, v. 21, n. 12, p. 1139-1142.

Kelley, V.C., 1956, The Rio Grande Depression from Taos to Santa Fe: in Southeastern Sangre De Christo Mountains, NMGS guidebook, seventh field conference, p. 109-114.

Kelley, S.A., and Chapin, C.E., 1997, Internal structure of the southern Front Range, Colorado, from an apatite fission-track thermochronology perspective: Rocky Mountain Association of Geologists, p. 19-30.

Koelmel, M.H., 1986, Post-Mississippian paleotectonic, stratigraphic, and diagenetic history of the Weber Sandstone in the Rangely Field area, Colorado: AAPG Memoir, v. 41, p. 371-396.

Kulik, D.M., and Schmidt, C.S., 1988, Region of overlap and styles of interaction of Cordilleran thrust belt and Rocky Mountain Foreland: Memoir - Geological Society of America, v. 171, p. 75-98.

Laubach, S.E., and Lorenz, J.C., 1992, Preliminary assessment of natural fracture patterns in Frontier Formation sandstones, southwest Wyoming, *in* Mullen, C.E. Ed., Rediscover the Rockies: Wyoming Geological Association Forty-Third Field Conference Guidebook, p. 87-96.

Laubach, S. E., Tremain, C.M., 1994, Fracture Swarms: potential targets for methane exploration in Upper Cretaceous sandstone and coal, northern San Juan Basin, Colorado, *in* Ayers, W.B., Jr., and Kaiser, W.R., eds., Coal bed methane in the upper Cretaceous Fruitland Formation, San Juan Basin, New Mexico and Colorado: The University of Texas at Austin, Bureau of Economic Geology, topical report prepared for Gas Research Institute under contract no.5087-214-1544, p. 103-118.

LeMasurier, W.E., 1970, Structural study of a Laramide fold involving shallow seated basement rock, Front Range Colorado: GSA Bulletin, v.81, no.2, p. 435-450.

Liu, M., 2001, Cenozoic extension and magmatism in the North American Cordillera: the role of gravitational collapse: Tectonophysics, v. 342, p. 407-433.

Love, J.D., and Christiansen, A.C., 1985, State Geologic Map- Geologic map of Wyoming: U. S. Geological Survey, Reston, VA, United States.

Love, J.D., Christiansen, A.C., and Ver Ploeg, A.J., 1993, Map Series - Geological Survey of Wyoming Stratigraphic chart showing Phanerozoic nomenclature for the State of Wyoming: Map Series - Geological Survey of Wyoming.

Lowell, J.D., and Gries, R., eds., 1983, Rocky Mountain foreland basins and uplifts: Rocky Mountain Association of Geologist, p. 19-32.

Lowell, J., 1983, Foreland detached deformation: AAPG Bulletin, v. 67, n. 8, p. 1349-1349.

Maclachlan, M.E., 1972, Triassic system-Geologic Atlas of the Rocky Mountain region: Rocky Mt. Assoc. Geol., Denver, p. 166-176.

Manion, L. J., 1961, Geology of the Irish Canyon-Vermillion Creek area, Moffat County, Colorado: M.S. Thesis, University of Wyoming, p. 1-93.

Matthews, V., III, and Sherman, G.D., 1976, Origin of monoclinal folding near Livermore, Colorado: Mountain Geologist, v. 13, n. 2, p. 61-66.

Matthews, V., III, and Work, D.F., 1978, Laramide folding associated with basement block faulting along the northeastern flank of the Front Range, Colorado, *in* Matthews, V., III ed., Laramide folding associated with basement block faulting: Memoir - Geological Society of America 151, p. 101-124.

Mayer, V., 1960, Stratigraphy and paleontology of the Mississippian formations of Moffat County, Colorado: M.S. Thesis, University of Colorado.

McGookey, D.P., Haun, J.D., Hale, L.A., Goodell, H.G., McCubbin, D.G., Weimer, R.J., and Wulf, G.R., 1972, Cretaceous system-Geologic Atlas of the Rocky Mountain region, Rocky Mt. Assoc. Geol., Denver, p. 190-228.

Miall, A.D., 1978, Lithofacies types and vertical profile models in braided river deposits: a summary, *in* Miall, A.D., ed., Fluvial Sedimentology: Canadian Society of Petroleum Geologists, Memoir 5, p. 597-604.

Midland Valley Exploration Ltd, 2006, 2D Move v. 5.0, Glasgow, United Kingdom.

Molenaar, C.M., and Wilson, B.W., 1990, The Frontier Formation and associated rocks of northeastern Utah and northwestern Colorado: USGS Bulletin B1787M, Related information, 983.

Molzer, P., and Erslev, E.A., 1995, Oblique convergence on east-west Laramide arches, Wind River Basin, Wyoming: American Association of Petroleum Geologist Bulletin, v. 19, p. 1377-1394.

Mpodozis, C., and Ramos, V.A., 1989, The Andes of Chile and Argentina, in Ericksen, George, E., Pinochet, Maria Teresa, C., and Reinemund, John, A., eds.: Geology of the Andes and its relation to hydrocarbon and mineral resources: Circum-Pacific Council for Energy and Mineral Resources, Earth Science Series, Houston, TX, United States, Circum-Pacific Council for Energy and Mineral Resources, p. 59-90.

Morel, J., 1986, An interpretation of the subsurface structural style of the Beaver Creek Anticline, Moffat and Routt counties, Colorado: Rocky Mountain Association of Geologists, p. 195-201.

Narr, W., 1980, Origin of subsurface fracture systems; example from Altamont Field, Uinta Basin, Utah: AAPG Bulletin, v. 64, n. 5, p. 755-755.

Narr, W., 1982, Origin of fracture porosity; example from Altamont Field, Utah: AAPG Bulletin, v. 66, n. 9, p. 1231-1247.

Narr, W., 1998, Quantifying subsurface fracture sets: collecting and analyzing data with simulation in mind, *in* Hoak, T.E., Ed., Fractured reservoirs: practical exploration and development strategies, RMAG, p. 137-155.

Newhart, R., and Longman, M., 2005, 2005 Vermillion Basin fall field trip: Rock Springs, Wyoming to Irish Canyon, Colorado, (not published).

Nichols, D.J., 1987, Palynolgy of the Vermillion Creek coal bed and associated strata, *in* Roehler H.W., eds., Geologic investigations of the Vermillion Creek coal bed in the Eocene Niland Tongue of the Wasatch Formation, Sweetwater County, Wyoming: U.S Geological Survey Professional Paper, 1314-F, p. 107-122.

Nightingale, W.T., 1930, Geology of Vermillion Creek gas area in southwest Wyoming and northwest Colorado: Bulletin of the American Association of Petroleum Geologists, v. 14, n. 8, p. 1013-1040.

Oldow, J.S., Bally, A.W., Lallement, H.G.A., and Leeman, W.P., 1989, Phanerozoic evolution of the North American Cordillera; United States and Canada: Geological Society of America, v. A, p. 139-232.

Oldow, J.S., Bally A.W., and Lallement, H.G.A., 1990, Transpression, orogenic float, and lithospheric balance: Geology Boulder, v. 18, n. 10, p. 991-994.

Olsen, K.H., Baldridge, W.S., and Callender, J.F., 1987, Rio Grande rift: an overview, *in* Ramberg, I.E., Milanovsky, E.E., and Qvale, G., eds., Continental Rifts-Principal and Regional Characteristics: Tectonophysics, v. 143, p. 119-139.

Paulsen, T., and Marshak, S., 1999, Origin of the Uinta Recess, Sevier fold-thrust belt, Utah; influence of basin architecture on fold-thrust belt geometry: Tectonophysics, v. 312, n. 2-4, p. 203-216.

Paylor, E.D., II, and Yin, A., 1993, Left-slip evolution of the North Owl Creek fault system, Wyoming, during Laramide shortening, *in* Schmidt, C.J., Chase, R.B., and Erslev, E.A., eds., Laramide basement deformation in the Rocky Mountain foreland of the Western United States: Boulder, Colorado, Special Paper - Geological Society of America v. 280, p. 229-242.

Perry, W.J., Nichols, D.J., Dyman, T.S., and Haley, C.J., 1992, Sequential Laramide deformation of the Rocky Mountain foreland of southwestern Montana, Wyoming, and north-central Colorado: U.S. Geological Survey Bulletin, p. C1-C14.

Perry, W.J., and Flores, R.M., 1997, Sequential Laramide deformation and Paleocene depositional patterns in deep gas-prone basins of the Rocky Mountain region *in* Geologic controls of deep natural gas resources in the United States : Dyman, T. S., Rice, D. D., Westcott, P. A., eds., U. S. Geological Survey Bulletin, p. 49-59.

Peterson, J., 1984, Permian stratigraphy, sedimentary facies, and petroleum geology, Wyoming and adjacent areas: Guidebook - Wyoming Geological Association, v. 35, p. 25-64.

Petit, J., 1987, Criteria for the sense of movement on fault surfaces in brittle rocks: Journal of Structural Geology, v. 9, n. 5-6, p. 597-608.

Picard, M.D., and Mcgrew, P.O., 1955, Correlation of Cenozoic deposits of northwestern Colorado: RMAG Intermountain Assoc. Petroleum Geologist Guidebook, Geology of Northwestern Colorado, p. 50-52.

Powell, J.W., 1876, Report of the geology of the eastern portion of the Uinta Mountains and a region of country adjacent thereto: U.S. Geological and Geographical Survey of the Territories (Powell), p. 218.

Prucha, J.J., Graham, J.A., and Nickelsen, R.P., 1965, Basement controlled deformation in Wyoming province of Rocky Mountain foreland: AAPG bulletin, v. 49, n.7, p. 966-992.

Ramos, V.A., Cristallini, E.O., and Perez, D.J., 2002, The Pampean flat-slab of the Central Andes: Journal of South American Earth Sciences, v. 15, p. 59-78.

Raynolds, R., 1997, Synorogenic and post-orogenic strata in the central Front Range, Colorado: Rocky Mountain Association of Geologists, p. 43-48.

Reeside, J., 1955, Revised interpretation of the Cretaceous section on Vermilion Creek, Moffat County, Colorado: Guidebook - Wyoming Geological Association, v. 10, p. 85-88.

Ritzma, H.R., 1955, Early Cenozoic history of the Sand Wash basin, northwest Colorado, *in* Ritzma, H.R., and Oriel, S.S., eds., Guidebook to the geology of northwest Colorado: Intermountain Association of Geologists and Rocky Mountain Association of Geologists, p. 36-40.

Ritzma, H.R., 1969, Determination of oil shale potential, Green River Formation, Uinta Basin, northeast Utah: Special Studies - Utah Geological and Mineral Survey, p. 16.

Robbins, E.I., 1987, Paleoecology of the Niland Tongue, *in* Roehler, H.W., eds, Geologic investigations of the Vermillion Creek coal bed in the Eocene Niland Tongue of the Wasatch Formation, Sweetwater County, Wyoming: U.S Geological Survey Professional Paper, 1314-E, p. 77-95.

Roberts, R.J., Crittenden, M.D., Tooker, E.W., Morris, H.T., Hose, R.K., Cheney, T.M., 1965, Pennsylvanian and Permian basins in northwestern Utah, northeastern Nevada, and south-central Idaho: American Association of Petroleum Geologist Bulletin, v. 49, i. 11, p. 1926-1956.

Roehler, H.W., 1979, Vermillion Creek coal bed, high-sulfur, radioactive coal of paludal-lacustrine origin in Wasatch Formation of Vermillion Creek basin, Wyoming and Colorado: AAPG Bulletin, v. 63, n. 5, p. 839-839.

Roehler, H.W., 1985, Structural development and oil occurrence on northeast flank of Uinta Mountains near Irish Canyon, northwestern Colorado: AAPG Bulletin, v. 69, n. 5, p. 863-863.

Roehler, H.W., 1987, Geologic investigations of the Vermillion Creek coal bed in the Eocene Niland Tongue of the Wasatch Formation, Sweetwater County, Wyoming: U.S Geological Survey Professional Papers, 1314-A-L, 202 p.

Roehler, H.W., 1992, Correlation, composition, areal distribution, and thickness of Eocene stratigraphic units, greater Green River basin, Wyoming, Utah, and Colorado: U. S. Geological Survey Professional Paper, E1-E49.

Rowley, P.D., Tweto, O.L., Hansen, W.R., and Carrara, P.E., 1985, Geologic map of the Vernal 1˚ X 2˚ quadrangle, Colorado, Utah, and Wyoming: U.S. Geological Survey Miscellaneous Investigations Series Map I-1526, 1:250,000.

Ruf, J.C and Erslev, E.A, 2005, Origin of Cretaceous to Holocene fractures in the northern San Juan Basin, Colorado and New Mexico: Rocky Mountain Geology, v. 40, n. 1, p. 91-114.

Rye, R.O., 1987, Sulfur isotopic data, *in* Geologic investigations of the Vermillion Creek coal bed in the Eocene Niland Tongue of the Wasatch Formation, Sweetwater County, Wyoming: U.S Geological Survey Professional Papers, 1314-I, p. 167-169.

Sales, J.K., 1968, Crustal mechanisms of cordilleran foreland deformation: a regional and scale model approach: American Association of Petroleum Geologist Bulletin, v. 52, p. 2016-2044.

Sales, J.K., 1971, Structure of the northern margin of the Green River Basin, Wyoming: Guidebook - Wyoming Geological Association, v. 23, p. 85-102.

Schultz, A., 1920, Oil possibilities in and around Baxter Basin, in the Rock Springs Uplift, Sweetwater County, Wyoming: U. S. Geological Survey Bulletin, p. 1-107.

Sears, J.D., 1924, Geology and oil and gas prospects of a part of Moffat county, Colorado, and southern Sweetwater county, Wyoming: U.S. Geological Survey Bulletin 751-G, p. 269-319.

Sears, J.W., Graff, P.J., and Holden, G.S., 1982, Tectonic evolution of lower Proterozoic rocks, Uinta Mountains, Utah and Colorado: GSA Bulletin, v. 93, p. 990-997.

Sherrif, R.E., and Geldart, L.P., 1995, Exploration seismology, New York, Cambridge University Press, p. 592.

Sikich, S., 1960, Stratigraphy of the upper Triassic Stanaker Formations of the eastern Uinta Mountain area, northeastern Utah and northwestern Colorado: M.S. Thesis, University of Wyoming, p. 1-119.

Silliphant, L.J., Engelder, T., and Gross, M.R., 2002, The State of stress in the limb of the Split Mountain Anticline, Utah: constraints placed by transected joints: Journal of Structural Geology, v. 24, n. 200, p.155-172.

Smalley, R.F., Jr., and Isacks, B.L., 1987, A high resolution local network study of the Nazca Plate Wadati-Benioff zone under western Argentina: Journal of Geophysical Research, v. 92, p. 13,903-13,912.

Smith, L.B., Jr., Eberli, G.P., and Sonnenfeld, M., 2004, Sequence-stratigraphic and paleogeographic distribution of reservoir-quality dolomite, Madison Formation, Wyoming and Montana: AAPG Memoir, v.80, p. 67.

Smithson, S., Brewer, J.A., Kaufman, S., Oliver, J.E., and Hurich, C.A., 1979, Structure of the Laramide Wind River Uplift, Wyoming, From COCORP deep reflection data

and from gravity data: Journal of Geophysical Research, v. 84, n. B11, p. 5955-5972.

Spang, J.H., Evans, J.P., and Berg, R.R., 1985, Balanced cross section of small fold-thrust structures: The mountain Geologist, v.21, p. 37-46.

Spang, J.H., and Evans, J.P., 1988, Geometrical and mechanical constraints on basement-involved thrusts in the Rocky Mountain foreland province, *in* Schmidt, C.J., and Perry, W.J., Jr., eds., Interaction of Rocky Mountain foreland and the Cordilleran thrust belt: Memoir - Geological Society of America 171, p. 41-52.

Sprinkel, D.A., 2000, Geologic guide along Flaming Gorge Reservoir, Flaming Gorge National Recreation Area, Utah-Wyoming: Utah Geological Association Publication 28, p. 277-299.

Stanton, R.W., Minkin, J.A., and Moore, T.A., 1987, Petrographic and physical properties of coal and rock samples, *in* Roehler H.W., eds, Geologic investigations of the Vermillion Creek coal bed in the Eocene Niland Tongue of the Wasatch Formation, Sweetwater County, Wyoming: U.S Geological Survey Professional Paper, 1314-F, p. 105-120.

Steidtmann, J.R., and Middleton, L.T., 1991, Fault chronology and uplift history of the southern Wind River Range, Wyoming: Implications for Laramide and post-Laramide deformation in the Rocky Mountain foreland: Geological Society of America Bulletin, v. 103, p. 472-485.

Stearns, D.W., 1971, Mechanisms of drape folding in the Wyoming province: Wyoming Geological Association, 23rd Annual Field Conference, Wyoming Tectonics Symposium, Guidebook, p. 82-106.

Stearns, D.W., 1978, Faulting and forced folding in the Rocky Mountains foreland, *in* Matthews, V., III, ed., Laramide folding associated with basement block faulting in the western United States: Memoir - Geological Society of America, i. 151, p. 1-37.

Stevens, T., 2002, Late Cenozoic tectonic and geomorphic framework surrounding the evaporite dissolution area in west-central Colorado: Special Paper - Geological Society of America, v. 366, p. 15-30.

Stilwell, D., 1990, Cretaceous stratigraphy of the eastern Green Riverr basin, Wyoming and Utah: AAPG Bulletin, v. 74, p. 1346.

Stone, D.S., 1969, Wrench faulting and Rocky Mountain tectonics: the Mountain Geologist, v. 6, n. 2, p. 67-79.

Stone, D.S., 1984, The Rattle Snake Mountain, Wyoming debate: a review and critique of models: Mountain Geologist, v. 21, p. 37-46.

Stone, D.S., 1986, Seismic and borehole evidence for important pre-Laramide faulting along the Axial arch in northwest Colorado, *in* Stone, D.S., ed., New interpretations of northwest Colorado geology: Rocky Mountain Association of Geologists, p. 5-16.

Stone, D.S, 1993, Basement-involved thrust-generated folds as seismically imaged in the subsurface of the central Rocky Mountain foreland: Special Paper - Geological Society of America, v. 280, p. 271-318.

Stone, D.S., 1995, Structure and kinematic genesis of the Quealy wrench duplex: transpressional reactivation of the Precambrian Cheyenne belt in the Laramie Basin, Wyoming: American Association of Petroleum Geologist Bulletin, v. 79, p. 1349-1376.

Stone, D.S., 2005, Structures of the Rocky Mountain foreland; Dutton Creek-Cooper Cove anticlinal complex, western Laramie Basin: Mountain Geologist, v. 42, n. 1, p. 35-39.

Thomas, C.R., McCann, F.T., and Ramon, N.D., 1945, Mesozoic and Paleozoic stratigraphy in northwestern Colorado and northeastern Utah: Oil and Gas Investigations Chart.

Tweto, O., 1979, Geologic Map of Colorado

Untermann, G.E., and Untermann, B.R., 1954, Geology of Dinosaur National Monument and vicinity, Utah-Colorado: Utah Geol. and Min. Survey Bull. v. 42, p. 1-213.

U.S Army Corps of Engineers, 2005, Corpscon v. 5.11.08: Geospatial Applications Branch, Topographic Engineering Center, U.S. Army Engineer Research and Development Center, crunch.tec.army.mil/software/corpscon/corpscon.html.

Van Loenen, R.E., Selner, G., and Bryant, A.W., 1999, Geologic Map Of The Lazy Y Point Quadrangle, Moffat County, Colorado: USGS.

Verbeek, E.R., and Grout, M.A., 1992, Structural evolution of gilsonite dikes, eastern Uinta Basin, Utah, *in* Fouch, T.D., Nuccio, V.F., and Chidsey, T.C., Jr, eds., Hydrocarbon and mineral resources of the Uinta Basin, Utah and Colorado: Utah Geological Association Guidebook 20, p. 237-255.

Verbeek, E.R., and Grout, M.A., 1997, Joint networks in reservoir rocks: case studies of prediction at depth, *in* Hoak, T.E., Klawitter, A.L., and Blomquist, P.K., eds., Fractured reservoirs: characterization and modeling. RMAG Guidebook, p. 115-129.

Vollmer, F.W., 1989, Orient v. 1.6 Orientation Data Analysis Program, Crestline Software, Department of Geological Sciences, State University of New York.

Weeks, F., 1907, Stratigraphy and structure of the Uinta Range: Geological Society of America Bulletin, v. 18, p. 427-448.

Weil, A.B., Geissman, J.B., Ashby, J.M., 2006, A new paleomagnetic pole for the Neoproterozoic Uinta Mountain supergroup, Central Rocky Mountain States, USA: Precambrian Research, v. 147, p. 234–259.

Weimer, R.J., 1960, Upper Cretaceous stratigraphy, Rocky Mountain area: AAPG Bulletin, v. 44, n. 1, p. 1-20.

Whalen, M.T., 1991, Oceanographic restriction and deposition of the Permian Park City and Phosphoria Formations, northeastern Utah and western Wyoming: AAPG Bulletin, v. 75.3, p. 692-692.

White, C.A., 1889, On the geology and physiography of a portion of northwestern Colorado and adjacent parts of Utah and Wyoming: 9th ann: Report of the U.S. Geol. Survey, p. 683-712.

Wise, D.V. and Obi, C.M., 1992, Laramide basement deformation in an evolving stress field, Bighorn Mountain front, Five Springs area, Wyoming: AAPG Bulletin, v. 78, n. 4, p. 652-655.

APPENDIX A: Descriptions of the map units for the Irish Canyon Quadrangle

The Irish Canyon quadrangle was mapped in entirety. See Plate 1 located in the envelope on the back cover of thesis. Thickness and descriptions were taken from (Manion, 1961). These observations were verified in the field. Descriptions of the map units are as follows:

Surficial Deposits

Qal - Quaternary Alluvial Deposits (Holocene) – Quaternary Alluvial Deposits consist of silt, sand, gravel, and the occasional boulder deposited in the Gilberts Peak erosional surface and in stream channels and flood planes along Vermillion Creek and its tributaries. Clasts are well-rounded to sub-rounded, pebble-sized clasts in a sandy, silty, clayey matrix. These unconsolidated deposits are mainly buff to gray and are easily eroded. Thicknesses vary throughout the area.

Tbp - Browns Park Formation (Miocene) - The Browns Park Formation consists of white to light-gray non-resistant sandstones, tufaceous sandstones, tuffs, and a basal conglomerate. These volcano-clastic deposits overly all older deposits with angular unconformity and are up to 400 m thick.

Tbc - Bishop Conglomerate (Oligocene) - The Bishop Conglomerate is the basal unit of the Browns Park Formation. This course basal conglomerate consists primarily of clasts from the Uinta Mountain Group, but occasionally contains clasts of the Madison Limestone. These well-rounded clasts range from pebble to boulder size. These deposits range in thickness from 7 to 10 m in thickness.

Eun - Eocene, undivided (Eocene) - Consist of the interbedded sandstone and shales of the Green River Formation and the Wasatch Formation. These formations are difficult to differentiate and were not separated.

> **Green River Formation (Upper Eocene) -** Gray fissile shales and oil shales with occasional gray sandstones and limestones. This unit is in gradational contact with the underlying Wasatch Formation. These deposits range in thickness from 152 m to 360 m.
>
> **Wasatch Formation (Lower Eocene) -** The Wasatch formation consists of multi-colored clay shales interbedded with gray, tan, and red sandstones and occasional conglomerate and coal beds. The shales range in color from red, gray, yellow, and buff. These deposits range in thickness from 914 m to 2743 m.

Kmv - Mesaverde Group (Upper Cretaceous) - Resistant to moderately resistant light to medium brown, tan, orange, and gray lenses of sandstone, clay, shale, carbonaceous shale, and coal. These deposits range in thickness from 525 m to 690 m.

Kmc - Mancos Shale (Upper Cretaceous) - Interbedded gray, dark-gray, and light bluish-gray locally fossiliferous marine shales and brown, rust colored, and gray medium-grained sandstones. These deposits range in thickness from 1220 m to 1825 m.

Kf - Frontier Formation (Upper Cretaceous) - Resistant, fine-grained white, yellow, and tan marine sandstones with interbedded carbonaceous shale and coal of continental origin. The sandstones are locally cross-bedded and fossiliferous. These deposits range in thickness from 53 m to 76 m.

Km - Mowry Formation (Lower Cretaceous) - Soft, silver and bluish-gray to black thinly bedded siliceous marine shale containing fish scales and thin layers of bentonite. These deposits range in thickness from 18 m to 50 m.

Kd - Dakota Formation (Lower Cretaceous)- Resistant, white, light gray, yellow, tan, and rust colored cross-bedded fluvial sandstone with a basal pebble conglomerate and thin layers of shale and coal. These deposits range in thickness from 18 m to 54 m.

Jm - Morrison Formation (Upper Jurassic) - Green, gray-green, tan, red, light-purple, and violet calcareous shales, siltstones, and massive, clean, white, cross-bedded, calcareous sandstones interbedded with red calcareous siltstones and bentonite. Mainly of fluvial origin. These deposits range in thickness from 165 m to 198 m.

Jc - Curtis Formation (Jurassic) - Gray, dark-gray, and black shales with overlying light-gray calcareous, oolitic and crystalline limestone. Brachiopods and pelecypods are abundant. These deposits are up to 42 m in thickness. These deposits range in thickness from 10 m to 42 m.

Jec - Carmel-Entrada Formations, Undivided (Jurassic) - Due to the limited thicknesses of these units they are not mappable separately and thus were grouped.

> **Entrada (Jurassic) -** White, tan, and light rust-colored, massive, cross-bedded, quartz arenite and a layer of thin, dark-red, very fine-grained sandstone. These deposits range in thickness from 27 m to 45 m.
>
> **Carmel (Jurassic) -** Non-resistant, tan, light-gray and dark-red calcareous sandy shales and siltstones. These deposits range in thickness from 0 m to 15 m.

Trn - Navajo Sandstone (Lower Jurassic Upper Triassic) - Resistant, fine to medium-grained white, light-gray, and rust-colored, cross-bedded eolian sandstones. Also referred to as the Glen Canyon or the Nugget formation. These deposits range in thickness from 152 m to 305 m.

Trc - Chinle Formation (Upper Triassic) - Soft to medium-resistant, light-gray, light-green, purple, medium to dark-red siltstone, sandstone, shale, conglomerate, and claystone of mainly fluvial and lacustrine origin. The basal Gartra Grit member consists of light-yellow, light-gray, or pink cross-bedded sandstone and conglomerate of fluvial origin. These deposits range in thickness from 100 m to 107 m.

Trw - Woodside Formation (Triassic) - Tan and gray, fine- to very fine-grained sandstone and siltstones with interbedded gypsum and gray to gray-green shales. These deposits range in thickness from 152 m to 395 m.

Ppc - Park City Formation (Lower Permian)- Grey calcareous limestone, tan shaly sandstone, calcareous sandstone, and interbedded light- to dark-gray limestones, cherts, and sandstones. Marine in origin. Shaley units contain concretions of marcasite. The Park City caps the Weber Sandstone. These deposits range in thickness from 38 m to 83 m.

Pw - Weber Formation (Permian-Pennsylvanian) - Resistant, white, tan, and rust-colored fine to medium-grained calcareous, massive, cross-bedded quartz arenite. These deposits in thickness are up to 200 m in thickness.

Pm - Morgan Formation (Middle Pennsylvanian) - White and tan fine to medium fine-grained sugary sandstones with thin laminations of shale and limestone. The basal Molas member consists of white and rust-colored quartz arenite with thin layers of dark-brown and black carbonaceous shales and coal. These deposits range in thickness from 195 m to 200 m.

Mm - Madison Limestone (Mississippian) - Resistant, thin to massive-bedded light to dark gray, dense crystalline limestones, occasionally dolomitic and cherty. These deposits range in thickness from 152 m to 305 m.

Cl - Lodore Formation (Upper Cambrian) - White to red medium to coarse-grained sugary sandstones with interspersed, purple, thin beds of muscovite rich calcareous shale and siltstone. These deposits range in thickness from 0 m to 10’s of m.

Yu - Uinta Mountain Group (Precambrian)- Resistant, purple to dark-red, medium to coarse-grained, siliceous, massive sandstones. Red color is due to ferric iron staining. These deposits range in thickness from 4 km to 7 km.

APPENDIX B: Minor Fault Data, Stereonets and Explanation

List of Appendices and key to abbreviations and methods

Raw Data

Data Restored to Pre-Fold Orientation (Rotated 40 degrees SW about a N30W axis.)

B-35: Stereonets of Fault Planes, Slickenlines, and Ideal σ_1 Separated by Slip-sense (Restored to Pre-Fold Orientation)
B-36: Full Fault Data Set Restored to Pre-Fold Orientation
B-37: Stereonets and Rose Diagrams of Thrust Fault Data
B-38: Stereonets and Rose Diagrams of Left-Lateral Fault Data
B-39: Stereonets and Rose Diagrams of Right-Lateral Fault Data
B-40: Stereonets and Rose Diagrams of Normal Fault Data
B-41: Rose Diagrams of Slickenline Trends Separated by Slip-Sense and Restored to Pre-Fold Orientation
B-42: Rose Diagrams of Ideal σ_1Trends Separated by Slip-Sense and Restored to Pre-Fold Orientation
B-43: Stereonets and Rose Diagrams of Minor Fault Planes Restored to Pre-Fold Orientation and Separated by Slip-Sense
B-44: Stereonets and Rose Diagrams of Minor Faults Restored to Pre-Fold Orientation and Separated by Slip-Sense
B-45: Rose Diagrams of Ideal σ_1 Trends Restored to Pre-Fold Orientation and Subdivided by Station.
B-46: Rose Diagrams of Ideal σ_1 Trends Restored to Pre-Fold Orientation and Separated by Station, Unit, and Location.
B-47: Rose Diagrams of Ideal σ_1 Trends within the Pre-orogenic Strata Separated by Station and Slip-sense (Restored to Pre-Fold Orientation).

For full formation names see Appendix A. The full names for the abbreviated formations listed in the data table below are as follows: Ppc-Permian Park City Formation, Trn-Triassic Navajo Sandstone, Jc-Jurassic Curtis Formation, Kd-Cretaceous Dakota Formation.

The ideal σ_1 corresponds to the orientation of the maximum compressional stress and is found using the ideal σ_1 method of Compton (1966). Compton's method assumes σ_1 is on the plane perpendicular to a slickensided fault plane and that an angle α (set equal to 25 degrees for preliminary data shown in B-1 through B-33 and set equal to 20 degrees for final data shown in B-34 through B-46) lies between the fault plane and the σ_1 axis.

An Eigen Vector analysis of slickenlines represents the slip direction during deformation. The first Eigen Vector corresponds to the trend and plunge of the maximum shortening direction. An Eigen Value 1.0 represents a data set with zero dispersion of values and as the value approaches zero, the dispersion increases.

The vector mean is the average vector calculated from a data set. This is a 2D analyses of trends only, not plunges. A dispersion value of 0 equals no dispersion and a dispersion value of 1.0 equals 100 percent dispersion.

Digital minor fault data available in excel format from:
Eric Erslev
Department of Geosciences
Colorado State University
Fort Collins, CO 80523
erslev@warnercnr.colostate.edu

Appendix B-1: Tables showing all minor fault data. See previous page for key of abbreviations and methods.

Local-ity	Form-ation	Bedding Strike/ Dip	UTM Easting	UTM Northing	n=	Slickenline Vector Mean Dispersion	Slickenline Eigen Value/ Eigen Vector	Ideal σ1 Vector Mean Dispersion	Ideal σ1 (a=25) Eigen Value/Eigen Vector
1	Ppc	321-47	691238	4522531	18	29.53/.1746	E1=.7554/030-10	22.66/.2289	E1=.8076/023-24
							E2=.1809/169-77		E2=.1181/130-33
							E3=.0637/298-8		E3=.0743/265-47
2	Ppc	321-47	690976	4522779	24	21.71/.1515	E1=.7996/020-44	19.46/.204	E1=.8879/019-33
							E2=.1649/180-44		E2=.0885/121-18
							E3=.0355/280-10		E3=.0236/235-51
3	Jc	341-46	690479	4525775	33	343.74/.2828	E1=.6913/342-1	354.43/.2551	E1=.8161/353-9
							E2=.2254/073-63		E2=.126/093-45
							E3=.0833/252-27		E3=.0579/255-43
4	Jc	354-51	690534	4525657	23	333.74/.3695	E1=.7903/154-17	340.38/.1237	E1=.9049/161-0
							E2=.1688/062-9		E2=.0599/071-20
							E3=.0409/305-71		E3=.0352/251-70
5	Kd	350-53	690853	4525714	79	61.25/.1558	E1=.8453/061-41	49.47/.2986	E1=.844/049-36
							E2=.1126/238-49		E2=.084/149-10
							E3=.0422/330-2		E3=.072/250-52
6	Kd	348-52	691651	4524141	130	51.93/.6145	E1=.8142/045-48	48.86/.1446	E1=.8895/048-41
							E2=.1211/307-7		E2=.0638/241-48
							E3=.0647/211-41		E3=.0467/144-6
7	Kd	347-41	691825	4523902	21	51.93/.6145	E1=.8259/050-51	43.08/.1585	E1=.9421/043-47
							E2=.1489/140-0		E2=.041/153-18
							E3=.0252/230-39		E3=.0169/257-38
8	Kd	327-49	692000	4523000	24	29.34/.2117	E1=.9121/030-48	31.16/.0853	E1=.9369/031-32
							E2=.0579/291-7		E2=.0346/269-41
							E3=.0299/195-41		E3=.0265/145-33
9	Trn	328-40	694599	4518955	49	345.22/.1961	E1=..8336/345-9	359.33/.1355	E1=.8588/179-12
							E2=.1039/084-48		E2=.082/053-70
							E3=.0625/247-41		E3=.0592/272-16
11	Kd	326-49	692790	4522823	65	.31/.3859	E1=.8173/004-35	21.48/.3228	E1=.864/034-42
							E2=.1455/111-23		E2=.1061/128-4
							E3=.0372/227-46		E3=.0299/222-48
12	Kd	306-46	692484	4523091	185	359.87/4375	E1=.7922/359-33	25.3/.4084	E1=.8269/026-39
							E2=.1786/104-22		E2=.1474/120-4
							E3=.0291/221-49		E3=.0257/215-51
13	Jc	324-50	692038	4523178	20	316.56/.6917	E1=.5958/133-5	358.63/.5157	E1=.7268/357-24
							E2=.3745/039-38		E2=.2432/100-26
							E3=.0297/229-51		E3=.03/231-54
14	Jc	335-30	694510	4520340	26	18.36/.1947	E1=.9013/018-30	25.18/.1791	E1=.8878/025-5
							E2=.0855/122-22		E2=.098/117-23
							E3=.0132/242-51		E3=.0142/283-67
15	Kd	353-38	Variable	Variable	25	5.53/.3079	E1=.7591/181-3	354.13/.4442	E1=.7552/353-12
							E2=.2105/086-80		E2=.1996/088-20
							E3=.0303/273-30		E3=.0453/234-67
Full Data Set	Variable	Variable	Variable	Variable	722	15.18/.6121	E1=.6667/017-37	28.58/.4357	E1=.7414/029-34
							E2=.2572/126-23		E2=.192/135-23
							E3=.0761/241-44		E3=.0665/252-47

Appendix B-2: Irish Canyon Fault Station 1

Fault Planes

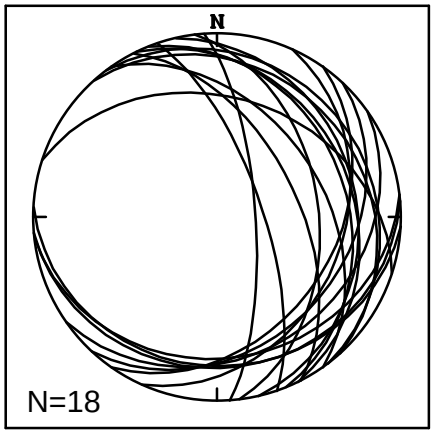

Slickenlines

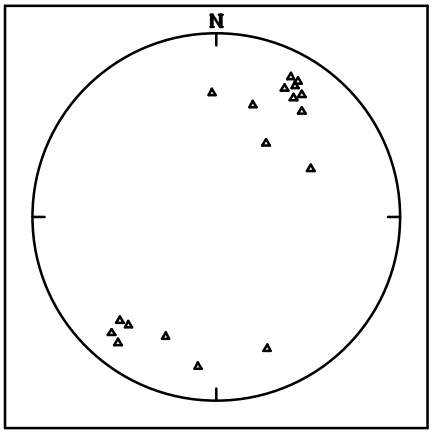

Ideal Sigma One

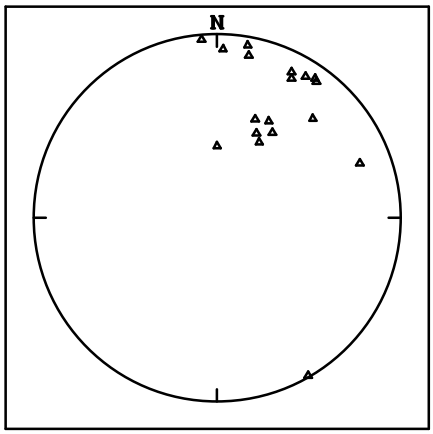

Rose Diagram of Ideal Sigma One Trends

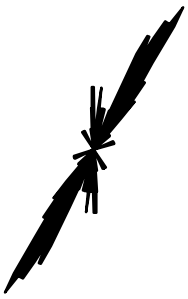

Stereonets of fault planes, slickenlines, ideal sigma one data, and rose diagram of ideal sigma one trends. Stereonets containing data sets of 50 points or more have a contour interval of 2 and rose diagrams have a smoothing increment of 10 degrees.

Appendix B-3: Irish Canyon Fault Station 2

Fault Planes

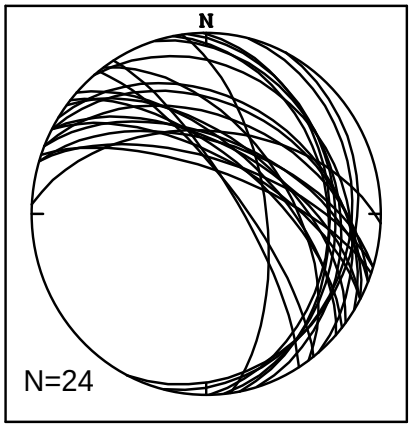

Slickenlines

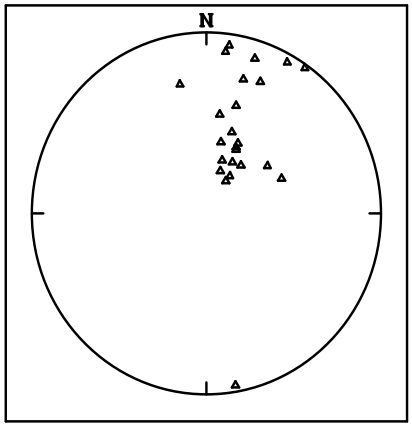

Ideal Sigma One

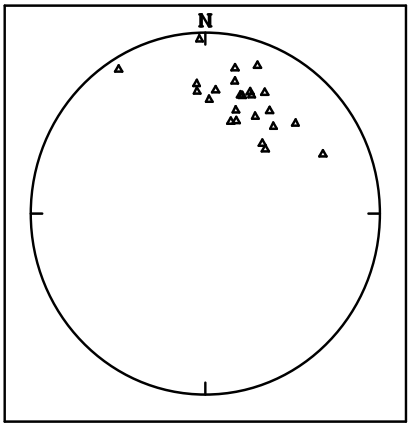

Rose Diagram of Ideal Sigma One Trends

Stereonets of fault planes, slickenlines, ideal sigma one data, and rose diagram of ideal sigma one trends. Stereonets containing data sets of 50 points or more have a contour interval of 2 and rose diagrams have a smoothing increment of 10 degrees.

Appendix B-4: Irish Canyon Fault Station 3

Fault Planes

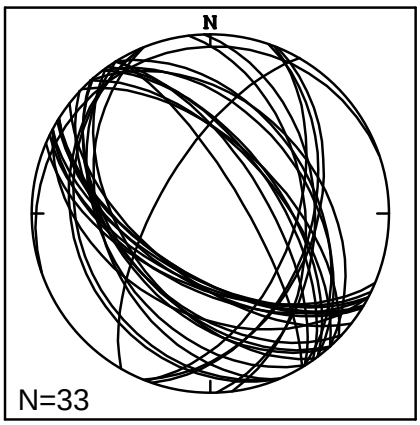

Slickenlines

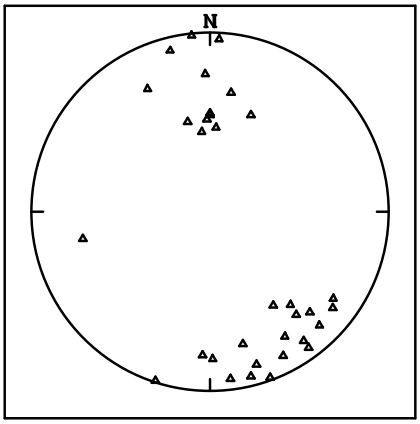

Ideal Sigma One

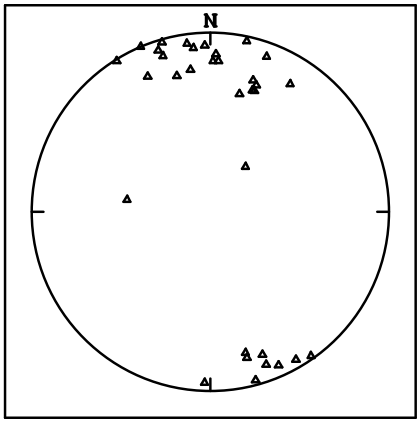

Rose Diagram of Ideal Sigma One Trends

Stereonets of fault planes, slickenlines, ideal sigma one data, and rose diagram of ideal sigma one trends. Stereonets containing data sets of 50 points or more have a contour interval of 2 and rose diagrams have a smoothing increment of 10 degrees.

Appendix B-5: Irish Canyon Fault Station 4

Fault Planes

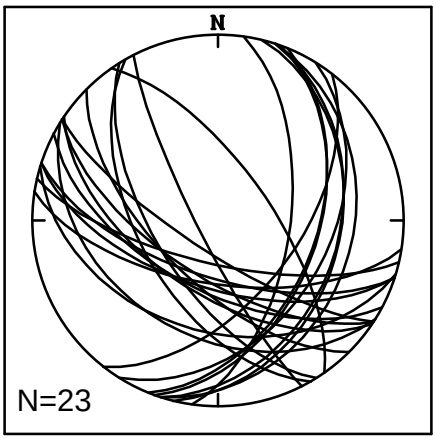

Slickenlines

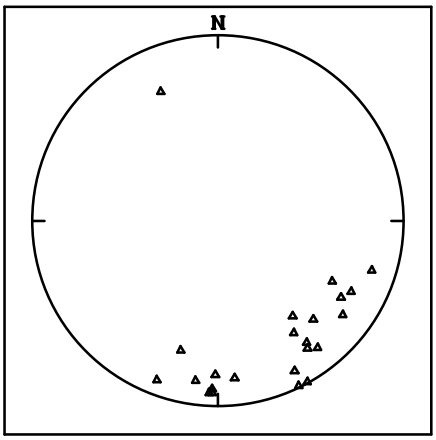

Ideal Sigma One

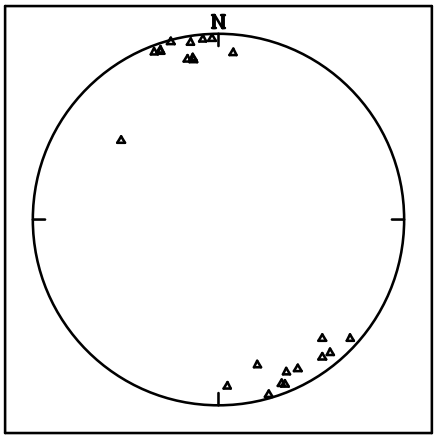

Rose Diagram of Ideal Sigma One Trends

Stereonets of fault planes, slickenlines, ideal sigma one data, and rose diagram of ideal sigma one trends. Stereonets containing data sets of 50 points or more have a contour interval of 2 and rose diagrams have a smoothing increment of 10 degrees.

Appendix B-6: Irish Canyon Fault Station 5

Fault Planes

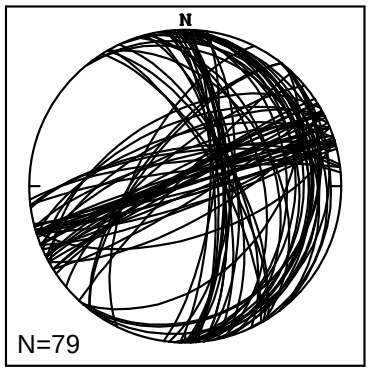

Poles to Fault Planes

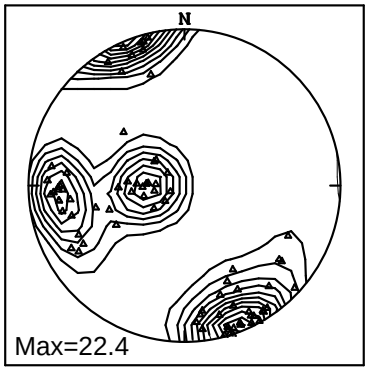

Slickenlines

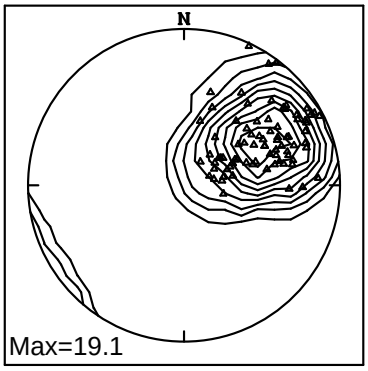

Ideal Sigma One

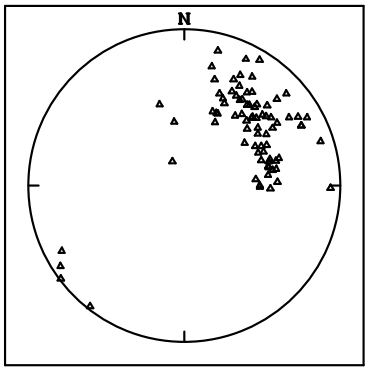

Ideal Sigma One

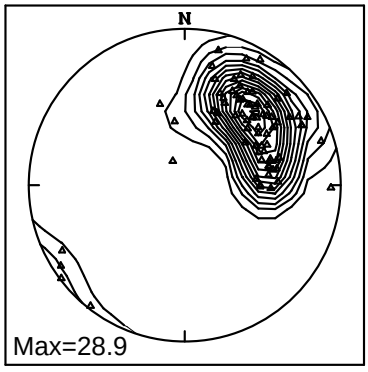

Rose Plot of Ideal Sigma One Trends

Stereonets of fault planes, poles to fault planes, slickenlines, ideal sigma one data, and rose diagram of ideal sigma one trends. Stereonets containing data sets of 50 points or more have a contour interval of 2 and rose diagrams have a smoothing increment of 10 degrees.

Appendix B-7: Irish Canyon Fault Station 6

Fault Planes

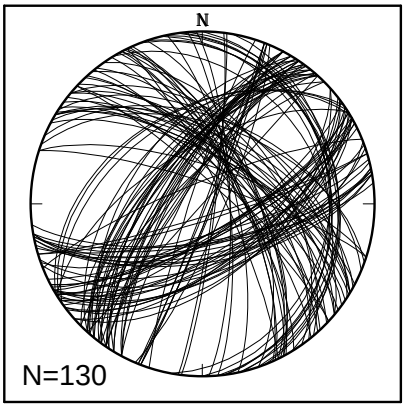

Poles to Fault Planes

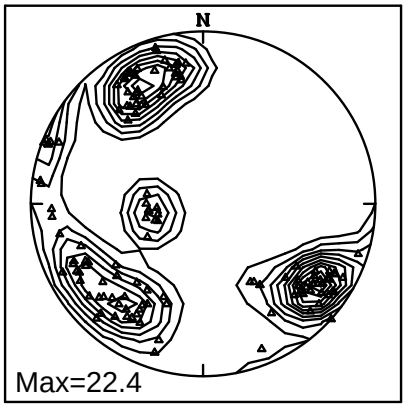

Slickenlines

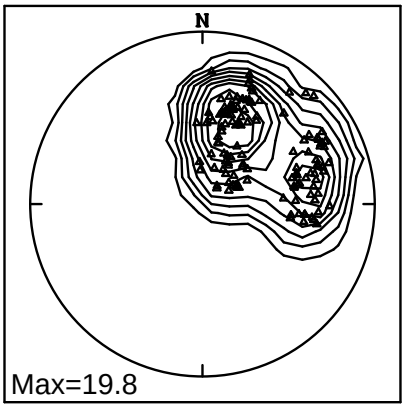

Ideal Sigma One

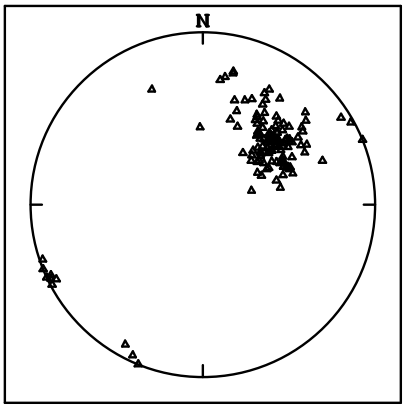

Ideal Sigma One

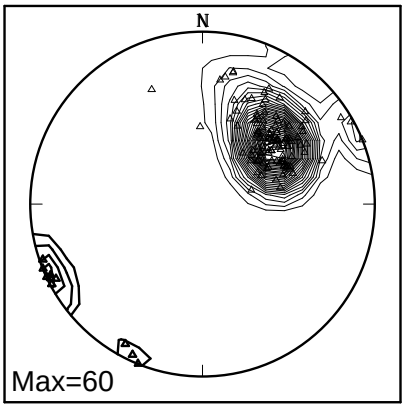

Rose Diagram of Ideal Sigma One Trends

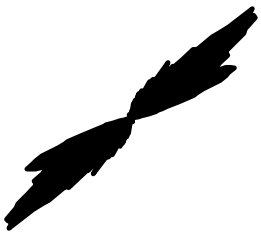

Stereonets of fault planes, poles to fault planes, slickenlines, ideal sigma one data, and rose diagram of ideal sigma one trends. Stereonets containing data sets of 50 points or more have a contour interval of 2 and rose diagrams have a smoothing increment of 10 degrees.

Appendix B-8: Irish Canyon Fault Station 7

Fault Planes

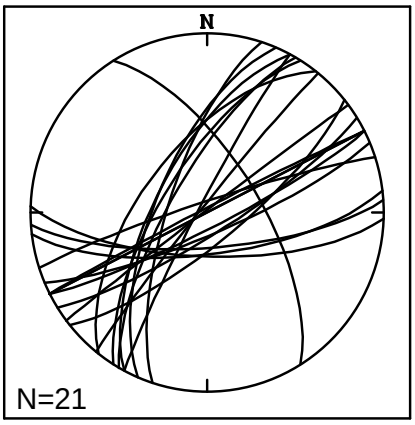

Slickenlines

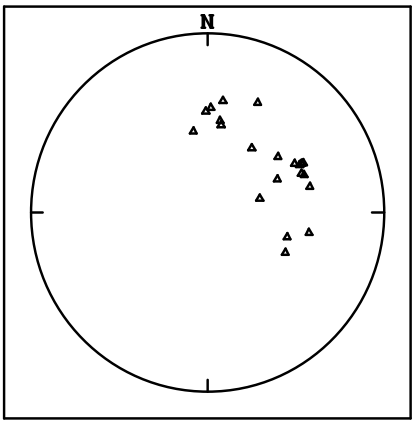

Ideal Sigma One

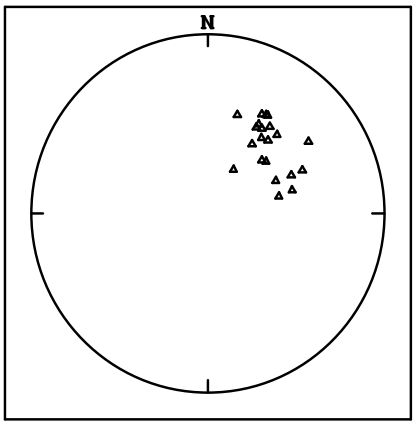

Rose Diagram of Ideal Sigma One

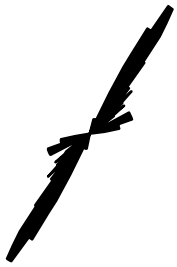

Stereonets of fault planes, slickenlines, ideal sigma one data, and rose diagram of ideal sigma one trends. Stereonets containing data sets of 50 points or more have a contour interval of 2 and rose diagrams have a smoothing increment of 10 degrees.

Appendix B-9: Irish Canyon Fault Station 8

Fault Planes

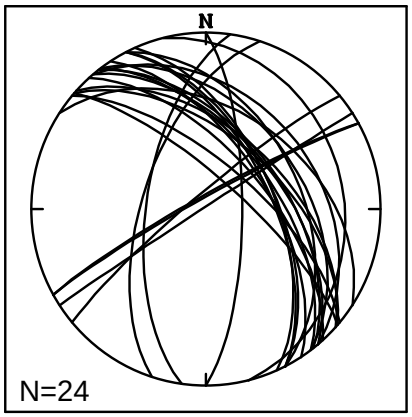

Slickenlines

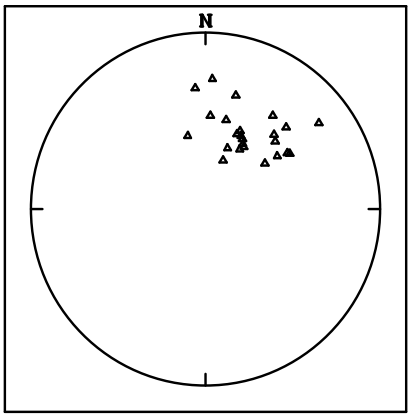

Ideal Sigma One

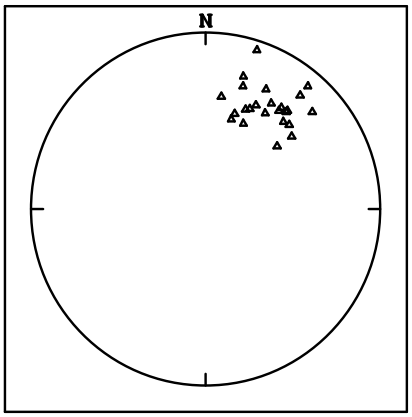

Rose Diagram of Ideal Sigma One Trends

Stereonets of fault planes, slickenlines, ideal sigma one data, and rose diagram of ideal sigma one trends. Stereonets containing data sets of 50 points or more have a contour interval of 2 and rose diagrams have a smoothing increment of 10 degrees.

Appendix B-10: Irish Canyon Fault Station 9

Fault Planes

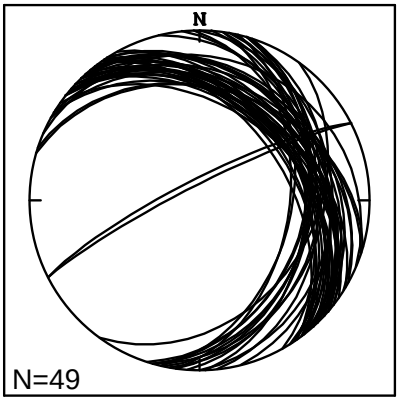

Poles to Fault Planes

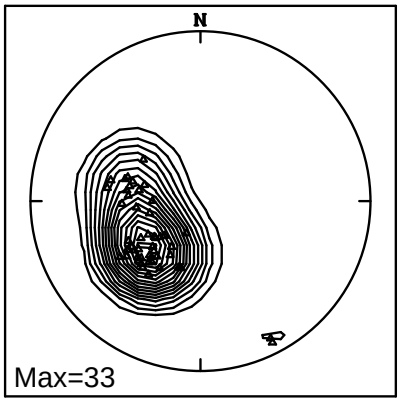

Slickenlines

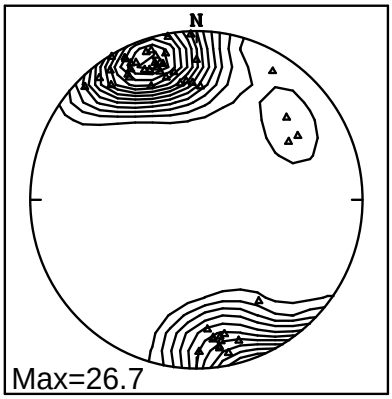

Ideal Sigma One

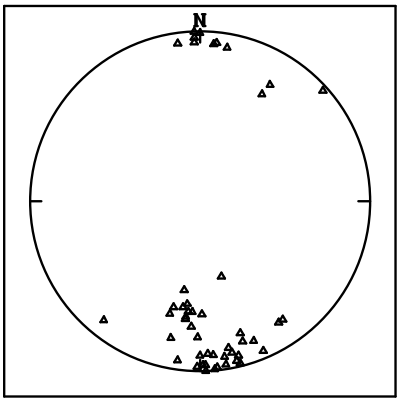

Ideal Sigma One

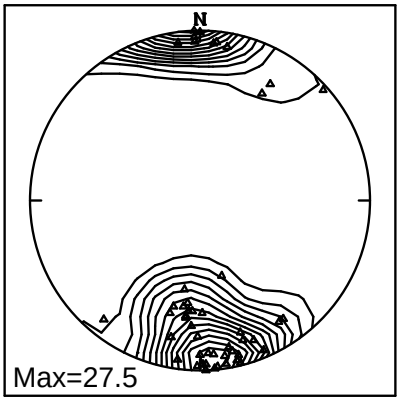

Rose Diagram of
Ideal Sigma One

Stereonets of fault planes, poles to fault planes, slickenlines, ideal sigma one data, and rose diagram of ideal sigma one trends. Stereonets containing data sets of 50 points or more have a contour interval of 2 and rose diagrams have a smoothing increment of 10 degrees.

Appendix B-11: Irish Canyon Fault Station 11

Fault Planes

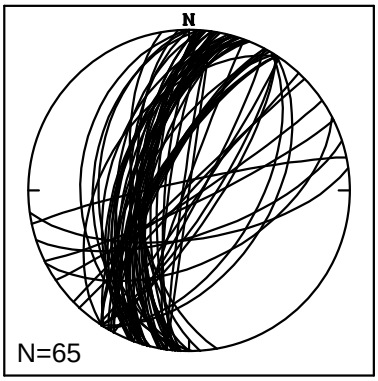

Poles to Fault Planes

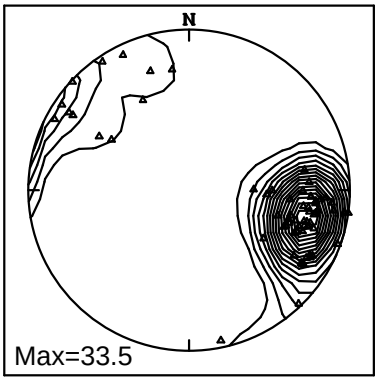

Slickenlines

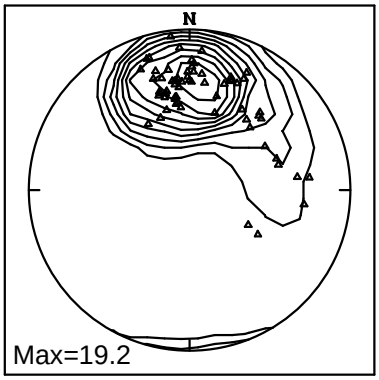

Ideal Sigma One

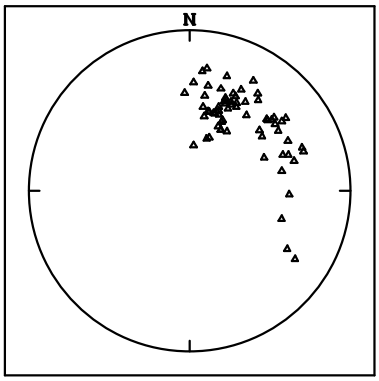

Ideal Sigma One

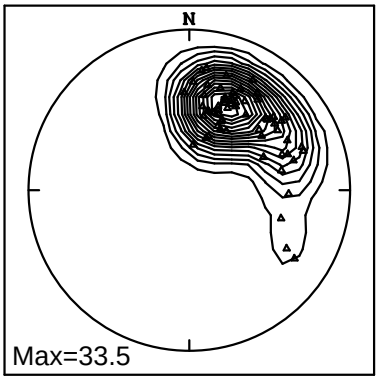

Rose Diagram of Ideal Sigma One Trends

Stereonets of fault planes, poles to fault planes, slickenlines, ideal sigma one data, and rose diagram of ideal sigma one trends. Stereonets containing data sets of 50 points or more have a contour interval of 2 and rose diagrams have a smoothing increment of 10 degrees.

Appendix B-12: Irish Canyon Fault Station 12

Fault Planes

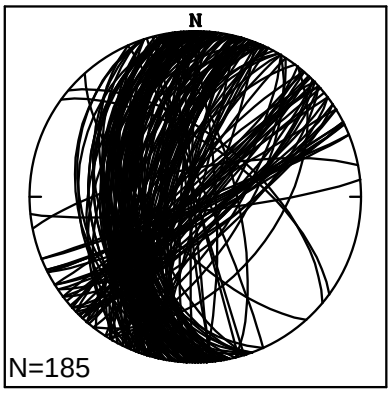

Poles to Fault Planes

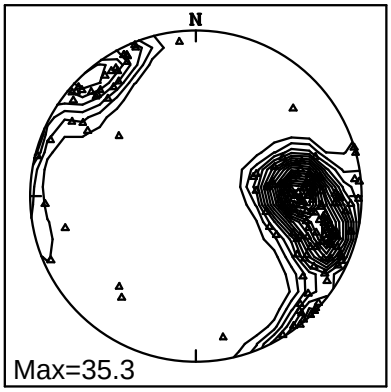

Slickenlines

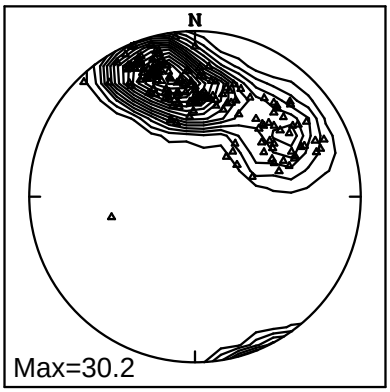

Ideal Sigma One

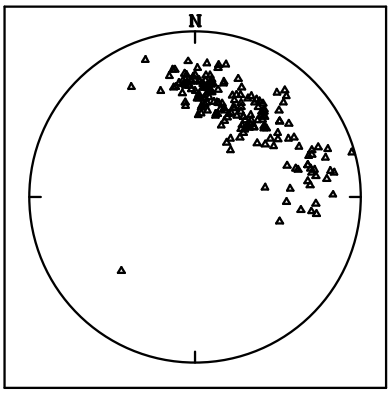

Ideal Sigma One

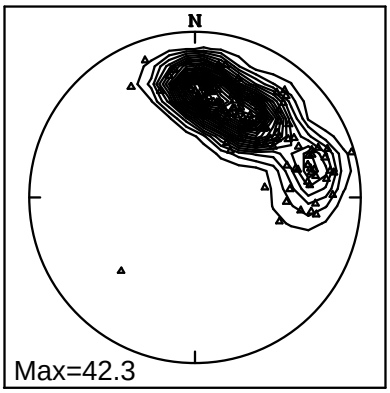

Rose Digram of
Ideal Sigma One Trends

Stereonets of fault planes, poles to fault planes, slickenlines, ideal sigma one data, and rose diagram of ideal sigma one trends. Stereonets containing data sets of 50 points or more have a contour interval of 2 and rose diagrams have a smoothing increment of 10 degrees.

Appendix B-13: Irish Canyon Fault Station 13

Fault Planes

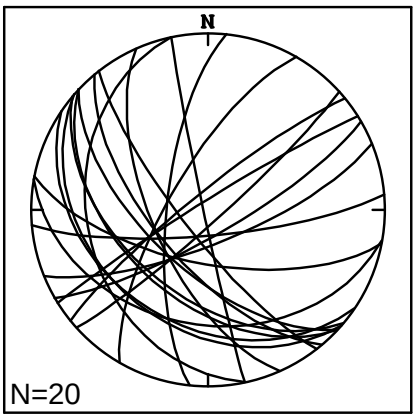

Slickenlines

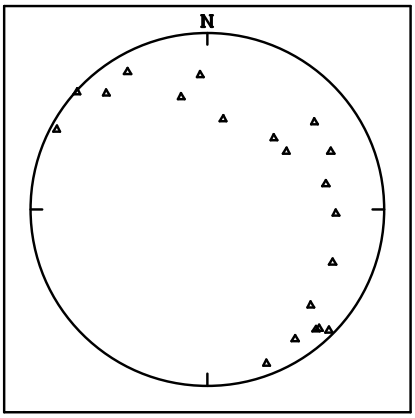

Ideal Sigma One

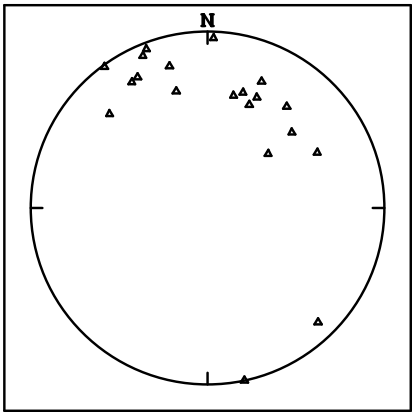

Rose Diagram of
Ideal Sigma One Trends

Stereonets of fault planes, slickenlines, ideal sigma one data, and rose diagram of ideal sigma one trends. Stereonets containing data sets of 50 points or more have a contour interval of 2 and rose diagrams have a smoothing increment of 10 degrees.

Appendix B-14: Irish Canyon Fault Station 14

Fault Planes

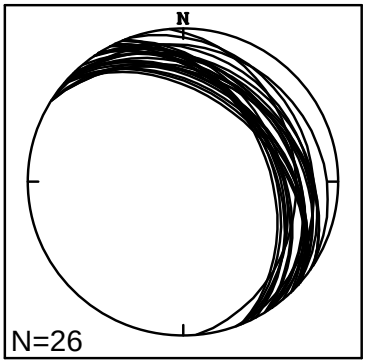

Slickenlines

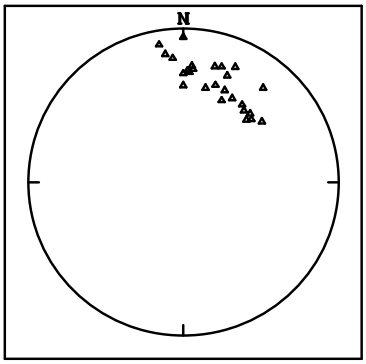

Ideal Sigma One

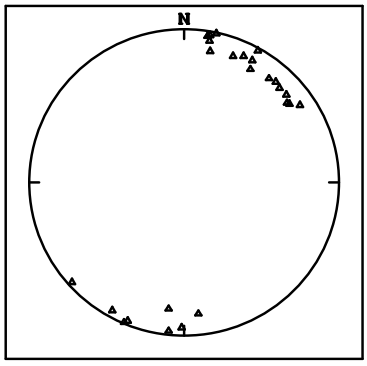

Rose Diagram of
Ideal Sigma One Trends

Stereonets of fault planes, slickenlines, ideal sigma one data, and rose diagram of ideal sigma one trends. Stereonets containing data sets of 50 points or more have a contour interval of 2 and rose diagrams have a smoothing increment of 10 degrees.

Appendix B-15: Irish Canyon Fault Station 15

Fault Planes

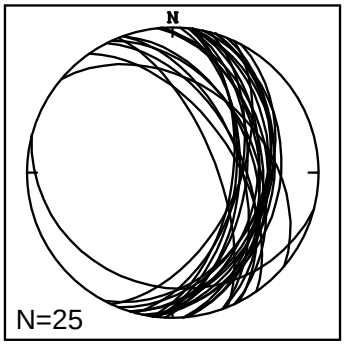

Slickenlines

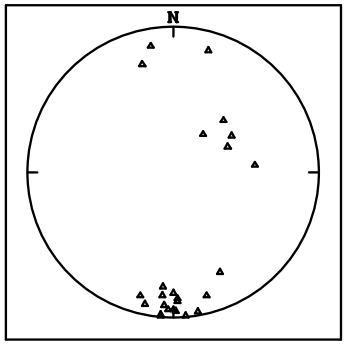

Ideal Sigma One

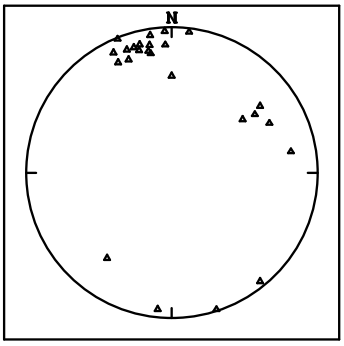

Rose Diagram of
Ideal Sigma One Trends

Stereonets of fault planes, slickenlines, ideal sigma one data, and rose diagram of ideal sigma one trends. Stereonets containing data sets of 50 points or more have a contour interval of 2 and rose diagrams have a smoothing increment of 10 degrees.

Appendix B-16: Irish Canyon Fault Stations 1-15

Fault Planes

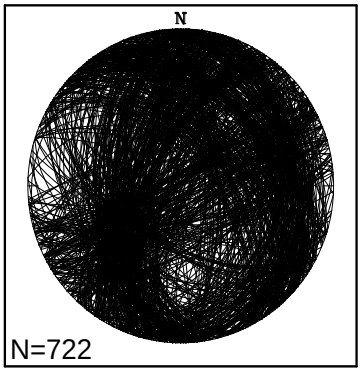

Poles to Fault Planes

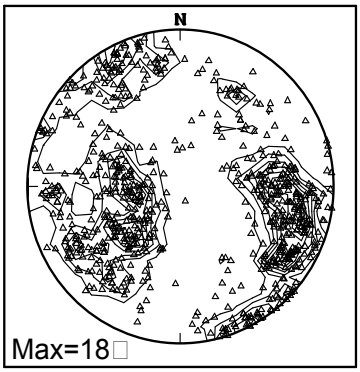

Slickenlines

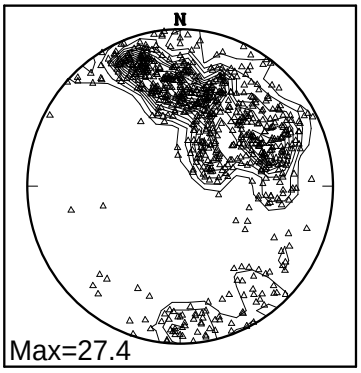

Ideal Sigma One

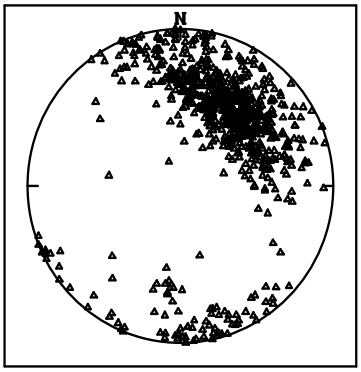

Ideal Sigma One

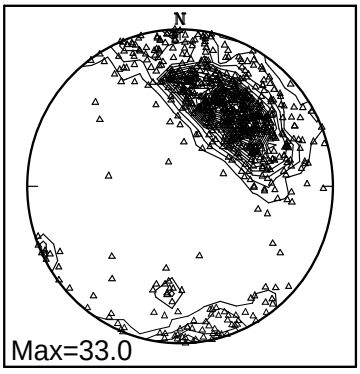

Rose Diagrams of
Ideal Sigma One Trend

Stereonets of fault planes, poles to fault planes, slickenlines, ideal sigma one data, and rose diagram of ideal sigma one trends. Stereonets containing data sets of 50 points or more have a contour interval of 2 and rose diagrams have a smoothing increment of 10 degrees.

Appendix B-17: Rose Diagrams of Slickenline Trends for Fault Stations 1-15
(Smoothing increment of 10 degrees)

FS-1

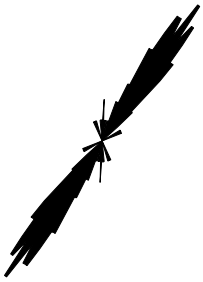

FS-2

FS-3

FS-4

FS-5

FS-6

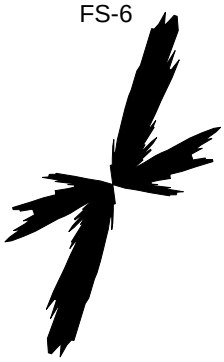

FS-7

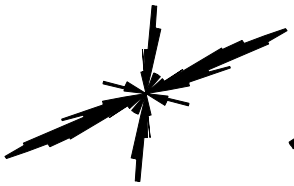

FS-8

FS-9

FS-11

FS-12

FS-13

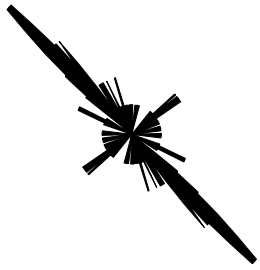

FS-14

FS-15

FS1-15

Appendix B-18: Rose Diagrams of Ideal Sigma One Trends for Fault Stations 1-15
(Smoothing increment of 10 degrees)

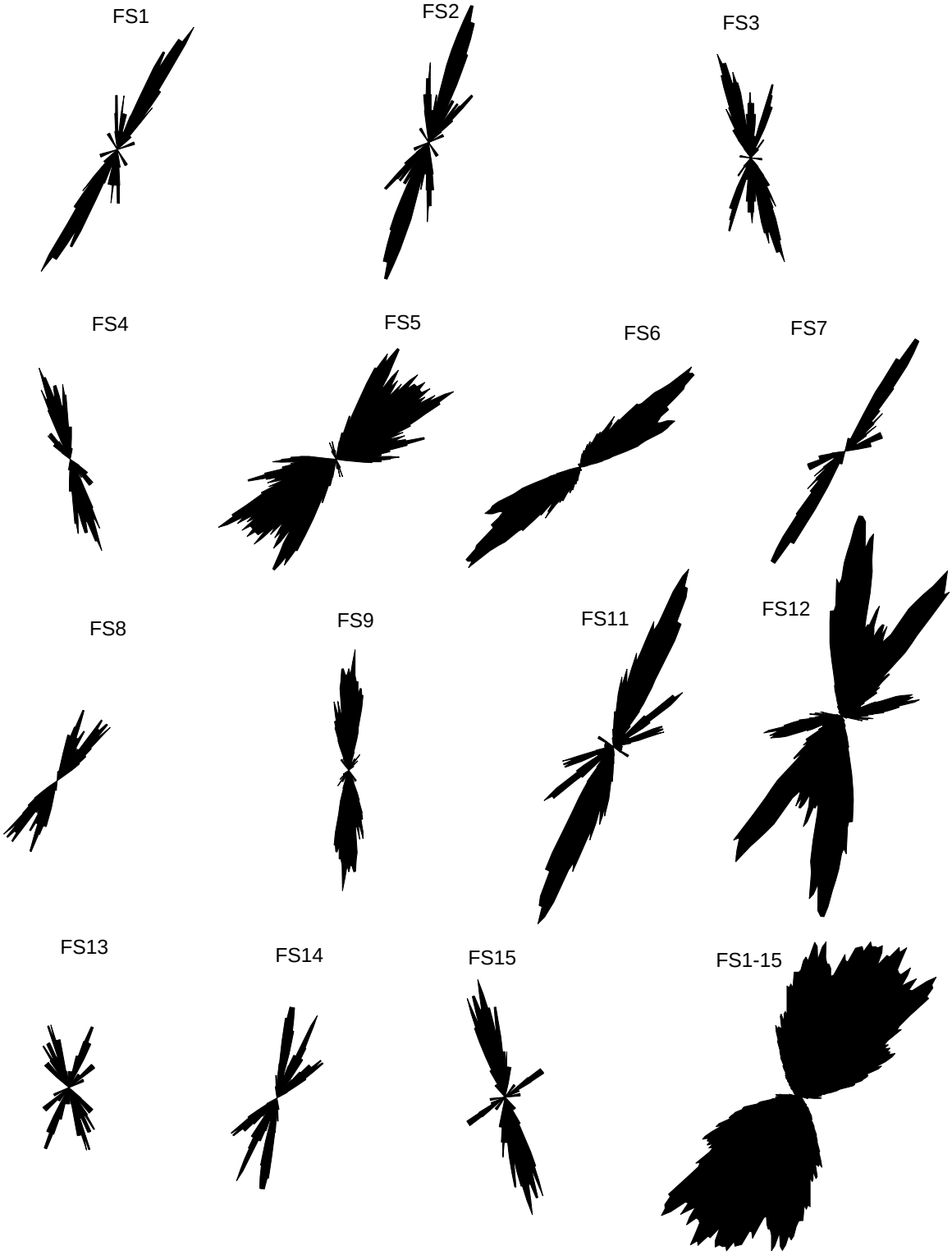

Appendix B-19: Rose Diagrams of Ideal Sigma One Trends for Fault Stations 1-15
Subdivided by Slip-Sense (Smoothing increment of 10 degrees)

Thrust Faults

Left-Lateral Faults

Right-Lateral Faults

Normal Faults

Full Data Set

Appendix B-20: Fault Planes and Poles to Fault Planes Divided by Slip-Sense

Thrust Faults

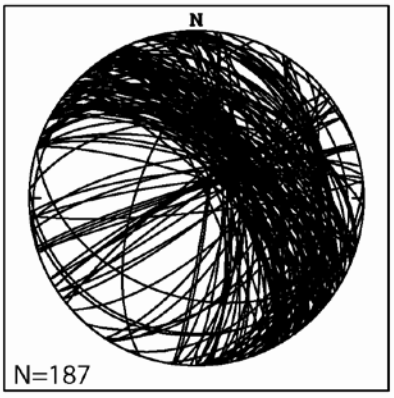

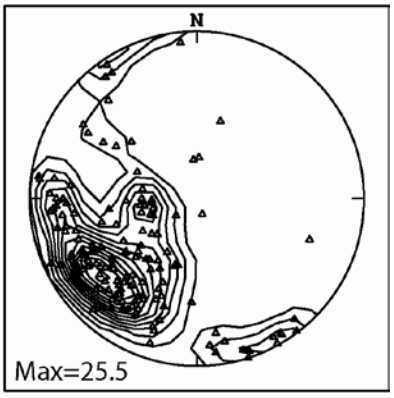

Left-Lateral Faults

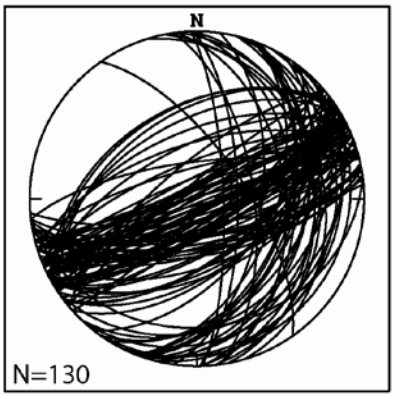

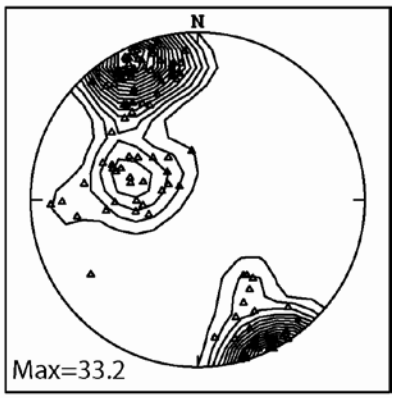

Right-Lateral Faults

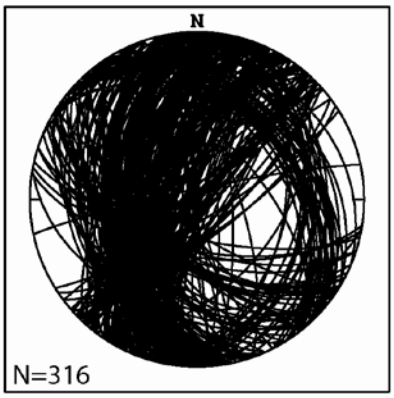

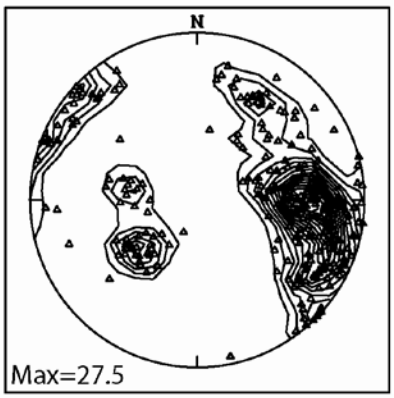

Normal Faults

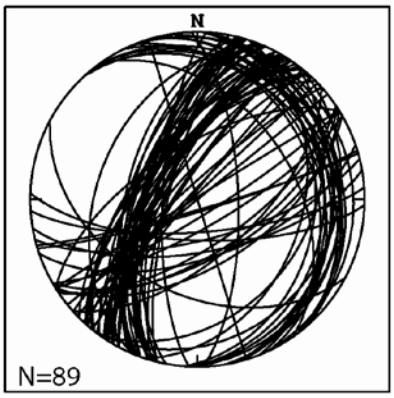

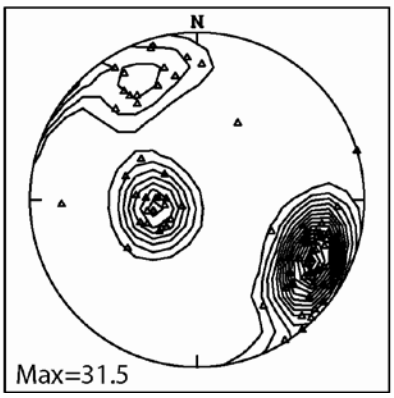

Appendix B-21: Stereonets of Thrust Fault Planes by Station

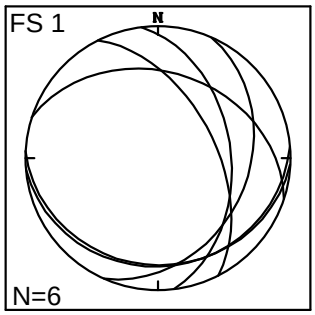

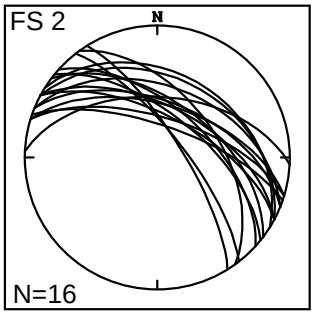

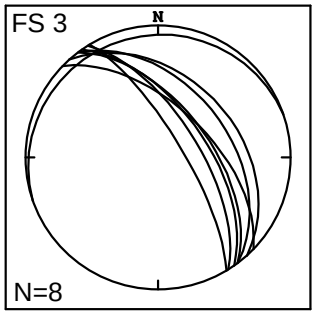

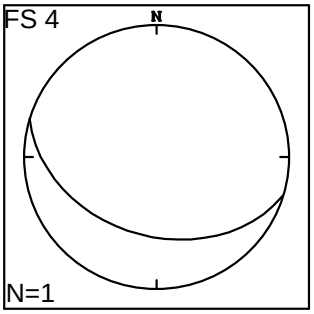

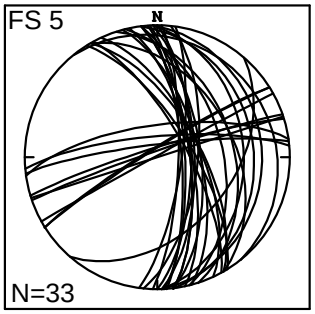

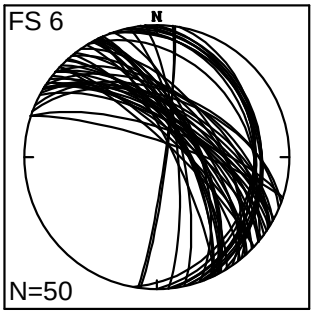

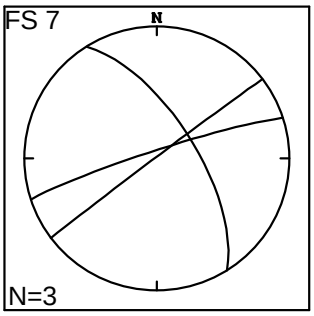

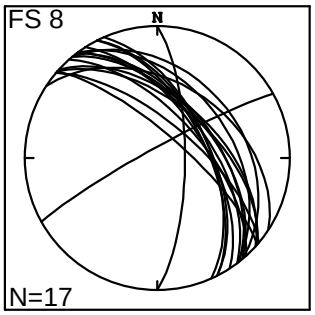

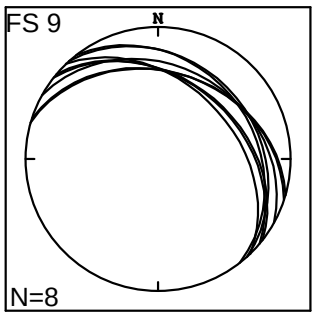

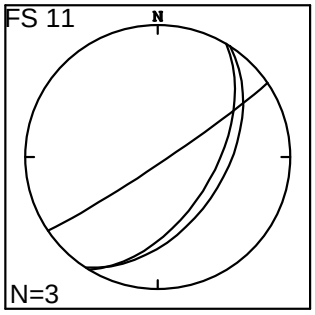

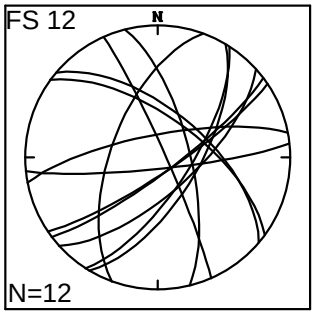

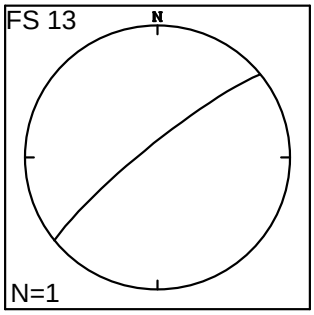

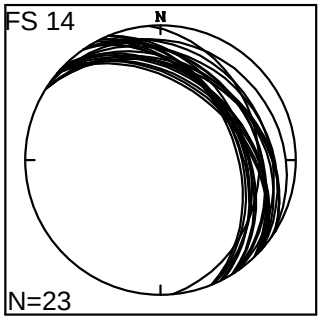

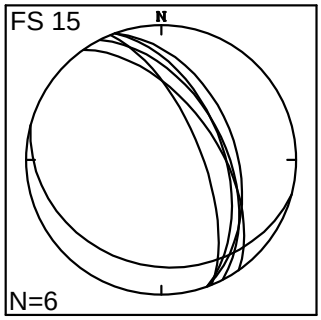

Appendix B-22: Stereonets of Thrust Fault Slickenlines by Station

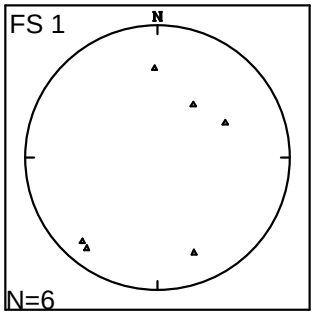

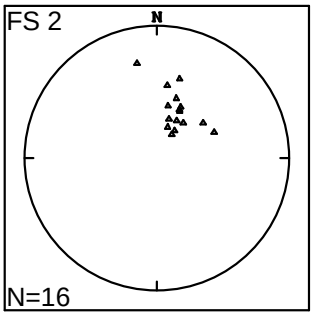

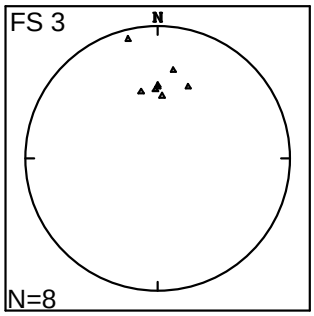

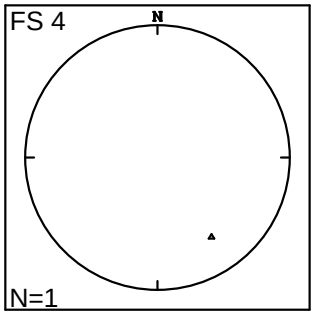

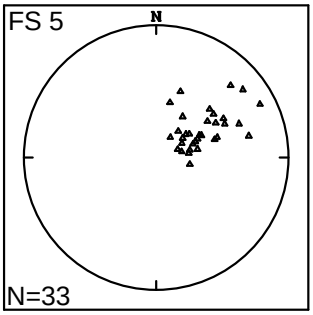

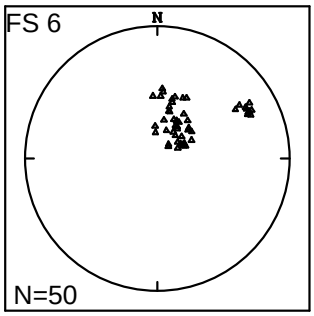

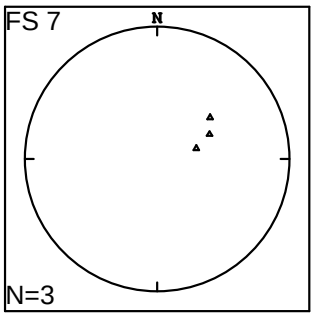

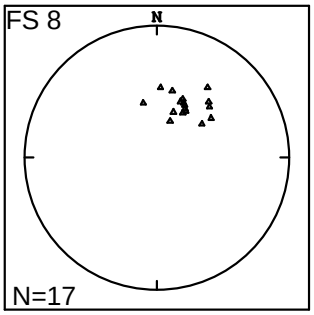

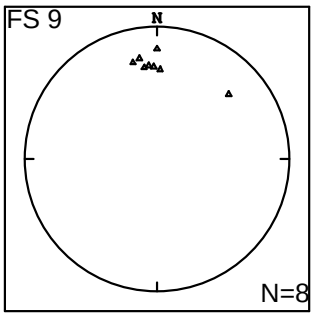

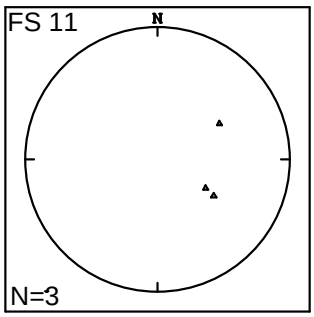

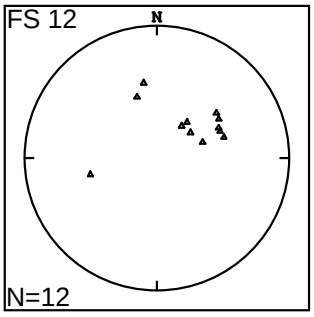

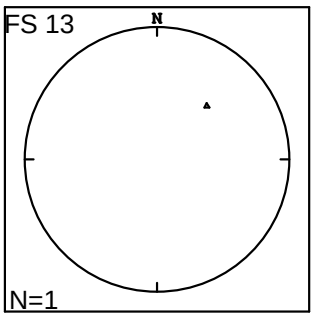

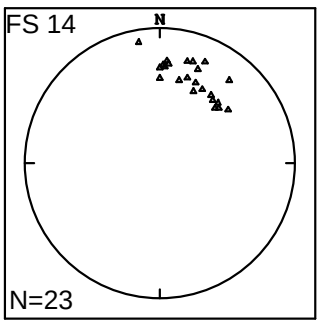

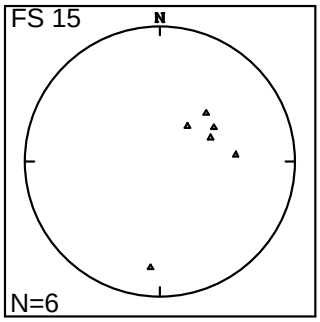

Appendix B-23: Stereonets of Thrust Fault Ideal Sigma One by Station

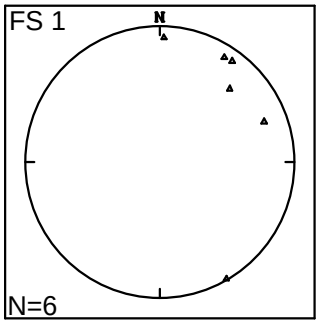

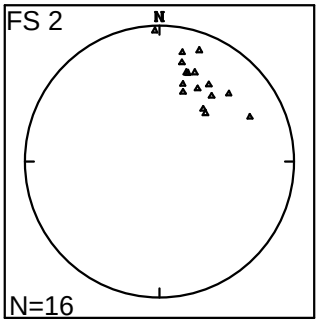

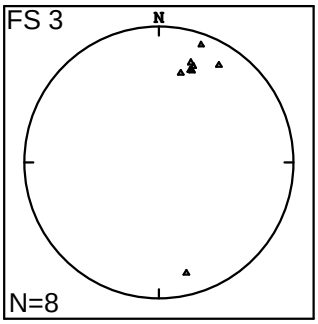

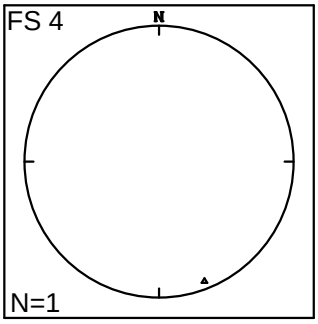

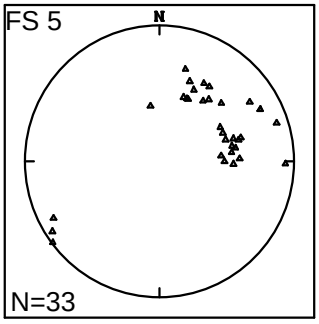

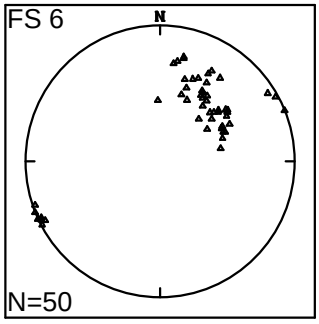

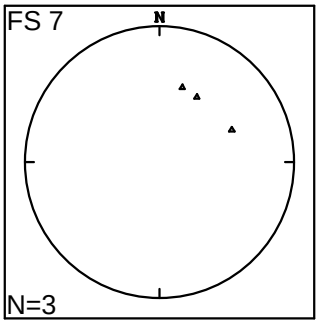

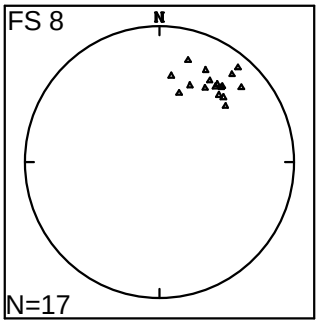

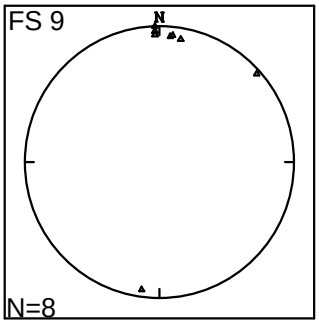

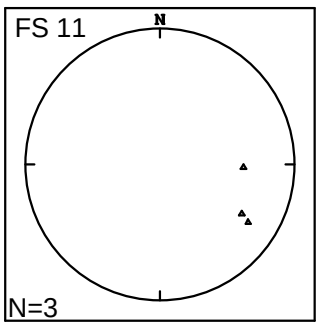

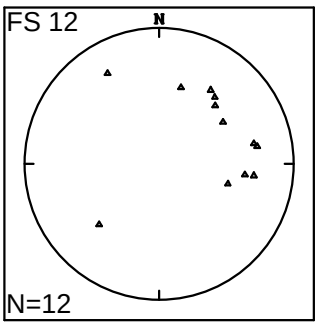

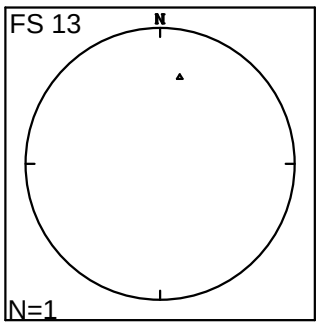

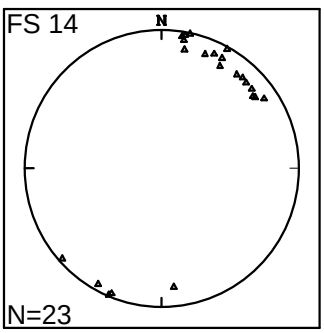

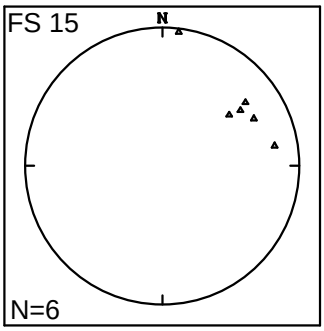

Appendix B-24: Stereonets of Left-Lateral Fault Planes by Station

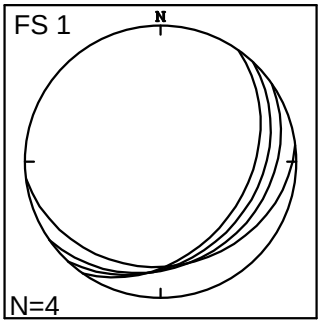

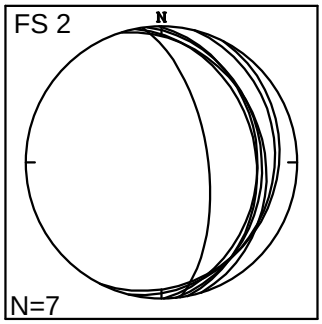

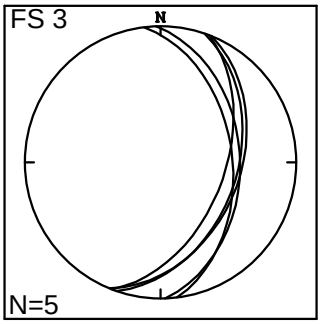

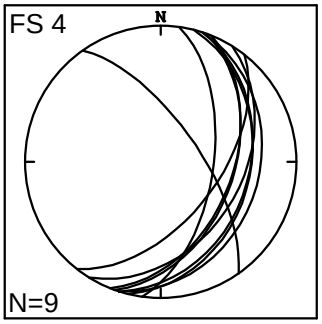

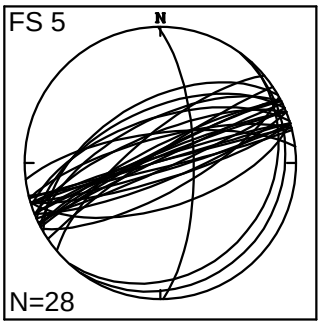

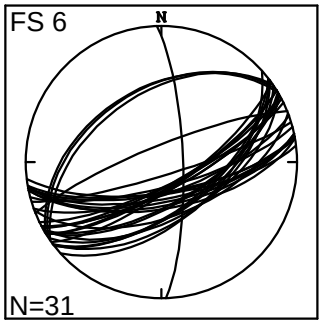

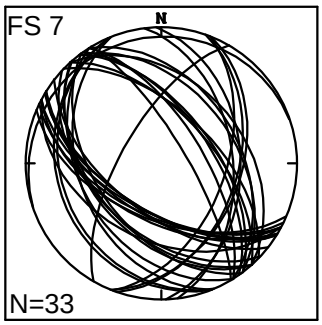

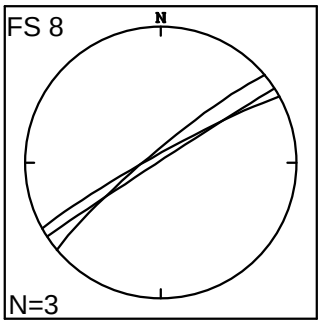

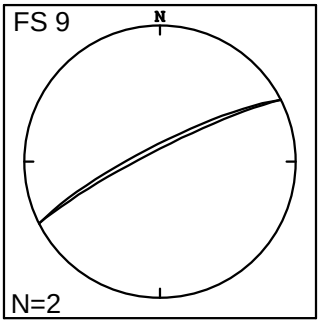

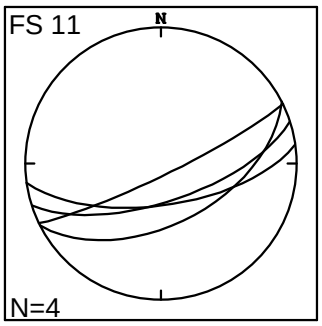

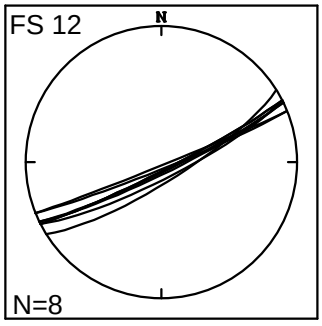

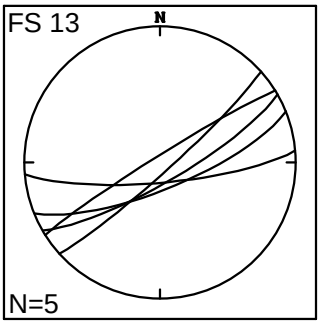

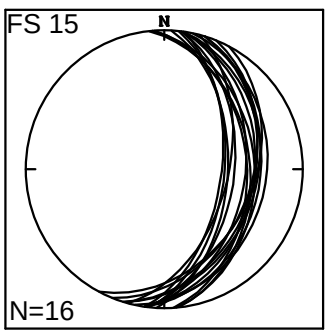

Appendix B-25: Stereonets of Left-Lateral Fault Slickenlines by Station

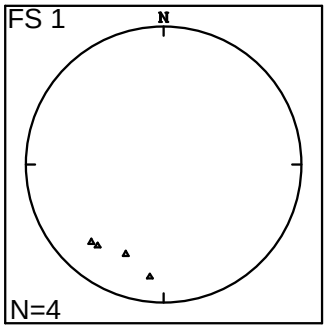

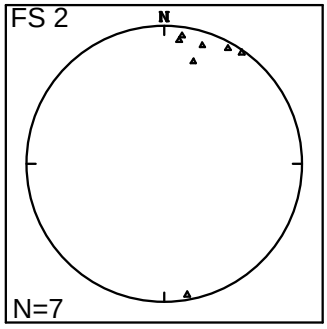

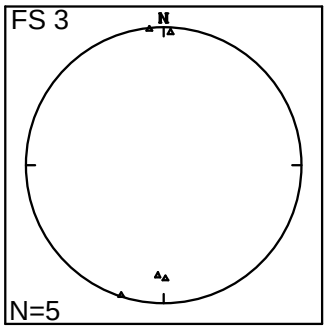

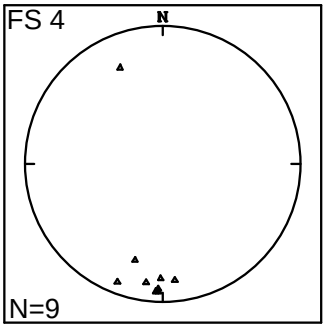

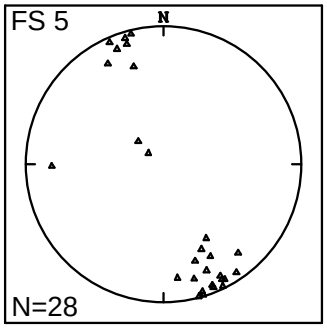

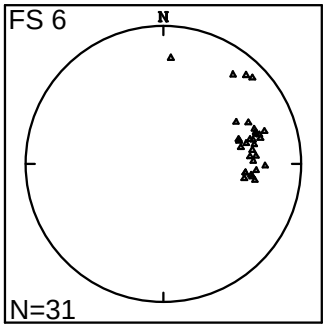

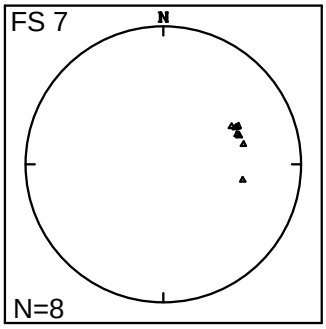

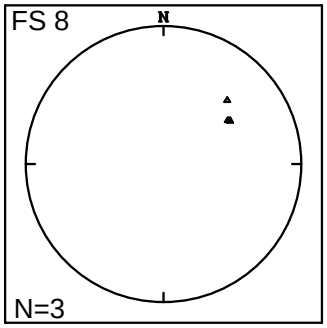

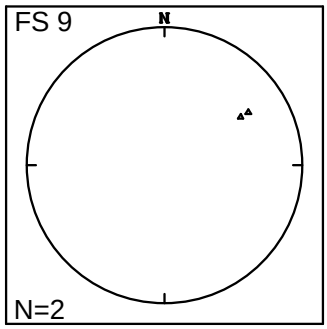

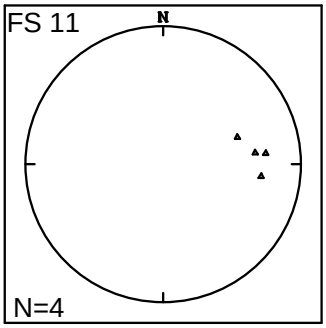

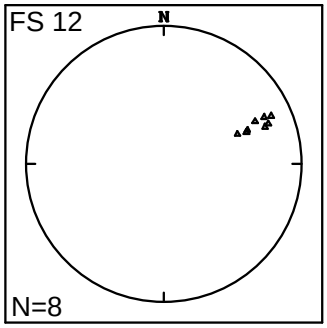

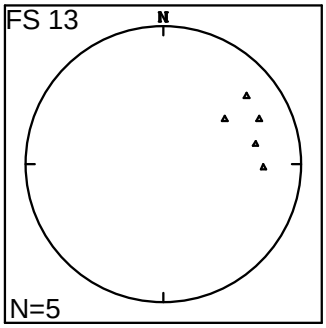

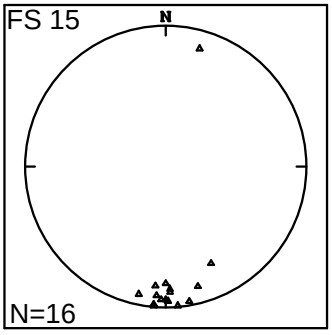

Appendix B-26: Stereonets of Left-Lateral Fault Ideal Sigma One by Station

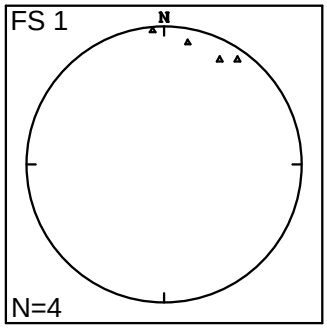

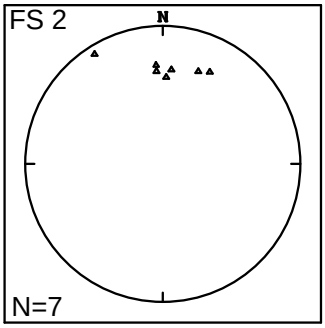

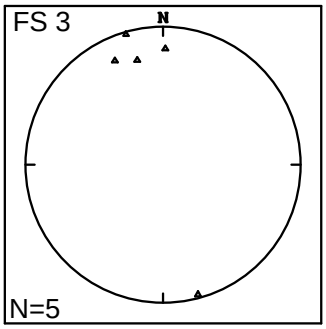

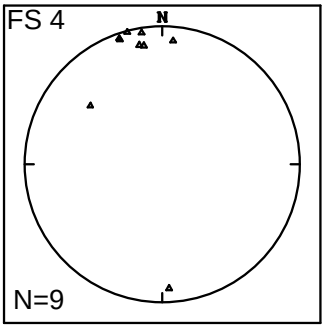

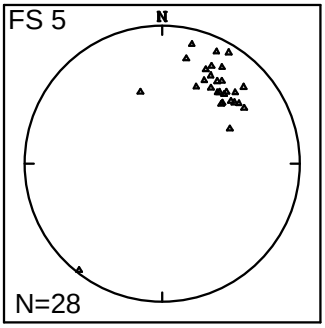

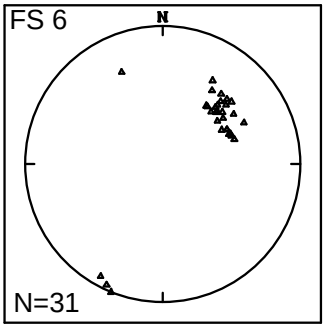

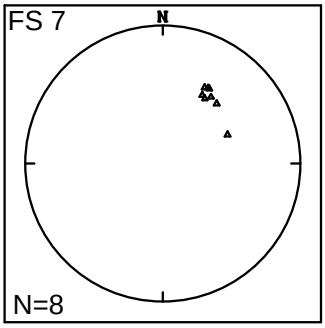

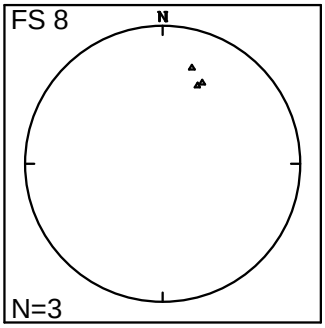

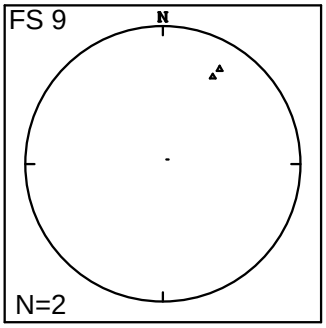

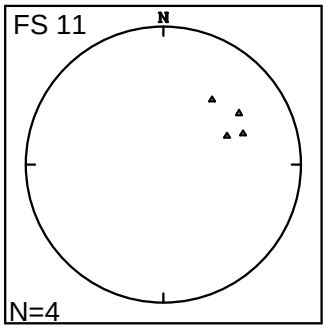

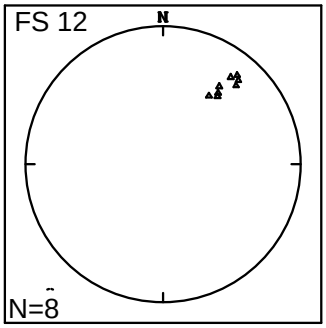

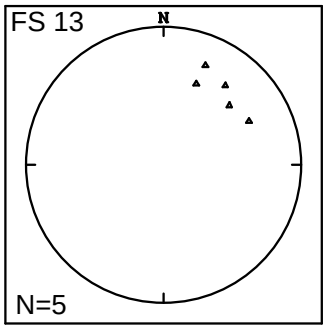

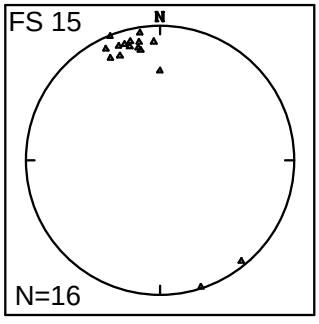

Appendix B-27: Stereonets of Right-Lateral Fault Planes by Station

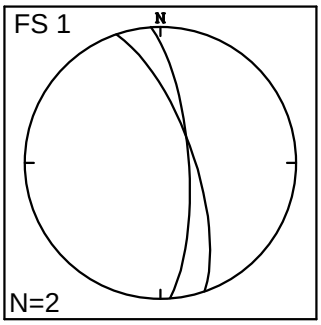

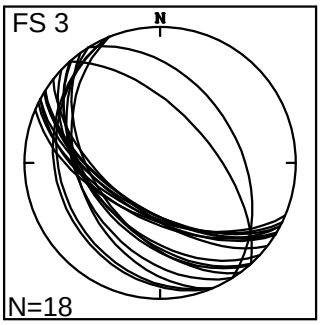

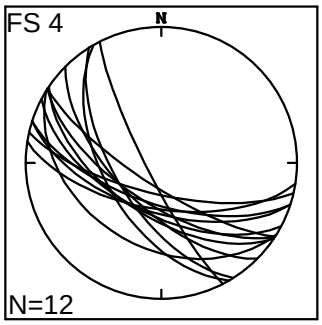

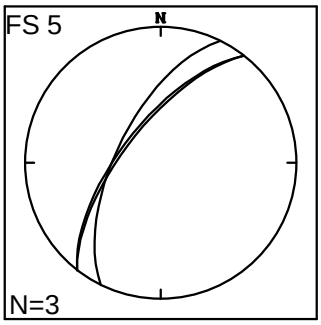

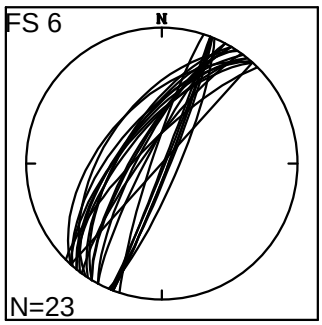

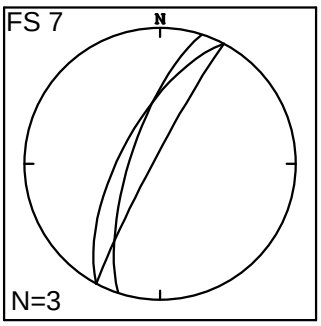

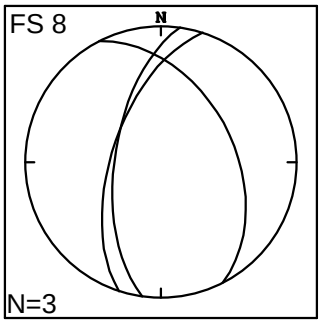

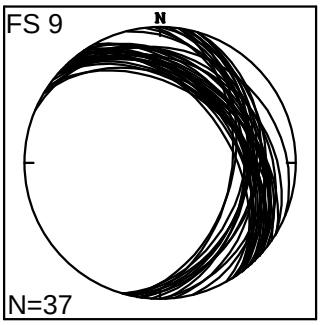

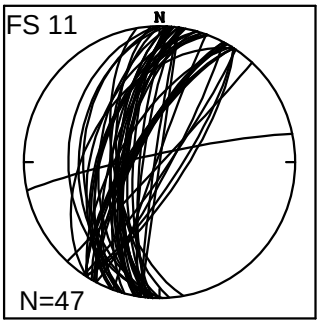

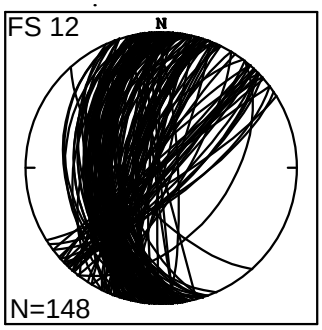

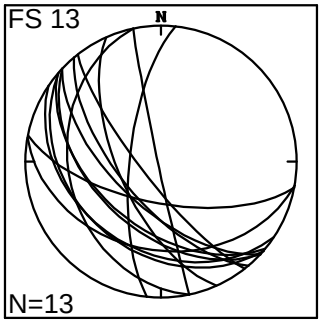

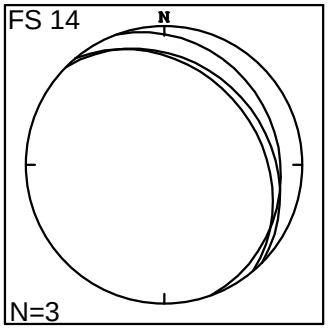

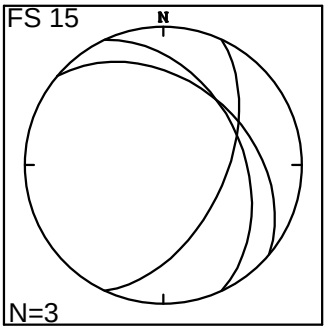

Appendix B-28: Stereonets of Right-Lateral Fault Slickenlines by Station

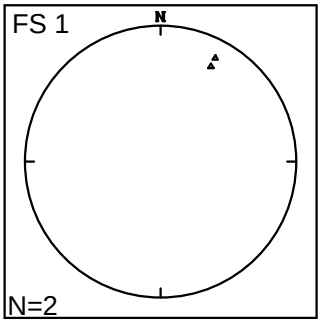

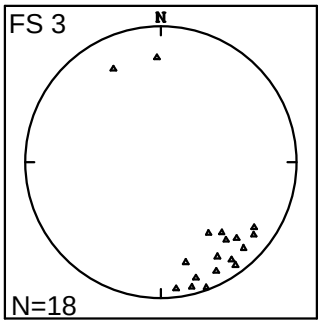

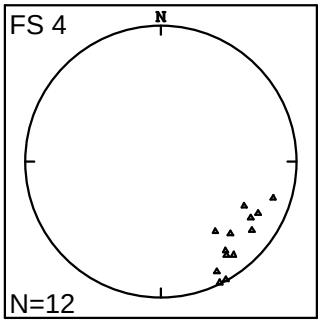

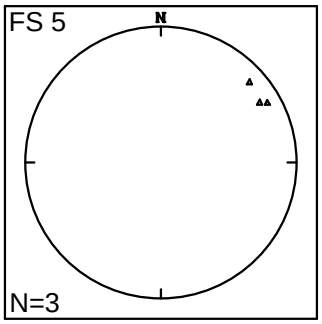

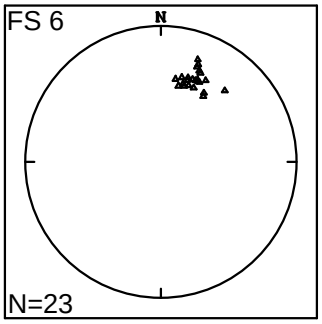

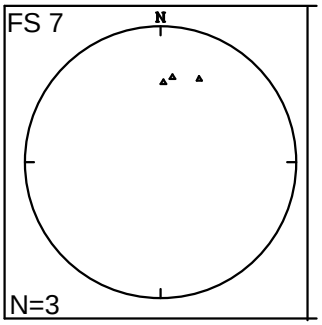

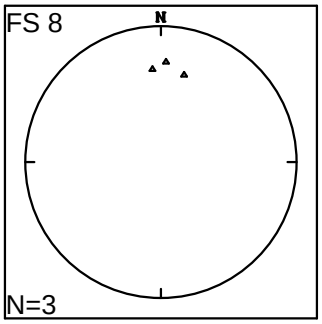

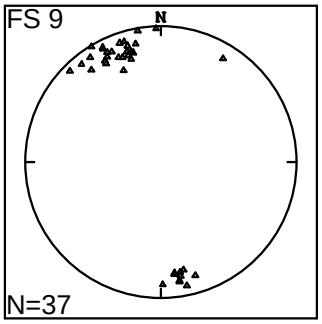

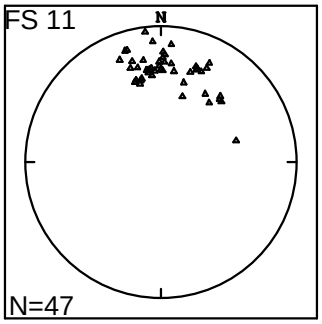

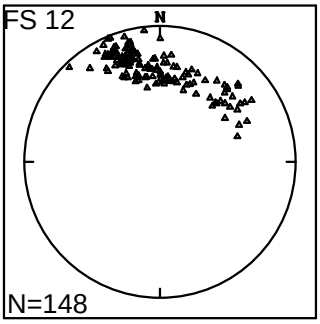

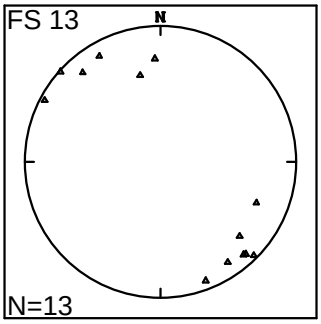

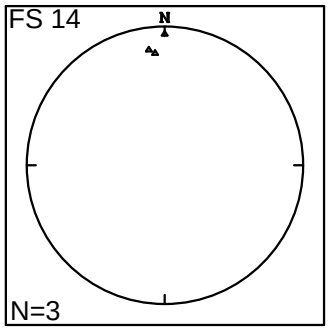

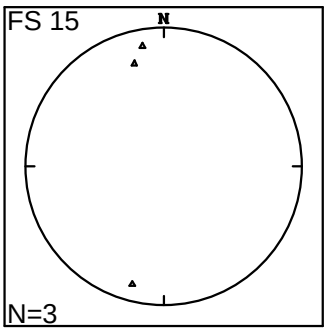

Appendix B-29: Stereonets of Right-Lateral Faults Ideal Sigma One by Station

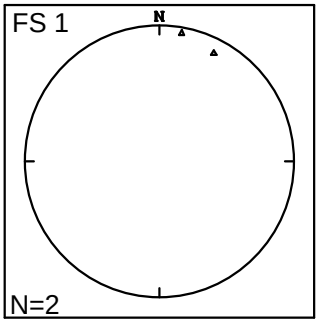

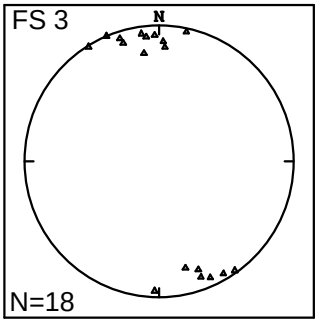

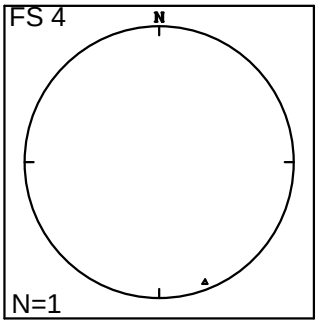

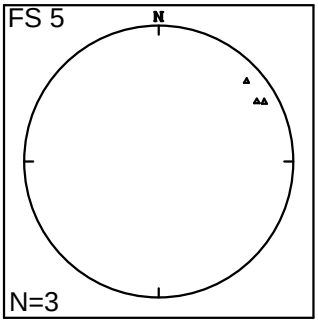

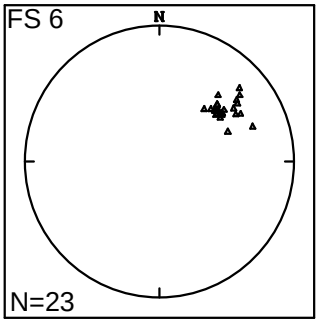

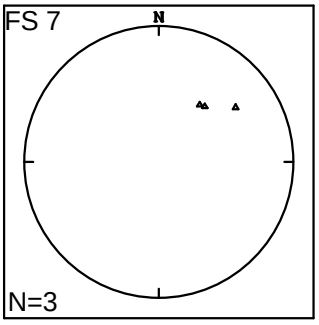

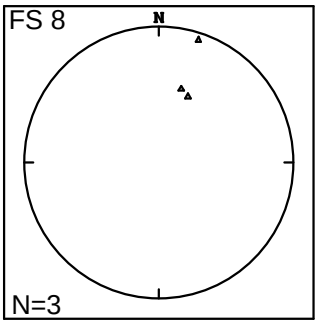

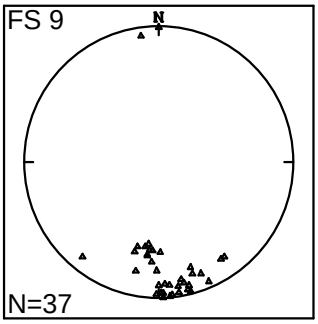

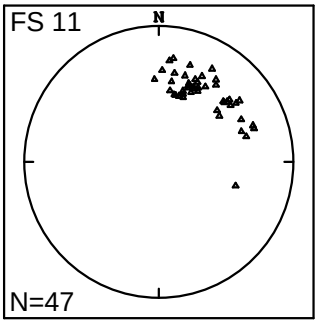

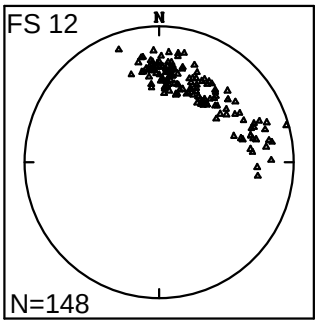

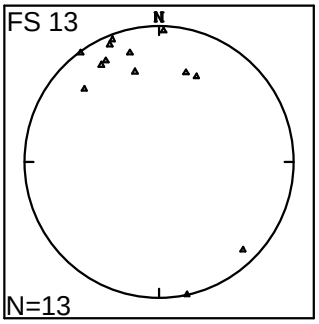

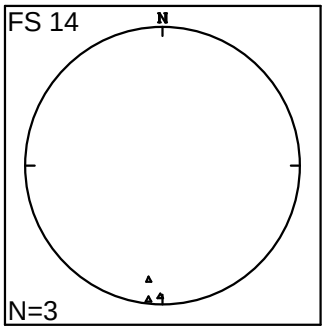

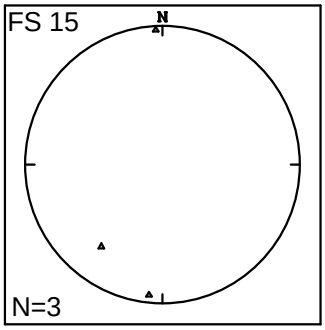

Appendix B-30: Stereonets of Normal Fault Planes by Station

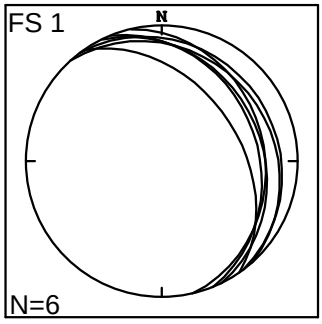

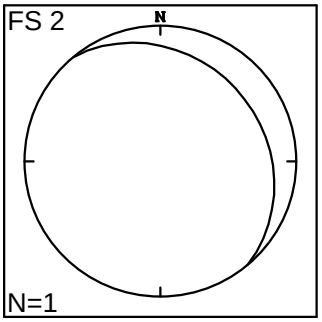

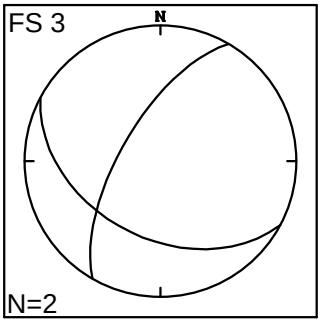

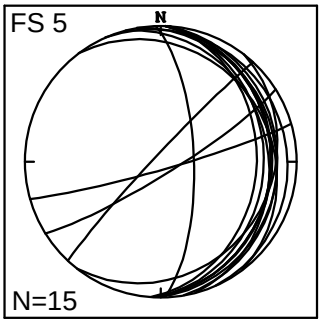

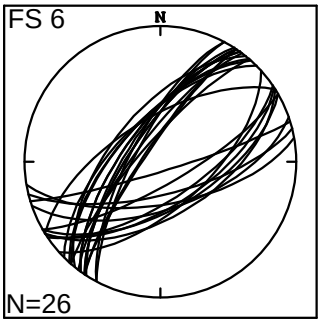

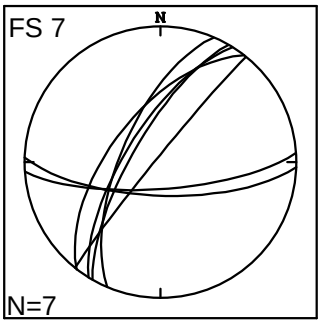

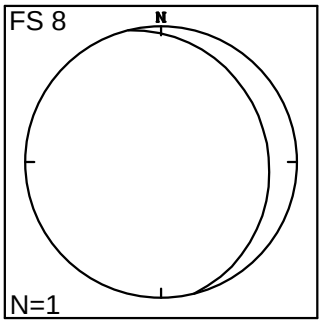

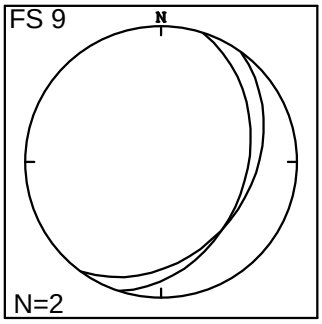

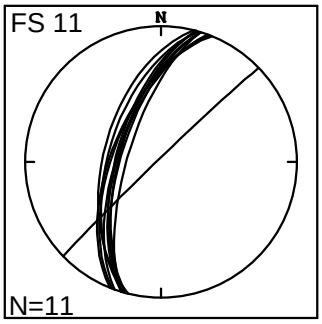

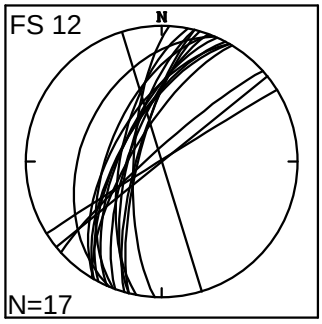

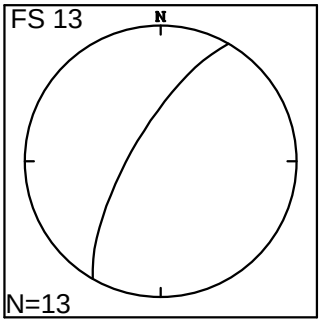

Appendix B-31: Stereonets of Normal Fault Slickenlines by Station

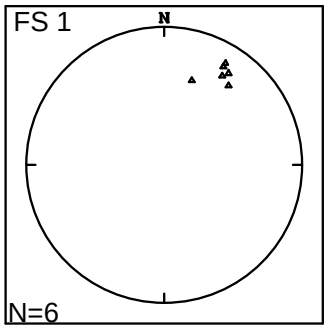

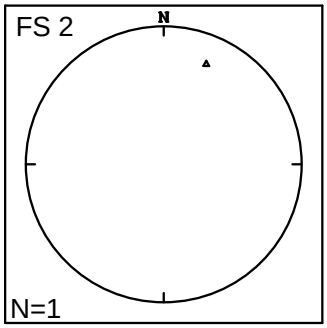

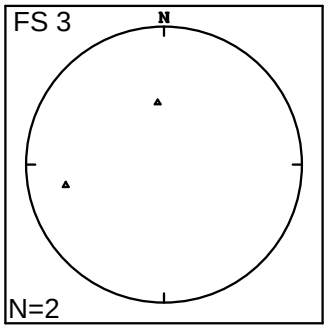

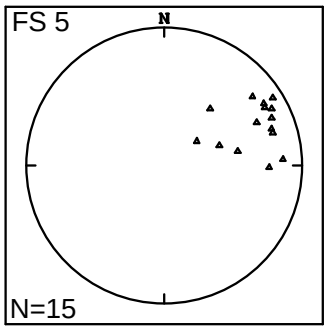

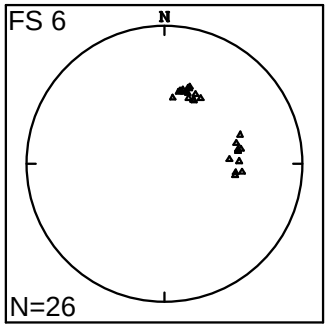

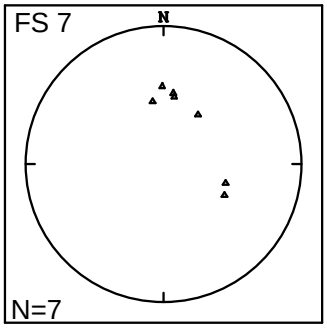

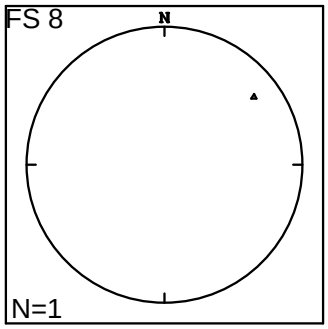

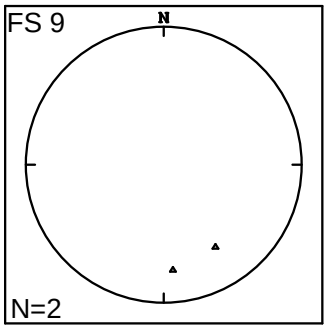

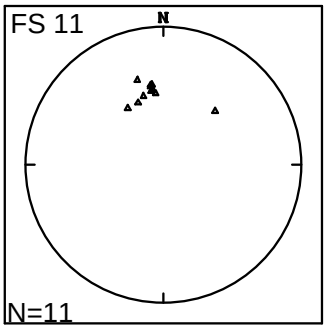

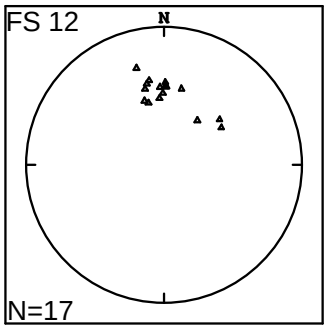

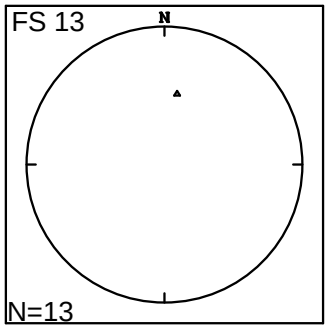

Appendix B-32: Stereonets of Normal Fault Ideal Sigma One by Station

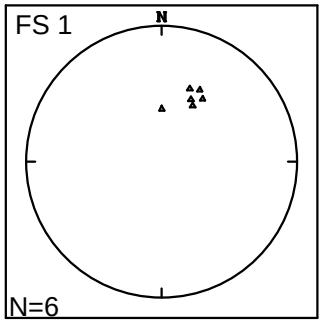

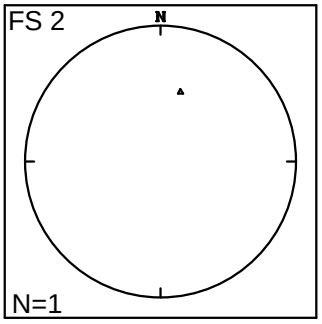

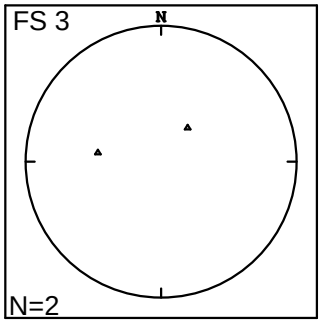

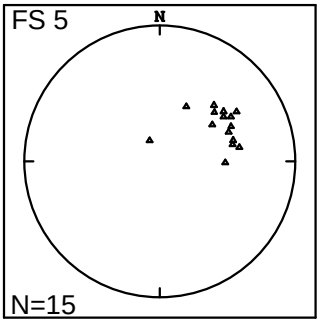

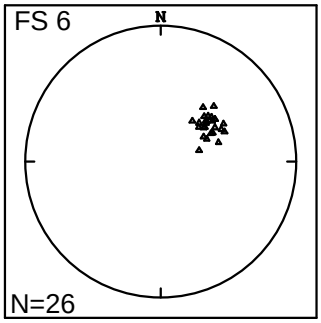

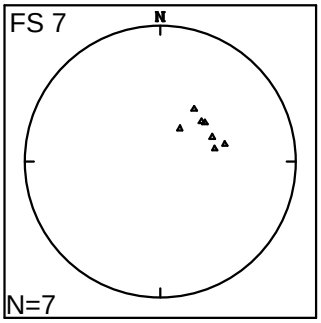

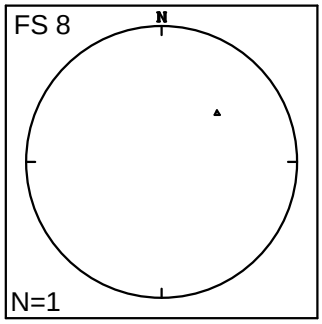

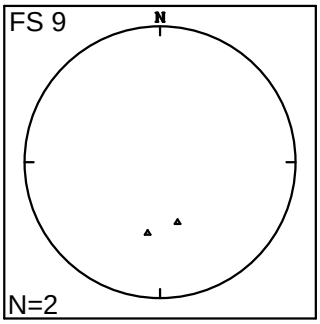

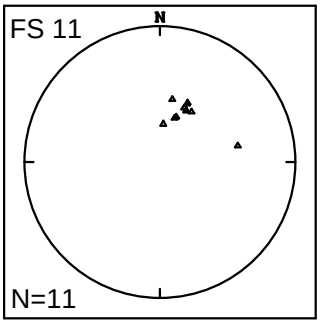

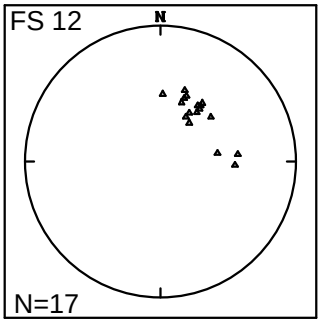

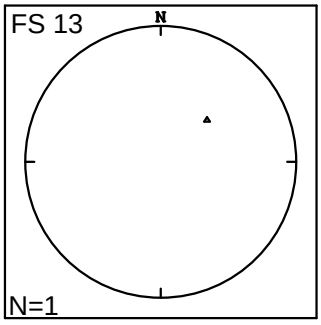

Appendix B-33: Stereonets of Fault Planes, Slickenlines, and Ideal Sigma One Divided by Slip-Sense (Raw Data)

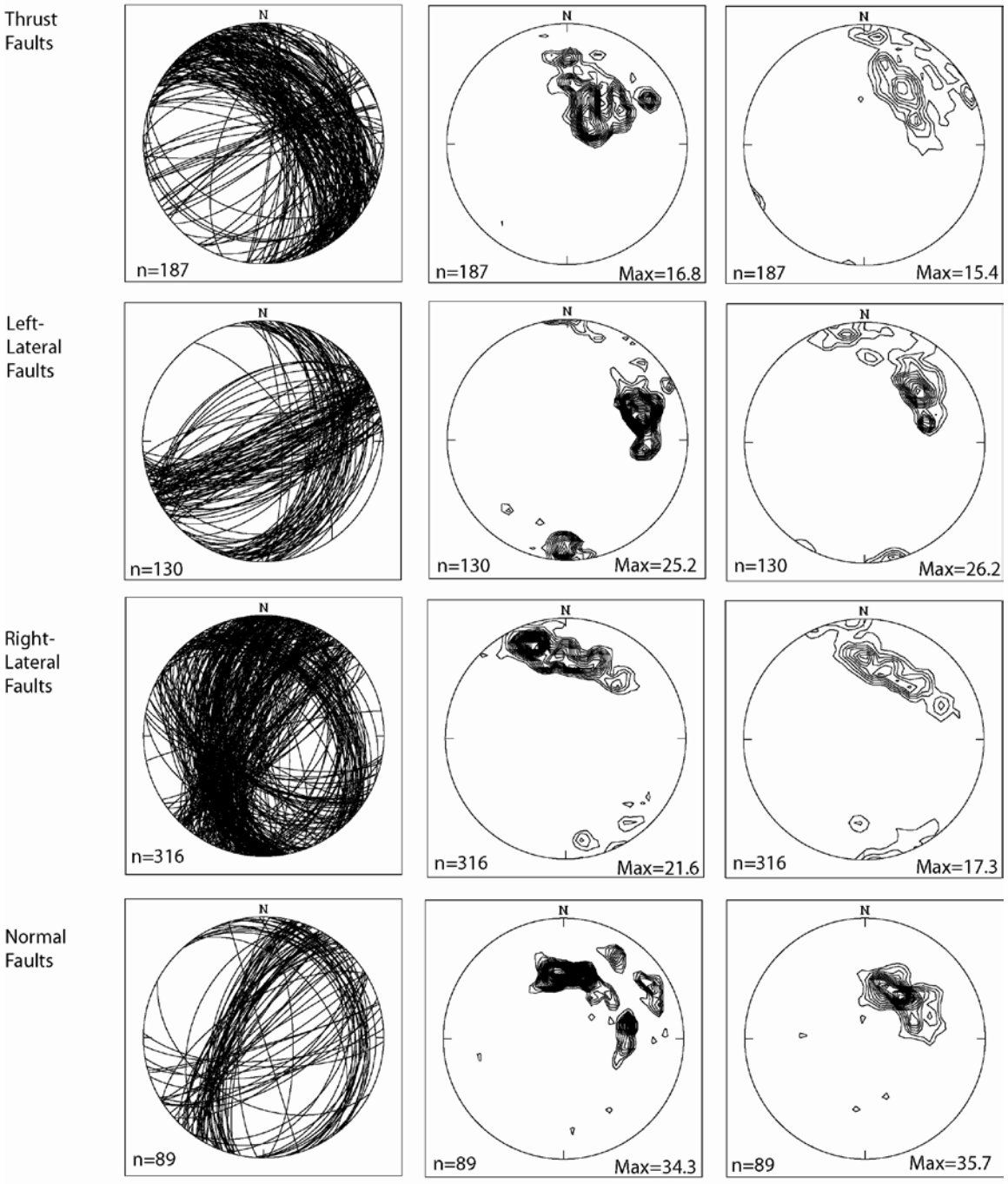

1st column = stereonets of fault plane strikes, 2nd column = slickenline trends, and 3rd column = ideal sigma one trends. Contour interval = 2.

Appendix B-34: Tables Showing Minor Fault Data Restored to Pre-Fold Orientation. (Rotated 40 degrees SW about a N30W axis).

n=	Slickenline Vector Mean/ Dispersion	Slickenline Eigen Value/ Eigen Vector	Ideal σ_1 Vector Mean/ Disperison	Ideal σ_1 (α=20) Eigen Value/ Eigen Vector
722	27.1/.5572	E1=.6664/027-05	30/.4256	E1=.7412/214-00
		E2=.2574/117-04		E2=.1982/134-22
		E3=.0763/244-84		E3=.0607/306-83
187	45/.2410	E1=.8180/045-15	42.4/.2960	E1=.2864/222-03
		E2=.1076/141-21		E2=.1388/131-12
		E3=.0744/281-63		E3=.0748/327-78
130	56.5/.2410	E1=.6825/238-11	35/.4155	E1=.7659/215-06
		E2=.2836/143-24		E2=.2018/125-06
		E3=.0339/350-63		E3=.0323/348-82
316	2.2/.3870	E1=.7768/002-03	19/.4580	E1=.7339/200-1
		E2=.1864/092-00		E2=.2121/110-5
		E3=.0368/186-87		E3=.0503/240-47
89	38/.3776	E1=.7549/038-10	49/.1761	E1=.8932/049-13
		E2=.1786/304-22		E2=.0656/315-16
		E3=.0665/151-66		E3=.0413/177-69

Appendix B-35: Stereonets of Fault Planes, Slickenlines, and Ideal Sigma One Divided by Slip-Sense
(Restored to Pre-fold orientation)

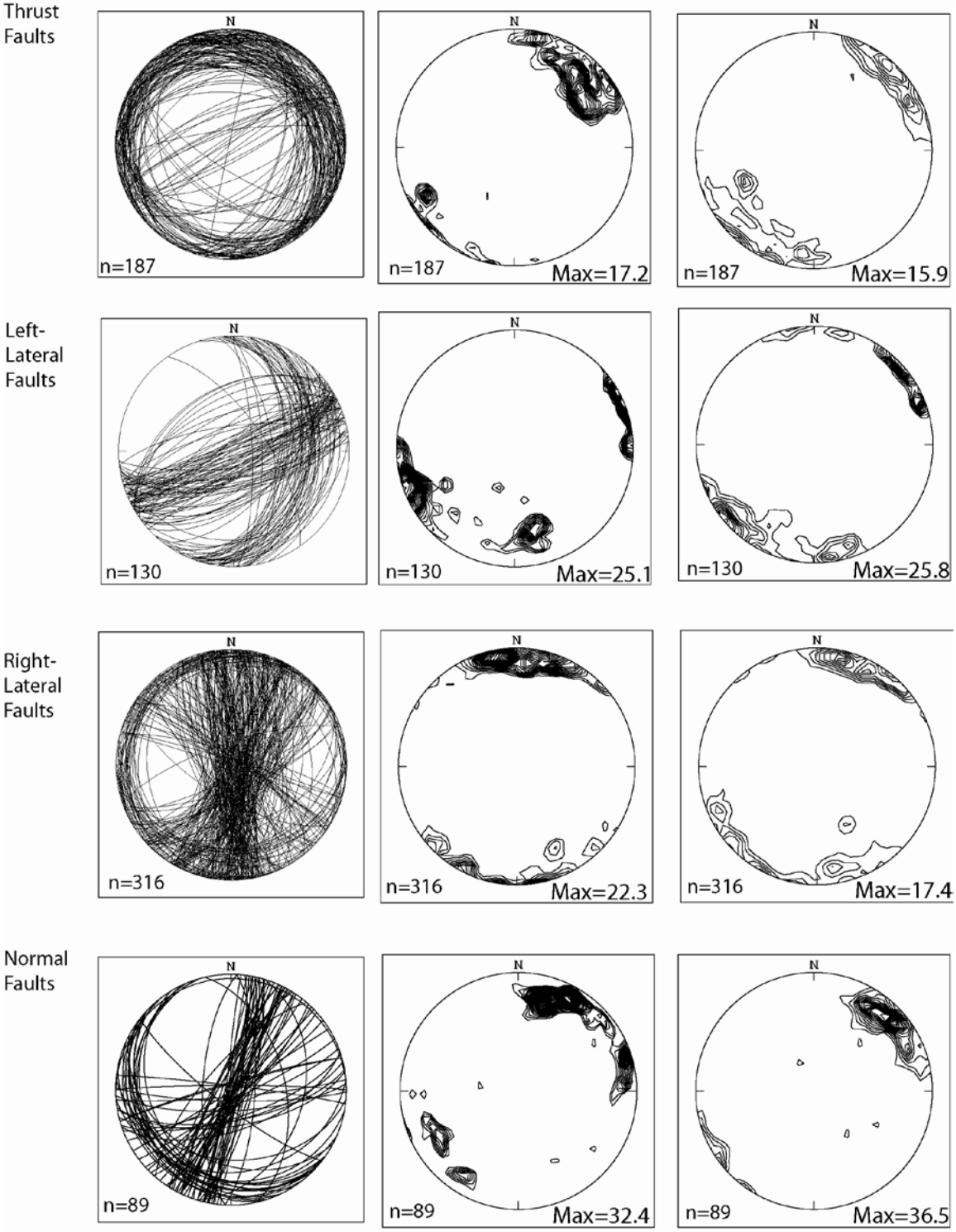

1st column = stereonets of fault plane strikes, 2nd column = slickenline trends, and third column = ideal sigma one trends. Contour interval = 2. Data rotated 40 degrees SW about a N30W axis.

Appendix B-36: Full Fault Data Set Restored to Pre-Fold Orientation

Fault Planes

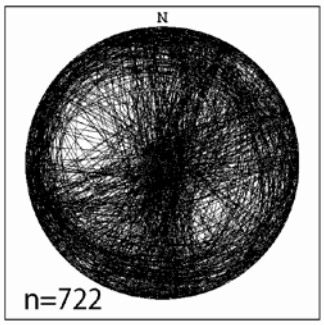

Rose Diagram of
Fault Plane Strikes

Slickenlines

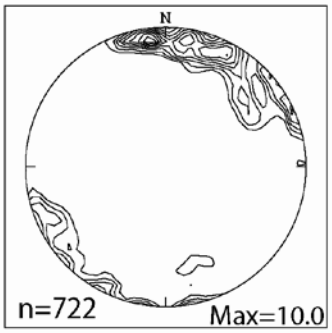

Rose Diagram of
Slickenline Trends

Ideal Sigma One

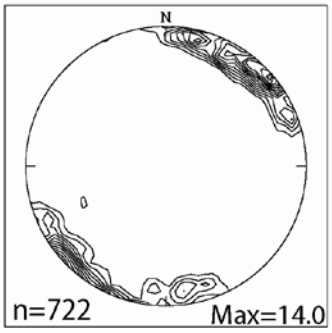

Rose Diagram of Ideal
Sigma One Trends

Stereonets of fault planes, slickenlines, and ideal sigma one data. Rose diagram of fault plane strikes, slickenline trends, and ideal sigma one trends. Stereonets containing 50 points or more have a contour interval of 2 and rose diagrams have a smoothing increment of 10 degrees. Data rotated 40 degrees SW about a N30W axis.

Appendix B-37: Stereonets and Rose Diagrams of Thrust Fault Data

(Rotated 40 degrees SW about a N30W axis)

Raw Data

Restored to Pre-Fold Orientation

Fault Plane Strikes

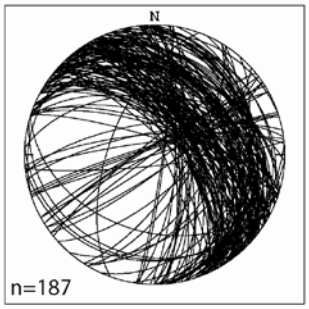

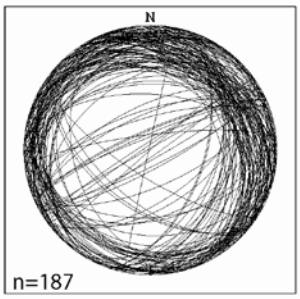

Slickenline Trends

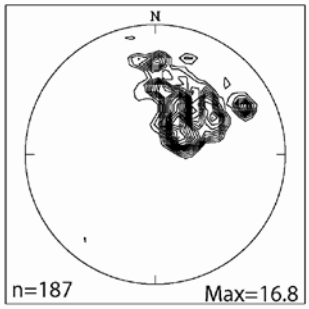

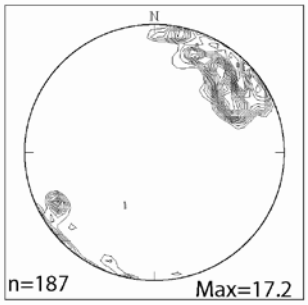

Ideal Sigma One Trends

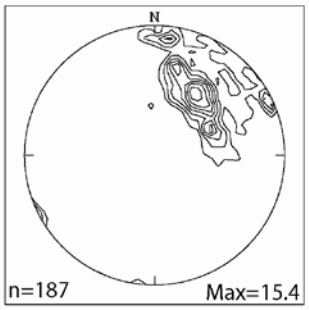

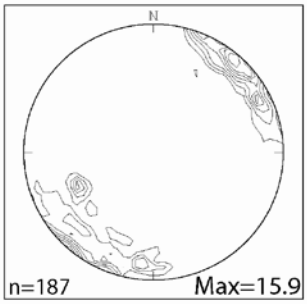

Rose Diagram of Slickenline Trends

Rose Diagram of Ideal Sigma One Trends

Appendix B-38: Stereonets and Rose Diagrams of Left-Lateral Fault Data

(Rotated 40 degrees SW about a N30W axis)

Raw Data

Restored to Pre-Fold Orientation

Fault Plane Strikes

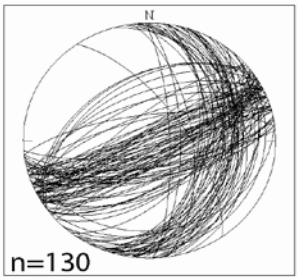

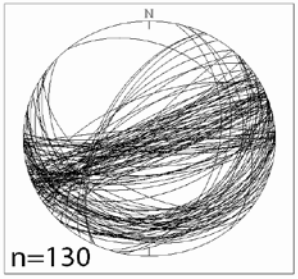

Slickenline Trends

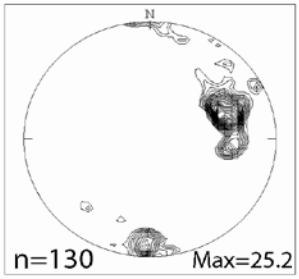

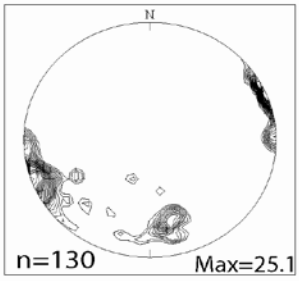

Ideal Sigma One Trends

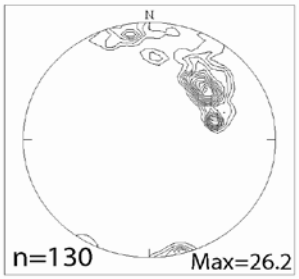

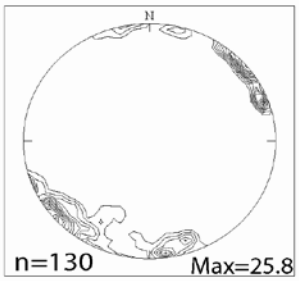

Rose Diagram of SlickenlineTrends

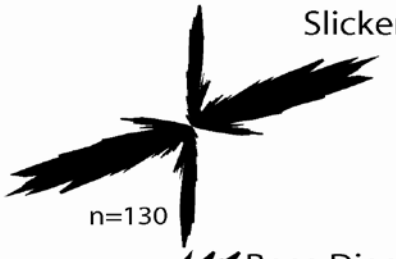

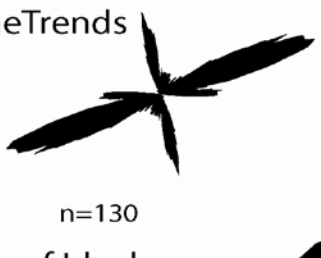

Rose Diagram of Ideal Sigma One Trends

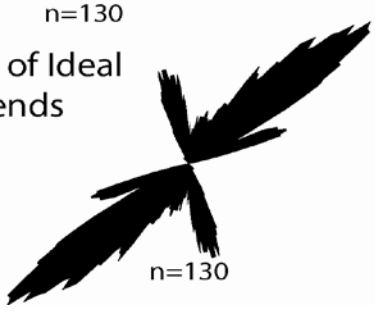

Appendix B-39: Stereonets and Rose Diagrams of Right-Lateral Fault Data

(Rotated 40 degrees SW about a N30W axis)

Raw Data

Restored to Pre-Fold Orientation

Fault Plane Strikes

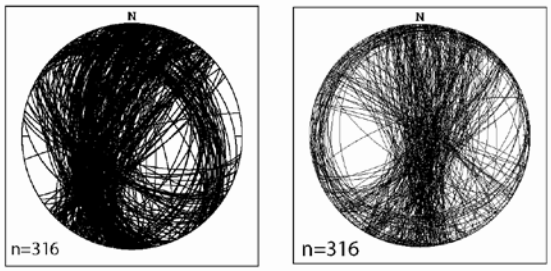

Slickenline Trends

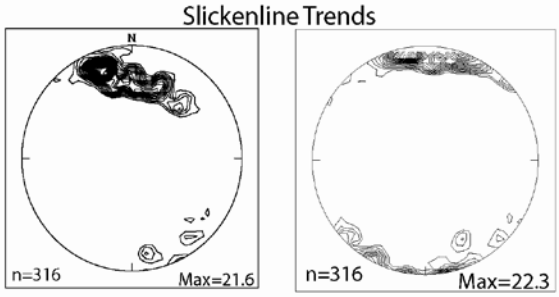

Ideal Sigma One Trends

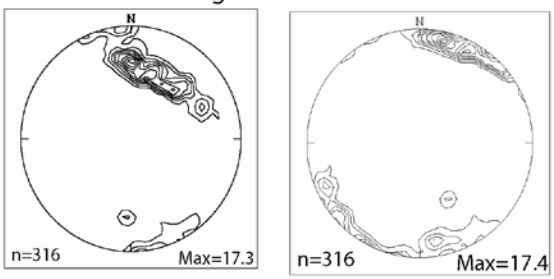

Rose Diagram of Slickenline Trends

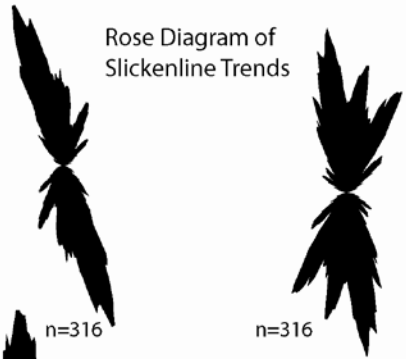

Rose Diagram of Ideal Sigma One Trends

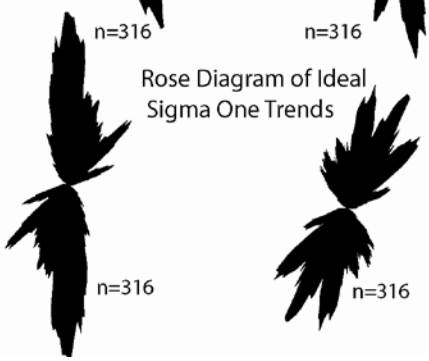

Appendix B-40: Stereonets and Rose Diagrams of Normal Fault Data

(Rotated 40 degrees SW about a N30W axis)

Raw Data

Restored to Pre-Fold Orientation

Fault Plane Strikes

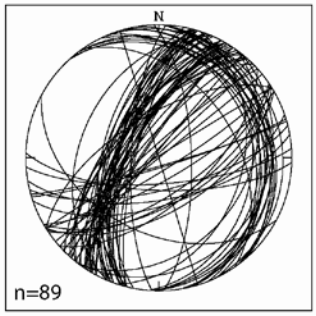

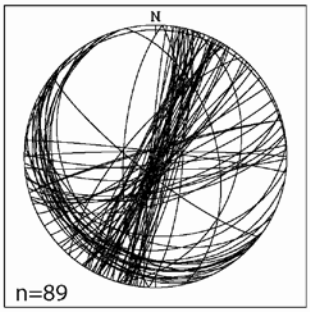

Slickenline Trends

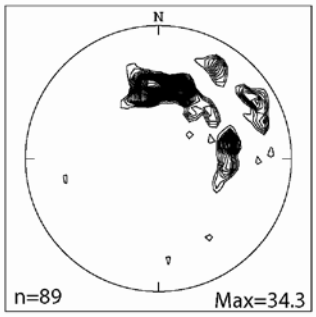

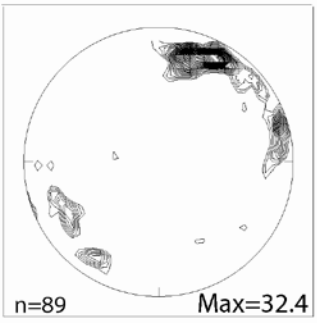

Ideal Sigma One Trends

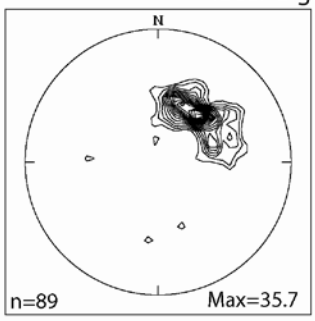

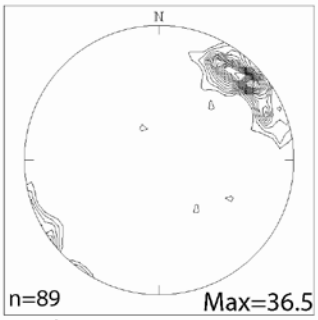

Rose Diagram of Slickenline Trends

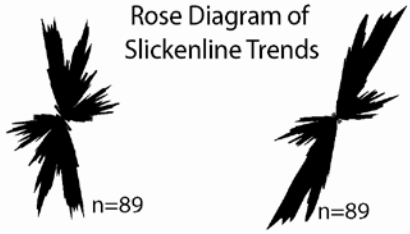

Rose Diagram of Ideal Sigma One Trends

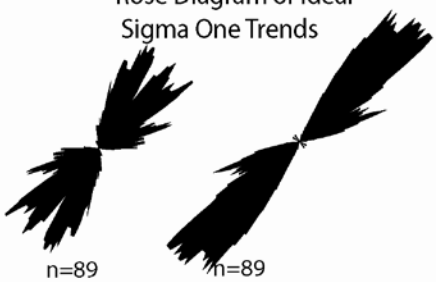

Appendix B-41: Rose Diagrams of Slickenline Trends Separated by Slip-Sense and Restored to Pre-Fold Orientation (Smoothed 10 degrees. Data rotated 40 degrees SW about a N30W axis)

Thrust Faults

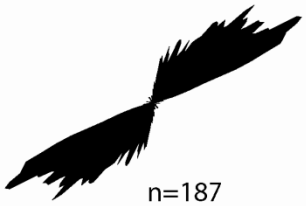

n=187

Left-Lateral Faults

n=130

Right-Lateral Faults

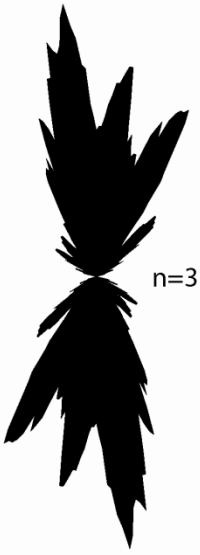

n=316

Normal Faults

n=89

Full Data Set

n=722

Appendix B-42: Rose Diagrams of Ideal Sigma One Trends Separated by Slip-Sense and Restored to Pre-Fold Orientation

(Smoothed 10 degrees. Data rotated 40 degrees SW about a N30W axis)

Thrust Faults

n=187

Left-Lateral Faults

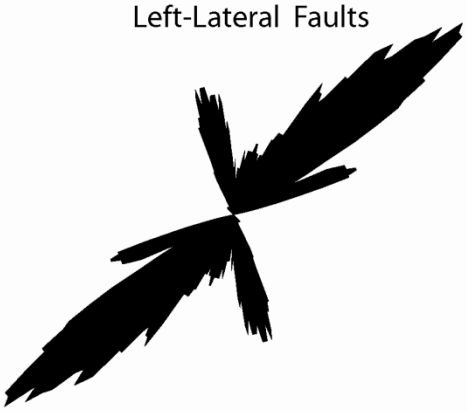

n=130

Right-Lateral Faults

n=316

Normal Faults

n=89

Full Data Set

n=722

Appendix B-43: Stereonets and Rose Diagrams of Minor Fault Planes Restored to Pre-Fold Orientation and Separated by Slip-Sense

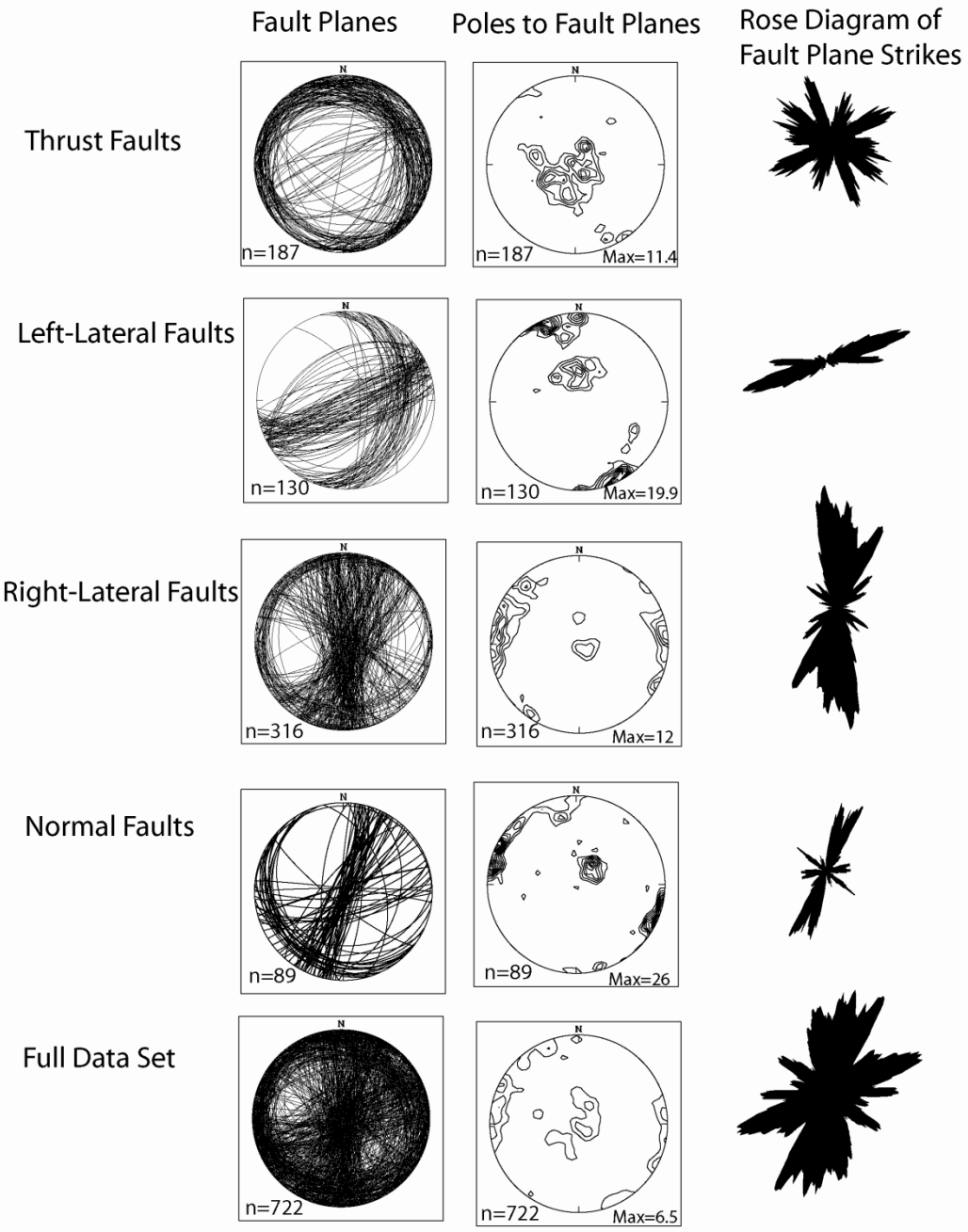

Stereonets of the strike of fault planes, the poles to fault planes, and rose diagrams of the strike of fault planes Contour interval of 2 for contoured stereonets and rose diagrams smoothed 10 degrees. Data rotated 40 SW about a N30W axis.

Appendix B-44: Stereonets and Rose Diagrams of Minor Faults Restored to Pre-Fold Orientation and Separated by Slip-Sense

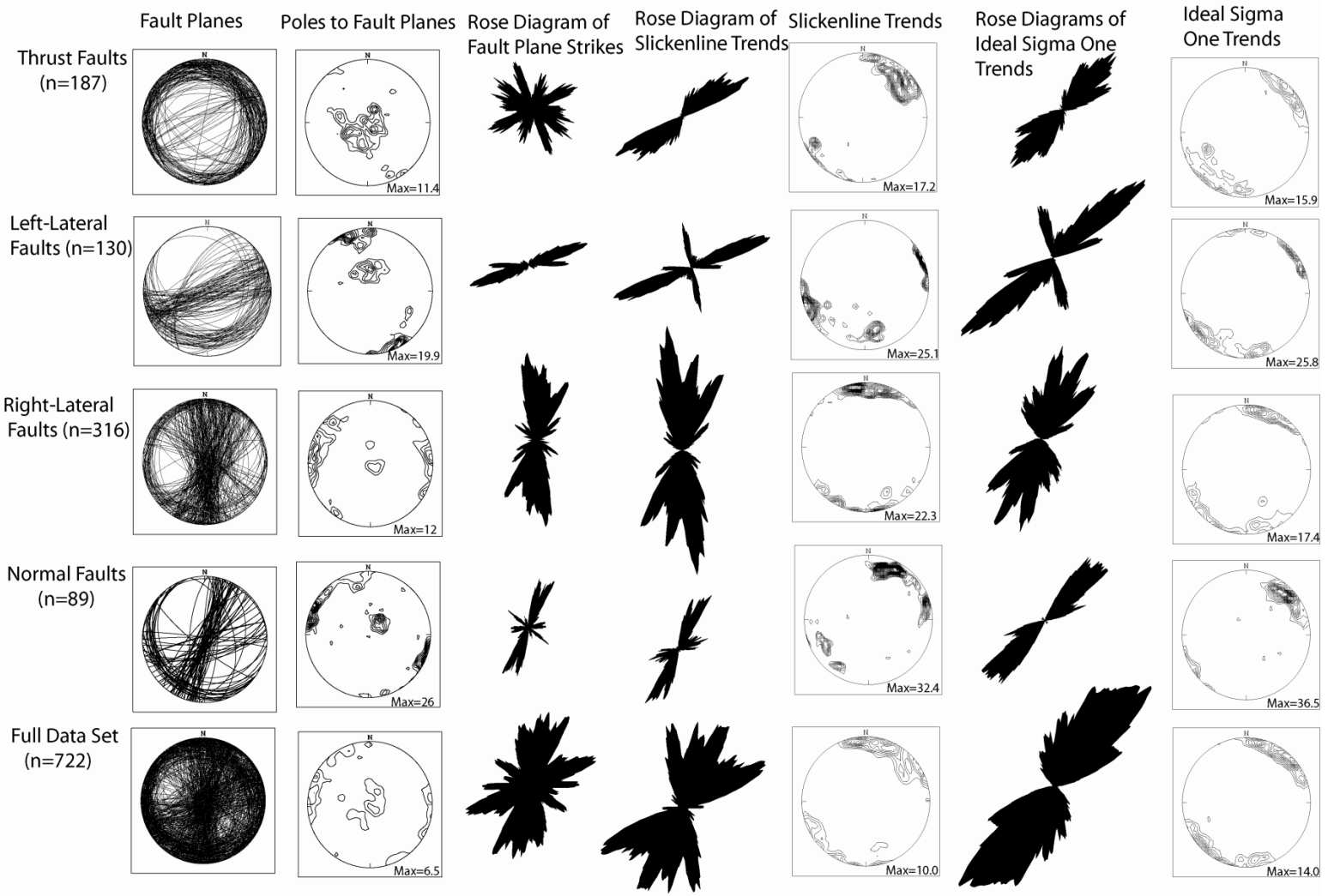

Contour interval of 2 for contoured stereonets and rose diagrams smoothed 10 degrees. Data rotated 40 SW about a N30W axis.

Appendix B-45: Rose Diagrams of Ideal Sigma One Trends Restored to Pre-Fold Orientation and Subdivided by Station

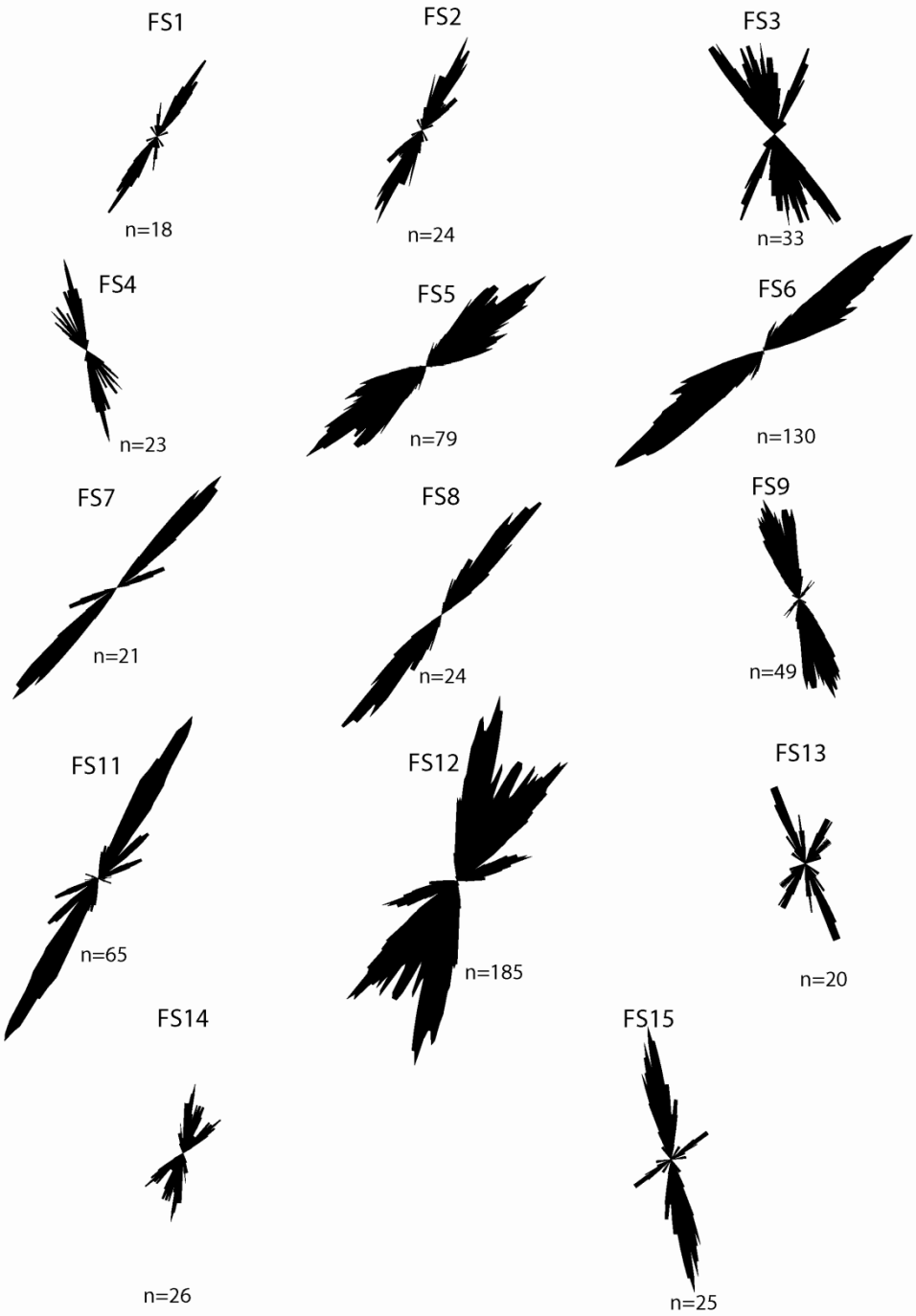

Rose diagrams have a smoothing of 10 degrees. An alpha angle of 20 degrees was used for calculation of the ideal sigma one . Data was rotated 40 degrees SW about a N30W axis.

Appendix B-46: Rose Diagrams of Ideal Sigma One Trends Restored to Pre-Fold Orientation and Separated by Station, Unit, and Location

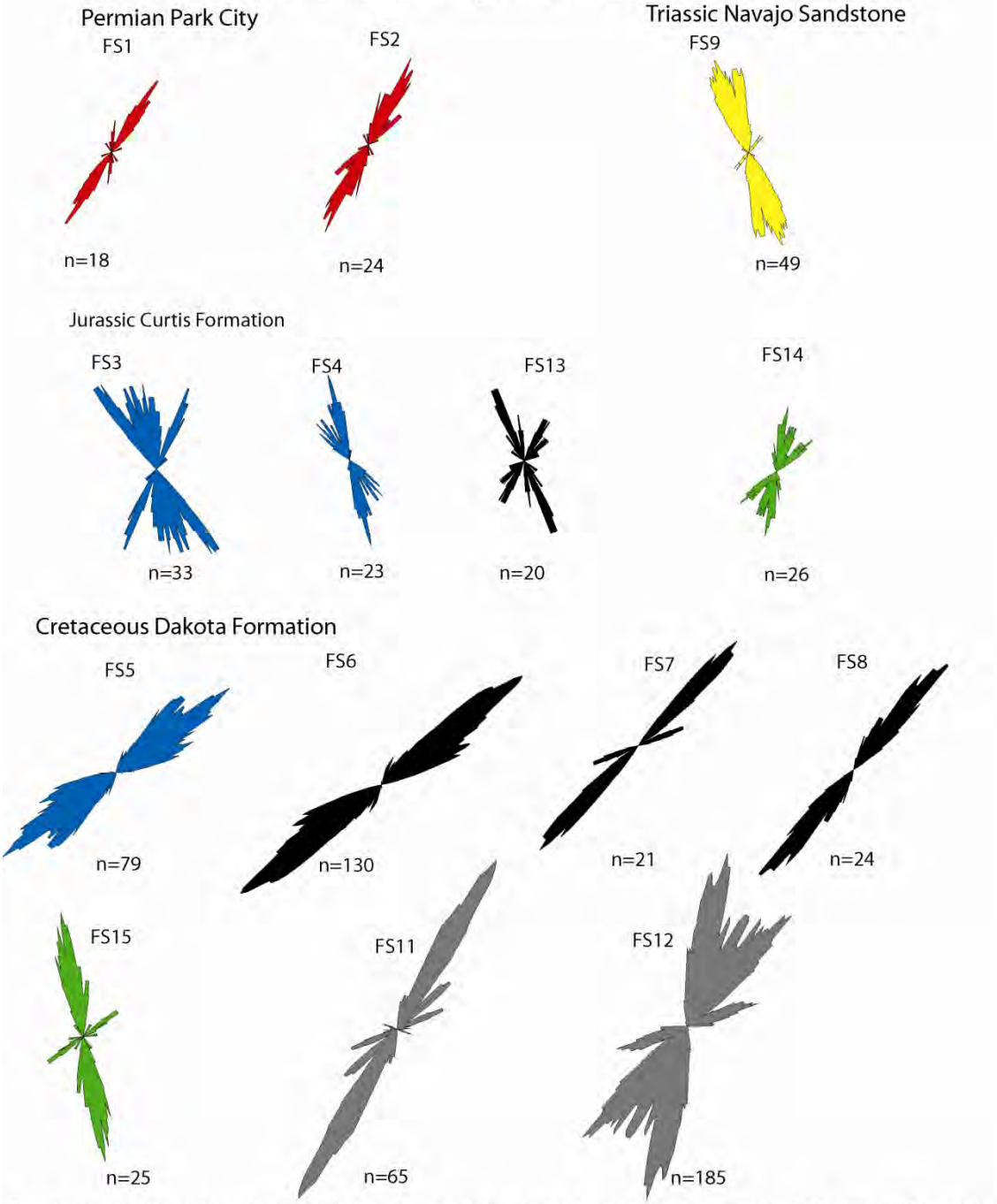

Rose diagrams have a smoothing of 10 degrees. An alpha angle of 20 degrees was used for calculation of the ideal sigma one. Colors identify the directly adjacent stations. Red, blue, and black correspond to the NW portion of the structure. Yellow and gray correspond to the middle portion of the structure. Green corresponds to the SE portion of the structure. Data was rotated 40 degrees SW about a N30W axis.

Appendix B-47: Rose Diagrams of Ideal Sigma One Trends Within the Pre-Orogenic Strata Separated by Station and Slip-Sense
(Data Restored to Pre-Fold Orientation. Rotated 40 degrees SW about a N30W axis to . Smoothing increment of 10 degrees for all roses)

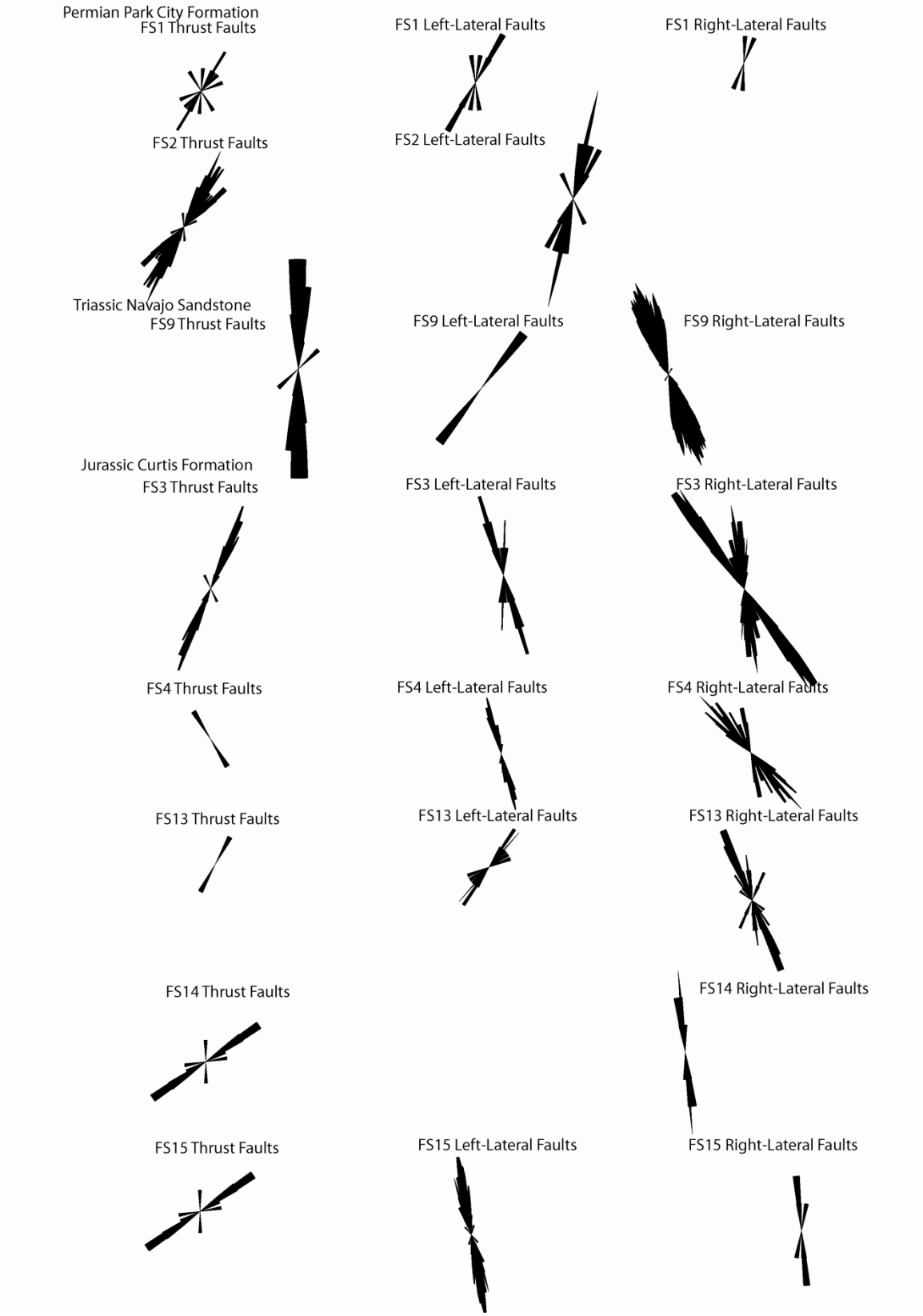

APPENDIX C: Joint Data, Stereonets and Explanation

List of Appendices and key to abbreviations and methods

Raw Data
C-1: Table showing all joint data
C-2: Stereonets of Triassic Navajo Sandstone Joint Strikes within Irish Canyon-Vermillion Creek Area
C-3: Stereonets of Oligocene Bishop Conglomerate and the Miocene Browns Park Joint Strikes within Irish Canyon-Vermillion Creek Area
C-4: Rose Diagrams of Navajo Sandstone Joint Strikes
C-5: Appendix C-5: Rose Diagrams of Oligocene Bishop Conglomerate and Miocene Browns Park Joint Strikes
C-6: Rose Diagram of the Strike of Joint Planes Superimposed on the Rose Diagram of the Strike of Normal Fault Planes Within the Browns Park Formation

Data Restored to Pre-Fold Orientation (Rotated 40 degrees SW about a N30W axis.)
C-7: Stereonets and Rose Diagrams of Raw Joint Data and of Joint Data Restored to Pre-Fold Orientation.

For full formation names see Appendix A. The full names for the abbreviated formations listed in the data table below are as follows: Trn-Triassic Navajo Sandstone, Kmv-Cretaceous Mesaverde Formation, Tbc-Oligocene Bishop Conglomerate, and Tbp-Miocene Browns Park Formation.

The vector mean is the average vector of joint strikes calculated from a data set. A dispersion value of 0 equals no dispersion and a dispersion value of 1.0 equals 100 percent dispersion.

An Eigen Vector analysis of joint strikes represents the average shortening direction responsible for forming the joints. The first Eigen Vector corresponds to the strike and dip of the maximum shortening direction. An Eigen Value 1.0 represents a data set with zero dispersion of values and as the value approaches zero, the dispersion increases.

Digital joint data available in excel format from:

Eric Erslev
Department of Geosciences
Colorado State University
Fort Collins, CO 80523
erslev@warnercnr.colostate.edu

Appendix C-1: Tables showing all joint data

Locality	Formation	Joint Set	Bedding Strike/Dip	UTM Easting	UTM Northing	n=	Vector Mean of Strikes	Dispersion	Eigen Value/ Eigen Vector
1	Trn	Full	339-43	692795	4522145	40	67.95	0.1607	E1=.9126/338-08
									E2=.0798/069-08
									E3=.0076/202-79
2	Trn	Full	331-41	692968	4521929	47	68.1	0.0632	E1=.9133/144-1
									E2=.0612/050-69
									E3=.0255/235-21
3	Trn	Full	350-27	693217	4521792	55	56.32	0.0933	E1=.9264/146-4
									E2=.0455/056-00
									E3=.0281/324-86
4	Trn	Full	337-34	693326	4521673	77	68.1	0.2122	E1=.8684/338-00
									E2=.1050/068-11
									E3=.0266/246-79
		J1	337-34	693326	4521673	74	68	0.1906	N/A
		J2	337-34	693326	4521673	2	358	0.0055	N/A
5	Trn	Full	338-33	693350	4521378	140	65.11	0.1437	E1=.9015/155-02
									E2=.0757/064-36
									E3=.0227/248-54
		J1	338-33	693350	4521378	132	66	0.058	N/A
		J2	338-33	693350	4521378	8	1	0.1076	N/A
6	Trn	Full	329-39	694331	4519535	145	64.32	0.9503	E1=.5143/158-05
									E2=.4578/067-04
									E3=.0280/275-80
		J1	329-39	694331	4519535	86	53	0.0916	N/A
		J2	329-39	694331	4519535	59	2	0.1616	N/A
7	Trn	Full	323-36	691869	4522662	101	347	0.8342	E1=.6422/064-39
									E2=.3299/320-17
									E3=.0279/212-46
		J1	323-36	691869	4522662	59	57	0.0554	N/A
		J2	323-36	691869	4522662	52	3	0.0249	N/A
9	Trn	Full	Variable	694593	4518749	36	97.2	N/A	E1=.5433/126-06
									E2=.4450/216-2
									E3=.0116/319-84
1 through 9	Variable	Full	Variable	Variable	Variable	641	61.94	0.5385	E1=.6884/152-1
									E2=.2594/061-21
									E3=.0522/244-69
		J1	Variable	Variable	Variable	457	72.9	0.1918	E1=.8537/342-02
									E2=.1029/074-36
									E3=.0434/249-54
		J2	Variable	Variable	Variable	47	1.49	0.04	E1=.9344/091-19
									E2=.0639/269-71
									E3=0017/001-01

1 through 9	Variable	Full	Variable	Variable	Variable	641	60.4	0.5413	E1=.6884/151-02
Restored									E2=.2594/241-19
									E3=.0522/056-71
		J1	Variable	Variable	Variable	457	71.45	0.2208	E1=.8537/161-06
									E2=.1029/251-03
									E3=.0434/009-83
		J2	Variable	Variable	Variable	47	0.79	0.0249	E1=.9344/271-16
									E2=.0639/038-65
									E3=0017/175-19
11	Tbc	Full	Variable	Variable	Variable	30	354.14	0.883	E1=.5275/088-07
									E2=.4271/357-08
									E3=.0454/217-79
		J3	Variable	Variable	Variable	13	323	0.1279	N/A
12	Tbc	Full	Variable	692956	4525139	30	329.25	0.5343	E1=.7210/059-03
									E2=.2646/329-04
									E3=.0144/184-85
		J3	Variable	692956	4525139	19	320	0.1923	N/A
13	Tbc	Full	358-18	692917	4525211	26	320.12	0.3026	E1=.8348/050-02
									E2=.1487/320-02
									E3=.0165/176-87
		J3	358-18	692917	4525211	25	321	0.1435	N/A
14	Tbp	Full	Variable	688286	4516456	31	303.96	0.3549	E1=.8046/034-01
									E2=.1730/124-03
									E3=.0224/275-87
		J3	Variable	688286	4516456	23	307	0.0583	N/A
15	Tbp	Full	342-14	693429	4525147	31	335.47	0.6849	E1=.6274/065-18
									E2=.3422/331-14
									E3=.0304/204-67
		J3	342-14	693429	4525147	18	315	0.0731	N/A
16	Tbc	Full	002-34	693252	4525115	17	335.81	0.411	E1=.7799/065-18
									E2=.1992/334-09
									E3=.0210/198-78
		J3	002-34	693252	4525115	9	320	0.0602	N/A
17	Tbc	Full	Variable	693087	4525235	25	324.52	0.2376	E1=.8628/055-05
									E2=.1169/324-01
									E3=.0203/220-85
		J3	Variable	693087	4525235	21	320	0.0844	N/A

		J3	Variable	693087	4525235	21	320	0.0844	N/A
18	Tbc	Full	Variable	689435	4525868	165	326.76	0.4058	E1=.7768/057-05
									E2=.1965/326-05
									E3=.0267/192-83
		J3	Variable	689435	4525868	109	321	0.1281	N/A
19	Tbp	Full	Variable	688654	4515519	27	303.83	0.2278	E1=.8408/215-06
									E2=.1070/305-03
									E3=.0522/061-84
		J3	Variable	688654	4515519	22	310	0.0662	N/A
11 through 19	Tbp and Tbc	Full	Variable	Variable	Variable	382	323.19	0.4777	E1=.7351/053-05
									E2=.2304/323-03
									E3=.0345/205-84
		J3	Variable	Variable	Variable	294	319.9	0.1621	E1=.8887/050-80
									E2=.0781/140-02
									E3=.0332/252-84

Appendix C-2: Stereonets of Triassic Navajo Sandstone Joints
Within the Irish Canyon-Vermillion Creek Area
(Equal Area)

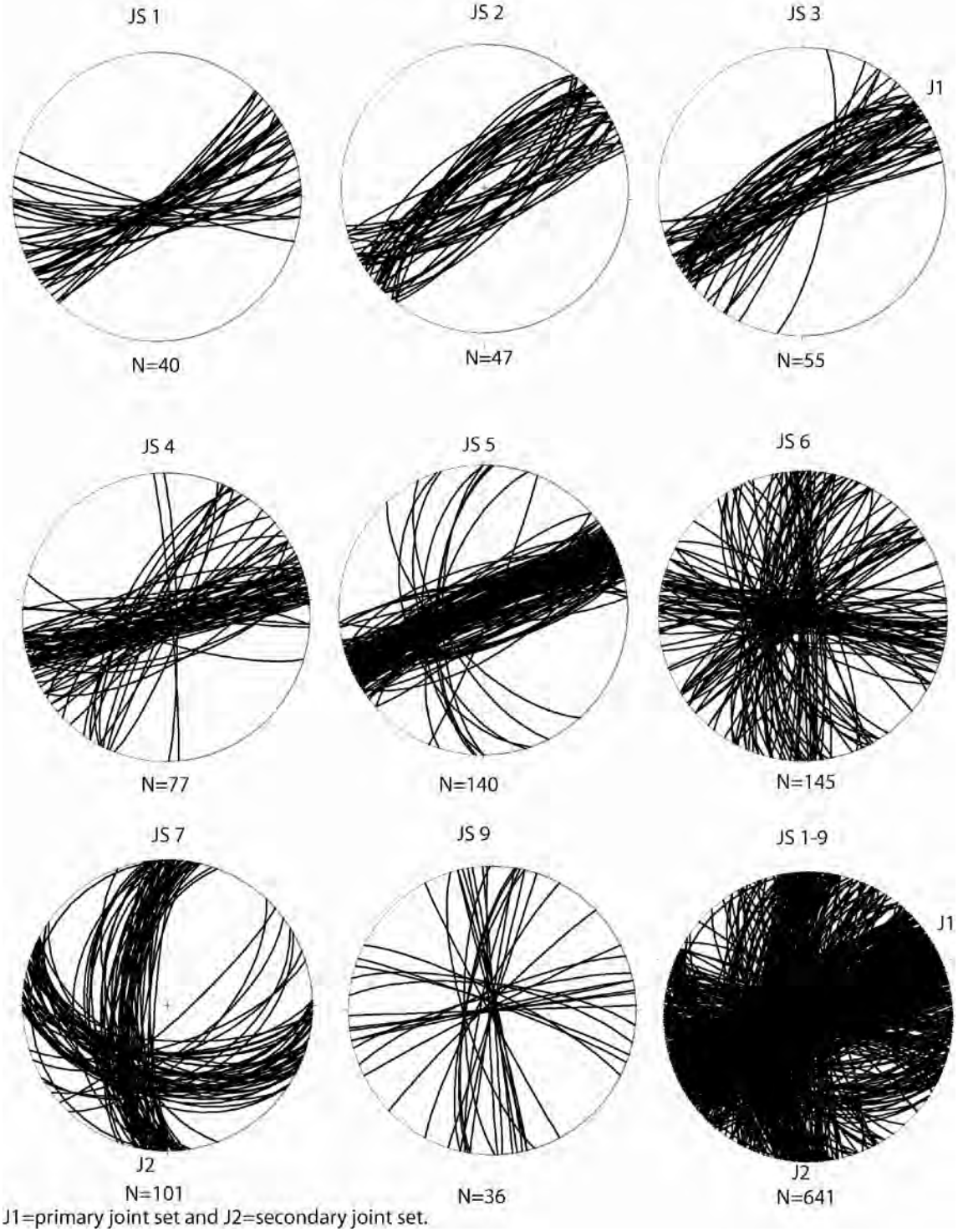

J1=primary joint set and J2=secondary joint set.

Appendix C-3: Stereonets of Oligocene Bishops Conglomerate and the Miocene Browns Park Joints Within the Irish Canyon-Vermillion Creek Area

(Equal Area)

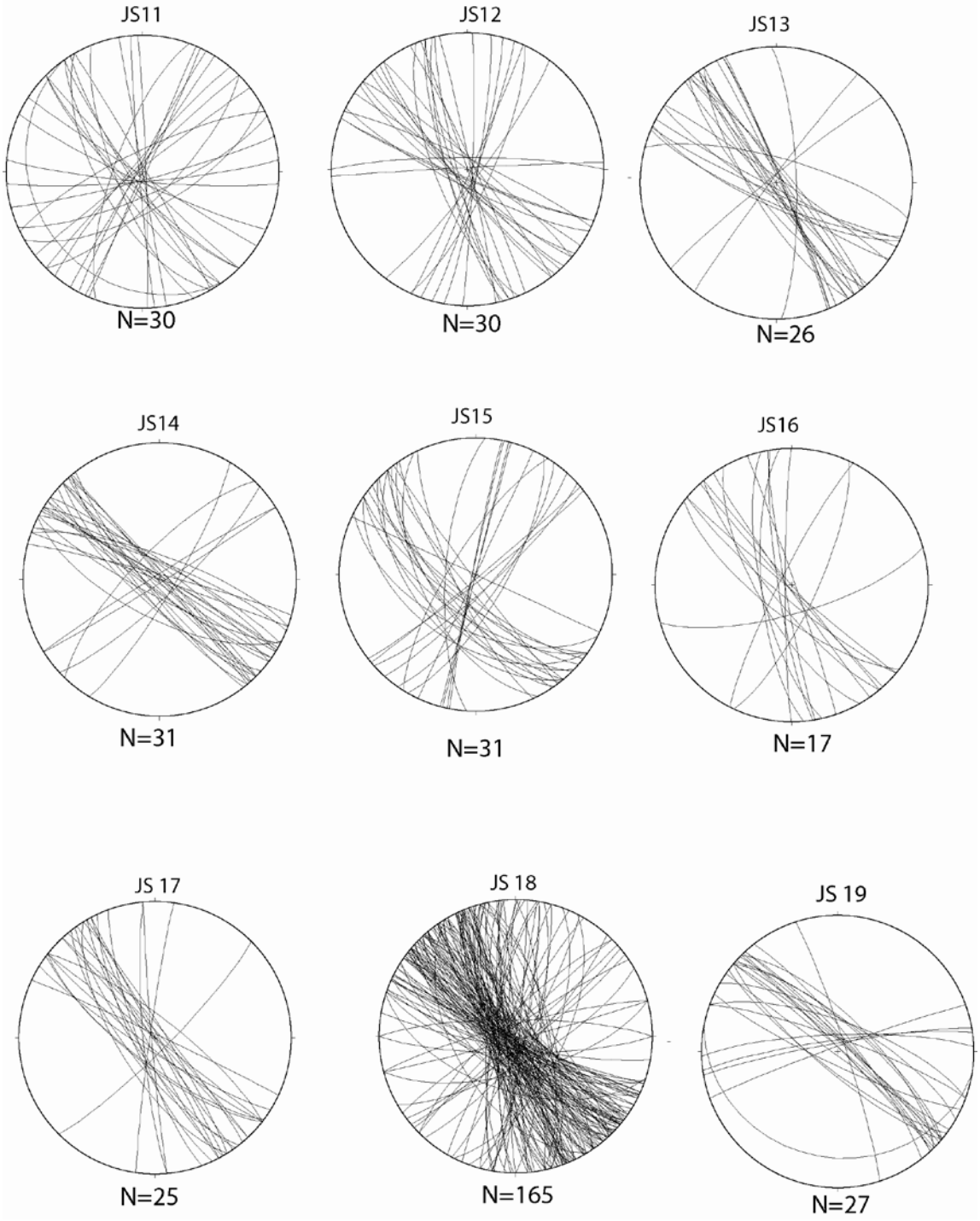

Appendix C-4: Rose Diagrams of Navajo Sandstone Joint Strikes
(Smoothed to 10 degrees)

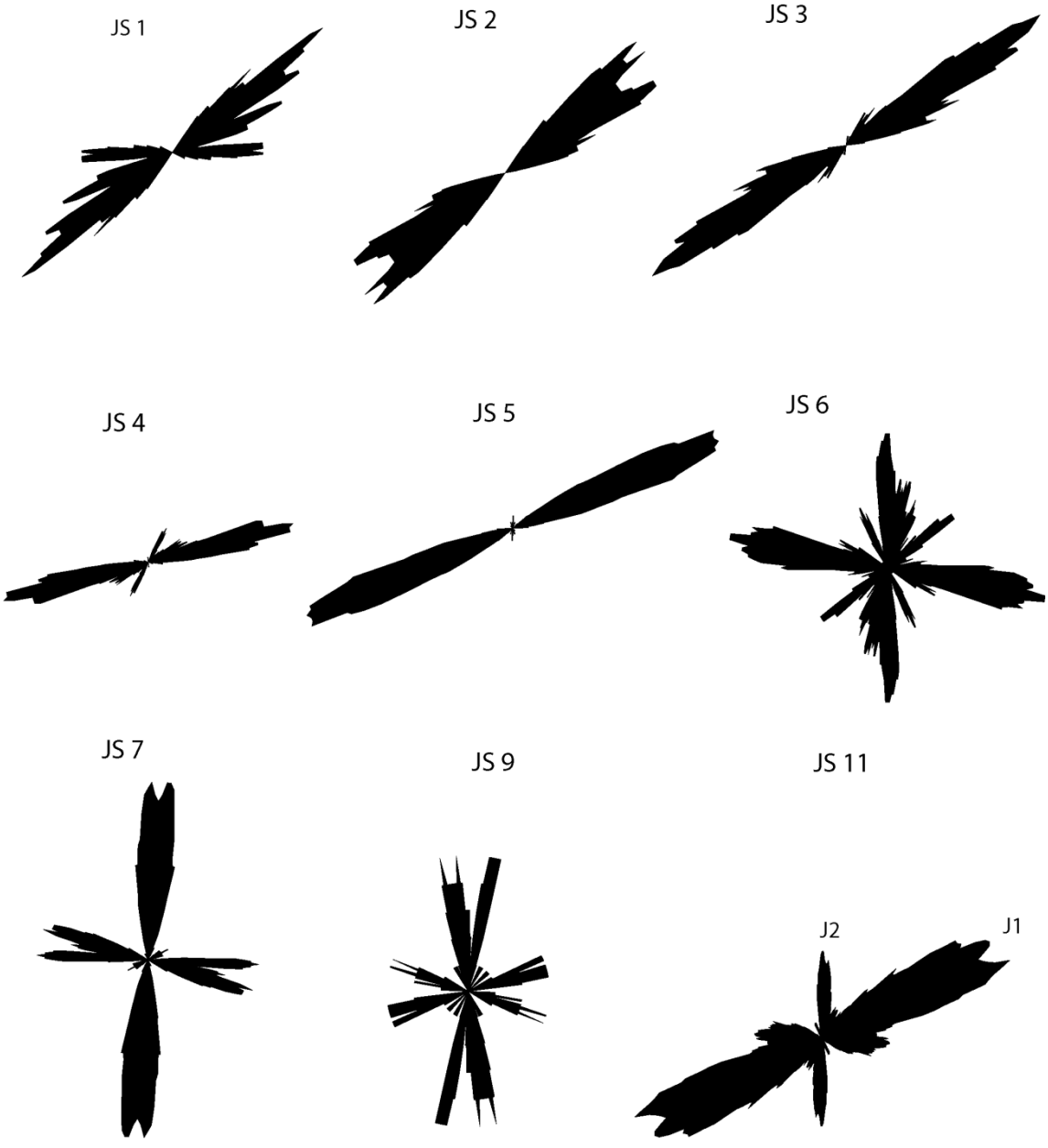

J1=primary joint set and J2=secondary joint set.

Appendix C-5: Rose Diagrams of Oligocene Bishops Conglomerate and Miocene Browns Park Joint Strikes (Smoothed to 10 degrees)

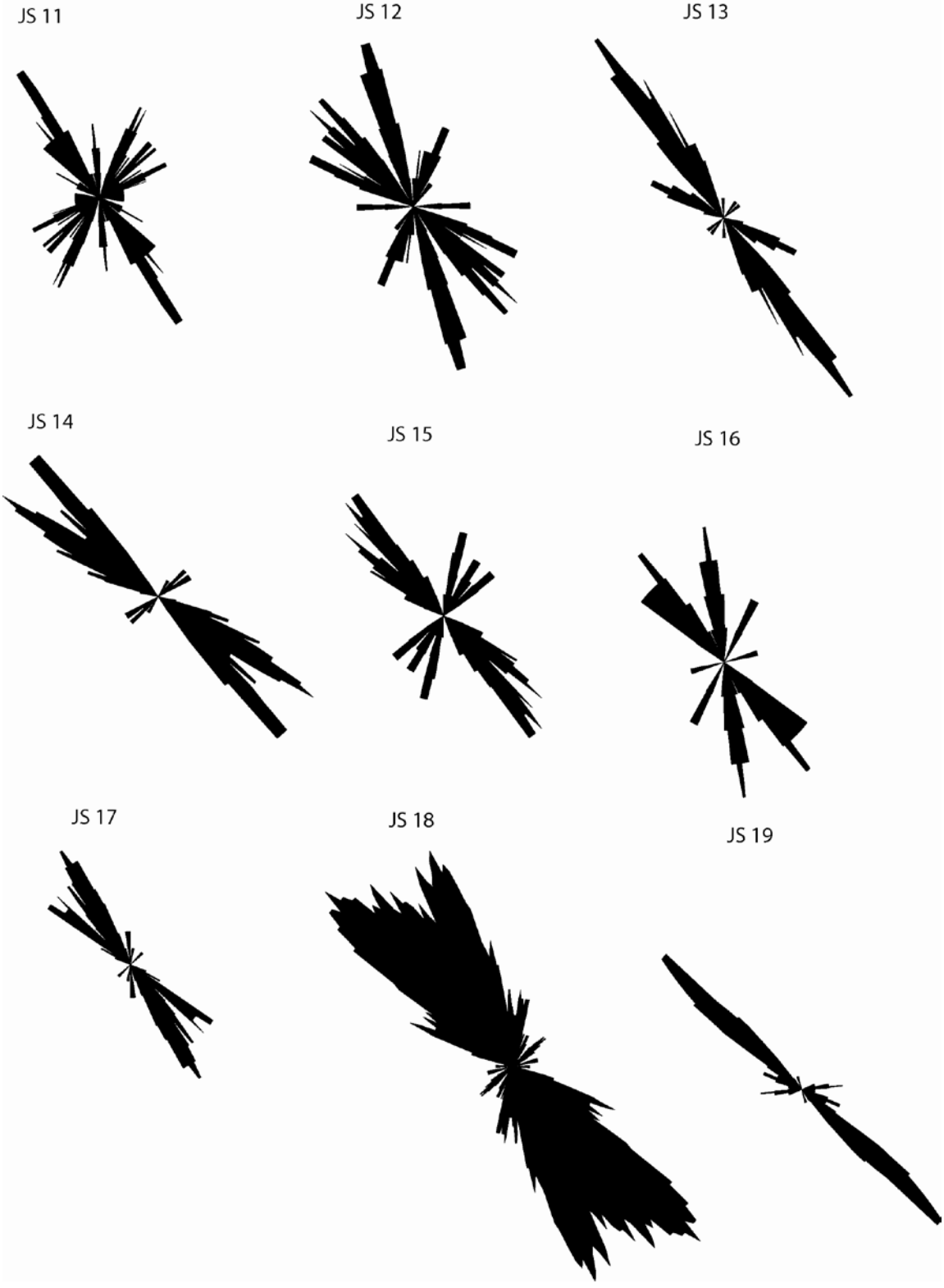

Appendix C-6: Rose Diagram of the Strike of Joint Planes Superimposed on the Rose Diagram of the Strike of Normal Fault Planes Within the Browns Park Formation (Smoothed 10 Degrees)

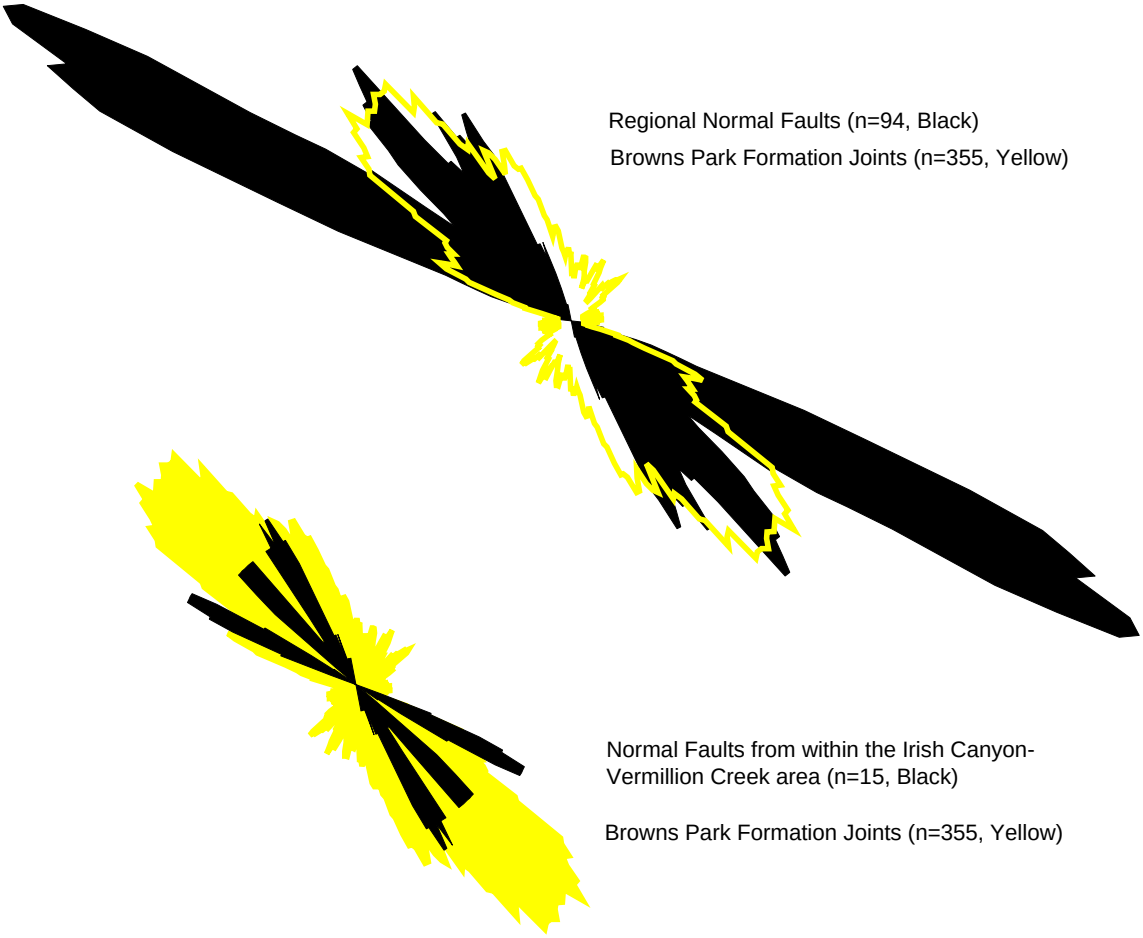

Regional Normal Faults (n=94, Black)

Browns Park Formation Joints (n=355, Yellow)

Normal Faults from within the Irish Canyon-Vermillion Creek area (n=15, Black)

Browns Park Formation Joints (n=355, Yellow)

Appendix C-7: Stereonets and Rose Diagrams of Raw Joint Data and of Joint Data Restored to Pre-Fold Orientation

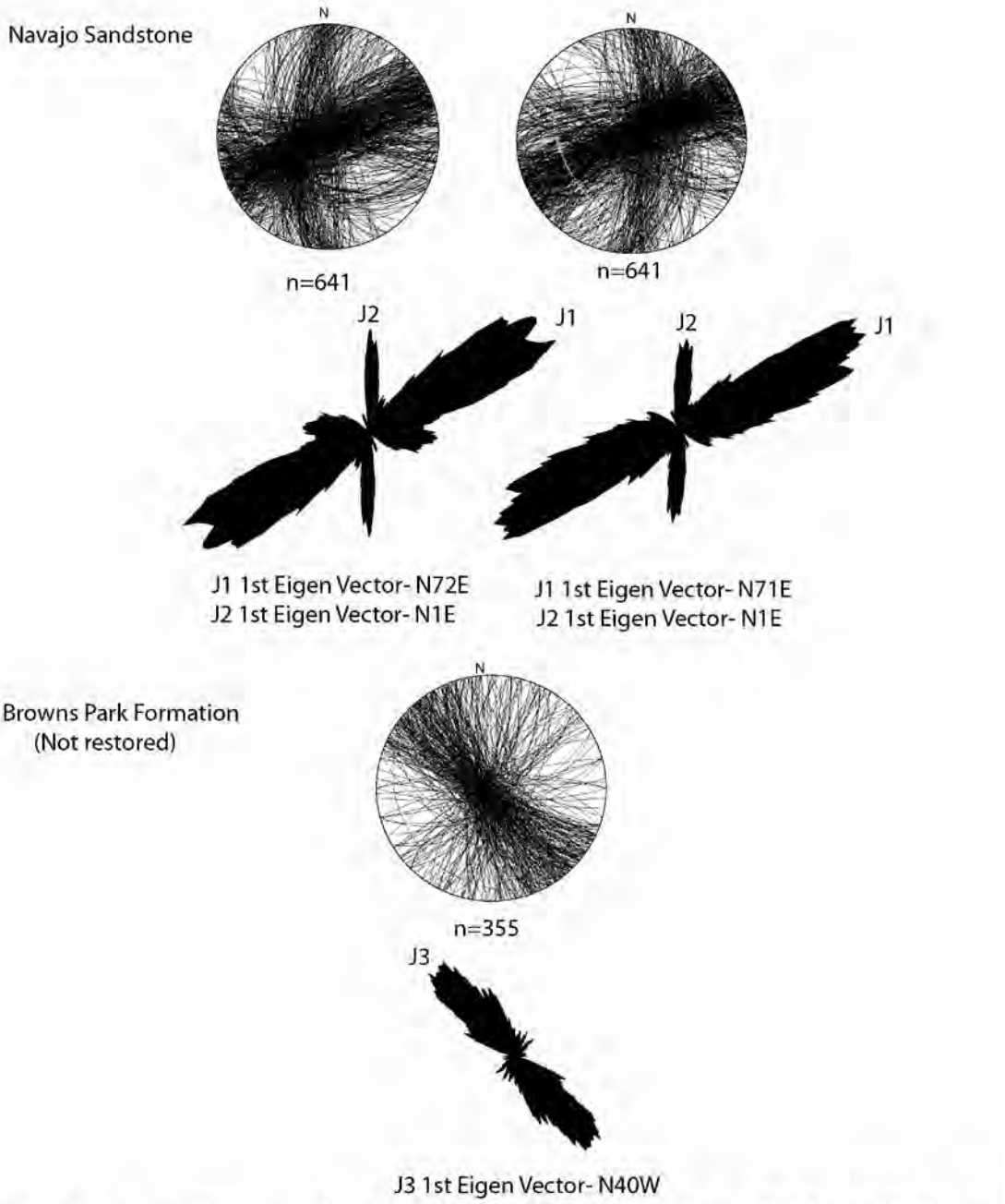

Smoothing increment of 10 degrees for rose diagrams. Data rotated 40 degrees SW about a N30W axis. Browns Park Data is interpreted as post-orogenic and was not restored.

Appendix C-8: Stereonets and Rose Diagrams of Fold Corrected Joint Strikes

Navajo Sandstone

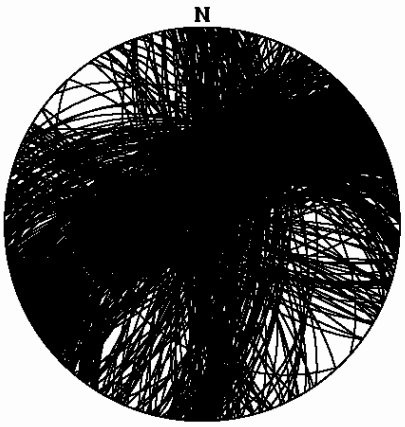

n=641

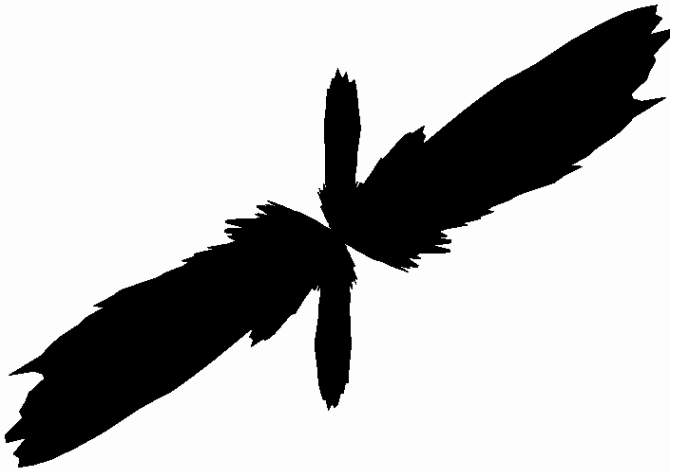

Vector Mean- N71E

Browns Park Formation

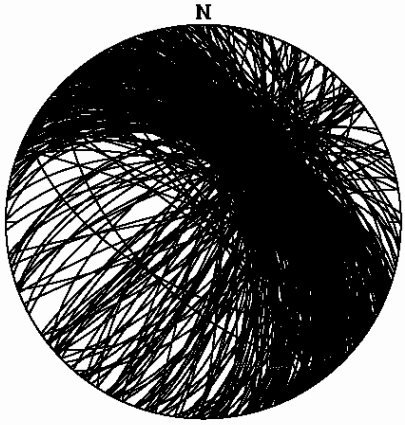

n=355

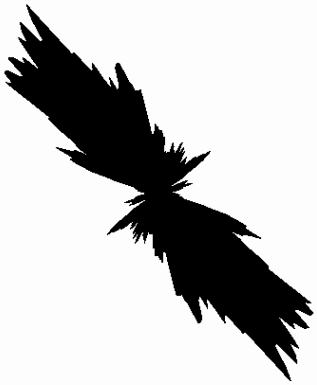

Vector Mean- N35W

Smoothing increment of 10 degrees for rose diagrams